Application of the Proper Orthogonal Decomposition to Slat Cove Noise Modeling

by

Tony Lau

B.S., Aerospace Engineering
University of California, Los Angeles, 2000

Submitted to the Department of Aeronautics and Astronautics
in partial fulfillment of the requirements for the degree of

Master of Science in Aeronautics and Astronautics

at the

MASSACHUSETTS INSTITUTE OF TECHNOLOGY

June 2003

Author .....
Tony Lau
Department of Aeronautics and Astronautics
May 23, 2003

Certified by..
Karen Willcox
Assistant Professor
Thesis Supervisor

Accepted by .....
Edward M. Greitzer
H.N. Slater Professor of Aeronautics and Astronautics
Chair, Committee on Graduate Students

Application of the Proper Orthogonal Decomposition to Slat Cove Noise Modeling

by

Tony Lau

Submitted to the Department of Aeronautics and Astronautics
on May 23, 2003, in partial fulfillment of the
requirements for the degree of
Master of Science in Aeronautics and Astronautics

Abstract

The Proper Orthogonal Decomposition (POD) is used to characterize the unsteady dynamic flow field in the slat cove region of the Energy Efficient Transport (EET) airfoil. Snapshots acquired from a computational fluid dynamics (CFD) simulation are analyzed *a posteriori* using the POD to extract the dominating coherent structures in the slat cove. The simulation is examined at three different angles of attack (4, 6, and 8 degrees), and the pressure and velocity fields of each system are decomposed into optimal basis functions. These POD modes are optimal in terms of their representation of energy present within the original data ensemble. Furthermore, it is found that many of the modes contain structures inherent to the actual phenomena present in the flow field.

The basis functions are then used to construct low-order approximations to the original data in a linear superposition. The eigenvalue spectrum indicates that most of the energy is contained in the leading POD modes, and reasonable fidelity is achieved in the reconstructions using less than 30 percent of the POD modes available.

An acoustic study determines the noise generated by the slat cove region using the POD reconstructions. Using an acoustic solver based on the Ffowcs Williams Hawkings equation, the acoustic signature is calculated for the POD reconstructions as well as the original CFD solutions based on a source line surrounding the slat region. The acoustic signal based on the POD reconstructions does not exactly reproduce the CFD generated acoustics, but instead tends to over-predict the resulting sound level output.

From the original CFD simulation data, it was seen that the flow field of the 8-degree system was noticeably less dynamic than the 4- and 6-degree systems and that a lower noise signature was computed for the 8-degree model. The nature of this change is evidenced by a cross-projection of the modes across the three systems, yielding a comparison of the structure and position of the initial POD modes in each basis set. Thus, a criterion for characterizing the dynamics in the slat cove region of the airfoil is established. Finally, to further enhance data reduction, a more compact, unified model is created using the basis set from the decomposition of a single system.

Thesis Supervisor: Karen Willcox
Title: Assistant Professor

Acknowledgments

In this age, which believes that there is a short cut to everything, the greatest lesson to be learned is that the most difficult way is, in the long run, the easiest.

–Henry Miller

This is what I've been waiting for – an opportunity to thank the many people in my life that have shared the pains and frustrations during my three-year stint at MIT, and more importantly the laughter and good times that made every day better than the previous.

First and foremost, this thesis could not have been completed without my advisor **Karen Willcox**, who entrusted me with the confidence and resources as one of the first student researchers in her nascent academic career. I have found her to be not only inspiring and motivating, but also understanding of the tribulations of being a student at MIT.

I must also acknowledge **Bart Singer**, my NASA technical advisor, along with the entire Computational Modeling and Simulation Branch at NASA Langley Research Center, who have been a wealth of knowledge and a fountain of information. I especially am indebted to **David Lockard** for his quick turnaround times in answering my multitude of questions. I would not have survived living in Virginia had I not met **Jillisa Hope Knutson**, still the best roommate in the world. I should probably also thank **Chris Thornton**, first for not killing me, and also for giving Jillisa and I more reasons to go to Busch Gardens!

I thank the **FDRL/ACDL** student researchers for contributing to a healthy working environment and also providing welcome diversions to the sometimes tedious days (and nights) in the office. From the beginning, **David Venditti** and **Victor Garzon** never failed to elevate my questions to the highest priority, regardless of what deadlines they may have been facing. I give thanks to **Alex Sauer-Budge**, my fellow Apple enthusiast, for showing me how I could do just about anything I want to on my trusty PowerBook, even lab work! If it were not for **Sudeep Lahiri** and his ability to think coherently late at night, I would not have had something to look forward after graduating. Thanks to **Mark Santi** for taking over when I could proofread no more. The **Back Office Crew**, an eclectic and ever-changing bunch, made every day an interesting one to say the least – **Larry Baskett** would pop in another tune into his 8-track player, **Ricardo Powell** would try to convince us that nothing is real and everything is relative, and **Sean Bradshaw** would show us the best way to get rich and retire early.

I cannot even begin to express how fortunate I am to have been in the company of so many good friends I have met during these past three years. I never thought I'd fit in anywhere when I first came to Boston, but was quickly proven otherwise by the **first-year Tang** crew. I was inspired to great heights by the always ambitious **Salil Soman**, kept alive by the culinary delights of **Mimi Lee**, and forced to socialize by the oh-so-gregarious **Stephanie Xie**. A special thank you goes out to **Nate Quitoriano**, who carried me through my most difficult times during my first year.

The **28 Windsor** crew, with whom I should have lived in the first place, gave me a welcome and necessary change of scenery from my second-year frustrations. **Joshua McConnell** and **Robert LePome** proved that death by turtle shells felt much better than death by control theory. I tried my best to emulate the always chill **Jason Sickler**, the two of us enjoying the stretch of an extended Master's program.

My list of friends has grown even larger with this year's **ghetto-retto** posse, whose name sums it all up. I thank **Vivian Lei** for all the social gatherings that bought us together, doughboy **Steve Kohen** for lending his blender to feed my smoothie obsession, and Queen Ghetto herself, **Sarah Rodriguez**, for her Strong Island influence. I was never out of the loop thanks to **Tyrone Hill**, whose verbal diarrhea kept me updated with all the news not fit to print. The days flew by thanks to **Shawn Kuo**, reliably supportive of my procrastinating efforts, whether it be for BOBA, smoothies, games, basketball, or ultimate. Finally, my sincerest appreciations go to **Chris Rycroft** for the many hours of thesis help – math genius, LaTeX guru, Iron Chef, master juggler – is there anything this kid can't do?! Best of luck to all of you, especially those who are in it for the long run.

Through all that, I can't forget about the **FobFive** basketball crew, for nothing other than sharing my cult obsession with the sport. Props to **Alex Wong**, **Junius Ho**, and **Jae Kim** for passing me the rock with confidence! It's all about the mid-range J! And even though we enjoyed more exquisite sushi dinners than pickup games together, I thank **Kelvin Chan** for providing a mirrored perspective of my own life in those fine discussions.

Thanks to the **Daly City Posse** for pushing me to new heights, backed with unyielding assurance and encouragement regardless of how many thousands of miles stand between us. To **Chester Chow**, **Lester Chow**, **Sharon Ferrer**, **Khristine Marcos**, **Katrina Segundo**, and **Tisza Lintoco**, I am grateful that you saw more potential in me that I could have ever imagined. There is not enough space to reminisce about the great times we've shared in the past, but I always look forward to creating new memories in the future.

Finally, I have nothing but love and respect for my family, who have endured over 24 years of my existence. I share a unique bond with my two sisters, **Maria** and **Agnes** – all those years growing up in each other's business have kept us close. I thank my parents, who themselves have sacrificed so much to fulfill their dreams of seeing their children succeed in all walks of life. I thrive on the encouraging words of my **Mom**, who knew the solution to every problem that was and ever will be. I strive to follow in the footsteps of my **Dad**, whose penchant for hard work and outpouring of unconditional support has found its way into my way of being. This thesis attests as much to the accomplishment of my parents as it does mine. And, of course, my dog **Lucky** deserves utmost praise and recognition for being the most loyal, fun-loving, and occasionally-obedient canine I ever knew.

This research was supported in part by Bart Singer, the NASA Langley Research Center, and the NASA Graduate Student Researchers Program.

Contents

1 Introduction **15**

1.1 Background 15

1.1.1 Airframe Noise 16

1.2 Recent Investigations 16

1.2.1 Experimental Work 16

1.2.2 Analytical and Computational Analyses 17

1.3 Motivation 18

1.3.1 Overview: The Proper Orthogonal Decomposition 19

1.4 Research Objectives 20

1.4.1 Thesis Overview 21

2 POD and Aeroacoustics Theory **23**

2.1 General POD Theory 23

2.1.1 Method of Snapshots 27

2.2 Acoustics Framework 29

3 POD Modes **33**

3.1 Data Setup 33

3.1.1 CFD Analysis 33

3.1.2 Snapshot Ensemble 37

3.2 POD Analysis 38

3.2.1 Eigenvalue Energy 39

3.2.2 POD Pressure Modes 43

3.2.3 POD Velocity Modes 60

3.3 Summary 71

4 Snapshot Reconstruction **77**

4.1 Low-Rank Approximations 77

4.1.1 Energy Considerations 77

4.1.2 Reconstructions 80

4.2 Data Reduction Aspects 90

4.3 Acoustic Predictions 91

4.3.1 Implementation 91

4.3.2 Acoustic Observations Based on POD Reconstructions 94

5 Parameterization of Slat Data **101**

5.1 Motivation 101

5.2 POD Modes Across Angles Of Attack 102

5.2.1 Cross-Projections 102

5.2.2 Reconstructions Utilizing Cross-Projections 109

6 Conclusion **115**

6.1 Summary 115

6.2 Future Work 116

A Eigenvalue Data **119**

B POD Modes **133**

B.1 POD Pressure Modes 13-36 133

B.2 POD Velocity Modes 13-36 146

List of Figures

1-1 Energy Efficient Transport Airfoil. 17

1-2 Measured acoustic spectra for EET slat 18

2-1 Schematic of **fwh2d** input/output. 31

3-1 Computational mesh in vicinity of slat. 34

3-2 Instantaneous vorticity field snapshots. 36

3-3 Pressure eigenvalues – Magnitude. 39

3-4 Pressure eigenvalues – Percent energy. 40

3-5 Velocity eigenvalues – Magnitude. 41

3-6 Velocity eigenvalues – Percent energy. 42

3-7 4-degree pressure modes 1–6. 44

3-8 4-degree pressure modes 7–12. 45

3-9 Temporal projection magnitudes of 4-degree pressure modes 1–10 46

3-10 Temporal projection magnitudes of 4-degree pressure modes 10–20 47

3-11 6° pressure mode 1 containing 32% energy. 48

3-12 6-degree Pressure Modes 1–6 50

3-13 6-degree pressure modes 7–12. 51

3-14 Temporal projection magnitudes of 6-degree pressure modes 10-20 52

3-15 Temporal projection magnitudes of 6-degree pressure modes 10-20 53

3-16 8-degree pressure modes 1–6. 56

3-17 8-degree pressure modes 7–12. 57

3-18 Temporal projection magnitudes of 8-degree pressure modes 1-10 58

3-19 Temporal projection magnitudes of 8-degree pressure modes 10-20 59

3-20 4-degree velocity modes 1–6. 61

3-21 4-degree velocity modes 7–12. 62
3-22 Temporal projection magnitudes of 4-degree velocity modes 1-10 63
3-23 Temporal projection magnitudes of 4-degree velocity modes 10-20 64
3-24 6-degree velocity modes 1–6. 65
3-25 6-degree velocity modes 7–12. 66
3-26 Temporal projection magnitudes of 6-degree velocity modes 1-10 67
3-27 Temporal projection magnitudes of 6-degree velocity modes 10-20 68
3-28 6-degree velocity mode 3. 69
3-29 8-degree velocity modes 1–6. 72
3-30 8-degree velocity modes 7–12. 73
3-31 Temporal projection magnitudes of 8-degree velocity modes 1-10 74
3-32 Temporal projection magnitudes of 8-degree velocity modes 10-20 75

4-1 Accumulated energy content of POD modes - Pressure energy. 79
4-2 Accumulated energy content of POD modes - Kinetic energy. 81
4-3 4-degree pressure reconstruction snapshots. 82
4-4 6-degree pressure reconstruction snapshots. 83
4-5 8-degree pressure reconstruction snapshots. 84
4-6 4-degree velocity reconstruction snapshots. 87
4-7 6-degree velocity reconstruction snapshots. 88
4-8 8-degree velocity reconstruction snapshots. 89
4-9 Source lines for acoustic propagation. 92
4-10 Acoustic signatures along source lines 93
4-11 Acoustic signatures at 4-degrees angle of attack. 95
4-12 Acoustic signatures at 6-degrees angle of attack. 97
4-13 Acoustic signatures at 8-degrees angle of attack. 98
4-14 Rate of convergence of acoustic signals 100

5-1 4-degree pressure modes cross-projected onto 6-degree pressure modes. . . . 103
5-2 4-degree pressure modes cross-projected onto 8-degree pressure modes. . . . 104
5-3 6-degree pressure modes cross-projected onto 4-degree pressure modes. . . . 105
5-4 6-degree pressure modes cross-projected onto 8-degree pressure modes. . . . 106
5-5 8-degree pressure modes cross-projected onto 4-degree pressure modes. . . . 107

5-6 8-degree pressure modes cross-projected onto 6-degree pressure modes. . . . 108
5-7 Extracted mean flows and linearization results. 110
5-8 4-degree pressure reconstruction snapshots using 6-degree modes. 112
5-9 8-degree pressure reconstruction snapshots using 6-degree modes. 113

B-1 4-degree pressure modes 13–18. 134
B-2 4-degree pressure modes 19–24. 135
B-3 4-degree pressure modes 25–30. 136
B-4 4-degree pressure modes 31–36. 137
B-5 6-degree pressure modes 13–18. 138
B-6 6-degree pressure modes 19–24. 139
B-7 6-degree pressure modes 25–30. 140
B-8 6-degree pressure modes 31–36. 141
B-9 8-degree pressure modes 13–18. 142
B-10 8-degree pressure modes 19–24. 143
B-11 8-degree pressure modes 25–30. 144
B-12 8-degree pressure modes 31–36. 145
B-13 4-degree velocity modes 13–18. 147
B-14 4-degree velocity modes 19–24. 148
B-15 4-degree velocity modes 25–30. 149
B-16 4-degree velocity modes 31–36. 150
B-17 6-degree velocity modes 13–18. 151
B-18 6-degree velocity modes 19–24. 152
B-19 6-degree velocity modes 25–30. 153
B-20 6-degree velocity modes 31–36. 154
B-21 8-degree velocity modes 13–18. 155
B-22 8-degree velocity modes 19–24. 156
B-23 8-degree velocity modes 25–30. 157
B-24 8-degree velocity modes 31–36. 158

List of Tables

4.1 Number of modes required to capture pressure energy. 80
4.2 Number of modes required to capture kinetic energy. 80

A.1 4° pressure eigenvalue data. 120
A.2 6° pressure eigenvalue data. 122
A.3 8° pressure eigenvalue data. 124
A.4 4° velocity eigenvalue data. 126
A.5 6° velocity eigenvalue data. 128
A.6 8° velocity eigenvalue data. 130

Chapter 1

Introduction

Aircraft noise has always been a leading environmental issue in the air transportation industry. Increasingly stringent aircraft noise requirements, in the form of restricted takeoff and landing slots as well as specific departure and arrival routings, have been placed on many aircraft at airports around the world. The need to discover ways to identify and reduce aircraft noise has come to the forefront in recent years, inspiring NASA to develop an environmentally friendly global air transportation system[1, 2].

1.1 Background

In 1997, NASA set a major objective to reduce aircraft noise with 10-year and 25-year goals to reduce aircraft noise by a factor of two and four, respectively, from 1997 baseline levels. Industry, academia, and the Federal Aviation Administration have been working with NASA to research and develop these technologies. This research supports that effort.

Inside the mission to reduce aircraft noise, three separate components are being considered by NASA: engine noise, airframe noise, and operations noise. Noise reduction in each of these three areas will allow for greater efficiency and productivity in the aviation industry as a whole. Operational noise has been minimized through careful airport planning, with revised departure and approach paths to lessen the impact on the environment. Furthermore, an extensive amount of research and development has already taken place to reduce powerplant noise. As operational control and high-bypass engines are refined to emit less noise, the airframe consequently has become responsible for a greater share of the total noise generated by an aircraft. This is distinctly apparent under approach and

landing conditions when aircraft engines are brought close to idle power and can account for nearly half of the noise produced by an aircraft[18]. It is because of this fact that there is an immense interest in analyzing airframe noise, such as that generated by slats, flaps, and landing gears.

1.1.1 Airframe Noise

Improved aerodynamics was the principal engineering objective when designing high-lift surfaces for airfoils. The leading edge slat of a multi-element wing was designed to delay the onset of main element separation by alleviating the suction side pressure peak of the main element leading edge. This was achieved by accelerating flow through the slat gap, which results in an increase of the wing $C_{L_{max}}$[47]. During the critical approach and landing phases of flight, the performance of these high-lift devices was given primary consideration, and issues of noise generation and propagation were overlooked in the systems' designs.

Only recently have the aeroacoustic effects of the slat leading edge and cove region become a focus of study. Due to the large computational cost required to analyze these complex flows, most analyses have necessarily been of the experimental nature. In recent years, however, computational modeling efforts have come to the forefront as numerical techniques improve and computing power increases.

1.2 Recent Investigations

Several studies have been performed to both identify and model the various mechanisms associated with aircraft noise. This section documents previous analytical and computational efforts to model the dynamics and aeroacoustics of airframe noise.

1.2.1 Experimental Work

Tests were conducted at the NASA Langley Research Center Quiet Flow Facility (QFF) during the late 1990's to investigate aeroacoustic effects at the trailing edge flaps[47, 11, 50]. A strong understanding of the flow field and associated acoustic phenomena in this region had been achieved in these studies using the NACA 63_2-215 airfoil. Attention next turned to analysis of the leading edge slat with experiments also performed in the QFF. These tests measured noise levels related to key slat flow features such as the blunt trailing edge

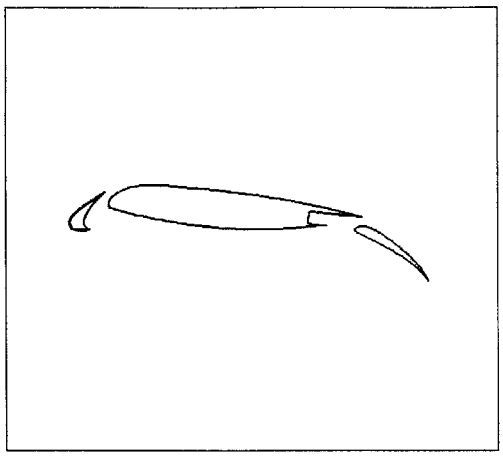

Figure 1-1: Energy Efficient Transport Airfoil.

and the slat gap width.

More recent experimental studies acquired acoustic data using the Energy Efficient Transport (EET) model[48], tested at the NASA Langley Low Turbulence Pressure Tunnel (LTPT)[56, 7, 31]. The EET configuration consists of a slat, a main wing, and a partial-span flap, as shown in Figure 1-1. The microphone array setup and subsequent data processing were developed using techniques at Boeing Commercial Airplane Company[59]. The noise signatures of the three-element EET airfoil were acquired at 20- and 30-degrees and are shown in Figure 1-2. Several interesting features in the acoustic measurements, such as the high-frequency tonal peak in Figure 1-2(b), were analyzed in subsequent computational studies.

1.2.2 Analytical and Computational Analyses

Both analytical and computational studies were pursued in an effort to simulate the aerodynamic effects in the slat region and replicate acoustic results. Analytical work included simple physics models that were created to model the fluid interactions. For example, Guo[26] employed a discrete vortex modeling approach to model the dynamics about the leading edge cusp. The resulting interactions in the slat cove and through the slat gap were captured by this model and related to acoustic phenomena. Khorrami *et al.*[31] and Singer *et al.*[56] conducted detailed computational aerodynamic and aeroacoustic studies on a slat having a blunt trailing edge. From these studies they were able to attribute the

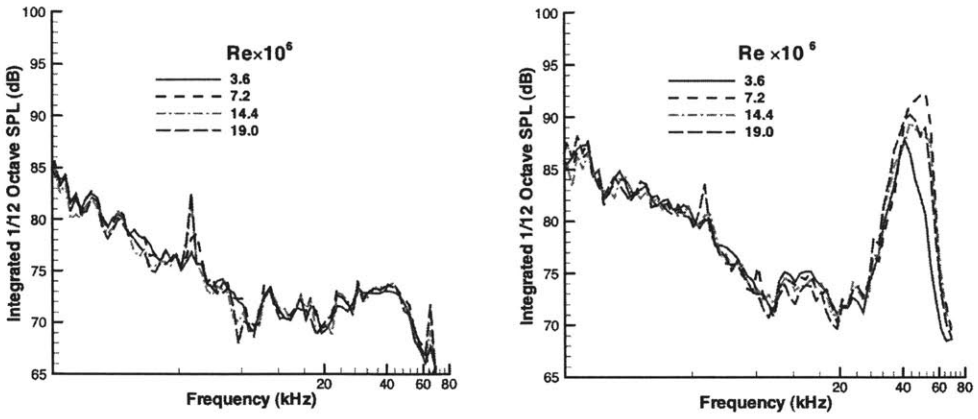

(a) 20° Slat Deflection

(b) 30° Slat Deflection

Figure 1-2: Measured acoustic spectra for EET slat with Ma=0.2. Reynolds number is based on stowed chord and frequencies are model scale frequencies

high-frequency tonal noise shown in Figure 1-2(b) to vortex shedding from the slat trailing edge. In further research, the computational framework was extended to model the slat cove free shear layer. Several attempts to model the dynamics in this region have been made, the most recent being an intensive computational effort utilizing an unsteady Reynolds Averaged Navier-Stokes (uRANS) solver[13, 32, 33]. It is this set of data that we revisit in this thesis with the application of the Proper Orthogonal Decomposition.

1.3 Motivation

It is widely known that the physics behind the mechanisms that generate noise are extremely complicated and expensive to model[39]. It is difficult to resolve the flow characteristics and capture the inherent unsteadiness of an aerodynamic flow. The computational fluid dynamics (CFD) code used to perform these calculations require long runtimes to reconcile the instabilities, separation regions, and turbulent eddies that contribute to the production of noise. The acoustic frequencies created by these instabilities are on the order of 100-10000 Hz, which translate to periods of 0.0001-0.01 seconds. Many time steps are required to resolve the large range of frequencies, and this can lead to extensive computational times for a complete simulation. The uRANS simulation, from which the data for our research is computed, required computational times on the order of months to complete.

Another difficulty in applying a CFD code to calculate aerodynamic noise is due to the dissipative nature of numerical schemes. Sound levels on the order of 100 dB, which is uncomfortably loud to the human ear, has a pressure level over 3000 times less than atmospheric pressure. As a result, acoustic flow phenomena are often masked by the larger-scale hydrodynamic fluctuations in a numerical simulation. As a result, it is computationally difficult to compute aeroacoustic effects simultaneously with fluid dynamics. An accepted alternative to determine acoustic data is to use acoustic analogy methods to calculate aerodynamic noise generated from the governing equations of fluid dynamics. These codes directly calculate far-field acoustic data from near-field unsteadiness by propagating pressure and velocity information through a medium. Using CFD combined with acoustic analogy methods is the current procedure for solving complex aeroacoustic problems. This has enabled fairly accurate acoustic predictions at a relatively inexpensive computational cost.

Computational analyses can be made more efficient by using a reduced order modeling approach. This technique allows for lower order models that require less computational power yet retain the high level of fidelity of a full-order solver. In many cases a reduced order model may decrease the number of states in a problem by several orders of magnitude. The Proper Orthogonal Decomposition is one technique that yields a basis suitable for model order reduction.

1.3.1 Overview: The Proper Orthogonal Decomposition

The Proper Orthogonal Decomposition (POD) was proposed by Lumley[43] as a method to extract organized large-scale coherent structures from turbulent flows. The mathematical basis for the POD is the Karhunen-Loève expansion[30, 41]. Its strength lies in its capability to provide an orthonormal basis for representing any given data in an optimal least squares sense. There have been several formulations of the POD in different fields and it has inherited a number of names, including Principal Components Analysis[29], Hotelling Analysis[28], Empirical Component Analysis[42], Singular Value Decomposition[24], and Empirical Eigenfunction Decomposition[57]. Its applications include obtaining low-dimensional descriptions of turbulent fluid flows[27], structural vibrations[17, 21], damage detection[54], and insect gait[36].

Because the classical POD method required a large number of calculations to determine the optimal basis vectors, this theory was seldom used until the advent of more

powerful computers. With the introduction of a more efficient formulation of the POD technique known the "method of snapshots," a number of highly complex problems became tractable. This included applications in facial recognition[35], signal analysis[3] and data compression[4]. In the field of fluid dynamics, the POD has been used to decompose turbulent flows, including the analysis of turbulent boundary layers[5], bounded flows[6], and shear flows[20].

For modeling efforts, the POD provides a suitable basis for building low-order dynamical models. Projected onto the Navier-Stokes equations, a truncated set of POD modes reduces a system of PDEs down to a low-order ODE system. Reduced order models of this kind have been created to investigate transitional flow[58] and to incorporate feedback control of a cylinder wake[23], for example.

1.4 Research Objectives

This research considers the application of reduced order modeling to complement existing computational and analytical technologies to create an efficient yet accurate resource for studying aeroacoustic phenomena. Combining the aeroacoustic calculations with the fluid dynamic data allows both noise generation and aerodynamic performance to be studied and quantitatively compared. The research performed in this study will concentrate on the data reduction aspects of the POD, which serves as a precursor to building a complete reduced order model.

The goal of this research effort is to apply the Proper Orthogonal Decomposition theory to provide an *a posteriori* analysis of the high-fidelity computational fluid dynamics simulations of the slat cove flow field. From the ensemble of flow field snapshots available, we are interested in identifying dominant coherent structures inherent in the flow. Reconstruction of the flow field data will be performed, and a correlation between the noise output and the large-scale coherent structures will be investigated. We attempt to distinguish the dynamics in the slat cove flow field at each angle of attack by comparing the POD modes for each system. Finally, a further data reduction experiment will be performed to create a unified model based on a single set of POD modes.

1.4.1 Thesis Overview

The Proper Orthogonal Decomposition theory will be presented in Chapter 2, with an emphasis on the method of snapshots. Properties of this POD method will be highlighted, and further application of the theory presented. The aeroacoustics framework will be discussed as a tool to calculate far-field acoustic data.

The application of the POD analysis to the slat cove simulations will be presented in Chapter 3. This chapter will discuss the different approaches used in analyzing the flow variables. A look at the modal energies as well as an examination of the coherent structures in the POD modes will be provided.

Chapter 4 will present the reconstructed data and its relation to the aeroacoustics framework. The flow field snapshots will be reconstructed using the POD modes as an approximation to the original data, and these results will be used to provide an acoustic analysis based on the low-order approximations. A convergence analysis will be performed on the acoustic results to illustrate how well the POD reconstructions provide data for acoustic analysis.

A comparison of the POD modes provided by the studies at three separate angles of attack (4-, 6-, and 8-degrees) will be given in Chapter 5. We aim to characterize changes in the slat flow dynamics between angle of attack by comparing the POD modes. Cross-projections between angle of attack cases will be utilized to reconstruct any member of the original data ensemble.

Chapter 6 summarizes the POD analyses and acoustic assessments for the slat cove study presented here. A discussion of the results of the Proper Orthogonal Decomposition, the acoustic implementation, and a recommended outline for future modeling studies on the slat cove utilizing POD theory will be given.

Chapter 2

POD and Aeroacoustics Theory

The Proper Orthogonal Decomposition will be introduced as a method of obtaining low-dimensional subspaces from an ensemble of high-dimensional data. The goal is to describe a given statistical ensemble with a minimum number of basis vectors. The general POD theory will be presented here as well as its implementation as the method of snapshots. An overview of the acoustic propagation tools used in this research will also be discussed.

2.1 General POD Theory

The Proper Orthogonal Decomposition theory in this section follows References [57, 27, 14].

Methodology

The objective of the POD is to extract coherent structures, which are defined by Lumley[43] as the deterministic functions Φ which are best correlated on average with the set of realizations $\mathbf{U}$. Let $\mathbf{U}$ represent a collection of state variables in the domain Ω. First we define the L_2 inner product between two sample functions $\mathbf{f}$ and $\mathbf{g}$ as

$$(\mathbf{f},\mathbf{g}) = \int_{\Omega} \mathbf{f}\cdot\mathbf{g}\; d\mathbf{x} = \int_{\Omega} \sum_{j=1}^{N} \overline{f}_j(\mathbf{x}) g_j(\mathbf{x})\; d\mathbf{x}, \tag{2.1}$$

where the bar denotes a complex conjugate and N is the dimension of the functions, or more specifically, the dimension of $\mathbf{U}$. The index j denotes the j-th element of the function.

We extract the mean flow from the ensemble by decomposing every $\mathbf{U}$ into a mean and

its fluctuating parts,

$$\mathbf{U} = \langle \mathbf{U} \rangle + \mathbf{u}, \tag{2.2}$$

where $\langle \mathbf{U} \rangle$ is an ensemble average, and thus $\langle \mathbf{u} \rangle = 0$. Having extracted the mean, suppose we wish to describe the functions using a finite linear combination of basis vectors

$$\mathbf{u} = \sum_n a_n(t)\Phi_n(\mathbf{x}). \tag{2.3}$$

This set of basis vectors $\{\Phi_n(\mathbf{x})\}$ may be any complete set of orthonormal functions, for example a Fourier series or the set of Legendre polynomials. Under a linear transformation, this basis set can be used to generate an infinite variety of other sets $\{\Psi_n\}$ by

$$\Psi_n = \sum_m \alpha_{nm}\Phi_m, \tag{2.4}$$

where the α are to be determined and subject only to the constraint

$$\sum_k \overline{\alpha}_{ik}\alpha_{jk} = \delta_{ij}. \tag{2.5}$$

The δ_{ij} is the Kronecker delta

$$\delta_{ij} = \begin{cases} 1 & \text{if} \quad i = j, \\ 0 & \text{if} \quad i \neq j. \end{cases}$$

We care to select a unique set of basis functions from the available functions such that it satisfies

$$\mathbf{u} = \sum_n A_n(t)\Psi_n(\mathbf{x}), \tag{2.6}$$

with the additional requirement that the modes are also uncorrelated and are equal to the solution of the eigenvalue problem shown later

$$\langle A_i, A_j \rangle = \lambda_i \delta_{ij}. \tag{2.7}$$

The goal of the Proper Orthogonal Decomposition is to provide the best linear representation of the basis vectors. That is, we wish to look for the function set $\mathbf{\Psi}$ which has the largest mean square projection on the observations, $|(\mathbf{u}, \mathbf{\Phi})|^2$. This will find the $\mathbf{\Psi}$ whose

structure is most nearly parallel to all the members of the ensemble $\mathbf{u}$. To this effect, we must maximize the expression

$$\frac{\langle |(\mathbf{u}, \mathbf{\Psi})|^2 \rangle}{\|\mathbf{\Psi}\|^2}, \tag{2.8}$$

where the $(\cdot, \cdot)$ is the inner product defined earlier and the $\|\cdot\|$ denotes the L_2 norm

$$\|\mathbf{f}\| = (\mathbf{f}, \mathbf{f})^{\frac{1}{2}}. \tag{2.9}$$

The function $\mathbf{\Psi}$ then corresponds to the particular solution of the constrained optimization problem in $\mathbf{\Phi}$

$$\max_{\mathbf{\Phi}} \frac{\langle |(\mathbf{u}, \mathbf{\Phi})|^2 \rangle}{\|\mathbf{\Phi}\|^2} = \frac{\langle |(\mathbf{u}, \mathbf{\Psi})|^2 \rangle}{\|\mathbf{\Psi}\|^2}, \tag{2.10}$$

subject to $(\mathbf{\Psi}, \mathbf{\Psi}) = \|\mathbf{\Psi}\|^2 = 1$.

Let us now introduce the two-point spatial correlation function $\mathbf{K}$ as

$$K_{mn}(\mathbf{x}, \mathbf{x}') = \langle u_m(\mathbf{x}, t) \overline{u}_n(\mathbf{x}', t) \rangle \tag{2.11}$$

or in vector notation,

$$\mathbf{K}(\mathbf{x}, \mathbf{x}') = \langle \mathbf{u}(\mathbf{x}, t) \otimes \overline{\mathbf{u}}(\mathbf{x}', t) \rangle. \tag{2.12}$$

The operator $\otimes$ denotes the dyadic, or outer, vector product. Substituting Equations 2.6 and 2.7 into 2.12, we get

$$\mathbf{K}(\mathbf{x}, \mathbf{x}') = \sum_n \lambda_n \Psi_n(\mathbf{x}) \overline{\Psi}_n(\mathbf{x}'), \tag{2.13}$$

which can be rewritten as

$$\int_\Omega \mathbf{K}(\mathbf{x}, \mathbf{x}') \mathbf{\Psi}(\mathbf{x}') \, d\mathbf{x}' = \lambda \mathbf{\Psi}(\mathbf{x}). \tag{2.14}$$

This is related to Equation 2.8 by the following calculation:

$$\begin{aligned}
(\mathbf{K}\mathbf{\Psi}, \mathbf{\Psi}) &= \left(\int_\Omega \langle \mathbf{u}(\mathbf{x}) \otimes \overline{\mathbf{u}}(\mathbf{x}') \rangle \mathbf{\Psi}(\mathbf{x}') \, d\mathbf{x}', \mathbf{\Psi}(\mathbf{x}) \right) \\
&= \int_\Omega \int_\Omega \langle \mathbf{u}(\mathbf{x}) \otimes \overline{\mathbf{u}}(\mathbf{x}') \rangle \mathbf{\Psi}(\mathbf{x}') \, d\mathbf{x}' \cdot \overline{\mathbf{\Psi}}(\mathbf{x}) \, d\mathbf{x} \\
&= \langle \int_\Omega \mathbf{u}(\mathbf{x}) \cdot \overline{\mathbf{\Psi}}(\mathbf{x}) \, d\mathbf{x} \quad \int_\Omega \overline{\mathbf{u}}(\mathbf{x}') \cdot \mathbf{\Psi}(\mathbf{x}') \, d\mathbf{x}' \rangle \\
&= \langle |(\mathbf{u}, \mathbf{\Psi})|^2 \rangle \geq 0.
\end{aligned} \tag{2.15}$$

It follows that $(\Psi, \mathbf{K}\Phi) = (\Psi, \langle \mathbf{u}, \overline{\mathbf{u}} \rangle \Phi) = \langle (\Psi, \mathbf{u})(\mathbf{u}, \Phi) \rangle = (\mathbf{K}\Psi, \Phi)$. Thus, $\mathbf{K}$ is a non-negative Hermitian operator, and spectral theory[53, 16] guarantees the maximization of Equation 2.10 and admits a solution equal to the largest eigenvalue of the problem in Equation 2.14. Spectral theory also assures us of the existence of a unique and complete set of basis functions, whose eigenvalues may be written as

$$\lambda_n = (\mathbf{K}\Psi_n, \Psi_n) = \langle |(\mathbf{u}, \Psi_n)|^2 \rangle = \lim_{T \to \infty} \frac{1}{T} \int_0^T |(\mathbf{u}, \Psi_n)|^2 \, dt. \tag{2.16}$$

The eigenvalue λ_n represents the mean energy of the system projected onto the basis Ψ_n. The mean energy in a flow field may be thought of as

$$E = \int_\Omega \langle u_j(\mathbf{x}) u_j(\mathbf{x}) \rangle \, d\mathbf{x}. \tag{2.17}$$

Substituting Equation 2.11 and employing Equation 2.14, we may exercise the orthonormality of Ψ to calculate the mean energy E of the system as

$$E = \sum_{j=1}^{N} \int_\Omega K_{jj}(\mathbf{x}, \mathbf{x}) \, d\mathbf{x} = \sum_n \lambda_n. \tag{2.18}$$

Because the eigenfunctions form a complete orthogonal set, every member of the original snapshots can be reconstructed by a modal decomposition using Equation 2.6. The coefficients A in Equation 2.6 are found using orthonormality conditions of the eigenfunctions Ψ

$$A_j = (\mathbf{u}, \Psi) = \sum_{i=1}^{N} \int_\Omega u_i(\mathbf{x}) \Psi_{ij}(\mathbf{x}) \, d\mathbf{x}, \tag{2.19}$$

where the ij index on Ψ refers to the component-wise multiplication over the j-th basis vector.

The POD modes generated by the eigenfunctions of the correlation matrix are optimal in the sense that the mean-square error resulting from a finite representation of the functions $\mathbf{u}$ is minimized. When ordered from largest to smallest, the eigenvalues determine the relative weight each mode contributes to the system model. If the eigenvalues decay quickly, then most of the system dynamics can be captured using a reduced number of modes. A set of K basis vectors can be chosen from the set determined by the POD which will represent the desired system behavior. Furthermore, the reduced set of basis vectors K can be selected

in such a way that the desired fidelity of the system is preserved. For any K-th order truncation of the series of Equation 2.6,

$$\|\mathbf{u} - \mathbf{u}_K\|^2 = \int_\Omega \left[\mathbf{u}(\mathbf{x}) - \sum_{n=1}^{K} A_n \Psi_n(\mathbf{x})\right]^2 d\mathbf{x} \tag{2.20}$$

is minimized if and only if the $\Psi_j(\mathbf{x})$ are eigenfunction solutions of Equation 2.14.

2.1.1 Method of Snapshots

Computational analyses and simulations deal with discretizations of continuous systems. In the case of a CFD simulation, the Navier-Stokes equation is computed at every node in a computational mesh, yielding a set of solutions for every timestep calculated in the simulation. More generally, this collection of data may be any realizable quantity, whether measured by experiment or calculated numerically from simulation. For example, the collection of N state variables may consist of strain gauge readings from a structure or N velocity probes in a fluid. More than one quantity may be measured at a location as well, such as the four state variables $(\rho, \rho u, \rho v, E)$ in a two-dimensional inviscid fluid flow simulation. Each quantity recorded simply becomes another realization in the set $\mathbf{u}$. For a numerical simulation performed on a large number of gridpoints N, the eigenvalue problem of Equation 2.14 becomes an $N \times N$ eigenvalue problem, and can quickly grow too large for today's computer systems.

Suppose instead we take M "snapshots" of the data set resulting in M images of the N simultaneously collected data points. In each snapshot, the relevant flow field quantities are recorded at each of the nodes in the computational mesh. We then have a collection of ensemble members which adequately describes the process, and that $\{\mathbf{u}^{(k)}\}_{k=1}^{M}$ represents the realizations of the grid quantities at each recorded time.

Sirovich[57] determined that when the number of linearly independent snapshots, M, is smaller than the dimension of N, it is more efficient to express the basis function as a linear combination of the original snapshots. As a result, $\mathbf{\Psi}$ takes on a special form in terms of the original data as

$$\mathbf{\Psi} = \sum_{k=1}^{M} \beta_k \mathbf{u}^{(k)} \tag{2.21}$$

where β_k are coefficients yet to be determined. Assuming ergodicity, the interchangeability

of the time average with the ensemble average, we may now write the correlation function in Equation 2.12 as

$$\mathbf{K}(\mathbf{x},\mathbf{x}') = \frac{1}{M}\sum_{n=1}^{M}\mathbf{u}^{(n)}(\mathbf{x})\otimes\mathbf{u}^{(n)}(\mathbf{x}'). \tag{2.22}$$

The discretized eigenvalue problem of Equation 2.14 then becomes

$$\left(\frac{1}{M}\sum_{i=1}^{M}\mathbf{u}^{(i)}(\mathbf{x})\otimes\mathbf{u}^{(i)}(\mathbf{x}'),\sum_{k=1}^{M}\beta_k\mathbf{u}^{(k)}(\mathbf{x})\right) = \lambda\sum_{k=1}^{M}\beta_k\mathbf{u}^{(k)}(\mathbf{x}). \tag{2.23}$$

This reduces to

$$\sum_{i=1}^{M}\left[\sum_{k=1}^{M}\frac{1}{M}(\mathbf{u}^{(i)}(\mathbf{x}),\mathbf{u}^{(k)}(\mathbf{x}))\beta_k\right]\mathbf{u}^{(i)}(\mathbf{x}) = \lambda\sum_{k=1}^{M}\beta_k\mathbf{u}^{(k)}(\mathbf{x}). \tag{2.24}$$

Thus, a sufficient condition for the solution of Equation 2.23 will be to find the coefficients β_k such that

$$\sum_{k=1}^{M}\frac{1}{M}(\mathbf{u}^{(i)}(\mathbf{x}),\mathbf{u}^{(k)}(\mathbf{x}))\beta_k = \lambda\beta_i \qquad i = 1,\ldots,M. \tag{2.25}$$

We now introduce $\mathbf{C} = \frac{1}{M}(\mathbf{u}^{(i)}(\mathbf{x}),\mathbf{u}^{(k)}(\mathbf{x}))$ as an inner product of the snapshot quantities, and the equation becomes

$$\mathbf{CV} = \lambda\mathbf{V}. \tag{2.26}$$

The above equation has a complete set of orthogonal eigenvectors with corresponding eigenvalues

$$\mathbf{V} = [\beta_1 \quad \beta_2 \quad \ldots \quad \beta_M]$$

$$\lambda_1 \geq \lambda_2 \geq \cdots \geq \lambda_M.$$

Equation 2.21 is used to construct the POD modes using the given eigenvector information. By employing the method of snapshots, the $N \times N$ system reduces down to an $M \times M$ eigenvalue problem.

Algorithm

The following algorithm is provided to guide the construction of the POD basis vectors using the method of snapshots.

1. Attain a set of realizations at prescribed intervals in time $\mathbf{u}^{(k)} = \mathbf{u}(\mathbf{x},t_k)$. The times

t_k are usually equally spaced in time but this is not necessary. This timestep should be small enough to capture the important dynamics of the system.

2. Form the $M \times M$ correlation matrix $\mathbf{C}$ by taking the inner product of the snapshots

$$\mathbf{C} = (\mathbf{u}^{(i)}, \mathbf{u}^{(j)}),$$

or in component notation as

$$C_{ij} = \sum_{k=1}^{N} u_k^{(i)} u_k^{(j)}.$$

3. Calculate the eigenvalues and eigenvectors of Equation 2.26. The eigenvalues λ_n indicate the relative importance of the POD modes.

4. The POD basis vectors, or modes, are constructed as linear combinations of the snapshots, using the eigenvector information calculated in the previous step

$$\Psi_n = \sum_{k=1}^{M} \beta_n^k \mathbf{u}^{(k)},$$

where the β_n^k corresponds to the k-th component of the n-th eigenvector.

5. The orthogonal POD modes $\mathbf{\Psi}$ can then be normalized such that

$$(\Psi_i, \Psi_j) = \delta_{ij}.$$

2.2 Acoustics Framework

An acoustic solver based on the Ffowcks Williams and Hawkings[22] equation has been written by Lockard at NASA Langley Research Center[38]. The solver computes the acoustic signal at a specified far-field observer location by integrating the FWH equation along a source line. The following methodology of the aeroacoustic solver is as given by Brentner and Farassat[10] and is referenced from [55]. The FWH equation may be written as

$$D^2 p'(\mathbf{x}, t) = \frac{\partial^2}{\partial x_i \partial x_j}[T_{ij} H(f)] - \frac{\partial^2}{\partial x_i}[L_i \delta(f)] + \frac{\partial}{\partial t}[(\rho_o U_n)\delta(f)] \tag{2.27}$$

where $D = \frac{1}{c^2}\frac{\partial^2}{\partial t^2} - \nabla^2$ is the wave operator, c is the ambient speed of sound, t is observer time, p' is the acoustic pressure, ρ' is the perturbation density, ρ_0 is the free-stream density, $f = 0$ describes the integration surface, $\delta(f)$ is the Dirac delta function, and $H(f)$ is the Heaviside function. The quantities U_i and L_i are defined as

$$U_i = (1 - \frac{\rho}{\rho_o})v_i + \frac{\rho u_i}{\rho_o} \tag{2.28}$$

and

$$L_i = P_{ij}\hat{n}_j + \rho u_i(u_n - v_n) \tag{2.29}$$

where ρ is the total density, ρu_i is the momentum in the i direction, and P_{ij} is the compressive stress tensor. For an inviscid fluid, $P_{ij} = p'\delta_{ij}$ where δ_{ij} is the Kronecker delta. The subscript n indicates the projection of a vector quantitiy in the surface-normal direction. To obtain a solution to Equation 2.27, the first term on the right-hand-side must be integrated over the volume outside the integration surface $f = 0$ wherever the Lighthill stress tensor T_{ij} is nonzero in this region. In the work reported here, this term is neglected. However, the main effects of nonzero T_{ij} within the flow can be included by choosing an integration surface that contains all of the volume with significant T_{ij} contributions.

The other terms on the right hand side of Equation 2.27 include terms that are determined by the unsteady flow-field data on the integration surface. Provided that the unsteady flow data on the integration surface $f = 0$ is correct, Singer *et al.*[55] demonstrated that the FWH equation correctly propagates the acoustic radiation from several source regions, including the complex signals associated with acoustic scattering from sharp edges.

Implementation

The **fwh2d** solver will be used as an acoustic analogy tool to determine far-field pressure disturbances propagated from a source. Inputs to the solver include the source line location, pressure and velocity information extracted from the source lines, and the locations of the observers to which the acoustic fields are propagated. The solver computes the far-field noise in the form of pressure perturbations in the frequency domain. An inverse Fast Fourier Transform is applied to the solution to recover the acoustic signal in the time domain. A schematic of the process is given in Figure 2.2.

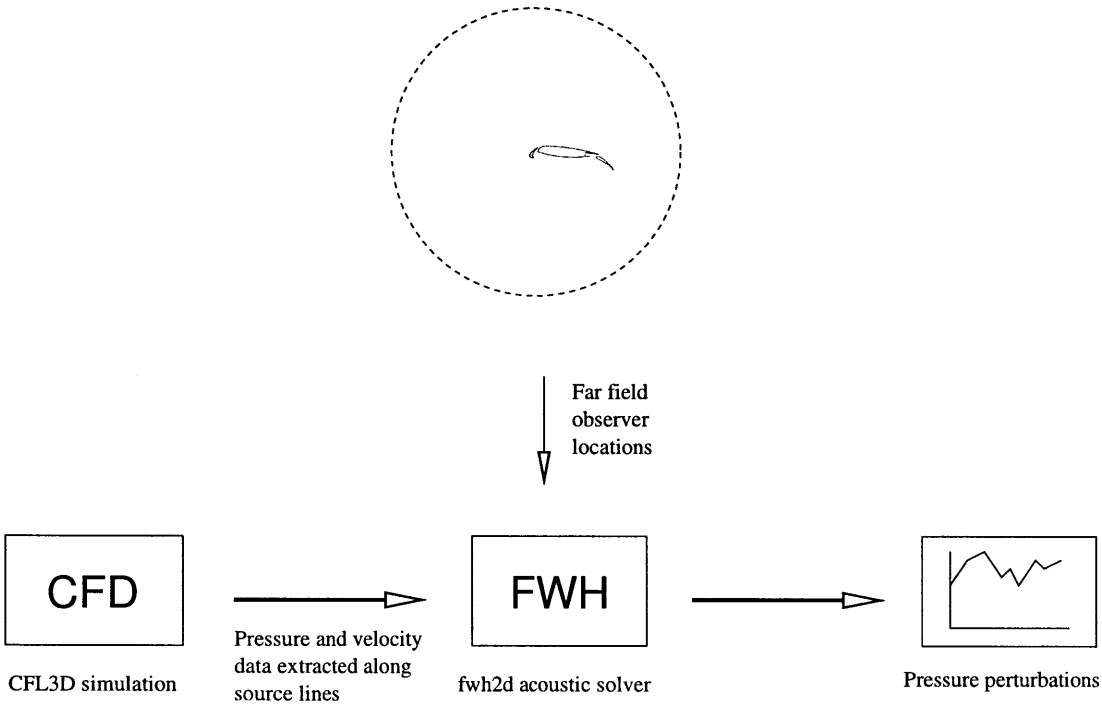

Figure 2-1: Schematic of **fwh2d** input/output.

Chapter 3

POD Modes

The strength of the Proper Orthogonal Decomposition comes from its ability to extract coherent structures from a seemingly random set of data. In this chapter a brief overview will be given detailing the computational fluid dynamics studies performed by Khourrami *et al.* at NASA Langley Research Center[32, 33]. The resulting solutions of the unsteady Reynolds Averaged Navier-Stokes simulation become the data set upon which the POD is applied. The POD is performed, and the eigenvalues and POD modes will be analyzed.

3.1 Data Setup

3.1.1 CFD Analysis

Two-dimensional unsteady computational fluid dynamics simulations were conducted on the multi-element, high-lift configuration Energy Efficient Transport airfoil[48]. The EET is an unswept three-element airfoil consisting of a slat, a super-critical main element, and a flap. The stowed chord of the airfoil has length 0.55 m, and the slat and flap chords equal 15.5% and 30% of the stowed airfoil chord, respectively. The numerical study was performed with the slat deflected at 30 degrees with respect to the main airfoil. A close-up view of the computational mesh in the slat vicinity is shown in Figure 3-1. There are over 200,000 nodes in the entire EET mesh, and over 50,000 nodes in the slat cove region alone. The computational fluid dynamics solver CFL3D[37] was utilized to perform an unsteady Reynolds Averaged Navier-Stokes simulation on this mesh, with reference conditions set at the LTPT test section entrance. Nondimensional quantities included the reference length l_∞

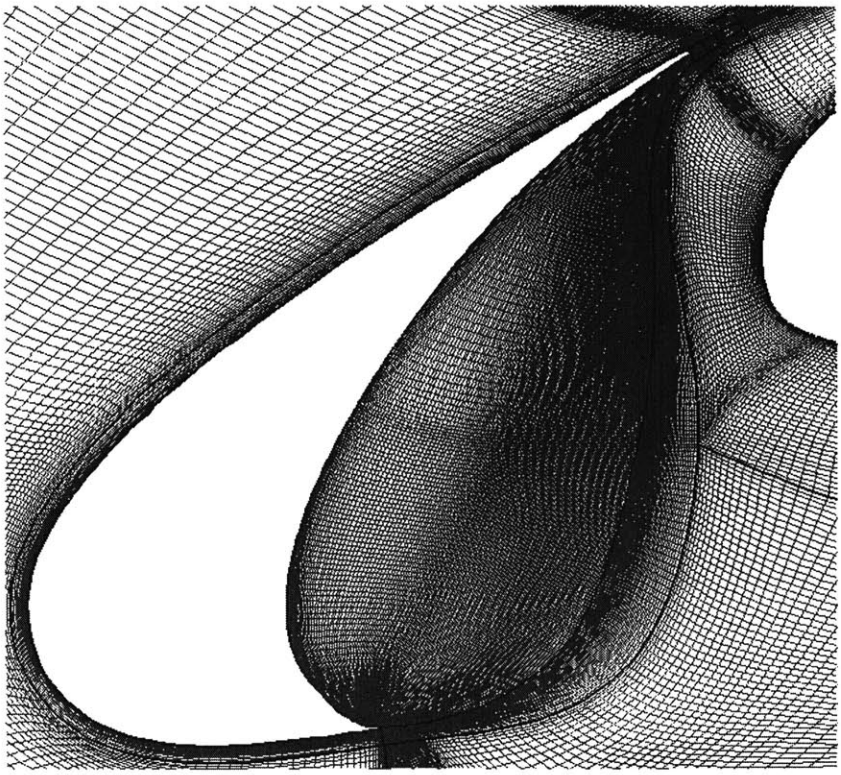

Figure 3-1: Computational mesh in vicinity of slat. Every other nodal point shown.

(based on the stowed chordlength), speed of sound a_∞, density ρ_∞, and kinematic viscosity ν_∞. The numerical tests were conducted at a Reynolds number Re = 7.2×10^6, Mach number Ma = 0.20, and a non-dimensional time step $\Delta t = 4.116 \times 10^{-4}$ based on the stowed chord length and free-stream speed of sound. The complete data set is comprised of solutions from simulations at three different angles of attack — 4, 6, and 8 degrees — in order to emulate the conditions in which the high-lift configuration is deployed. A brief discussion of the original flow field will be given here. For a more detailed discussion of the vorticity evolution, the reader is encouraged to read Khorrami *et al.*[33]

Instantaneous vorticity snapshots are shown in Figure 3-2 for each of the angles of attack at a time after all the initial transients have settled. The 4- and 6-degree cases exhibit similar behavior in their respective flow dynamics, and will be discussed together. In both of these cases, a large vortex core forms in the center of the slat cove region due to the dynamic forces. This positive sign vorticity is fed by the shear-layer vortices that are shed off of the leading edge of the slat. As these smaller vortices move along the cove free-shear layer, some are entrained into the central core vortex.

There is no regularity to the manner by which these shear-layer vortices travel about the free-shear layer. They are created at the leading edge and driven into the shear layer by the fluid dynamics of the system. They then travel up the free-shear layer toward the rear of the slat cove region, where most are then entrained into the backflow along the inner surface toward the leading edge. Some vortices interact with the slat inner surface boundary layer and force instant roll-up of negative sign vorticity along that edge. As a consequence, opposite sign vortex pairing is induced into the shear layer as the negative-sign vortices propagate into the free-shear layer . Furthermore, a number of vortices as well as positive-negative vortex pairs are ejected through the gap between the slat and the main element into the freestream flow. This again occurs at a random rate, and no periodic pattern has been identified.

The 8-degree simulation (Figure 3-2(c)) presents a significantly different result regarding the evolution of the slat free-shear layer. Unlike the 4- and 6-degree simulations, the 8-degree simulation does not exhibit the highly active circulating vortex core in the center of the slat cove region. Instead, positive sign vortices are formed at the leading-edge cusp and are convected through the free-shear layer of the slat region. Once they reach the reattachment point, most vortices are trapped in the circulating region and are convected back along

(a) Instantaneous 4-degree vorticity field snapshot

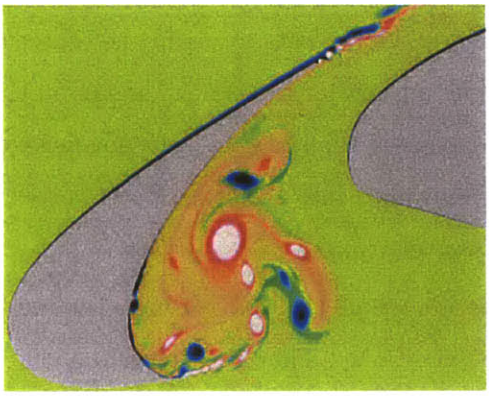

(b) Instantaneous 6-degree vorticity field snapshot

(c) Instantaneous 8-degree vorticity field snapshot

Figure 3-2: Instantaneous vorticity field snapshots.

the inner surface towards the slat cusp. There is no strong core vortex into which the smaller vortices can be ingested. The vortices simply move back along the inner surface towards the slat cusp and are reinserted into the slat free-shear layer as they roll off the leading edge cusp. The motion of the vortices along the slat bottom surface cause some of the boundary layer to separate, releasing opposite-sign vorticity into the flow as well. However, these dissipate soon after entering the free shear layer. It has also been observed that some positive-sign vortices (but no negative-sign vortices) escape into the free-stream flow through the slat gap. As in the 4- and 6-degree cases, there is no recognizable pattern for which the vortices are swept away.

3.1.2 Snapshot Ensemble

Ensemble Size

The full CFD analysis resulted in a collection of over 35,000 solutions per angle of attack simulation. After discarding the initial transient segment, 32,768 timesteps were retained for analysis[1]. By following the time evolution of a vortex in the slat cove region, it was determined that a full vortex progression cycle required approximately 3,000 timesteps. This effectively captured the time duration for which a vortex was shed off of the leading-edge cusp, convected through the free-shear layer, and returned to the cusp area through the recirculation region. For the purposes of this study, it was presumed that in order to capture the representative flow dynamics, at least two full cycles of vortex evolution should be employed in the POD ensemble. Doing so would ensure that the POD results would represent a valid segment of the slat flow, and thus provide a model representative of the total slat flow region.

Two cycles of vortex evolution were captured in 6,000 timesteps. Because the time-domain solutions were highly resolved, and the POD identifies variations in snapshot data, it was concluded that no significant changes in the continuous flow field data would be seen by adding more solutions. As a result, the POD ensemble was established to contain every 16th snapshot covering 6,400 timesteps, for a total of 400 snapshots.

[1]For the 8-degree case, only the last 16,384 timesteps were available due to unrecoverable data corruption during processing.

Ensemble Norm

It should be noted that the Proper Orthogonal Decomposition is an unbiased mathematical formulation, and therefore does not take into consideration the type or dimensions of data it is analyzing. Certain ensemble norms will result in an energy consideration amenable to physical quantities, such as the total kinetic energy resulting from a POD analysis of the velocity fields. In the evaluation of other ensemble norms, the associated energy may not represent a physical quantity, and thus should not be regarded as such. This will be discussed further in Section 3.2.1.

Several different ensemble norms were taken into consideration when performing this study. In the initial analysis, all four state variables of the two-dimensional CFD study were used to create a norm containing all the information available. Because of the extensive amount of data, however, the analysis proved computationally expensive. Furthermore, ensemble norms based on the individual state variables were determined to provide more efficient analyses and a more focused decomposition of that particular variable field.

For the purposes of this study, the POD will be applied to the pressure variables as well as the velocity data in separate implementations. This not only lets us analyze the two properties individually, but also facilitates later acoustic calculations using the acoustic solver. The acoustic solver requires as inputs the pressure data as well as the velocities for a specified source line. This is to be expected, since acoustic energy is primarily attributed to pressure perturbations in a medium and velocity perturbations affect the propagation of those pressure fields.

3.2 POD Analysis

We now apply the Proper Orthogonal Decomposition on the data ensemble containing the 400 snapshots of the flow field quantities calculated by the CFL3D fluid dynamics solver. We wish to identify and analyze the coherent structures most relevant to all snapshots in the ensemble. We will perform the POD on the pressure and velocity fields separately, and discuss the results individually.

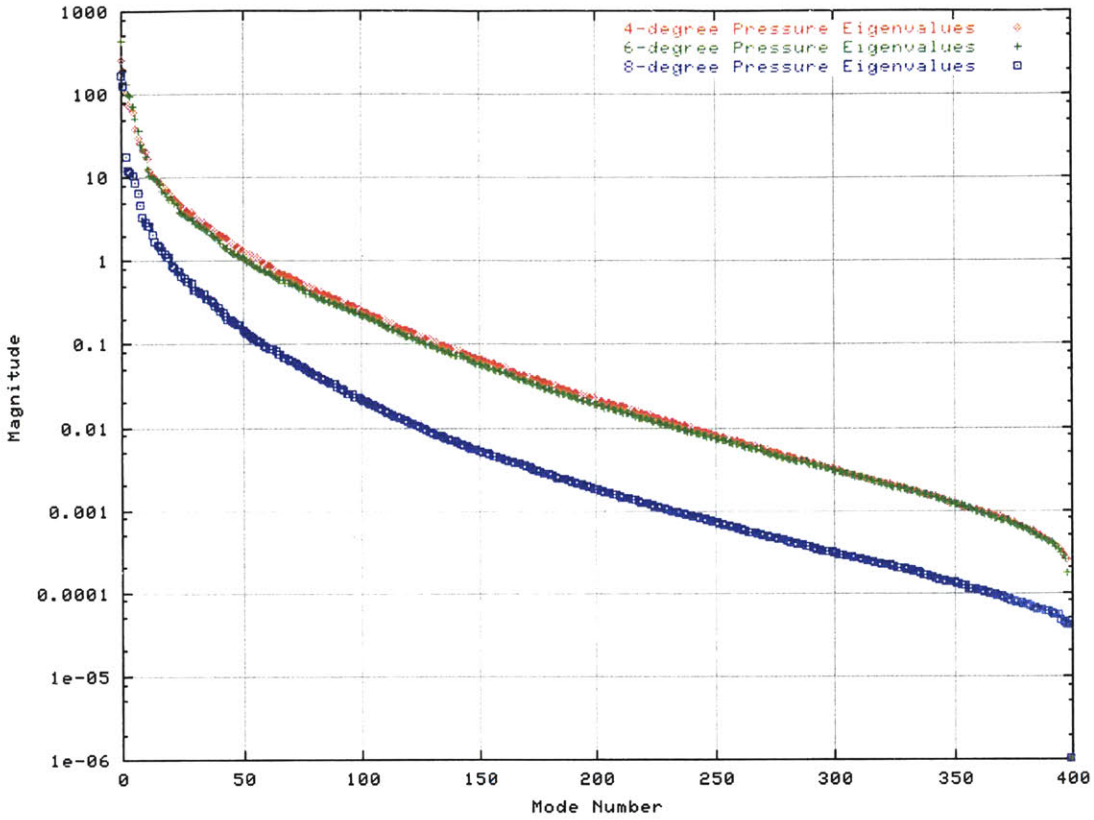

Figure 3-3: Pressure eigenvalues – Magnitude.

3.2.1 Eigenvalue Energy

The Proper Orthogonal Decomposition was performed on the ensemble set detailed in the previous section. A correlation was performed between the snapshots of the ensemble, and the resulting eigenvalues and eigenvectors were calculated as solutions to Equation 2.26, repeated here as

$$\mathbf{CV} = \lambda \mathbf{V}$$

The eigenvalues represent the energy content contained within the POD modes, and are ordered from largest to smallest by the POD. The eigenvectors will be used later to create the basis functions, also known as the POD modes, using Equation 2.21. A sample of the computed eigenvalue data from which these plots are generated may be found in Appendix A.

The eigenvalues calculated from Equation 2.26 represent the amount of modal energy

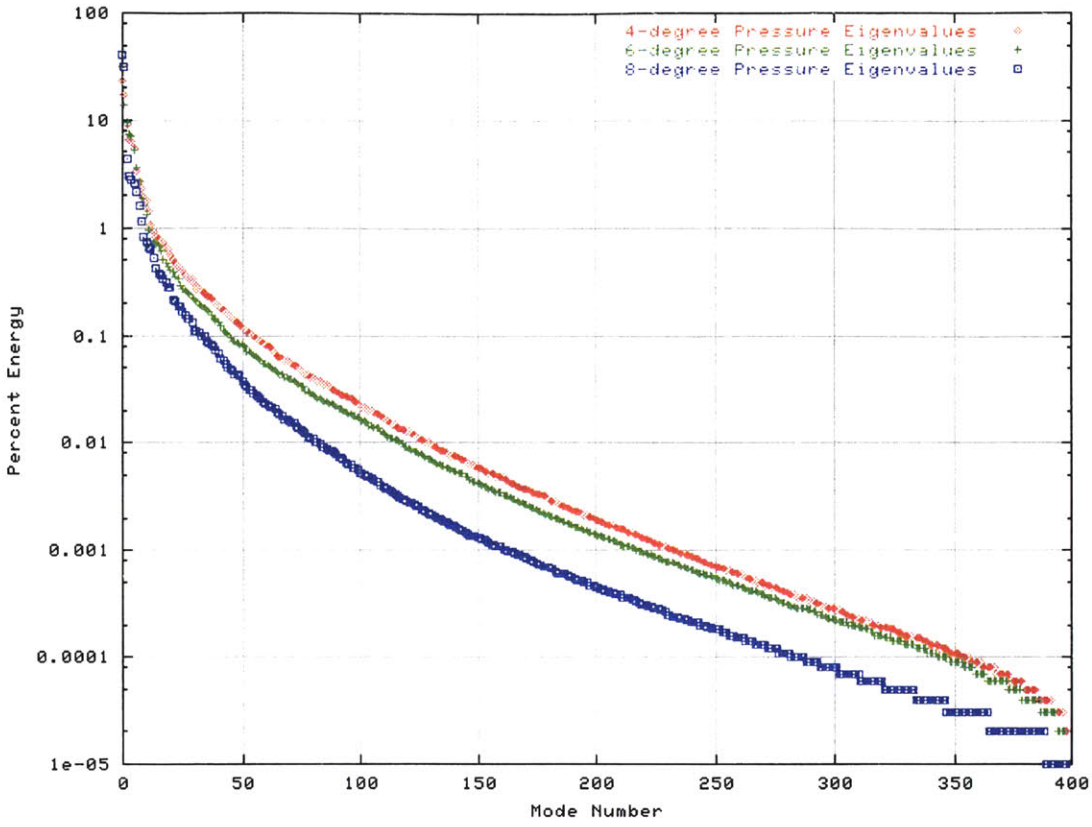

Figure 3-4: Pressure eigenvalues – Percent energy.

contained in the corresponding POD mode. Note that this metric of energy does not necessarily denote a physical energy. The characterization of these quantities depends on the types of measurements taken in the POD ensemble. For instance, in incompressible fluid mechanics, a POD analysis on velocity will yield eigenvalue energy that is related to the fluid kinetic energy. In a POD analysis on vorticity, the eigenvalue energies will correspond to the system enstrophy. For analyses of other ensemble norms, or combinations of different quantities, the eigenvalues may not correspond to any specific type of energy. Thus regarding the POD eigenvalues as energy in a general mechanical context is incorrect in principle and may lead to misleading results[12].

Pressure Eigenvalues

The eigenvalue spectrums are plotted on a semi-log scale in Figure 3-3 for the POD pressure analyses at 4-, 6-, and 8-degrees angle of attack. For all analyses performed in this study,

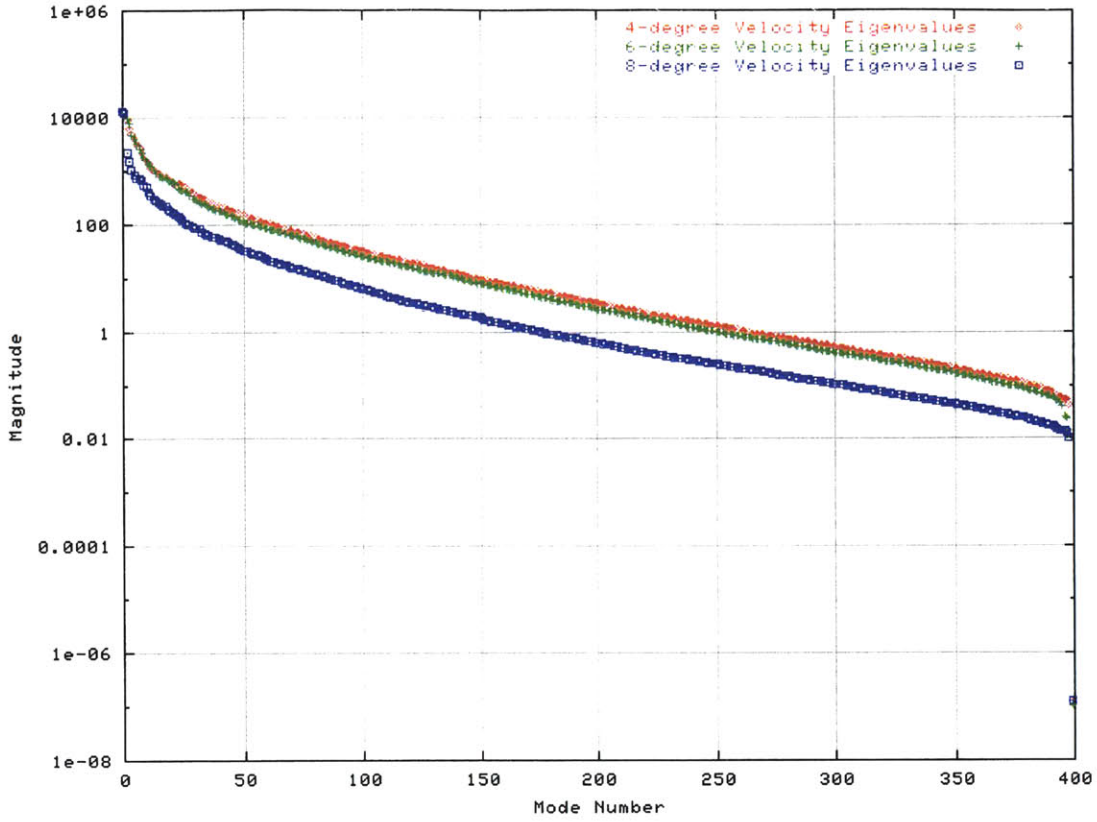

Figure 3-5: Velocity eigenvalues – Magnitude.

the POD was applied to the set of perturbation data after having extracted the mean states. This eliminates what would have been the most dominant mode in the spectrum, which by construct would have contained the mean flow in an eigenvalue several orders of magnitude larger than all other eigenvalues. We are mainly interested in the perturbations from the mean, and this method was taken to enhance analysis of the results. For all three angles of attack, it can be seen that the magnitudes of the eigenvalues fall off rapidly within the first few modes, and gradually taper off as the eigenvalues get smaller. Thus it is apparent that the structures of the first few modes contain coherent structures that dominate throughout the snapshot ensemble.

The eigenvalue information can be seen more clearly in Figure 3-4, where the magnitudes are shown as a percentage of the total system energy

$$\% \text{ Energy} = \frac{\lambda_j}{\sum_{i=1}^{M} \lambda_i}.$$

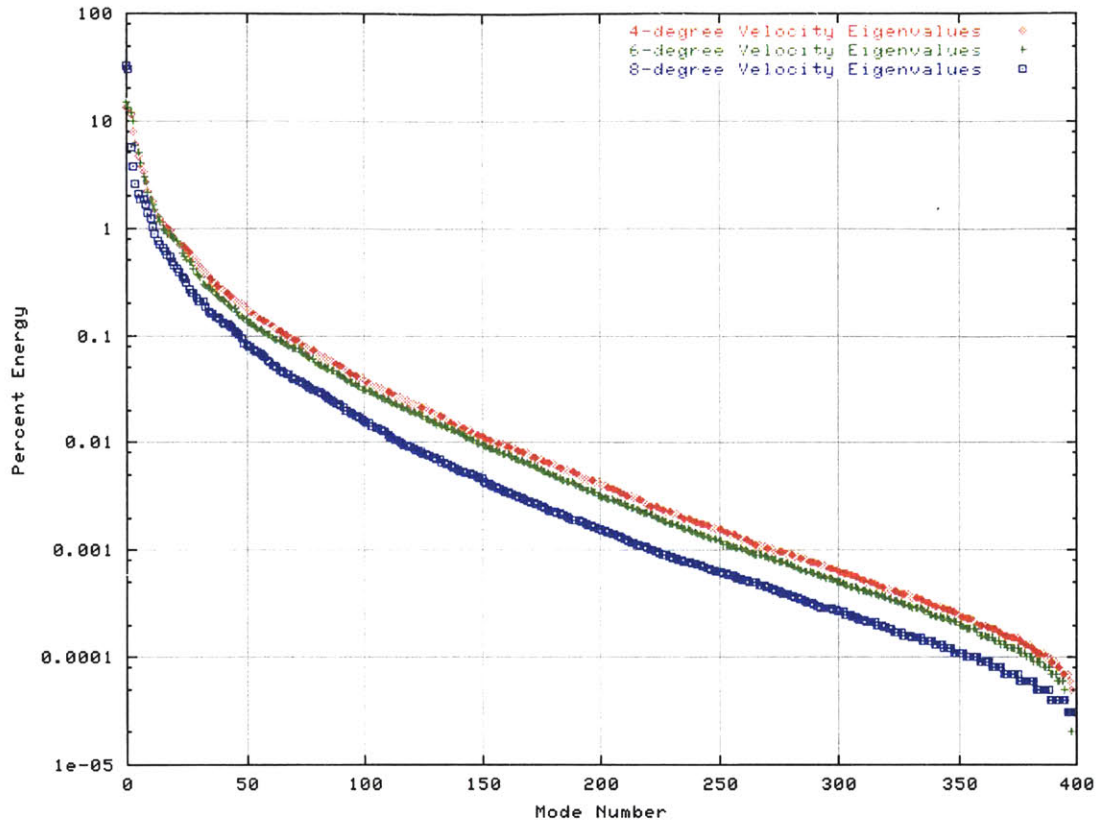

Figure 3-6: Velocity eigenvalues – Percent energy.

This represents the percent energy contained in mode j. The first eigenvalue of the 6-degree study corresponds to the most dominant mode in its system, with 32% of the total pressure energy contained in the first mode. In parallel studies using the 4- and 8-degree snapshot ensembles, the eigenvalues exhibited similar trends in magnitude. The dominant eigenvalue in the 4-degree case contributes 23%, while the 8-degree case expressed the highest energy in the first mode with 41%. It can be seen that the dropoff in the 8-degree case was steepest, due to a greater amount of energy contained in the earlier eigenvalues. The residual error Res_j, calculated as the sum of the eigenvalues contained in the remaining modes, can be expressed as

$$\text{Res}_j = \sum_{i=j+1}^{M} \lambda_i.$$

Thus for approximations at the same rank, the residual energy will be lowest using the 8-degree modes, which suggests that the underlying low-dimensional manifold is easier to

approximate.

Velocity Eigenvalues

The eigenvalues calculated from a POD analysis of the velocity data are shown in Figures 3-5 and 3-6. A similar trend is found in the velocity eigenvalues as in the pressure eigenvalues. The initial modes contain the most energy, with 14%, 15%, and 33% kinetic energy in the 4-, 6-, and 8-degree systems, respectively. Again, the 8-degree system contains the most energy within the first few modes of the system compared to the other two angles of attack. The magnitudes of the later modes drop off more quickly, and thus of the three systems, the 8-degree kinetic energy field can be best approximated for a given number of modes. Note that the trailing end of the percentage-energy spectrums of both the pressure and velocity eigenvalues show banding in percent magnitude values. We attribute this to numerical rounding errors in computing the solution to the eigenvalue problem, rather than actual eigenvalue behavior.

3.2.2 POD Pressure Modes

A discussion of the pressure mode shapes, or POD basis functions, will be given in this section. Due to the fact that the 4- and 6-degree systems exhibit similar behavior, the pressure POD modes for both systems will be discussed together from the 6-degree standpoint. The reader may infer from the discussion and the figures an analysis of the 4-degree system, whose POD modes and related modal behavior can be seen in Figures 3-7 through 3-10. For the figures in this section, the scaling of the pressure fields have been chosen to clearly illustrate the structures in the POD modes. Scaling legends, which indicate the perturbation pressures, are provided beside each of the figures plotted.

6-degree Modes

The POD analysis performed on the 6-degree pressure snapshots results in a number of coherent structures in the initial modes. The first 6-degree mode, shown in Figure 3-11, contains two large opposite sign pressure regions which dominate the cove region. The scope of the two regions are nearly identical but opposite in sign, and are approximately divided at the vertical midpoint of the slat surface. From the eigenvalue energy spectrum

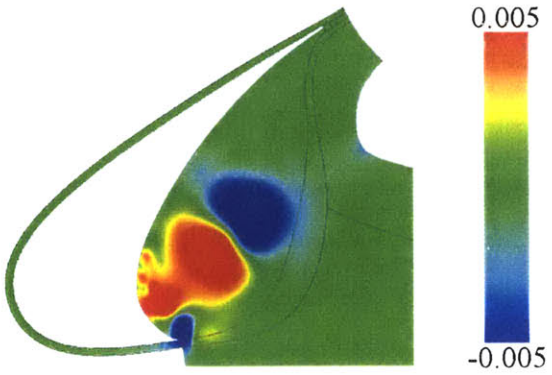

(a) 4° pressure mode 1

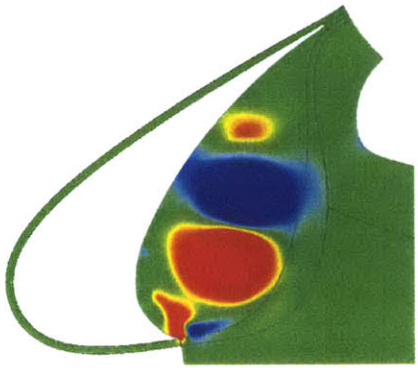

(b) 4° pressure mode 2

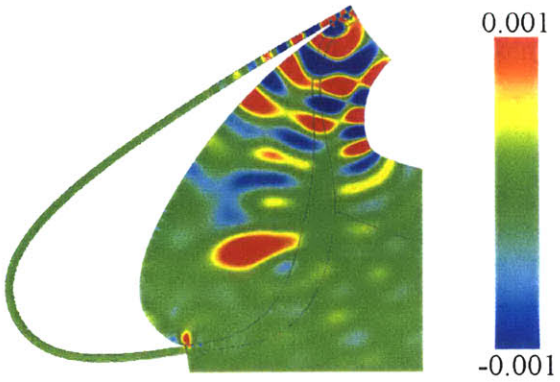

(c) 4° pressure mode 3

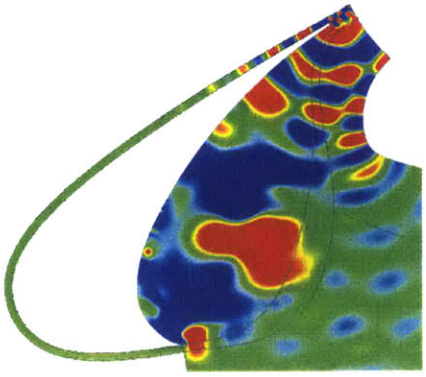

(d) 4° pressure mode 4

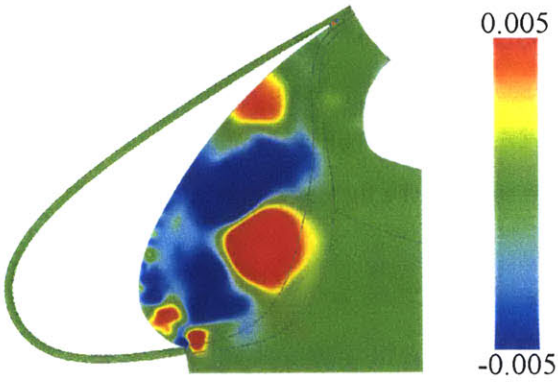

(e) 4° Pressure Mode 5

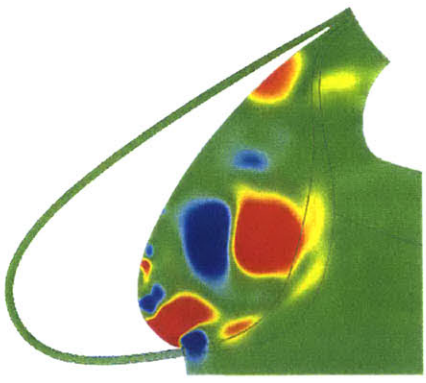

(f) 4° pressure mode 6

Figure 3-7: 4-degree pressure modes 1–6.

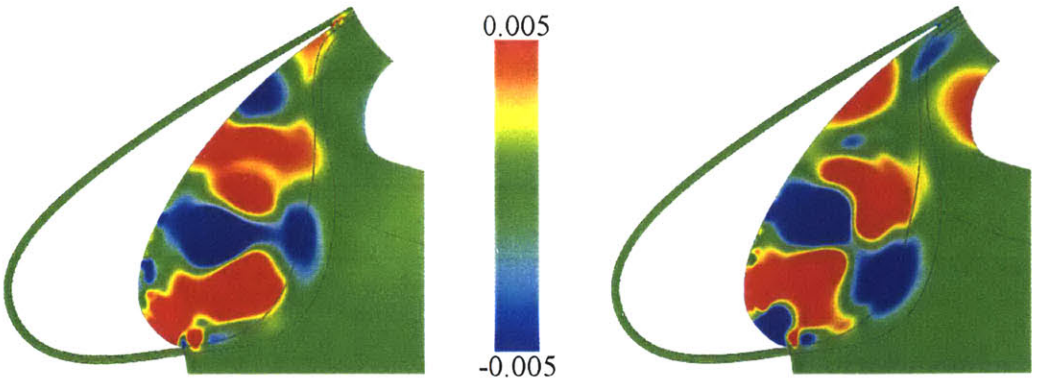

(a) 4° pressure mode 7

(b) 4° pressure mode 8

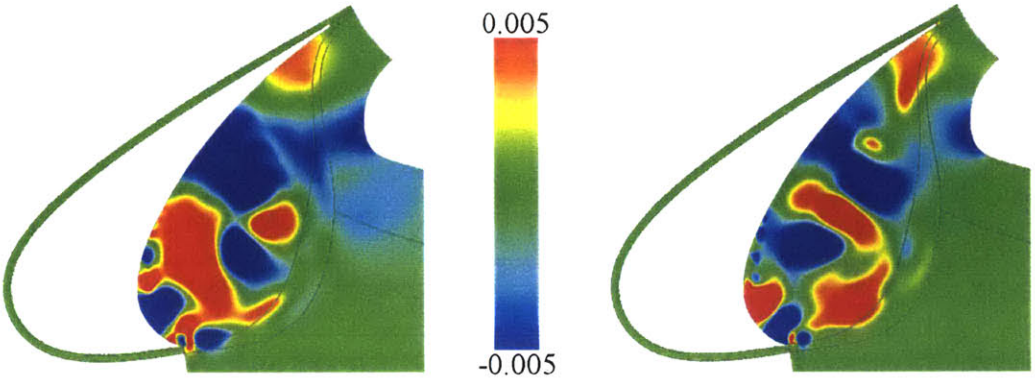

(c) 4° pressure mode 9

(d) 4° pressure mode 10

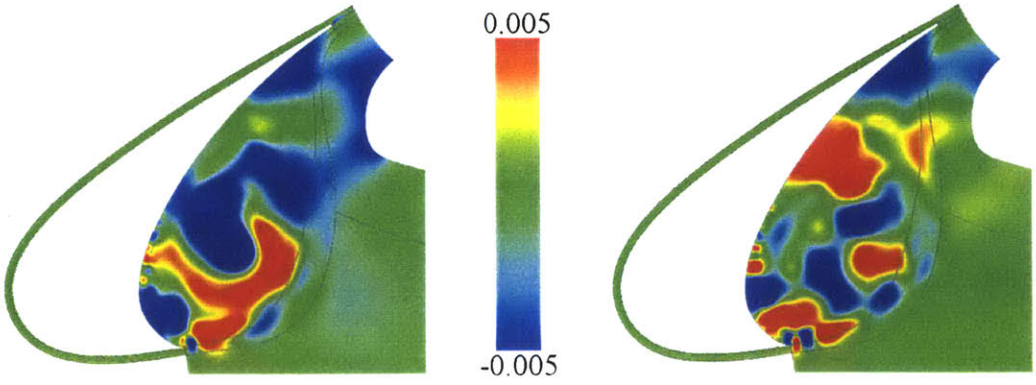

(e) 4° pressure mode 11

(f) 4° pressure mode 12

Figure 3-8: 4-degree pressure modes 7–12.

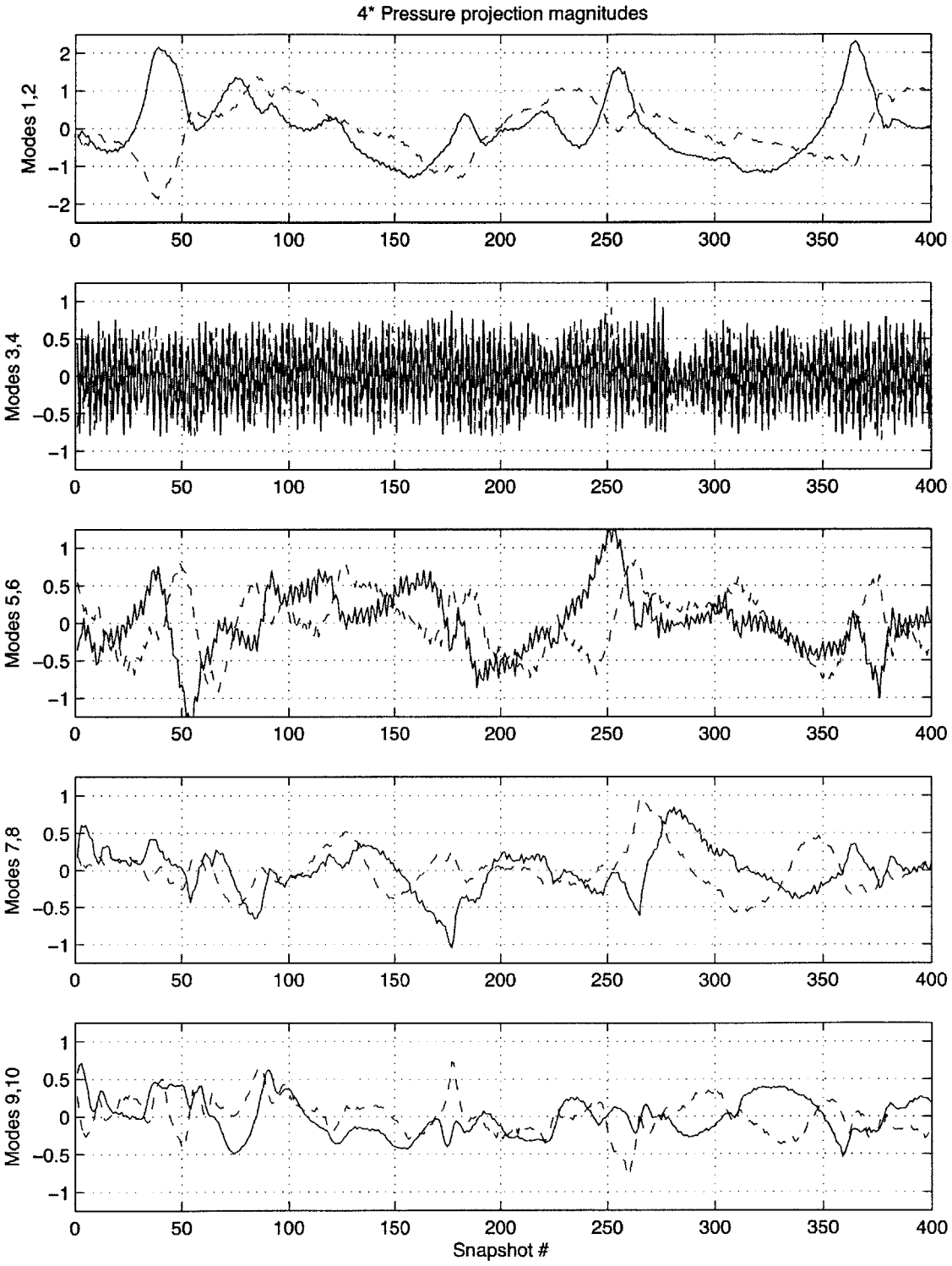

Figure 3-9: Temporal projection magnitudes of 4-degree pressure modes 1–10 onto all snapshots.
——— Odd-numbered modes – – – – – Even-numbered modes

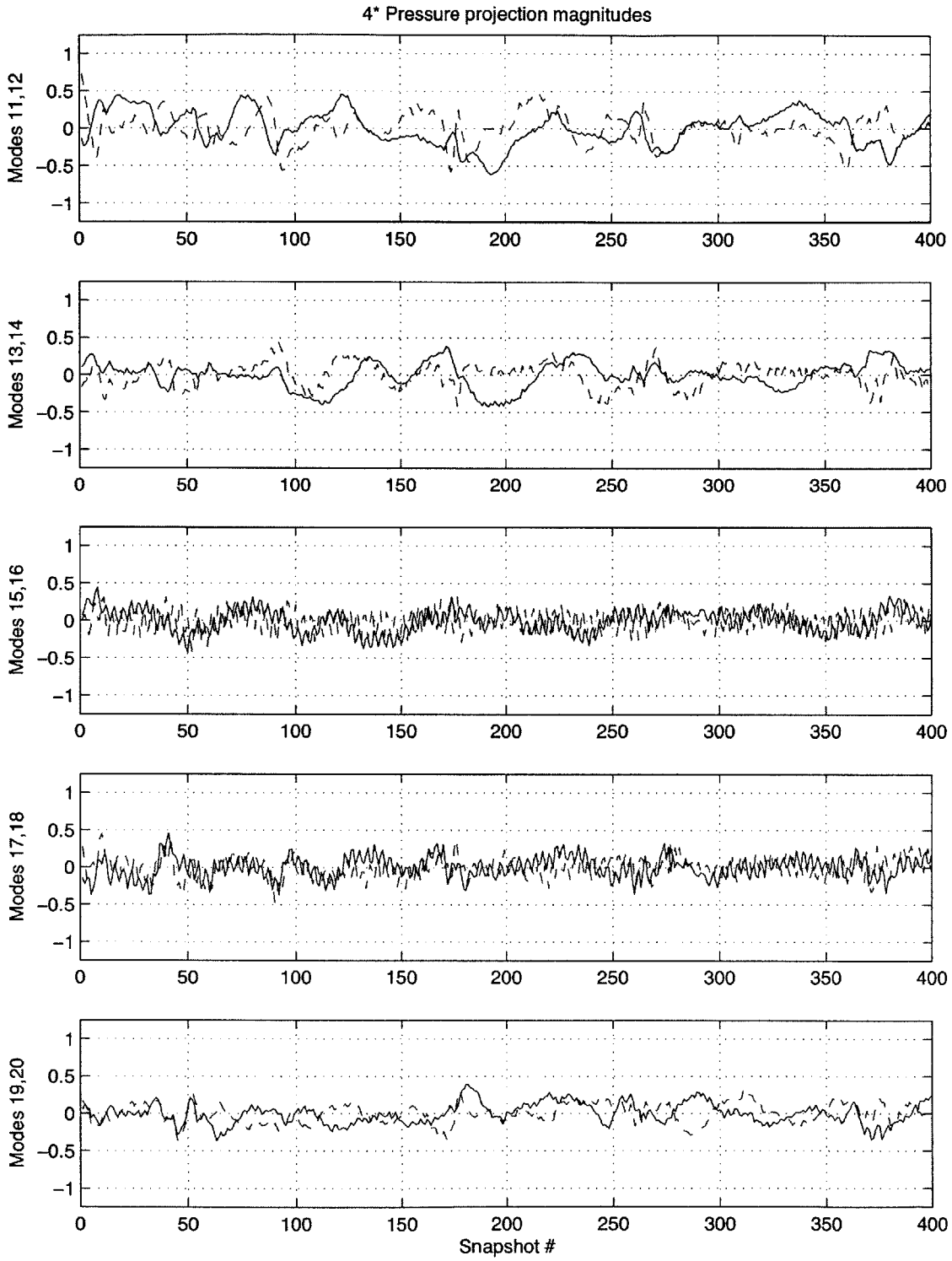

Figure 3-10: Temporal projection magnitudes of 4-degree pressure modes 10–20 onto all snapshots.

——— Odd-numbered modes – – – – – Even-numbered modes

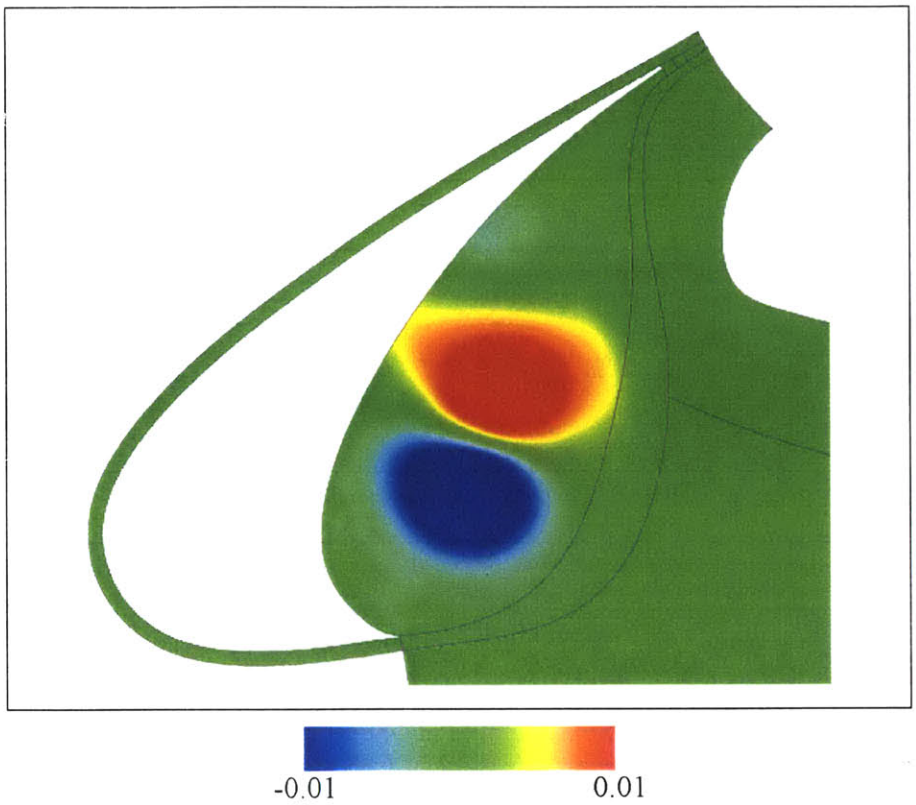

Figure 3-11: 6° pressure mode 1 containing 32% energy.

shown earlier, it can be seen that this structure contributes approximately 32% of the energy contained throughout the snapshot ensemble.

The second mode, shown in Figure 3-12(b), also exhibits two cohesive, opposite-sign pressure regions. This mode contains approximately 14% of the total pressure energy. Whereas the dominant structures were vertically separated in the first mode, they are horizontally separated in the second mode.

The third and fourth modes exhibit a distinctly different nature than the first two modes. Mode three consists of bands of alternating positive and negative pressure perturbations, while mode four exhibits the same structure of pressure bands, though opposite in phase. Also note that there is very little activity in the center of the slat cove in these modes, which suggests that the majority of the central core motion was captured in the first two modes. Rather, the third and fourth mode contribute a disperse pressure field through the snapshots, akin to the propagation of pressure waves from a source.

Modes five and six return to the larger coherent structures located in the center of the slat cove region. These two modes contribute 7% and 5% of the total pressure energy, respectively. Although they are not as dominant as the first two modes, they do contain features that appear to contribute to the main core circulation. As we move to the higher mode numbers in Figure 3-13, it can be seen that the coherent structures decrease in size. There still appears to be some structure in the shapes of the pressure zones, yet they tend to become more random with increasing mode numbers. It can also be seen that some artifacts of the smaller-scale structures begin to appear in these modes and higher, in the order that they are most correlated with the entire ensemble.

Figures 3-14 and 3-15 show the temporal projection magnitudes of the modes projected onto the original snapshots. These plots depict the temporal nature of the modes, showing the influence of the mode across the snapshot ensemble. Note that the temporal projections show that the first two modes have approximately the same period. This suggests that the shifting of phase dominance between these two modes may act to drive the slower, large-scale behavior of the central vortex core. Modes 3 and 4 contain extremely fast oscillations, corresponding to the convection of the narrow pressure bands that appear throughout the ensemble set. Modes 5 and 6 have periods slightly shorter than modes 1 and 2 and likely contribute to the cove circulation as well. Neglecting the extremely fast oscillatory nature of modes 3 and 4, the frequency of the POD modes are seen to increase in their temporal

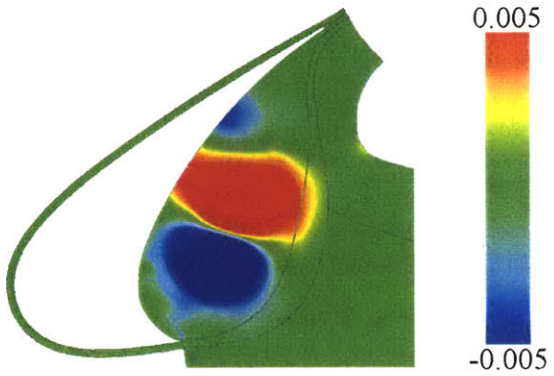

(a) 6° pressure mode 1

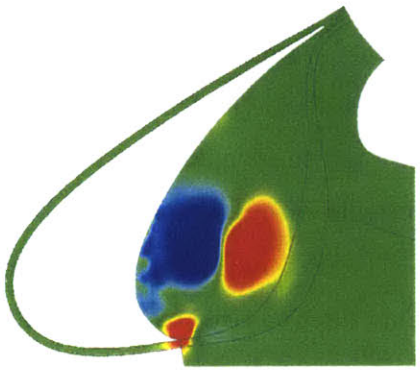

(b) 6° pressure mode 2

(c) 6° pressure mode 3

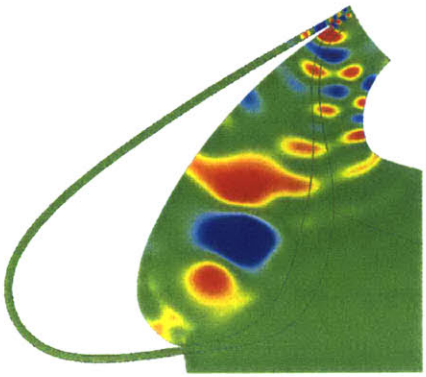

(d) 6° pressure mode 4

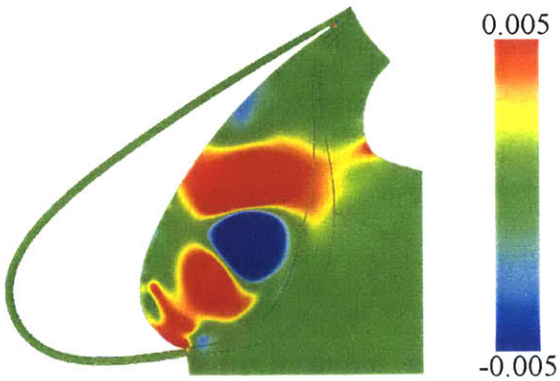

(e) 6° pressure mode 5

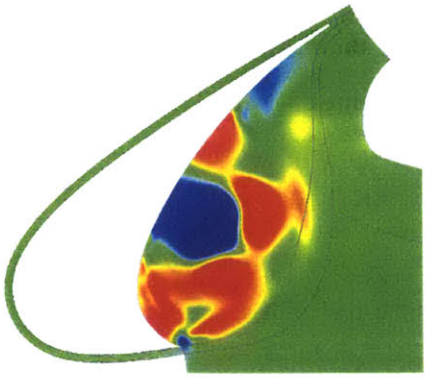

(f) 6° pressure mode 6

Figure 3-12: 6-degree Pressure Modes 1–6

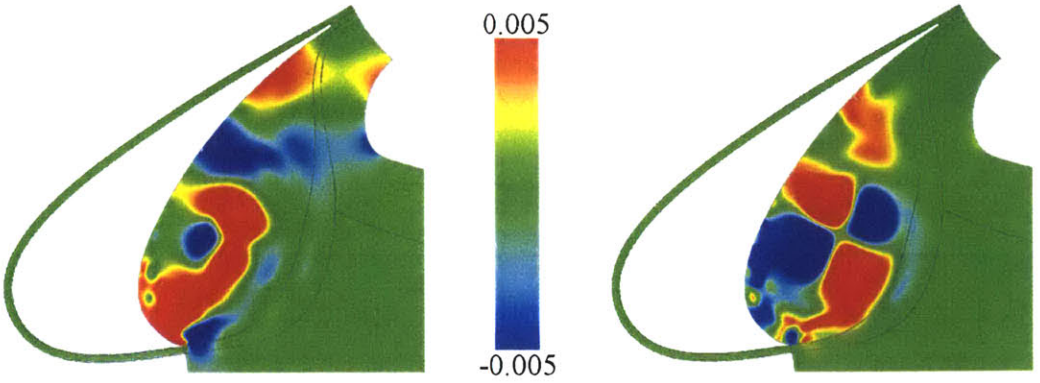

(a) 6° pressure mode 7

(b) 6° pressure mode 8

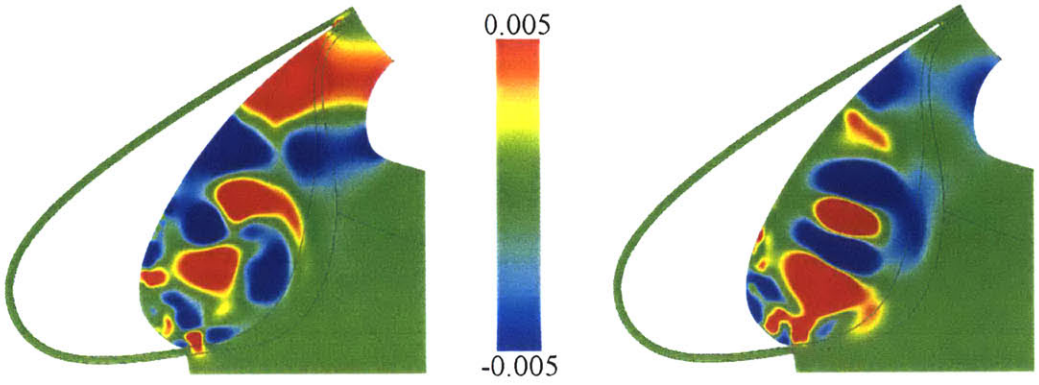

(c) 6° pressure mode 9

(d) 6° pressure mode 10

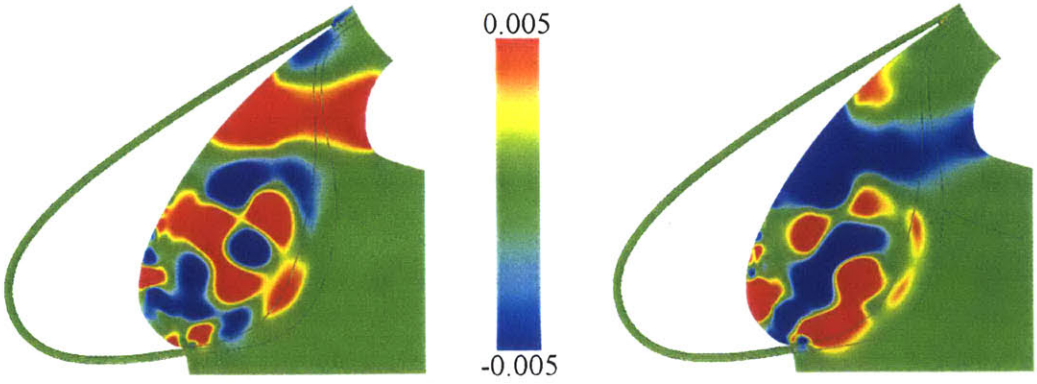

(e) 6° pressure mode 11

(f) 6° pressure mode 12

Figure 3-13: 6-degree pressure modes 7–12.

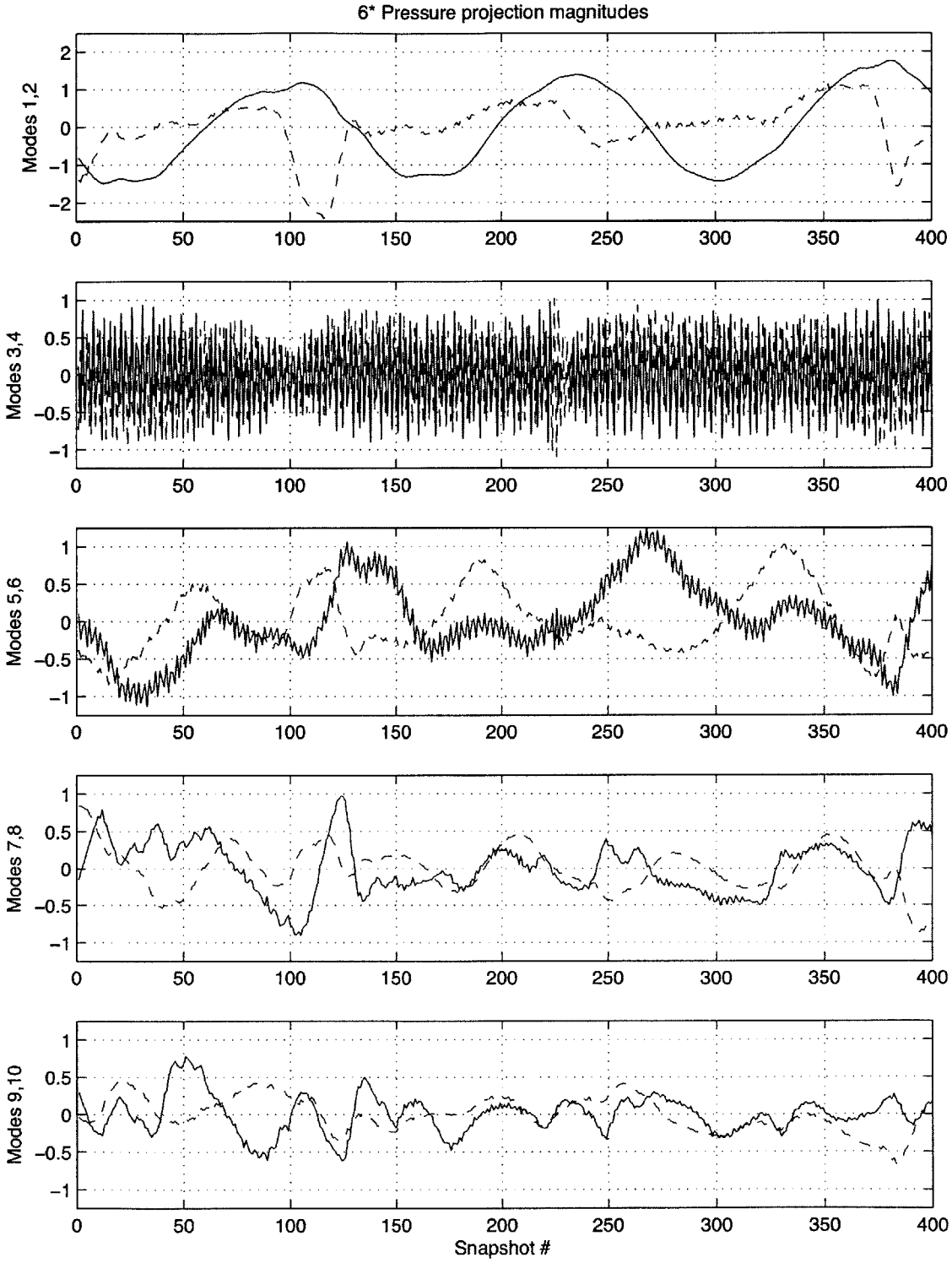

Figure 3-14: Temporal projection magnitudes of 6-degree pressure modes 1–10 onto all snapshots.

——— Odd-numbered modes – – – – – Even-numbered modes

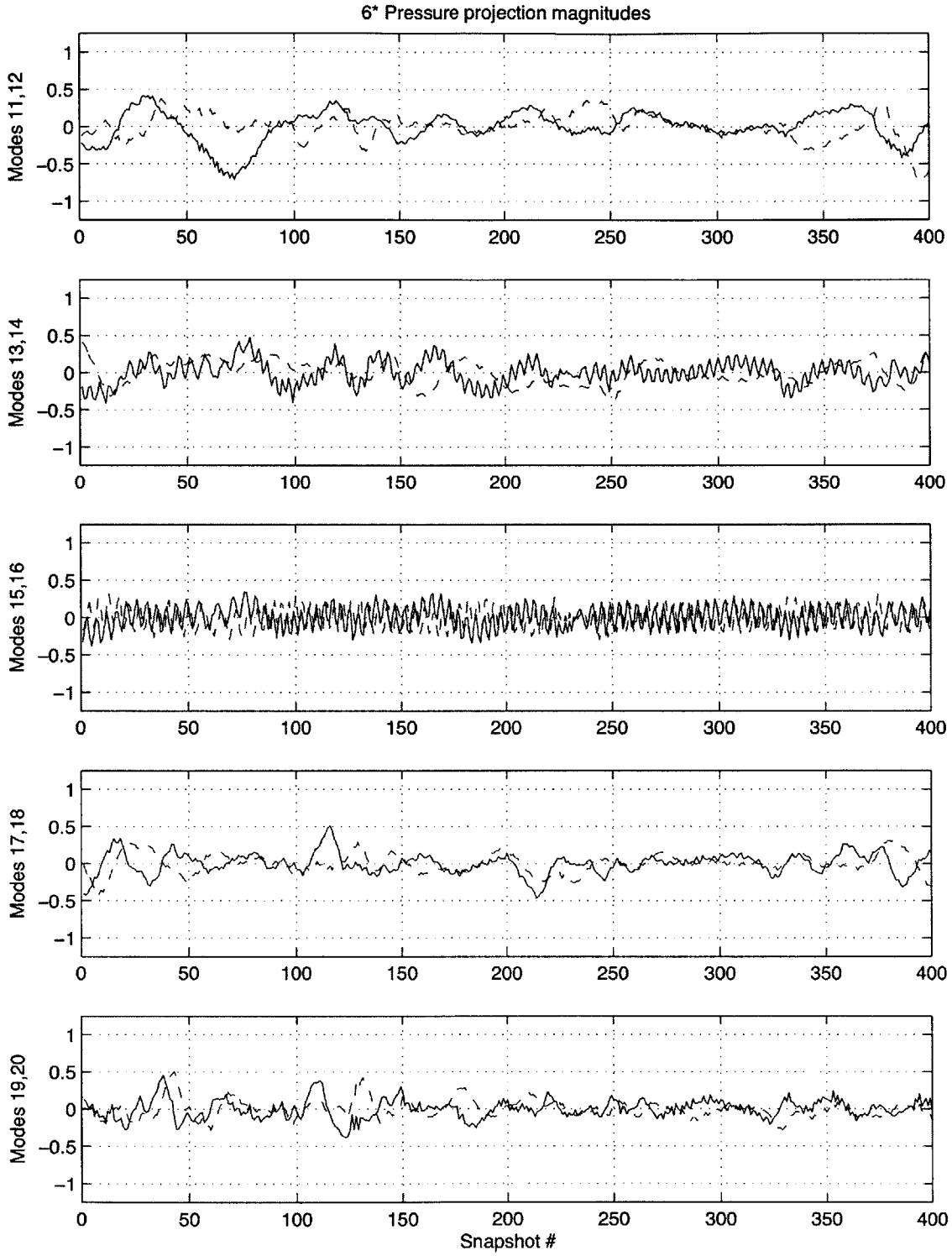

Figure 3-15: Temporal projection magnitudes of 6-degree pressure modes 10–20 onto all snapshots.

——— Odd-numbered modes – – – – – Even-numbered modes

projections onto the snapshots. Combined with the observation that the extent of each structure decreases in size with increasing mode number, this suggests that content in higher mode numbers contribute to the smaller-scale effects in the flow field. Furthermore, it should be noted that the magnitudes of the projections decrease with higher mode numbers, which suggests that these modes shift the system state less drastically than do the earlier modes.

Because there are very few small-scale structures in the first six modes of the 6-degree POD basis (neglecting modes 3 and 4), it is presumed that the larger coherent structures are what induce circulation about the center of the slat cove. These large structures act to shift the pressure away from the mean pressure field. Since each of these modes is slightly out of phase with one another, this suggests that the energy is transferred to each mode at different instances in time. This contributes to the unsteady motion in the central region of the slat cove.

An extended collection of the pressure modes is provided in Appendix B.1 for modes 13–36. In the later modes the structures in the modes appear smaller and more defined. Because each mode is orthogonal to all the modes educed prior to it, the larger features that have already been extracted do not appear again. The remaining features thus include the formation of structures comprising the positive-negative vortex motion along the slat inner surface as well as the vortices that travel through the free-shear layer. Note that because the modes are ordered from largest to smallest, the structures that appear in the later modes are necessarily less dominant than the earlier formations. This is expected, as from a pure data perspective, the POD attempts to locate the flow features that are most parallel to all the members of the ensemble. Smaller structures tend to be more dispersed and convect at random intervals through the shear layer, thus leading to a lower correlation throughout the ensemble set. It is also for this reason that the central core circulation appears earliest in the POD basis.

8-degree Modes

The first twelve 8-degree modes are shown in Figures 3-16 and 3-17. Recall that the original solution flow field for the 8-degree case was significantly less energetic in the slat cove region, particularly in the central core (see Figure 3-3). This is made evident by the initial modes of the POD analysis. The first two modes do not exhibit the large coherent structures that perturb the core region as seen in the initial 6-degree modes. On the contrary, the first two

8-degree modes show pressure bands which populate the entire flow field. The nature of these pressure bands are strongly associated with the effects of trailing edge vortex shedding, as evidenced by Khorrami *et al.*[31]

The temporal projections of the first twenty 8-degree POD modes onto the entire 8-degree snapshot ensemble are shown in Figures 3-18 and 3-19. Here we see the fast oscillations corresponding to the pressure bands in Modes 1 and 2. The long wavelength in mode 3 corresponds to the large structure that is found in that mode, which likely contributes to some of the general features in the cove area. Features representing the inner slat vortices appear as tightly bound pressure cores in Modes 4 and 5. It can be seen that the two modes depict roughly the same pressure cores, although they are out of phase between mode numbers. This suggests that the vortices are convecting along this tight path along the inner surface of the slat. The pressure banding once again reappears in modes 5 and 6. However, these bands are narrower, and appear to emanate at approximately twice the density of the bands in modes 1 and 2. This should correspond to higher frequency pressure waves propagating at a smaller wavelength.

Earlier, it was seen in the corresponding 8-degree eigenvalues that the first mode contains 41% of the pressure energy and the second contains 31%. Since the pressure banding in the first two modes dominate over 70% of the flow, this suggests that the flow characteristics of interest (e.g. convection of vortex-pressure cores, etc.) are contained in the remaining 30%. With the smaller modes relative to the 4- and 6-degree cases, it can be concluded that the 8-degree system is less energetic. Indeed, as much of the varying flow field structures are contained in just 30% of the pressure energy, it can be concluded that the 8-degree slat flow is less random. Thus, when compared to the other two angle of attack studies, the 8-degree simulation exhibits a more organized flow field overall.

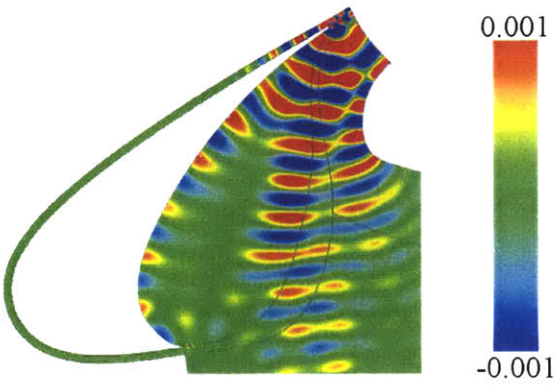

(a) 8° pressure mode 1

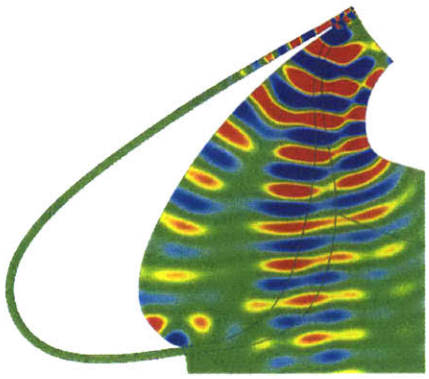

(b) 8° pressure mode 2

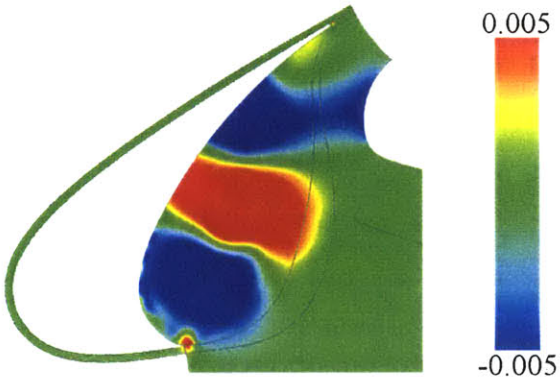

(c) 8° pressure mode 3

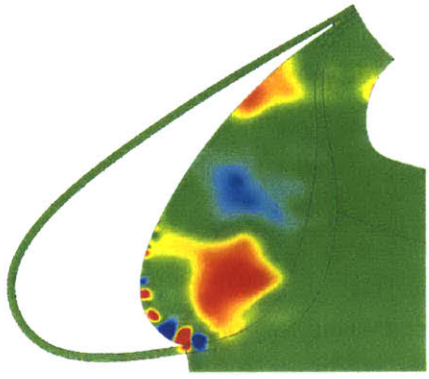

(d) 8° pressure mode 4

(e) 8° pressure mode 5

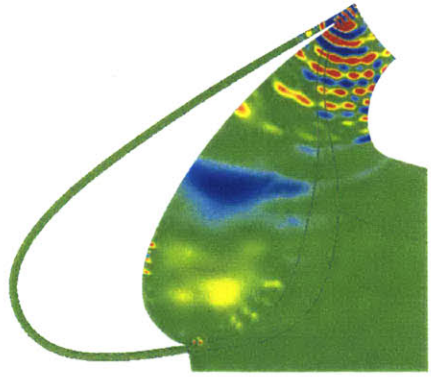

(f) 8° pressure mode 6

Figure 3-16: 8-degree pressure modes 1–6.

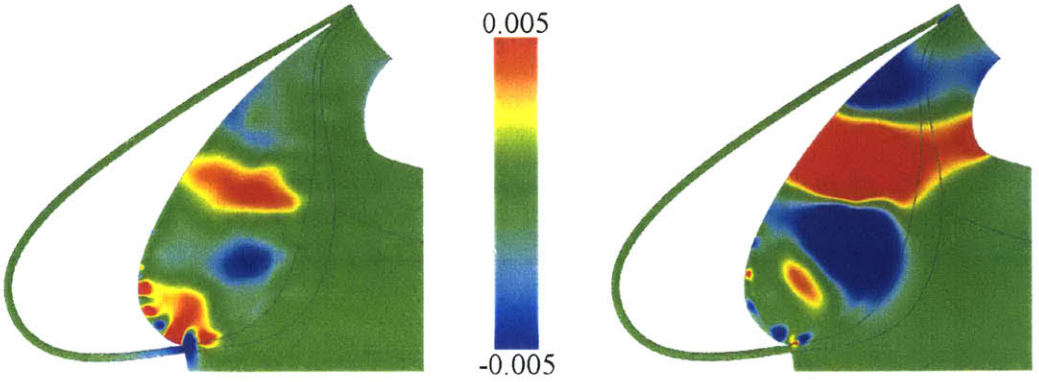

(a) 8° pressure mode 7

(b) 8° pressure mode 8

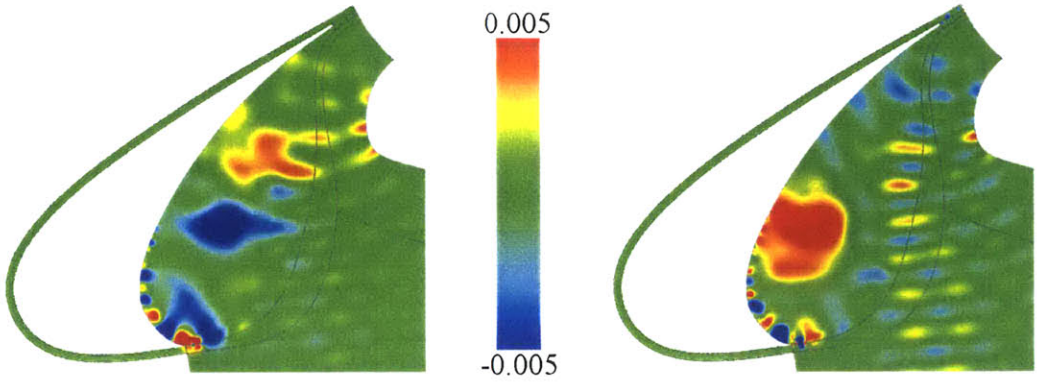

(c) 8° Pressure Mode 9

(d) 8° pressure mode 10

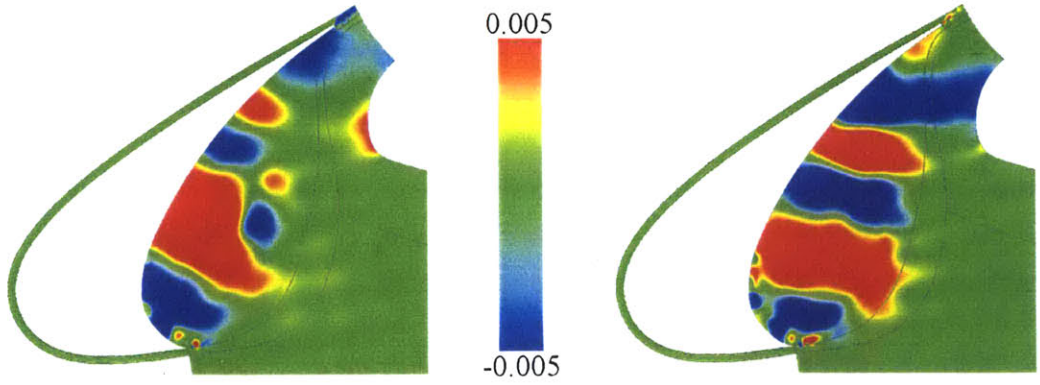

(e) 8° pressure mode 11

(f) 8° pressure mode 12

Figure 3-17: 8-degree pressure modes 7–12.

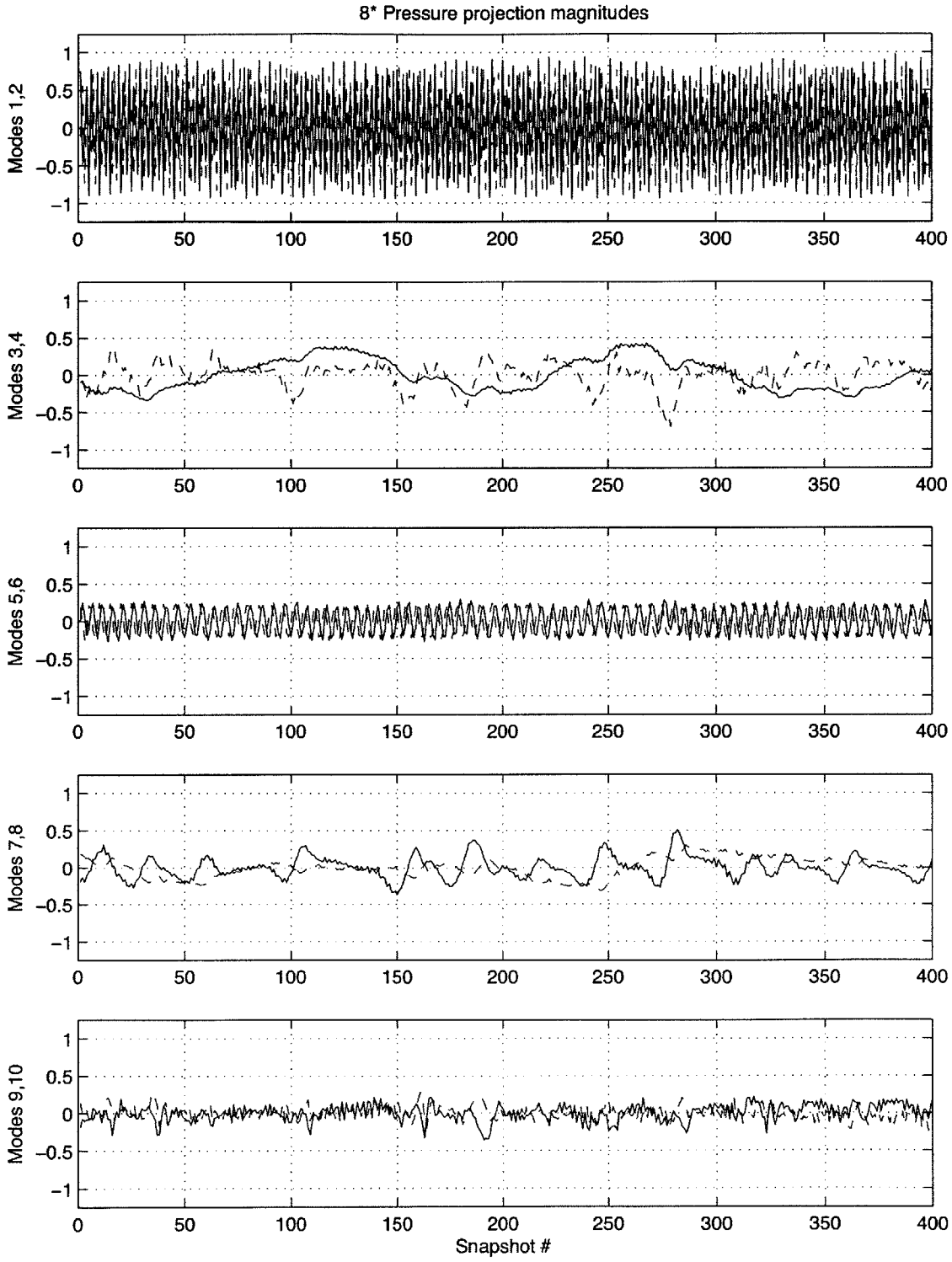

Figure 3-18: Temporal projection magnitudes of 8-degree pressure modes 1–10 onto all snapshots.

——— Odd-numbered modes – – – – – Even-numbered modes

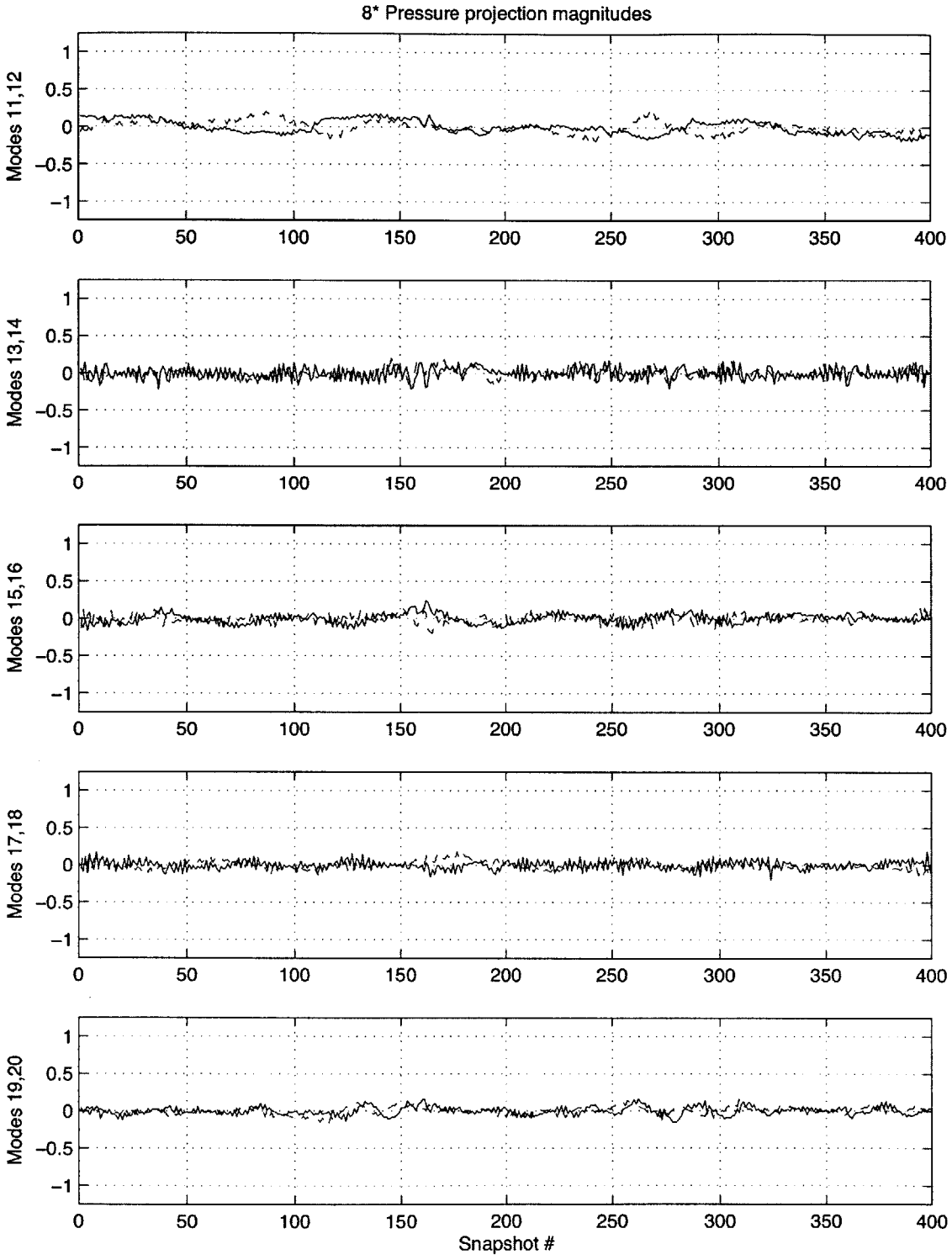

Figure 3-19: Temporal projection magnitudes of 8-degree pressure modes 10–20 onto all snapshots.

——— Odd-numbered modes – – – – – Even-numbered modes

3.2.3 POD Velocity Modes

The Proper Orthogonal Decomposition was also applied to the velocity components of the flow, in an analysis similar to that of the pressure POD. In this study, both u-direction and v-direction velocities were combined to create the POD ensemble. An analysis of the results is presented here. As stated earlier, the 4-degree system exhibited many similarities to the 6-degree system. Mode shapes and temporal projections for the 4-degree velocity POD analysis are given in Figures 3-20 through 3-23. The reader may infer a similar examination of the 4-degree system from the following discussion of the 6-degree velocity POD modes. An extended collection of the POD velocity modes may be found in Appendix B.2.

6-degree Modes

The eigenvalue spectrum of the POD analysis on velocity is shown in Figure 3-5. These eigenvalues denote the amount of kinetic energy in the system. The velocity modes are presented in Figures 3-24 and 3-25 for modes 1 through 12. The vectors represent the direction and relative magnitude at every fifth nodal point in the mesh. These vectors are superimposed upon a contour plot of the magnitude of the velocity fields, so as to give a better indication of where the strongest fields occur. The brighter areas represent a high scalar velocity while darker areas represent low scalar velocity. Scaling legends, which indicate the magnitude of the perturbation velocities, are provided for each of the figures plotted.

The initial two modes for the 6-degree velocity analysis show the regions of activity to be largely contained in the vortices at the trailing edge of the slat[2]. This is not unexpected since the CFD analysis uses a highly refined mesh in that area to capture the trailing edge effects. The strength of the velocity fields here and the fact that their behavior is highly correlated placed this region at the most energetic end of the POD spectrum. Note that the energies of the first two modes are very close to each other in magnitude, respectively containing 13% and 12% kinetic energy. In the assumption that these two modes do capture the trailing edge vortex street, it would be expected that these two modes form an eigenvalue pair. This is similar in nature to other simple flows, such as a vortex street trailing off of

[2]Velocity vectors were removed from the trailing edge region of the slat. Due to the highly refined mesh in this area, the velocity vectors were so densely spaced that they could not be recognized. The contour plot of velocity magnitude should suffice as an indication of the kinetic energy in this region relative to the rest of the slat cove.

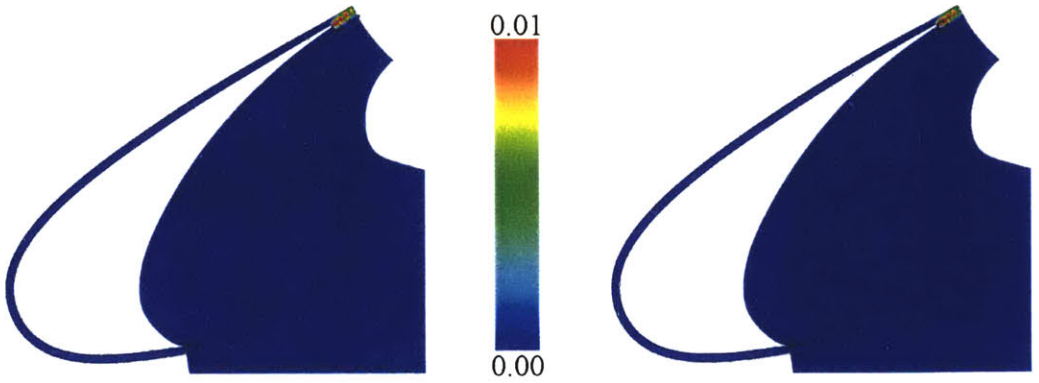

(a) 4° velocity mode 1

(b) 4° velocity mode 2

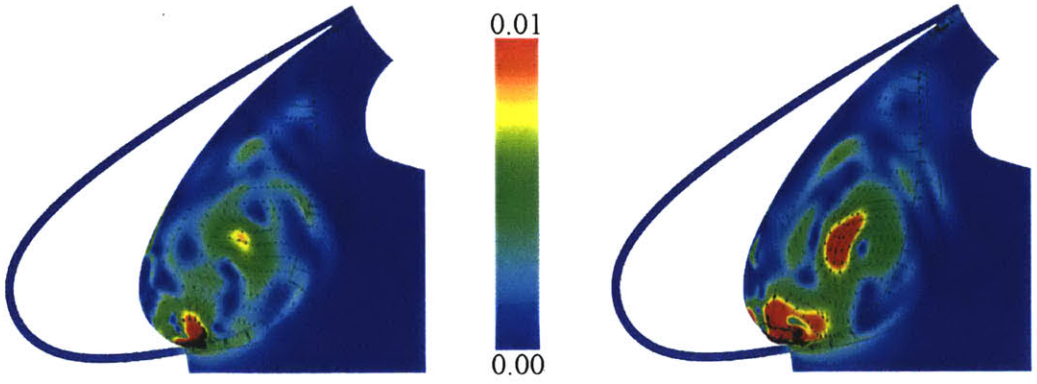

(c) 4° velocity mode 3

(d) 4° velocity mode 4

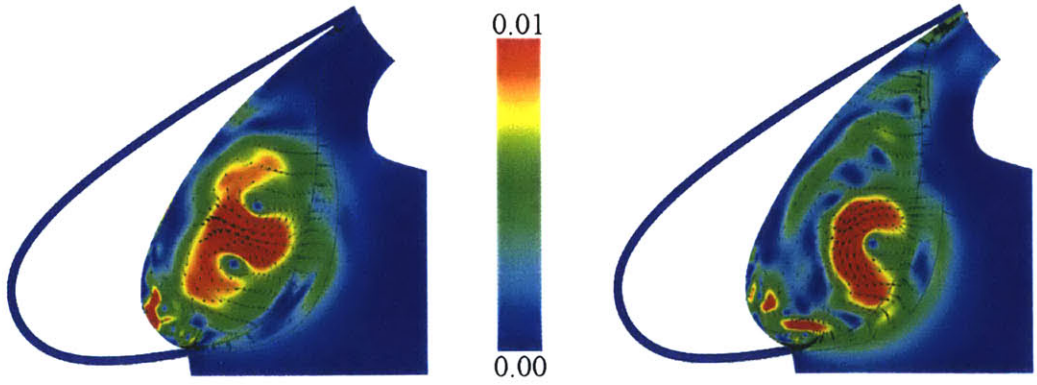

(e) 4° velocity mode 5

(f) 4° velocity mode 6

Figure 3-20: 4-degree velocity modes 1–6.

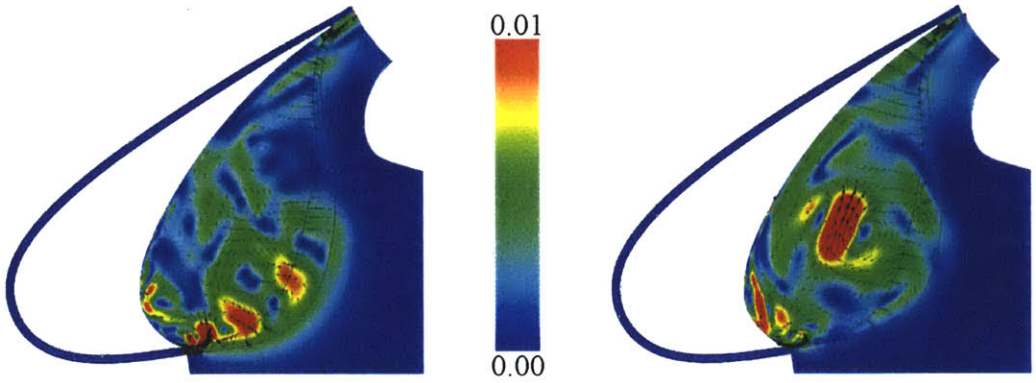

(a) 4° velocity mode 7

(b) 4° velocity mode 8

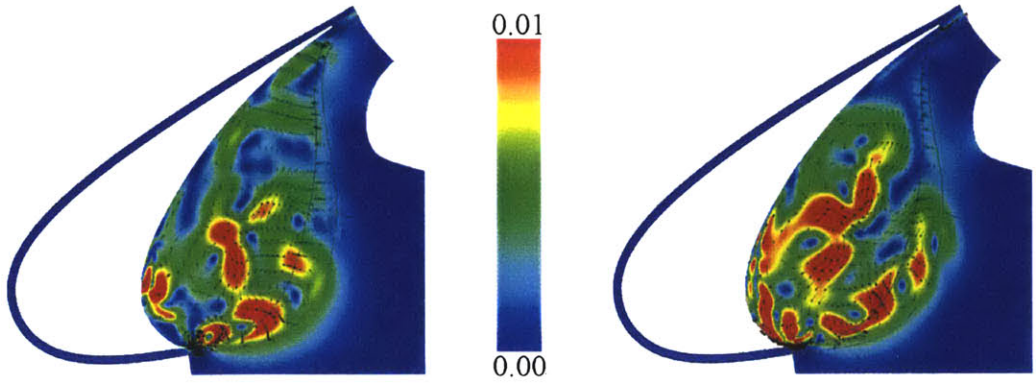

(c) 4° velocity mode 9

(d) 4° velocity mode 10

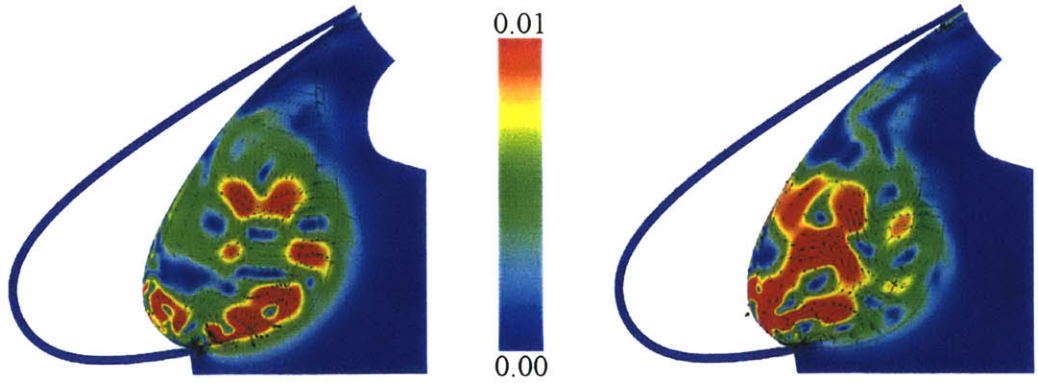

(e) 4° velocity mode 11

(f) 4° velocity mode 12

Figure 3-21: 4-degree velocity modes 7–12.

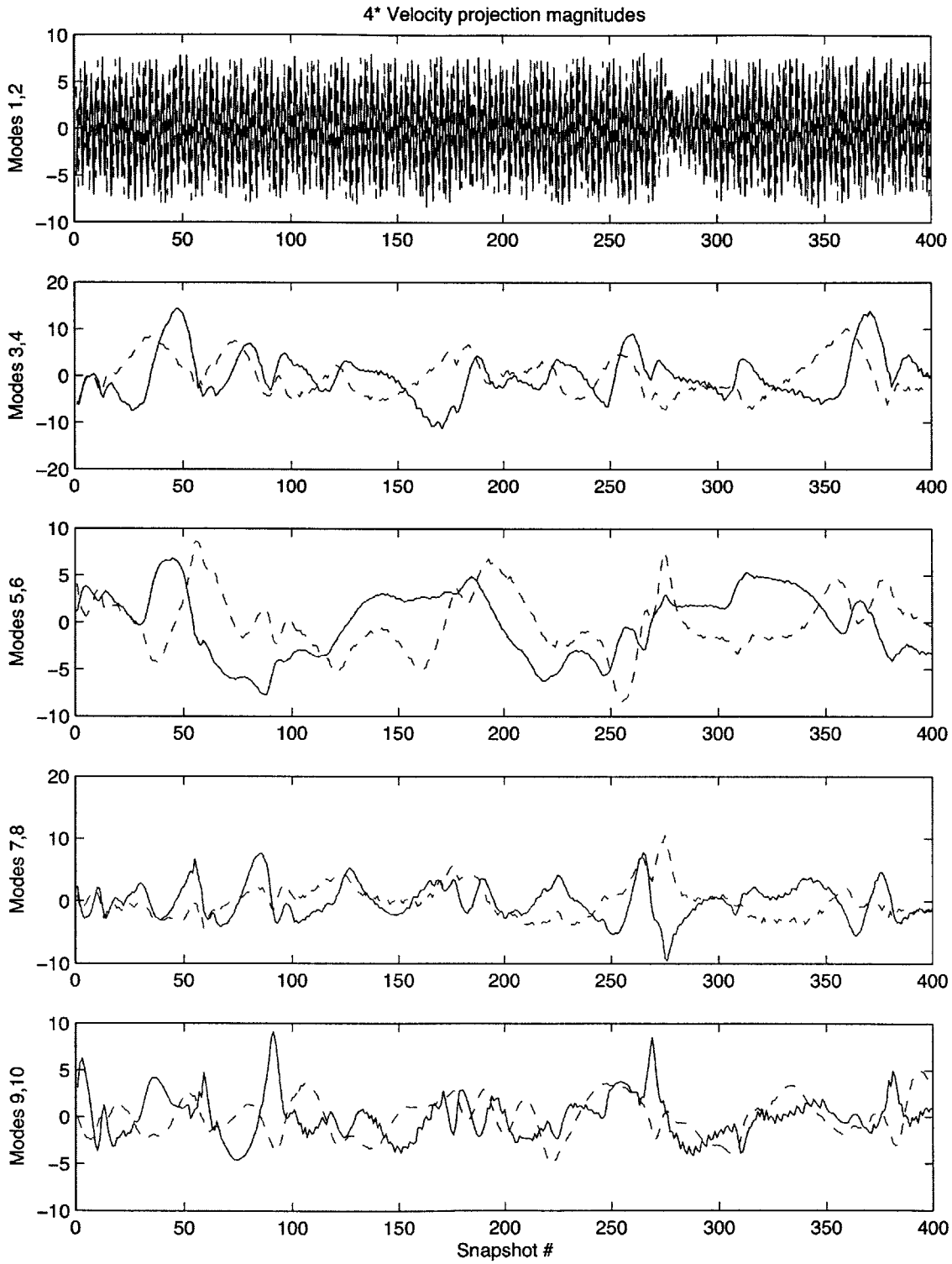

Figure 3-22: Temporal projection magnitudes of 4-degree velocity modes 1–10 onto all snapshots.

——— Odd-numbered modes - - - - - Even-numbered modes

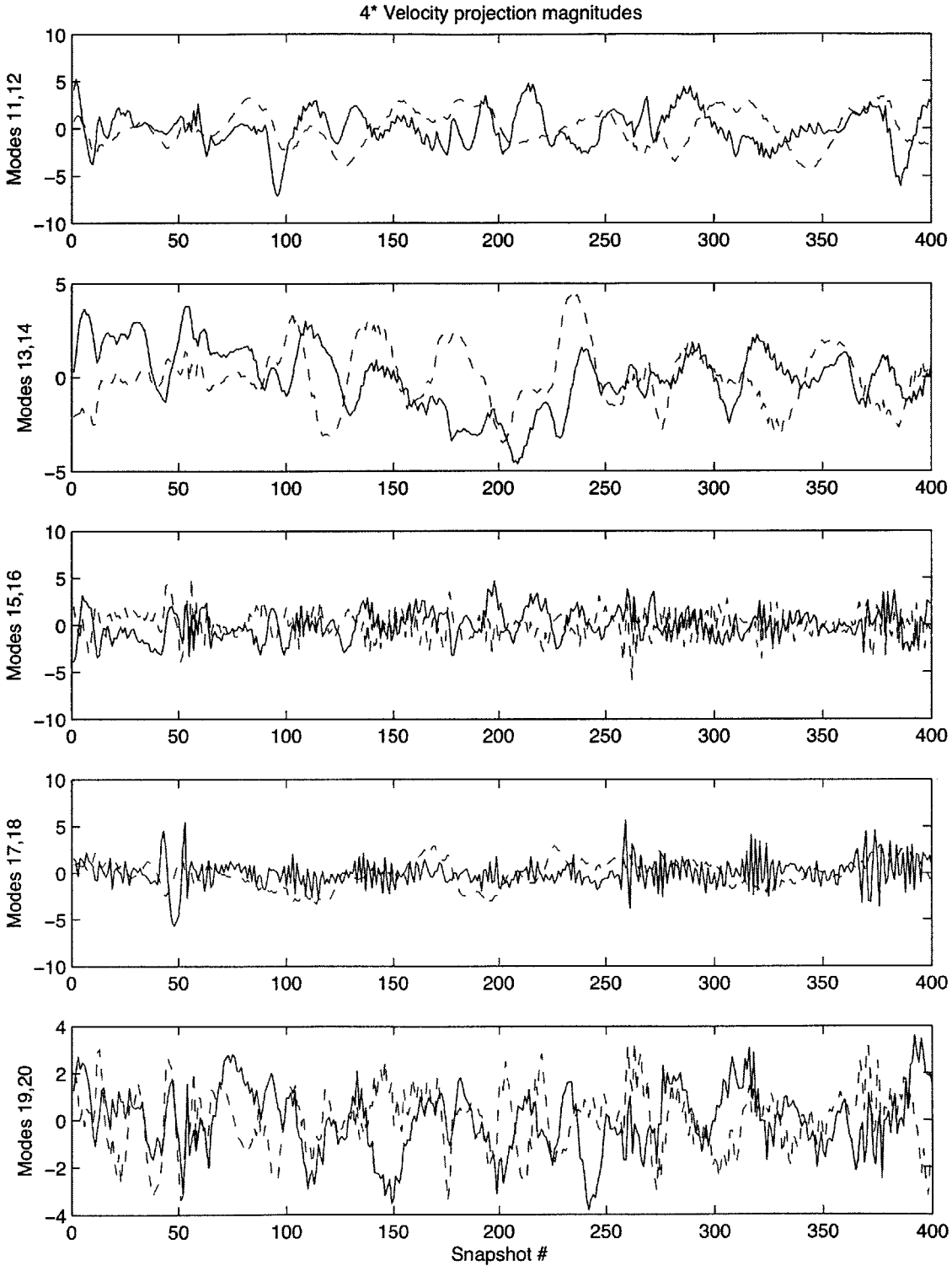

Figure 3-23: Temporal projection magnitudes of 4-degree velocity modes 10–20 onto all snapshots.
——— Odd-numbered modes – – – – – Even-numbered modes

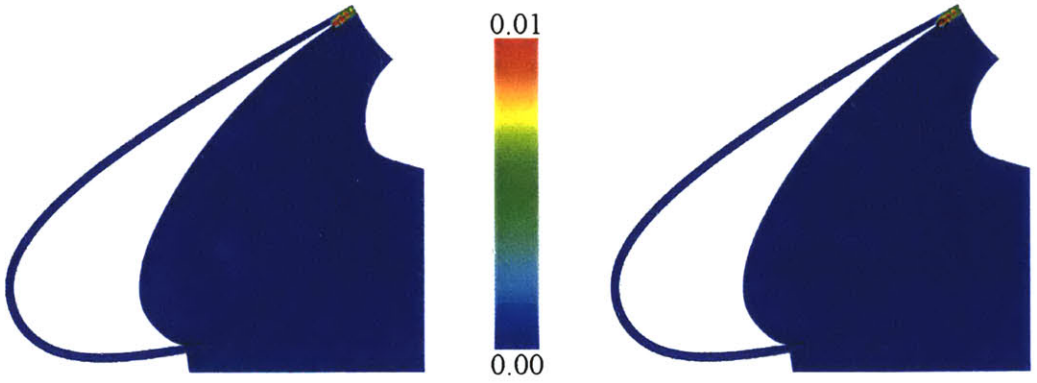

(a) 6° velocity mode 1

(b) 6° velocity mode 2

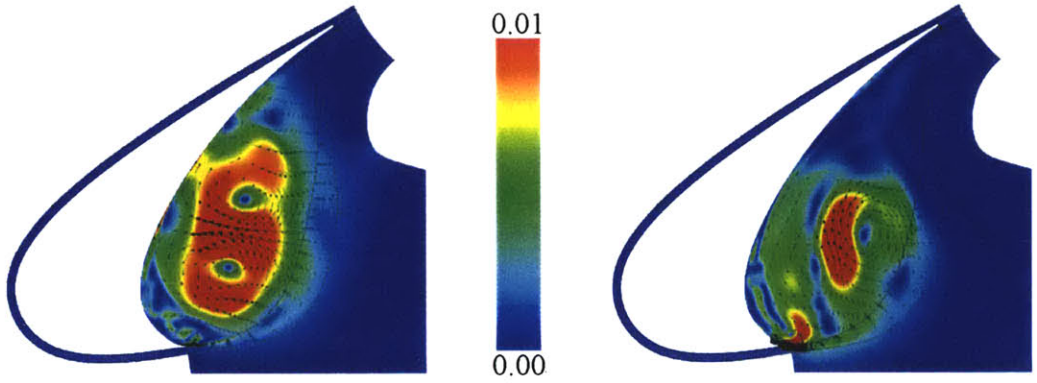

(c) 6° velocity mode 3

(d) 6° velocity mode 4

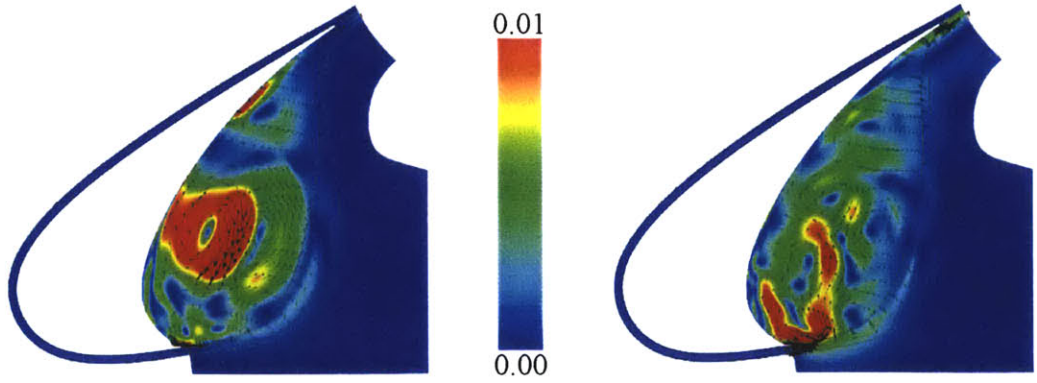

(e) 6° velocity mode 5

(f) 6° velocity mode 6

Figure 3-24: 6-degree velocity modes 1–6.

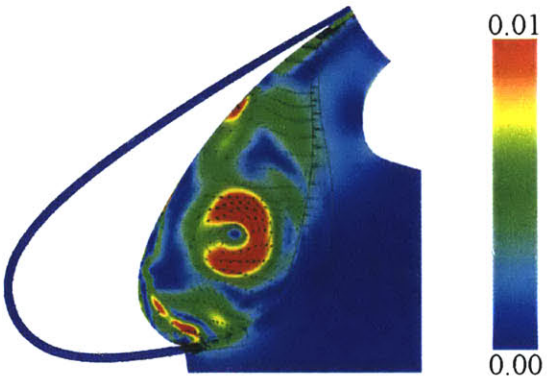

(a) 6° velocity mode 7

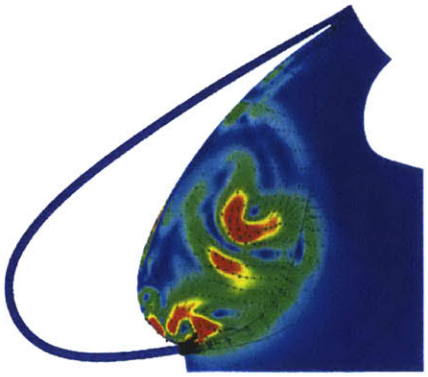

(b) 6° velocity mode 8

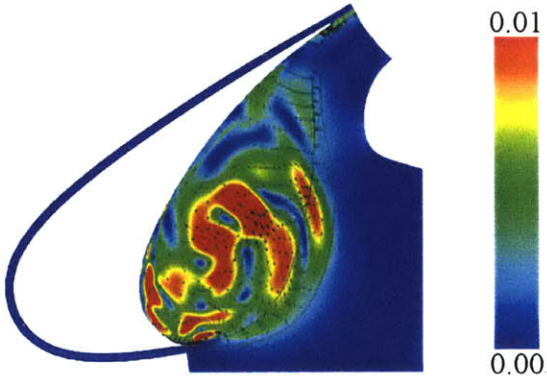

(c) 6° velocity mode 9

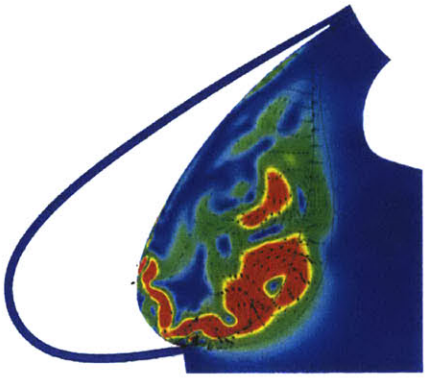

(d) 6° velocity mode 10

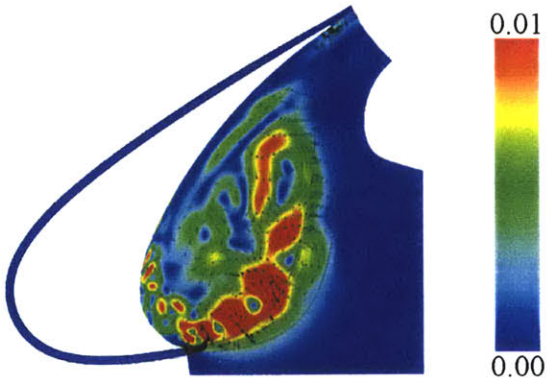

(e) 6° velocity mode 11

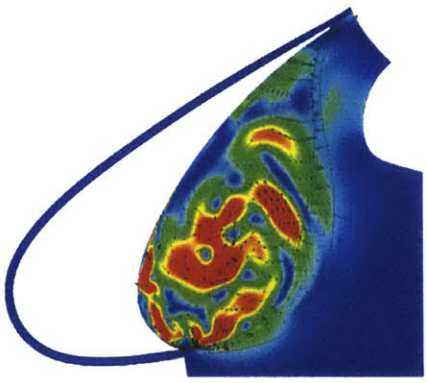

(f) 6° velocity mode 12

Figure 3-25: 6-degree velocity modes 7–12.

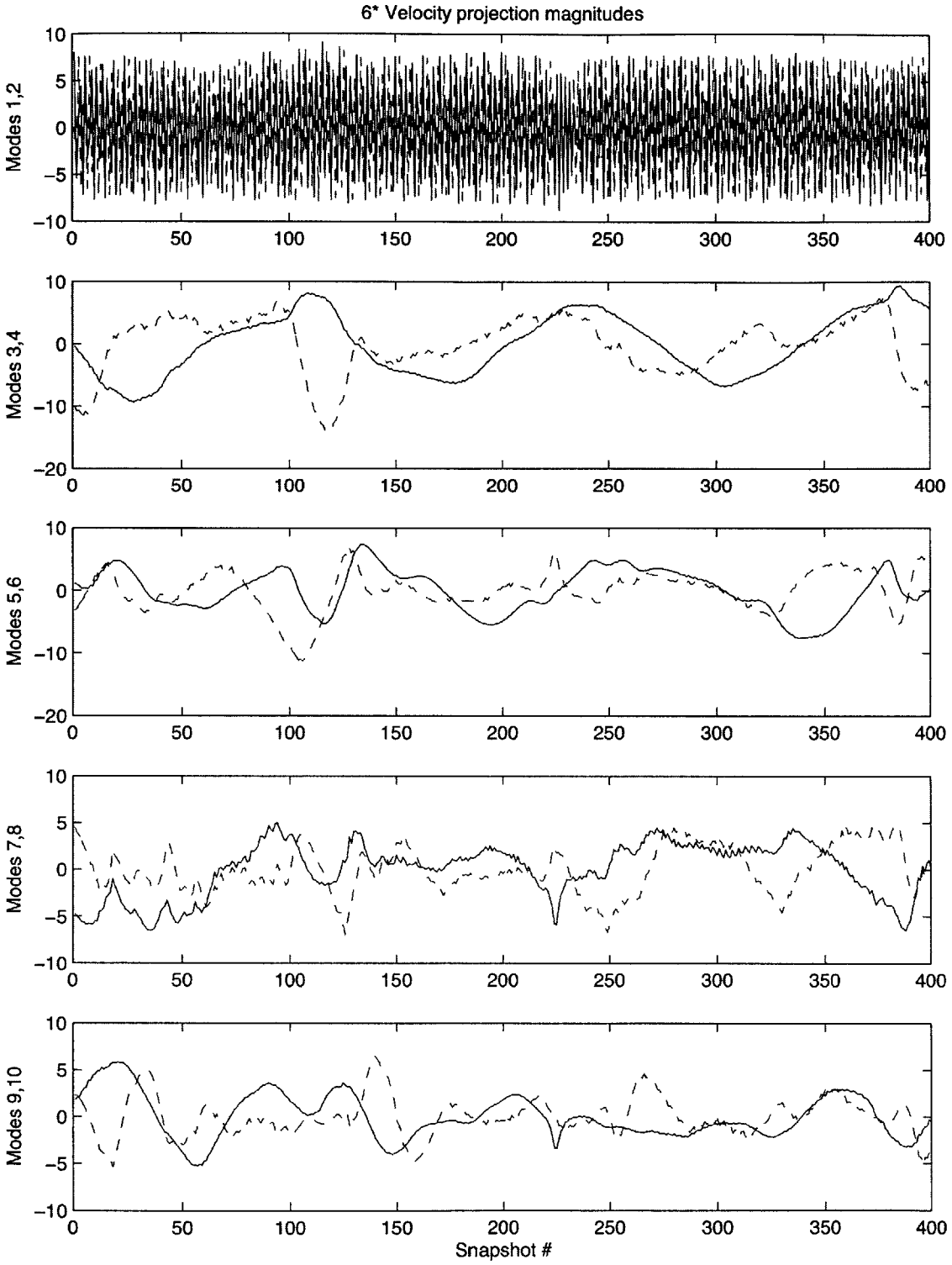

Figure 3-26: Temporal projection magnitudes of 6-degree Velocity Modes 1--10 onto all snapshots.

——— Odd-numbered modes - - - - - Even-numbered modes

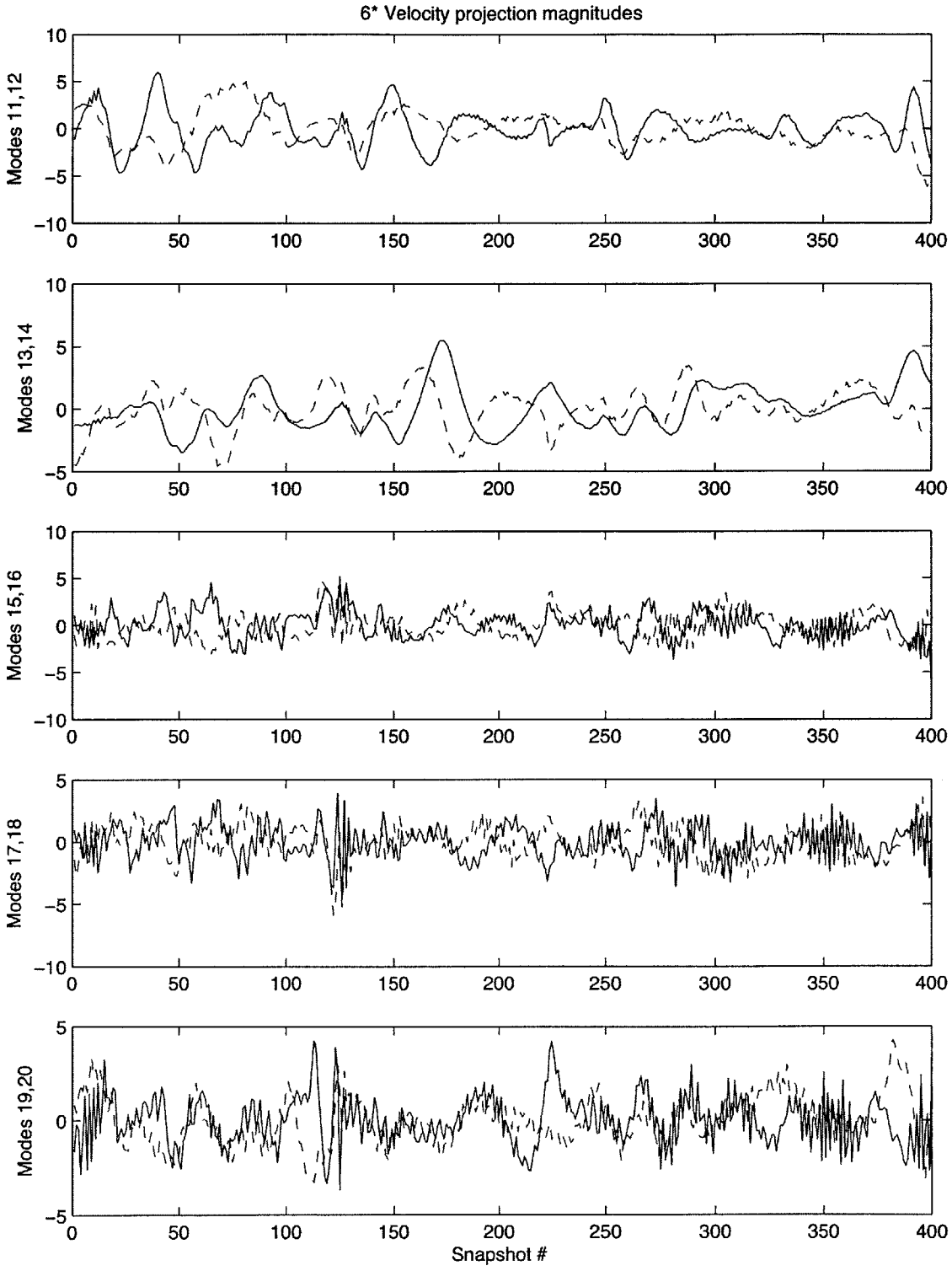

Figure 3-27: Temporal projection magnitudes of 6-degree Velocity Modes 10–20 onto all snapshots.
——— Odd-numbered modes – – – – – Even-numbered modes

a cylinder, where this type of eigenvalue pairing is also evident[19]. In those studies, it was found that eigenvalue pairing and antisymmetric modal shapes suggest convection in a medium. Although it cannot be seen in the figure due to lack of vector resolution, the eigenvalue energy and highly localized velocity fields in modes 1 and 2 suggest the same convective phenomenon of a vortex street trailing from the slat trailing edge, and this is confirmed by analysis of the original snapshots.

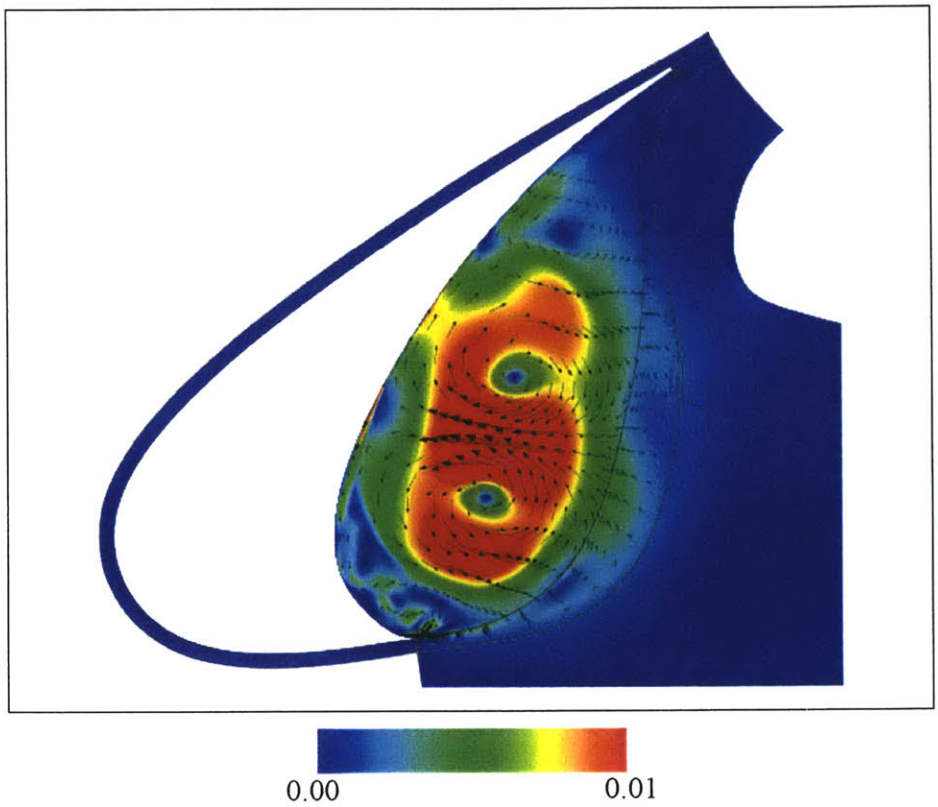

Figure 3-28: 6-degree velocity mode 3.

Velocity fields corresponding to motion in the central vortex core do not appear until modes 3 and higher. A closer view of the modal vector field in mode 3 is shown in Figure 3-28. In mode 3, it can be seen that the velocity vectors take on a circular motion about two cores. The velocity fields rotate clockwise in the upper region and counterclockwise in the lower region. These velocity cores are remarkably similar to the pressure cores in mode 1 of the POD pressure analysis.

In fact, a separate POD analysis on the combination of variables (pressure and $u-$ and $v-$component velocities) showed that the velocity fields do correspond to the pressure fields

of corresponding mode numbers. In that study, the velocity fields also indicated a clockwise circulation around the strong pressure cores, and a counter-clockwise circulation about the opposite-sign pressure cores. This matching of velocity fields and pressure cores remained apparent throughout the ensemble set. However, as explained earlier, it was decided to use separate ensemble norms for pressure and velocity to provide more efficient decompositions in each. This results in optimal velocity modes, which may not exactly match up with the pressure cores in the optimal pressure modes.

8-degree Modes

Similar to the 4- and 6-degree velocity POD modes, the initial two modes of the 8-degree system are dominated by the trailing edge vortices (Figure 3-29). However, unlike the 4- and 6-degree cases, these first two modes contain 33% and 30% of the kinetic energy, roughly double the energy contained in the first two modes of the other cases. Because over 60% of the kinetic energy was captured in the trailing edge flow, this suggests that there is less information in the remaining modes, as the trailing edge vortices take up a much greater proportion of the kinetic energy in the overall flow field. In higher mode numbers, the leading edge and trailing edge activity continues to dominate. The exception is found in modes 5 and 6, where some activity in the cove center region can be detected. The set of modes 7-12 shown in Figure 3-30 are again dominated by the leading and trailing edge flows.

It can be seen in the temporal projections (Figures 3-31 and 3-32) that the high-frequency oscillations are due to the activity in the leading and trailing edge regions. Very little activity can be seen at the trailing edge in modes 3 and 4, and the corresponding temporal data shows the longer wavelength fluctuations related to the larger features in the cove region. In higher modes, it can be seen that much of the kinetic energy is concentrated at the leading edge cusp. The velocity vectors here are clearly stronger in magnitude than any activity in the slat cove center.

In the other two angle of attack systems, the kinetic energy is more evenly proportioned throughout the modes, suggesting a greater distribution of the energy throughout the later modes. This is perhaps more evident in the eigenvalue spectrum of Figure 3-6. Because there is such a large percentage of kinetic energy captured in modes 1 and 2 of the 8-degree system, there is a corresponding large dropoff in kinetic energy of successive modes. Much

of the later modes contain smaller structures to capture the disperse small scale vortex motion evident in the snapshots. Another indicator of the strength of the POD modes is the magnitude of the temporal projections as seen in Figures 3-31 and 3-32. The projection magnitudes follow a decreasing trend with increasing mode number. As the higher POD modes are extracted from the system, they appear to have less influence on the overall formation of the velocity fields.

3.3 Summary

We have seen the decomposition of the pressure and velocity fields into optimal modes generated by the Proper Orthogonal Decomposition. The initial mode shapes contained coherent structures that dominated the slat cove region. This was more apparent in the 4- and 6-degree POD modes compared to the 8-degree modes since the former two systems had a more dynamically active central cove region. A high level of organization was apparent in each mode as well. Features apparent in the individual POD modes as well as certain mode pairs could be linked to phenomena in the actual flow field. Building on this notion we will see in the next chapter how low-order approximations to the original flow field data can be constructed using these POD modes.

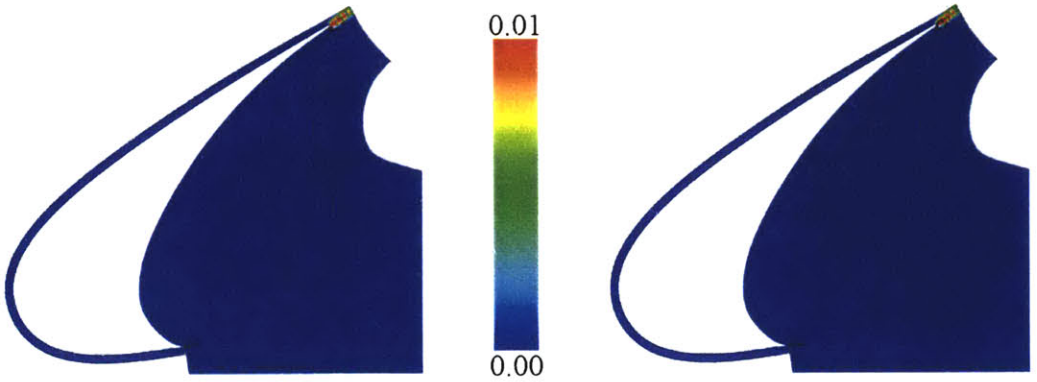

(a) 8° velocity mode 1

(b) 8° velocity mode 2

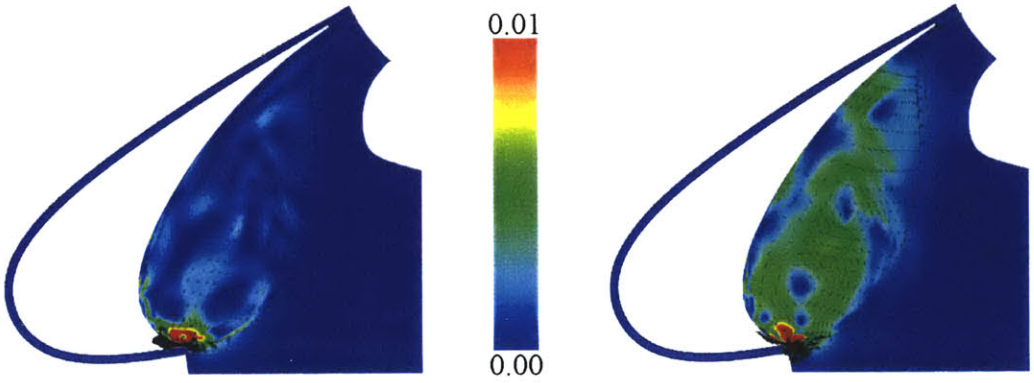

(c) 8° velocity mode 3

(d) 8° velocity mode 4

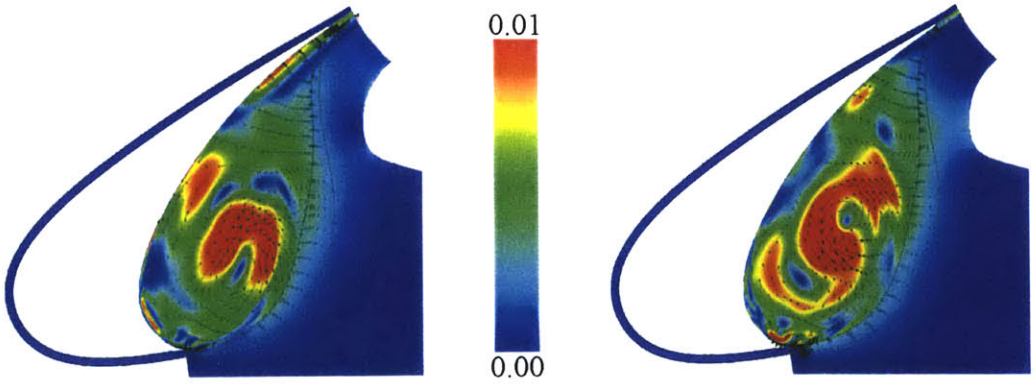

(e) 8° velocity mode 5

(f) 8° velocity mode 6

Figure 3-29: 8-degree velocity modes 1–6.

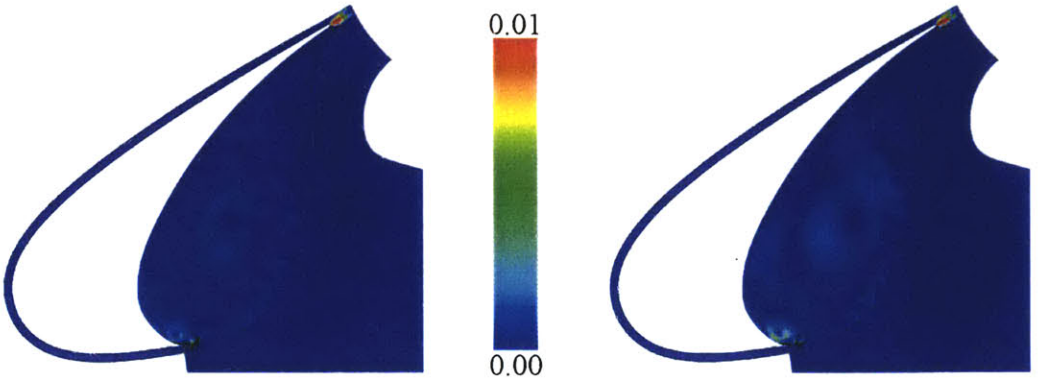

(a) 8° velocity mode 7

(b) 8° velocity mode 8

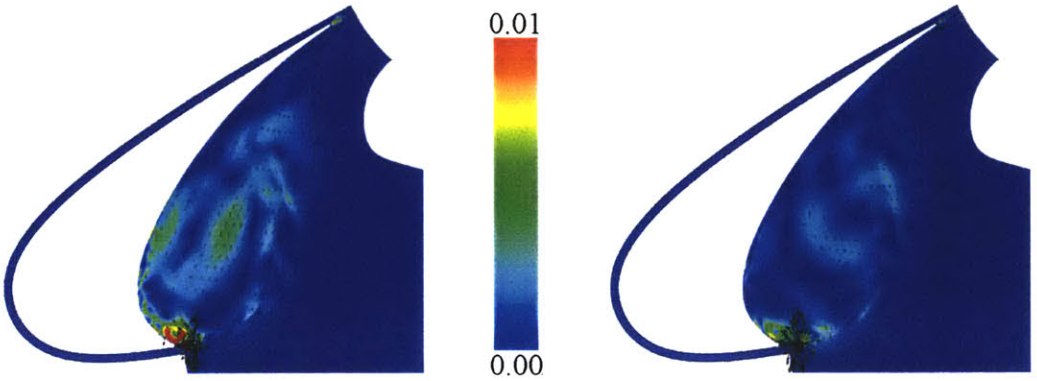

(c) 8° velocity mode 9

(d) 8° velocity mode 10

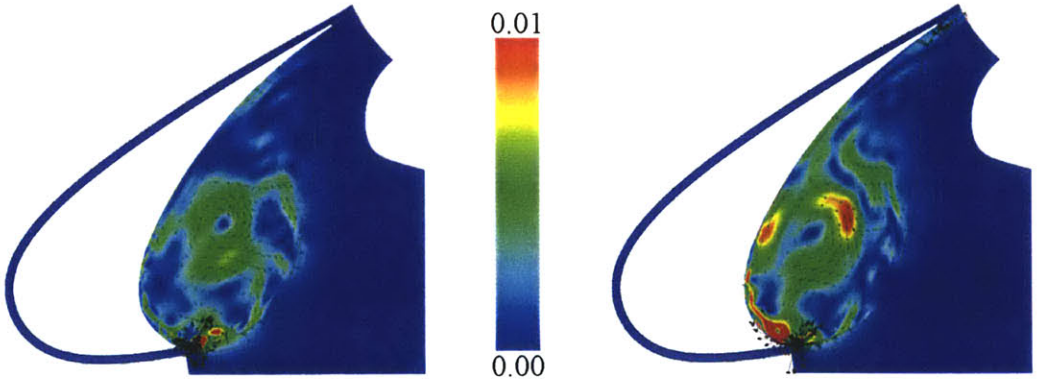

(e) 8° velocity mode 11

(f) 8° velocity mode 12

Figure 3-30: 8-degree velocity modes 7–12.

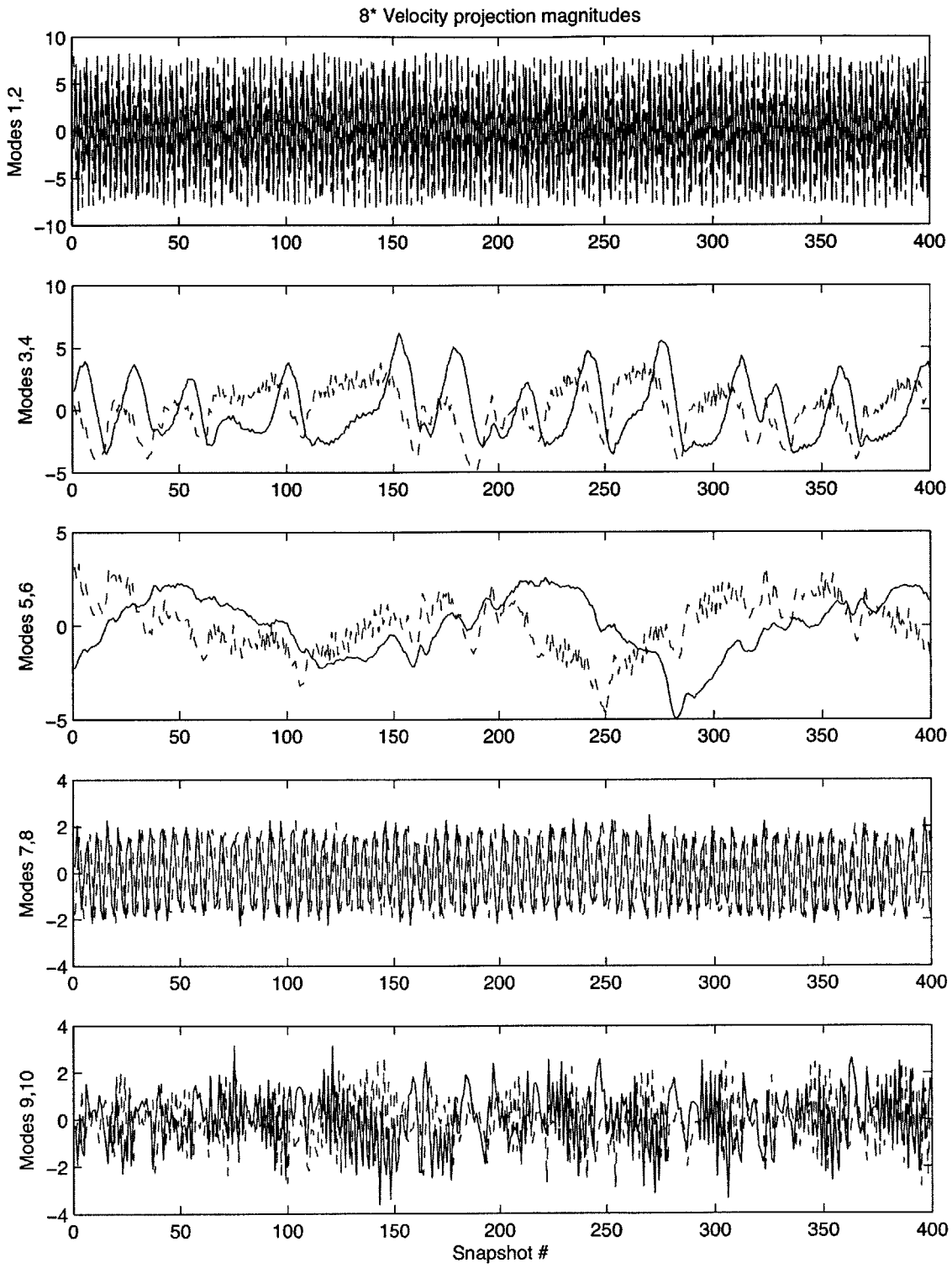

Figure 3-31: Temporal projection magnitudes of 8-degree Velocity Modes 1–10 onto all snapshots.
——— Odd-numbered modes – – – – – Even-numbered modes

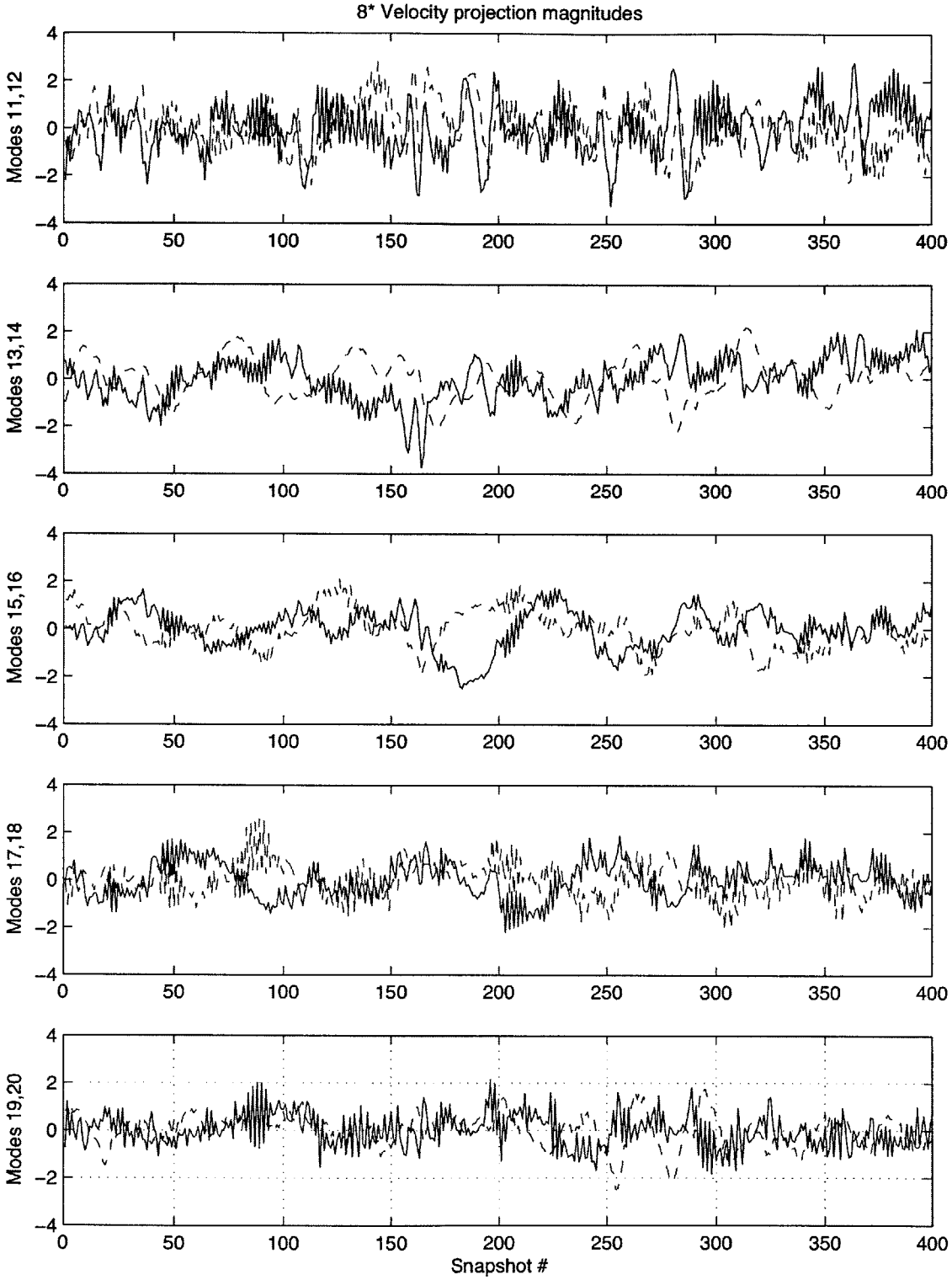

Figure 3-32: Temporal projection magnitudes of 8-degree Velocity Modes 10–20 onto all snapshots.

——— Odd-numbered modes – – – – – Even-numbered modes

Chapter 4

Snapshot Reconstruction

We have seen how the dominant structures are extracted and ordered by the Proper Orthogonal Decomposition. A low-rank approximation of the original data set may be constructed using these extracted modes. In this chapter, we will look at reconstructed snapshots to see how well they represent the original data. The reconstructions will then be used as the input to the acoustic propagation solver, and far-field acoustic spectra based on the slat cove flow approximations will be discussed for the EET airfoil.

4.1 Low-Rank Approximations

The optimality of the POD basis functions ensures that the low-rank approximation formed using an arbitrary number of K leading POD modes will be the optimal representation of the set $\mathbf{u}$ in a least-squares sense (Equation 2.20). Among all linear decompositions, for a given number of modes K, no other orthonormal basis set provides a better representation of the energy on average than those provided by the Proper Orthogonal Decomposition[8]. This enables us to reconstruct low-order systems using a minimum amount of data.

4.1.1 Energy Considerations

Low-order approximations can be formulated using a reduced set of POD modes. Because the eigenvalues drop in magnitude rapidly, adding information through the use of additional modes has a decreased effect as the number of modes is increased. Referring to the eigenvalue spectrum as a percentage of total energy, for example the pressure eigenvalues of Figure 3-4, the rate at which the eigenvalues decrease for each angle of attack provides a clue as

to how dominant the POD modes are. The initial modes contain the most energy, and subsequent modes drop off quickly. For instance, the first 8-degree mode has the highest energy content of the three angle-of-attack studies, and the magnitudes of its later modes drop off at a faster rate than the 4-degree and 6-degree modes. It can thus be deduced that the 8-degree slat dynamics are better correlated across the ensemble. Furthermore, although the higher mode numbers appear to contribute a relatively small percentage to the total system energy, they still contain important information used to reconcile the sparse yet locally intense vortex formations in the shear layer. The aperiodic behavior and sparseness of the vortex evolution leads to the decomposition into a larger number of important POD modes.

It is apparent that the approximation will become more precise as a larger number of modes are included. Theoretically, incorporating all the modes will recover the original data image. In order to construct a low-order approximation, however, it is necessary to determine a measure by which we can be confident in the fidelity of our data. In other words, the question arises as to how many modes are desired to create the reconstruction. It is perhaps more easily understood when the eigenvalue spectrum is recalculated to show the accumulated energy content of the POD modes. The accumulated energy content of the POD modes may be defined by

$$AEC = \frac{\sum_{i=1}^{K} \lambda_i}{\sum_{i=1}^{M} \lambda_i}, \tag{4.1}$$

where K is the arbitrarily selected cutoff point for the number of modes selected. This criterion has been up for debate, because there is no definitive answer as to what value is appropriate. Sirovich suggested the standard of taking the number of modes equivalent to representing 99% of the data captured. The same standard will be used henceforth in this study and we will also include other benchmarks for comparison. To show the quality of the reconstructions of the slat flow analysis, the number of modes representing 70%, 90%, 99%, and 99.9% energy are provided in this study.

Figures 4-1 and 4-2 illustrate the accumulated energy content of the POD modes for the pressure and velocity analyses, up to the first 100 modes. Here, it is clearly apparent that the accumulated energy in the 8-degree case rises faster than the other two angle of attack conditions. The first mode itself contains over 40% of the pressure energy, the first two

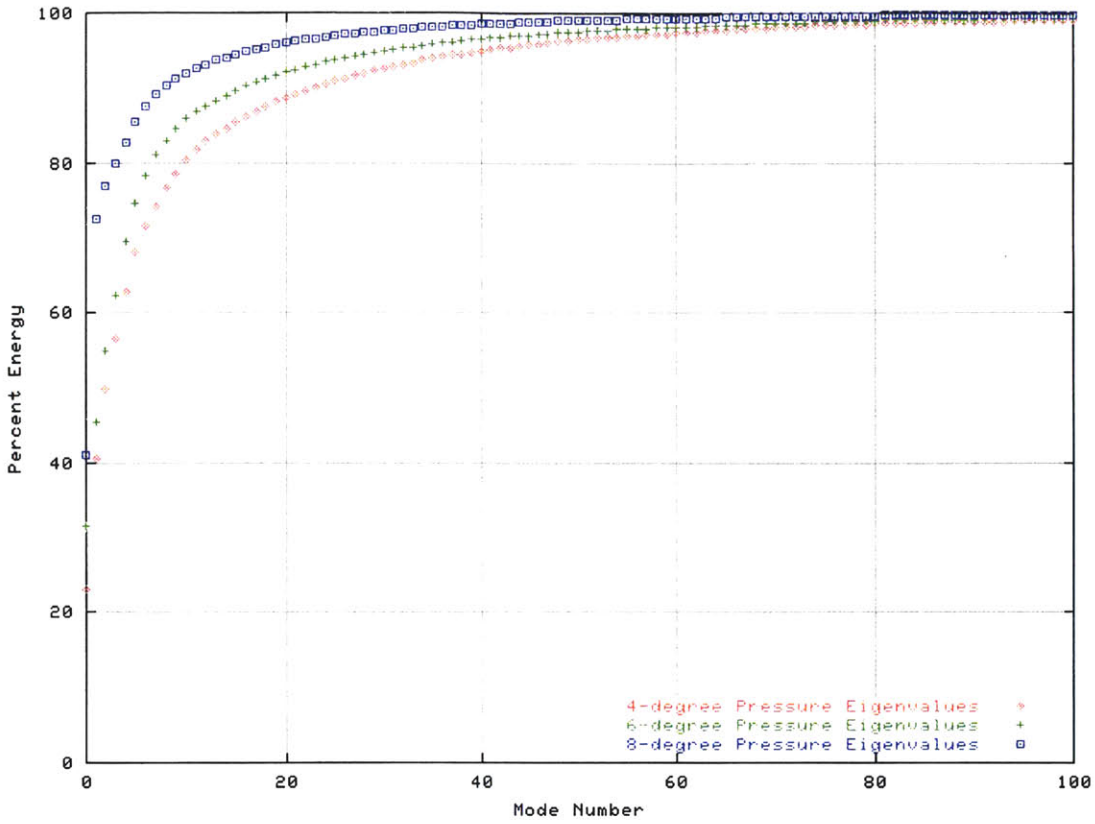

Figure 4-1: Accumulated energy content of POD modes - Pressure energy.

modes contain over 70%, and the first 9 modes together combine to contribute over 90% of the energy. The accumulated energy spectrum slowly asymptotes as it reaches beyond 90% since the modal energy represented by the eigenvalues decreases rapidly. A larger number of modes are necessary to accumulate further energy since these modes contain smaller and/or fewer coherent structures. Still, 99% of the pressure energy in the 8-degree system is captured in the first 50 modes and 99.9% is recovered in 130 modes.

In contrast, the 6-degree modes contain less energy in each of the leading modes, requiring 17 modes to recover 90% of the energy and 84 modes to capture 99%. Again, as in the 8-degree system, a larger number of modes are required to capture further energy simply due to the dropoff in energy of the higher modes. For the 6-degree case, 185 modes are required to regain 99.9% of the pressure energy. The number of modes required to capture specified amounts of pressure and kinetic energy at specified ensemble energies at the preselected benchmarks are given in Tables 4.1 and 4.2, respectively.

Pressure Energy	# of Modes		
	4-degrees	6-degrees	8-degrees
70%	7	5	2
90%	24	17	9
99%	96	84	50
99.9%	199	185	130
99.99%	309	301	249

Table 4.1: Number of modes required to capture pressure energy.

Kinetic Energy	# of Modes		
	4-degrees	6-degrees	8-degrees
70%	11	9	4
90%	35	29	18
99%	124	115	84
99.9%	239	227	191
99.99%	341	333	310

Table 4.2: Number of modes required to capture kinetic energy.

4.1.2 Reconstructions

Using the accumulated energy spectrum shown previously, we can reconstruct any snapshot in the original ensemble set to the desired accuracy. Equation 2.2 is used along with Equation 2.6, beginning with the mean flow and linearly superposing each of the modes as specified by the coefficients A_n as determined by orthogonality conditions (Equation 2.19). The contour scalings in the figures that follow were chosen to be the same across all three angles of attack in order to illustrate the behavior of the systems in relation to each other.

Pressure Snapshots

To demonstrate the ability to create linear reconstructions of the original data set using the POD basis modes, arbitrary snapshots were selected out of the ensemble set to be reconstructed. An arbitrary snapshot was taken at each of the three angles of attack to provide a broader analysis, as shown in Figures 4-3 through 4-5. Each of the reconstruction diagrams shown in the figures displays the mean flow, reconstructions at 70%, 90%, 99% and 99.9% pressure energy, and finally the original snapshot. The scaling legends indicate the actual flow field pressures and are provided for each of the figures plotted.

The original snapshot at 4-degrees (Figure 4-3(f)) contains a the strong central core,

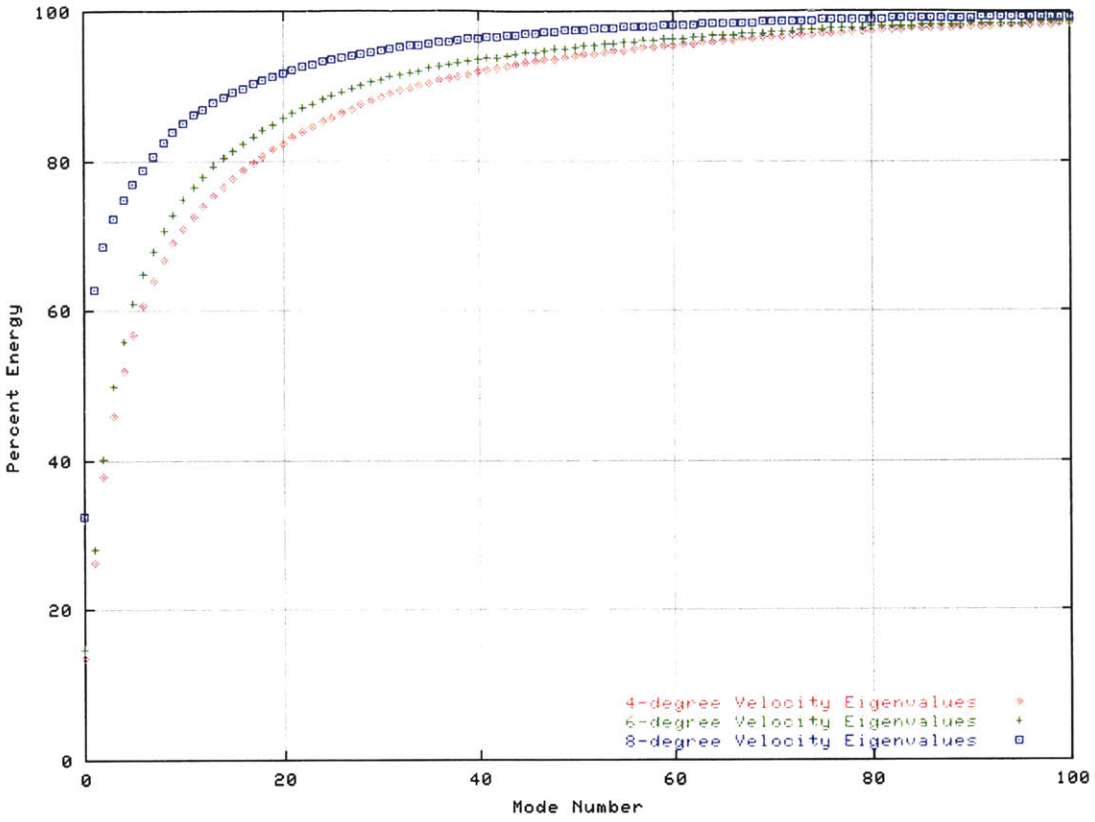

Figure 4-2: Accumulated energy content of POD modes - Kinetic energy.

with three major positive-negative vortex pairings along the inner surface of the slat. There is also a vortex pressure core toward the top of the slat free shear layer which is just beginning to convect back toward the leading edge. The mean flow shows the main core section that was extracted from the entire ensemble, and acts as the starting point for this reconstruction analysis. The 70% reconstruction resolves the larger features of the flow, using the first 7 modes from the POD basis set. The central core is stronger compared to the mean flow, and minor details in the smaller vortices rolling up along the inner surface toward the leading edge cusp can be seen forming. The central core begins to take a final shape in the 90% reconstruction, along with a more refined vortex at the leading edge cusp. The pressure cores along the inner surface are still diffuse, but the general locality of these structures can be identified in the mode. The 99% reconstruction clearly defines the locations of all significant pressure cores, along with the upper region vortex that is beginning to recirculate. The 99.9% reconstruction provides a cleaner snapshot of

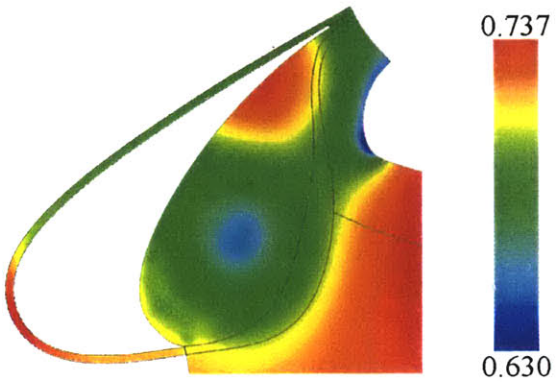

(a) 4° pressure snapshot – Mean flow

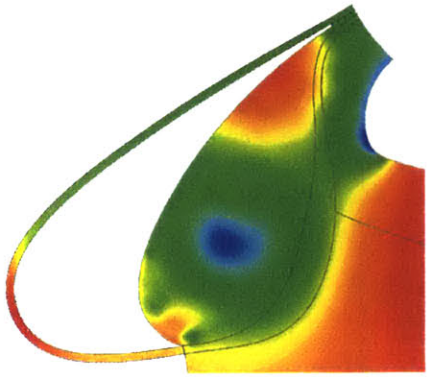

(b) 4° pressure snapshot – Mean + 70% perturbation energy

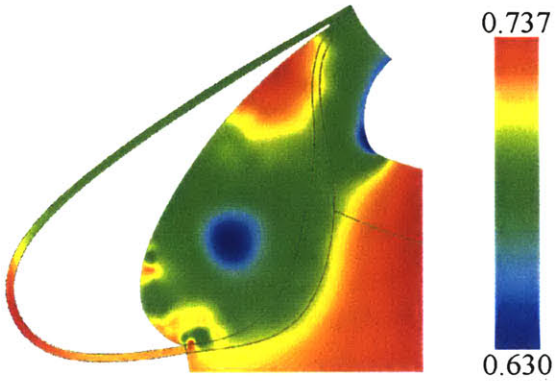

(c) 4° pressure snapshot – Mean + 90% perturbation energy

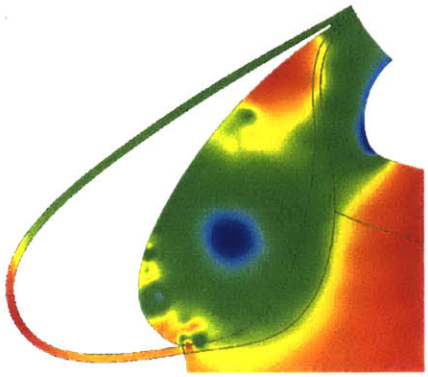

(d) 4° pressure snapshot – Mean + 99% perturbation energy

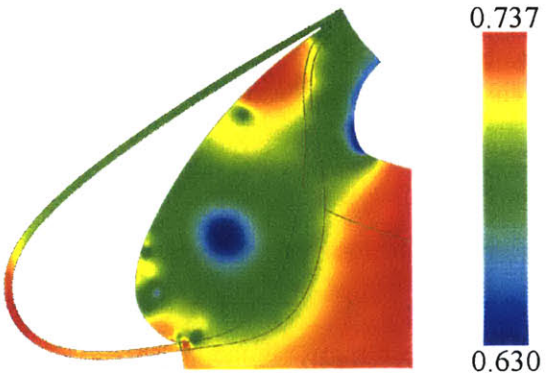

(e) 4° pressure snapshot – Mean + 99.9% perturbation energy

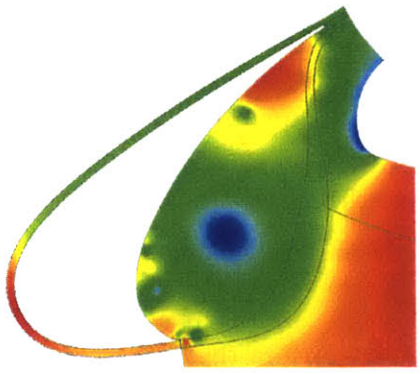

(f) 4° original pressure snapshot

Figure 4-3: 4-degree pressure reconstruction snapshots.

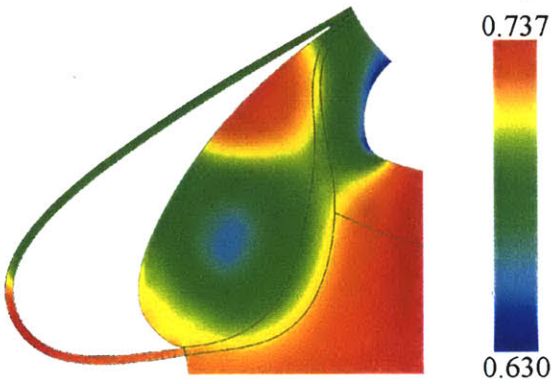

(a) 6° pressure snapshot – Mean flow

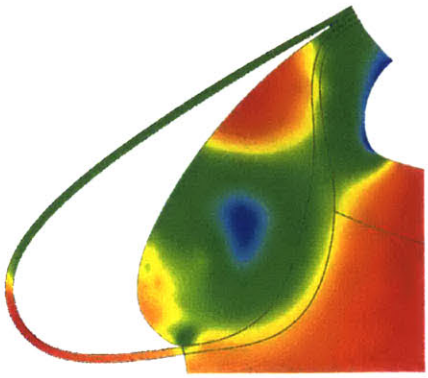

(b) 6° pressure snapshot – Mean + 70% perturbation energy

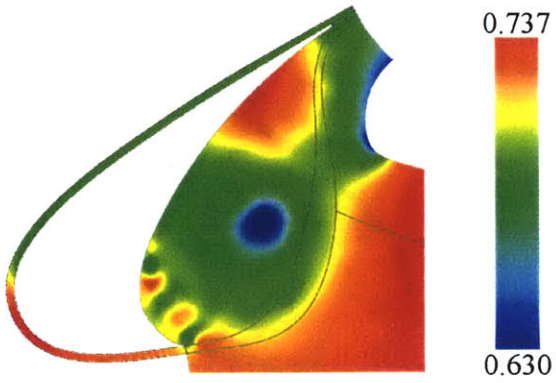

(c) 6° pressure snapshot – Mean + 90% perturbation energy

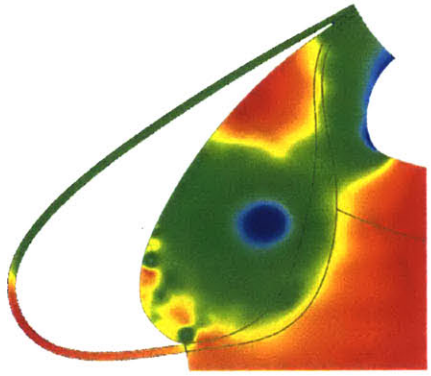

(d) 6° pressure snapshot – Mean + 99% perturbation energy

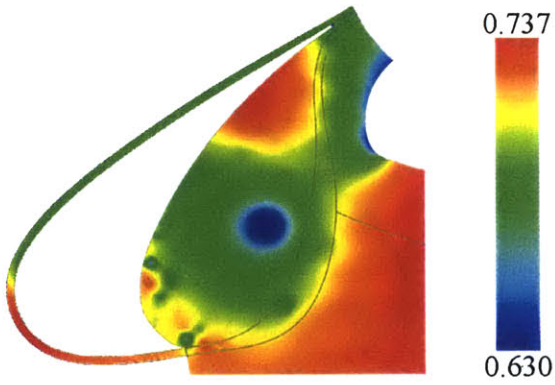

(e) 6° pressure snapshot – Mean + 99.9% perturbation energy

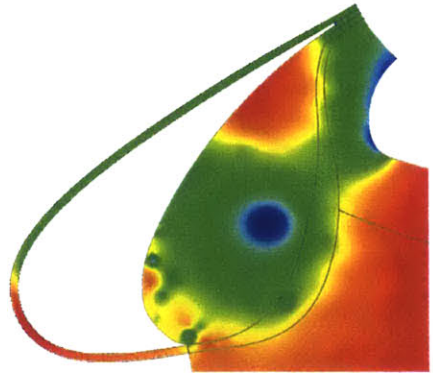

(f) 6° original pressure snapshot

Figure 4-4: 6-degree pressure reconstruction snapshots.

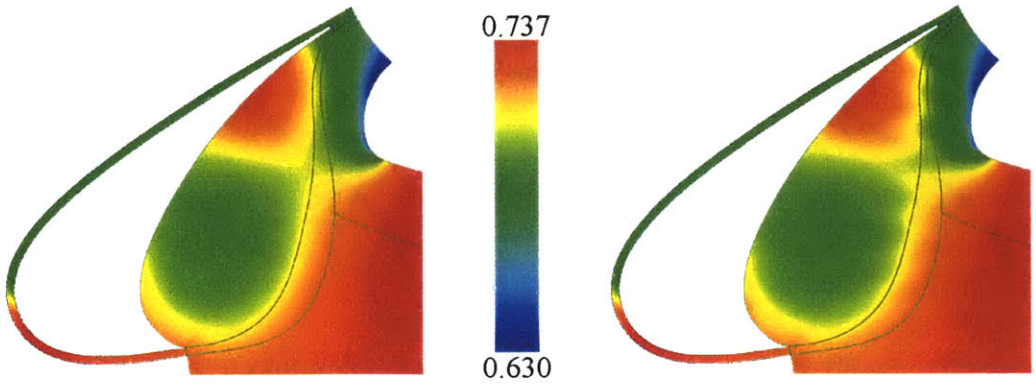

(a) 8° pressure snapshot – Mean flow

(b) 8° pressure snapshot – Mean + 70% perturbation energy

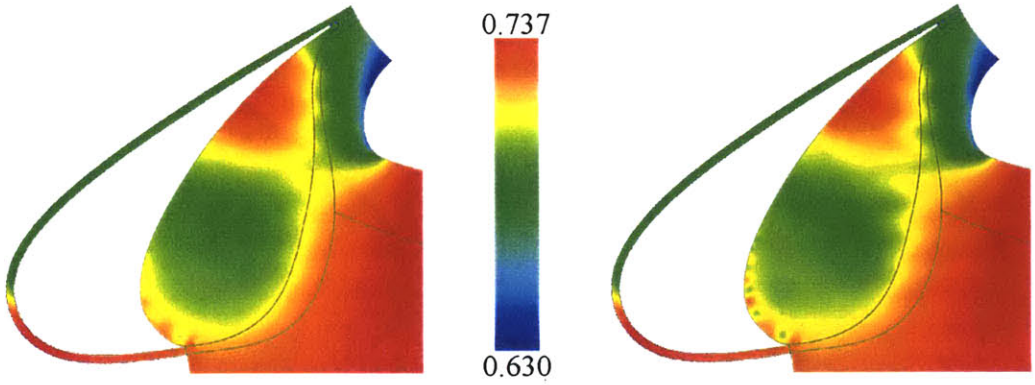

(c) 8° pressure snapshot – Mean + 90% perturbation energy

(d) 8° pressure snapshot – Mean + 99% perturbation energy

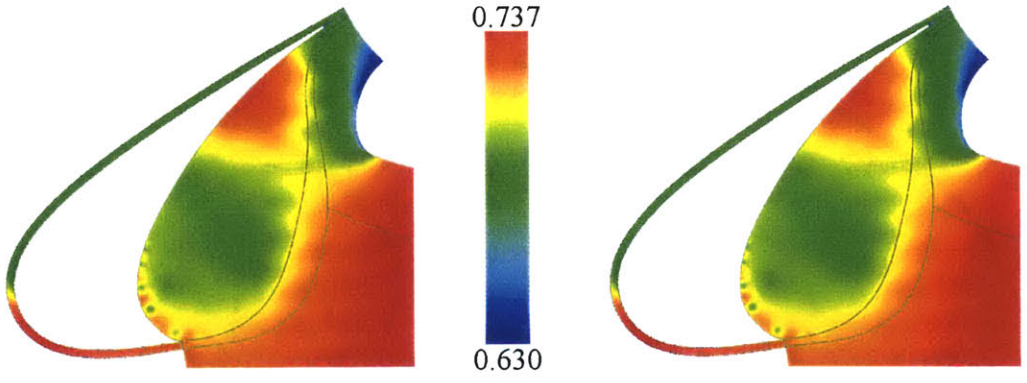

(e) 8° pressure snapshot – Mean + 99.9% perturbation energy

(f) 8° original pressure snapshot

Figure 4-5: 8-degree pressure reconstruction snapshots.

the flow than the 99%, though at a high cost of an extra 103 POD modes. All pressure regions are clearly defined using this reconstruction, with smoother variations between neighboring contours. This snapshot reconstruction is virtually indistinguishable from the original snapshot from a visual perspective.

Capturing 70% of the pressure energy in the 6-degree system requires the leading 5 POD modes. No major flow features are clearly defined, though note that the central core is beginning to shift to the right of the cove center. A small pressure core is seen at the leading-edge cusp, but there are not yet enough modes to resolve this feature clearly. 90% of the pressure energy is recovered using the first 84 modes of the POD. This resolves the most dominant pieces of the flow field and provides a reasonable reconstruction for visualization purposes. The central core has shifted to its final position on the right, and appears to be on the correct order of magnitude as the original snapshot. Regions defining the small strong pressure cores have become apparent, however they are not yet fully defined. There is a slight fuzziness about the edges of these zones, resulting in a diffusive appearance. At 99% reconstructed energy, the snapshot does not differ significantly from the 90% reconstruction. All smaller pressure cores are now clearly defined and are also more tightly rendered. 99.9% of the energy is captured using 227 POD modes in the reconstruction. Again, there are only slight improvements to the snapshot when analyzed visually. Contours are smoother, and the last diffuse pressure vortex found in the free-shear layer has now become fully resolved.

The original pressure field of the 8-degree snapshot appears less dynamic when compared to the other two angle-of-attack snapshots. The central core region is relatively calm, with several small vortex cores developing along the inner surface. Only the first two POD modes are required to capture 70% of the reconstructed perturbation energy in the 8-degree snapshot. That 70% flow field, however, is masked by the mean flow, which appears to remain dominant throughout the snapshot reconstructions. In contrast to the 4- and 6-degree reconstructions, the 8-degree case does not require a large shift in the mean flow to match the current snapshot set. This is because the original ensemble solutions exhibited a relatively stable cove region, and much of that energy had been extracted out to the mean flow variable. There is very little activity in the central core that needs to be decomposed into the leading POD modes. As with the 90% reconstruction, the general appearance of the snapshot remains the same, with a slight variation on the inner surface near the leading edge cusp. Fifty modes capture 99% of the pressure energy, and it is here that we begin to

recognize small vortex-induced pressure cores along the forward edge of the inner surface. The onset of the pressure bands becomes more apparent as well along the edges of the free shear layer, with the variations becoming most obvious in a line leading directly down from the trailing edge of the slat. The inner surface vortices become clearly defined in the 99.9% reconstruction (130 modes), though no new features are found in comparison with the 99% reconstruction. Again, this is indistinguishable from the original pressure field snapshot.

Velocity Snapshots

The same reconstruction technique was applied to the velocity snapshots, as shown in Figures 4-6 through 4-8. Velocity vectors are only shown only in the two sub-meshes that constitute the slat cove region. Because the velocity vectors are difficult to visualize, they are superimposed upon a contour flood of the velocity magnitude. Again, three arbitrary snapshots at the three angles of attack are shown. Scaling legends are included with the figures to indicate the actual flow field velocities in the contour maps.

Similar trends may be found in the reconstructions of the velocity fields as was seen in the pressure field reconstructions. The snapshots are primarily dominated by the mean flow, with most visually identifiable features found in the smaller perturbations along the inner surface towards the leading edge cusp. The 4-degree mean flow exhibits a strong central circulation with a uniform velocity magnitude. The 90% kinetic energy reconstruction shows a more centralized core, with the main flow still circulating around it. Smaller velocity perturbations are now seen along the inner slat towards the leading edge. It is here that the smaller vortices are becoming more resolved. Only slight differences can be found in the behavior of the kinetic energy field between the 90% and 99% reconstructions. It is surmised that very incidental changes in vector direction and magnitude are applied in the later stages of the reconstruction to individual nodes in the mesh, but yet are not great enough to appear in the visualization. Because the movement of the vortices along the leading edge and through the free-shear layer were highly random in nature, the snapshots were highly uncorrelated and the decomposition of the velocity fields required a broader number of POD modes to characterize the system kinetic energy about the entire ensemble set.

The 6-degree snapshot chosen in Figure 4-7 contains more of the random vortex structures convecting through the slat cove. The region of the central core circulation appears to

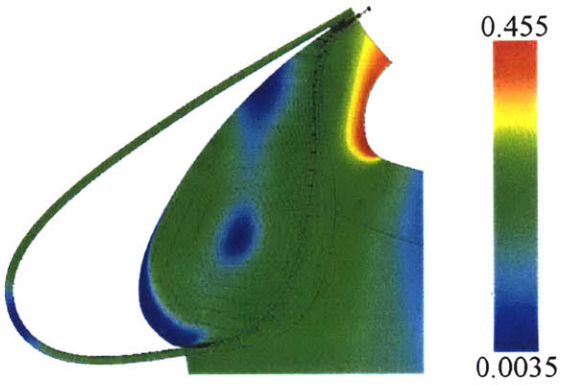

(a) 4° velocity snapshot - Mean flow

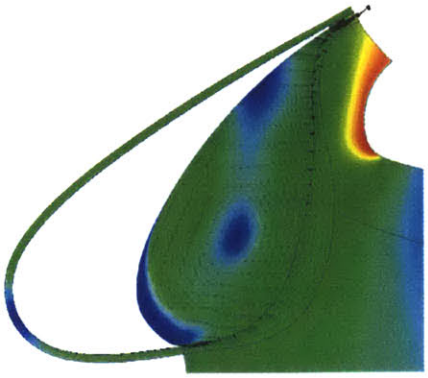

(b) 4° velocity snapshot – Mean + 70% perturbation kinetic energy

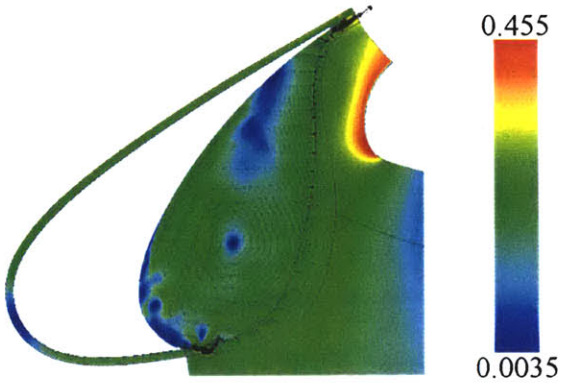

(c) 4° velocity snapshot – Mean + 90% perturbation kinetic energy

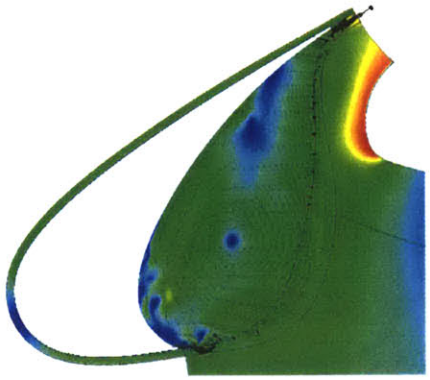

(d) 4° velocity snapshot – Mean + 99% perturbation kinetic energy

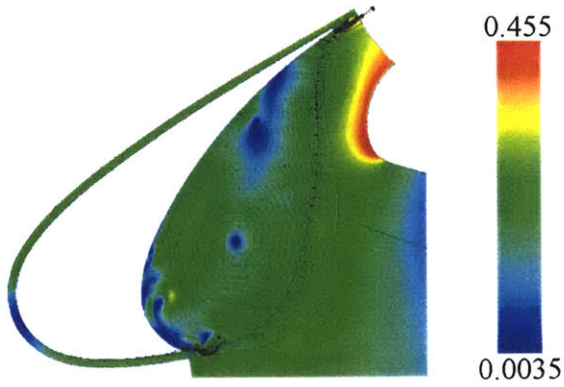

(e) 4° velocity snapshot – Mean + 99.9% perturbation kinetic energy

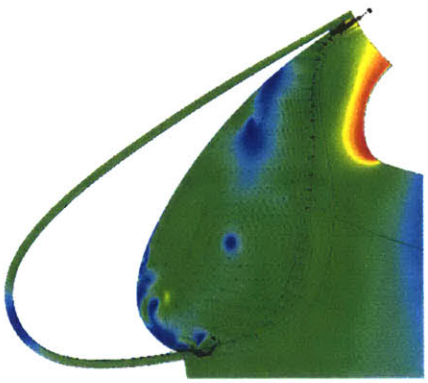

(f) 4° original velocity snapshot

Figure 4-6: 4-degree velocity reconstruction snapshots.

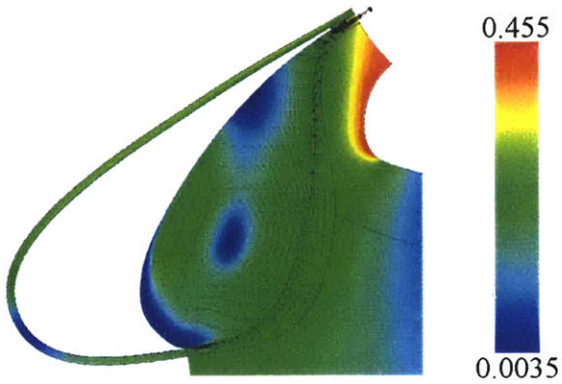

(a) 6° velocity snapshot - Mean flow

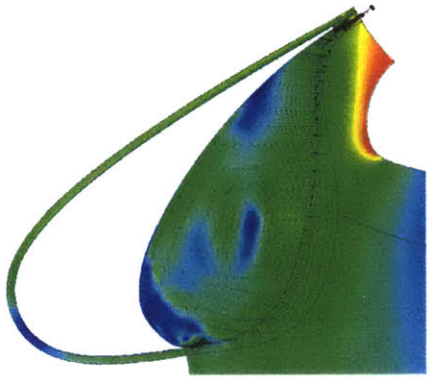

(b) 6° velocity snapshot – Mean + 70% perturbation kinetic energy

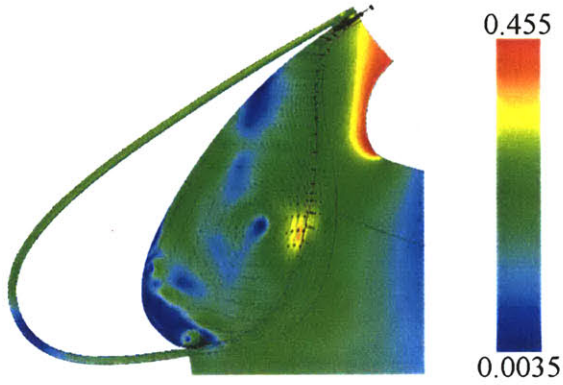

(c) 6° velocity snapshot – Mean + 90% perturbation kinetic energy

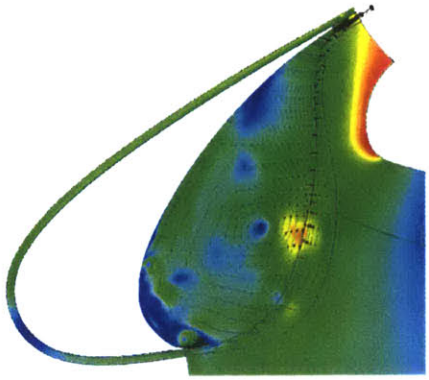

(d) 6° velocity snapshot – Mean + 99% perturbation kinetic energy

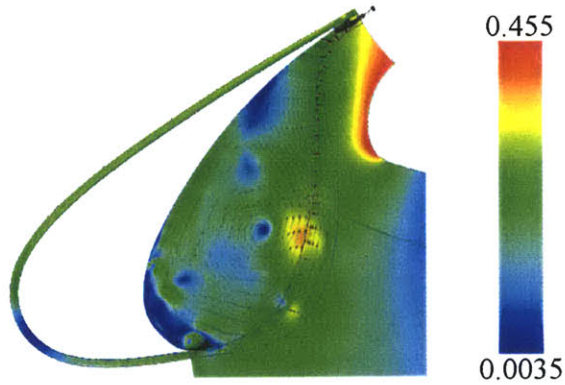

(e) 6° velocity snapshot – Mean + 99.9% perturbation kinetic energy

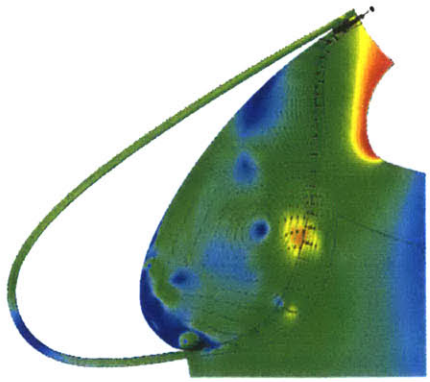

(f) 6° original velocity snapshot

Figure 4-7: 6-degree velocity reconstruction snapshots.

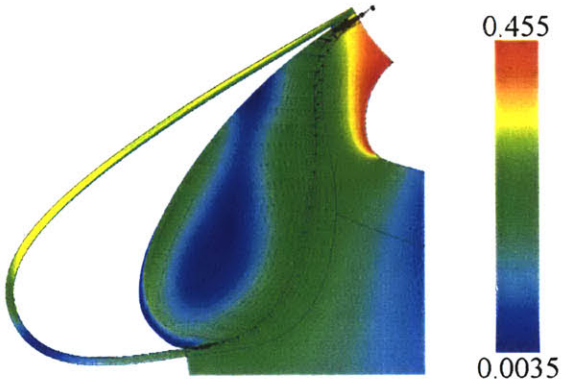

(a) 8° velocity snapshot - Mean flow

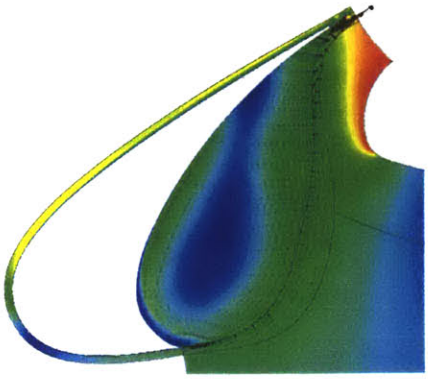

(b) 8° velocity snapshot – Mean + 70% perturbation kinetic energy

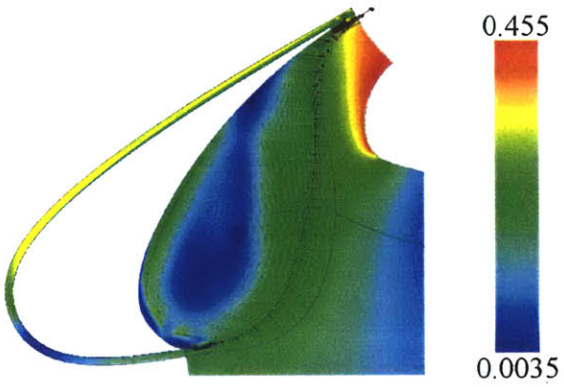

(c) 8° velocity snapshot – Mean + 90% perturbation kinetic energy

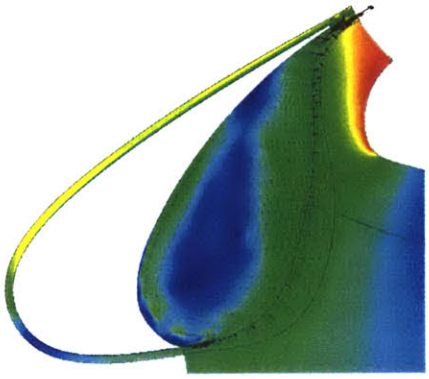

(d) 8° velocity snapshot – Mean + 99% perturbation kinetic energy

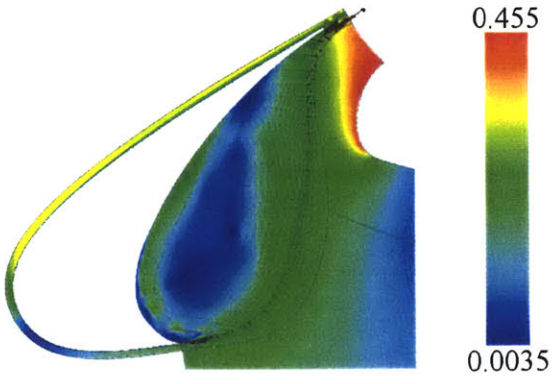

(e) 8° velocity snapshot – Mean + 99.9% perturbation kinetic energy

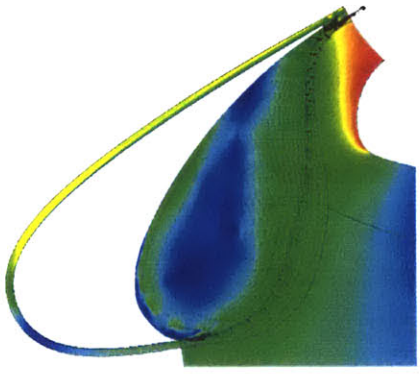

(f) 8° original velocity snapshot

Figure 4-8: 8-degree velocity reconstruction snapshots.

take a tighter shape as the snapshot is reconstructed using the 70% and 90% kinetic energy. Minor artifacts defining regions of vorticity begin to take shape at 90% and become more clearly defined using 115 modes to capture 99% of the kinetic energy of the system. Again, no significant differences in the magnitude of the velocity vectors can be seen between the 99% and 99.9% snapshot reconstructions, which suggests that minor corrections are being applied to refine the direction and magnitude of the vectors.

The original 8-degree snapshot shown in Figure 4-8(f) illustrates the relatively more organized structure of the slat flow compared to the previous two examples. The general motion in the slat core is about an elongated orbit spanning the domain of the cove region. The core region transforms from a single core of low pressure to two low-pressure regions of roughly the same magnitude. No change is seen between the mean flow snapshot and the 70% reconstruction. Using the first 18 POD modes in the 90% reconstruction snapshot, we begin to visualize a shift in the central pressure core, along with an increase in activity along the slat inner surface towards the leading edge. At 99% the activity in the central region is more closely correlated to that of the original snapshot. For the 8-degree snapshot reconstructions, the 84 modes used in the 99% reconstruction provide a sufficient visualization for the velocity fields.

4.2 Data Reduction Aspects

By optimizing the principal components of the data ensemble, the Proper Orthogonal Decomposition extracts the most dominant features of the system into orthogonal bases. One major advantage of this process is that because the POD modes are ordered from most energetic to least energetic, most of the energy of the system can be retained when approximating the system using a reduced number of modes. This was shown by the minimization of Equation 2.20, which is achieved with the POD basis. Thus, a minimum number of modes is required to describe a system for a given error.

We have seen that the POD provides low-order approximations ideal for visualization purposes. In the reconstructions of the pressure and velocity fields, the 99.9% and even the 99% reconstructions were virtually indistinguishable from the original flow field. To illustrate the magnitude of data reduction, an average across the three angles of attack was taken of the number of modes required to achieve a certain fidelity. For the pressure

snapshots, these reconstruction states required an average of 170 and 77 leading POD modes to attain 99.9% and 99% fidelity, respectively. The average number of modes required to reconstruct the velocity snapshots at the same kinetic energy benchmarks were 219 and 107, respectively. Hence, such high accuracy is achieved using approximately half of the available POD data or less. When less accurate predictions are acceptable, the system can be reconstructed with less than a quarter of the POD modes. Therefore, a large reduction in terms of the amount of data required is achieved. In future studies, this has the important benefit of being able to reasonably reconstruct the data without having to retain the entire set of POD modes.

4.3 Acoustic Predictions

Having performed the Proper Orthogonal Decomposition on the numerical solutions from the CFD solver, we have seen that reasonable low-order approximations may be made using a reduced set of optimal POD modes. We are interested not only in being able to recreate the original snapshots using the optimal POD basis, but also to obtain an acoustic signal based on this data. The ability to generate an acoustic signal based on the pressure and velocity data gathered is provided by a Ffowcs Williams Hawkings (FWH) acoustic propagation solver. The following study will concentrate on how well the acoustic spectra based on POD data represents original baseline calculations. This will illustrate how well the POD-based reconstructions perform as inputs to the acoustic solver.

4.3.1 Implementation

To perform an acoustic analysis of the computed fluid dynamics data, pressure and velocity information is passed into **fwh2d**, an acoustic propagation solver written by Lockard[38] at Nasa Langley Research Center. This solver is an acoustic propagation code based on the FWH equation and computes the acoustic signature at a far field observer location generated from a nearfield source.

The FWH solver accepts pressure and velocity data along prescribed source lines and generates noise data at a fixed distance from the slat trailing edge. Prior studies extracted data along source lines enclosing the entire airfoil for acoustic studies [56]. Because this POD analysis concentrated solely on the slat cove region, a new source line was created enclosing

just the slat body. Figure 4-9 displays the integration surface used for the acoustic study.

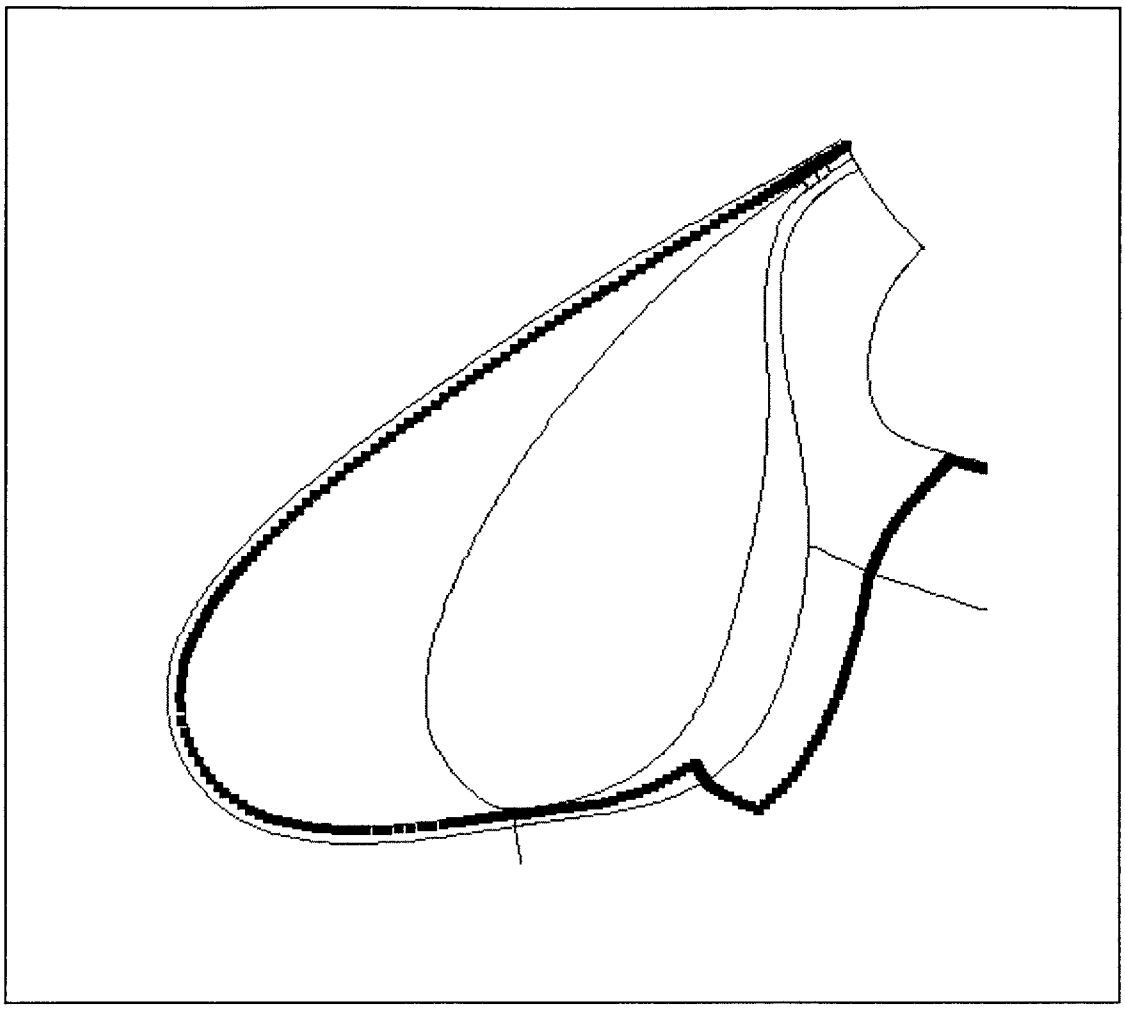

Figure 4-9: Source lines for acoustic propagation.

This source line is in essence a truncation of the source line used in the analysis by Singer *et al.* This effectively captures the cove region between the slat and the main element and includes the shed vortices in the free-shear layer. The observers are located a fixed distance from the slat trailing edge, in a circle of radius 2.05 non-dimensional units surrounding the slat.

The baseline acoustic study was performed using the original snapshot ensemble corresponding to the same 400 snapshots used in the POD analyses, taken from every 16th solution in the CFD compilation. Pressure and velocity data were extracted along the source line shown above and input to the FWH solver. Results for all three angles of at-

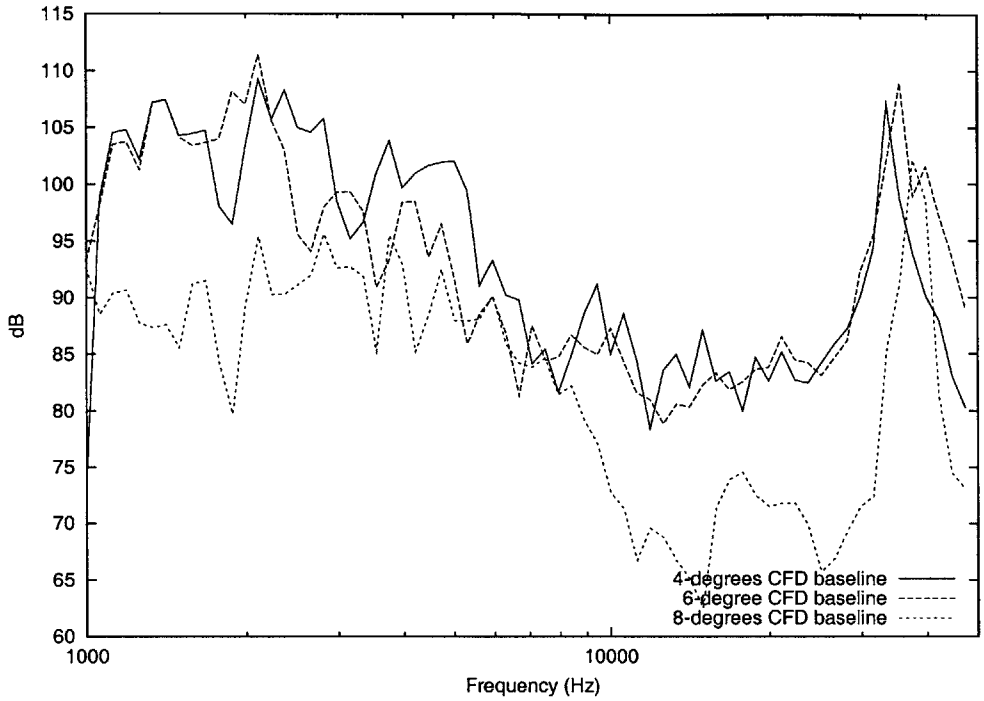

Figure 4-10: Acoustic signatures along source lines. Inputs provided from original CFD solutions.

tack are shown in Figure 4-10, at the observer location directly beneath the airfoil. The acoustic pressure output was converted to 1/12th octave bands to correspond to previous experimental measurements[1].

The EET airfoil model is scaled at approximately 10% of the mean aerodynamic chord of a Boeing 757, so the equivalent full scale frequencies can be obtained by multiplying by 0.1 – i.e., 10 kHz in the model scale corresponds to a 1 kHz in the full scale. We are interested in gathering results to at least 4 kHz full scale because human hearing is most sensitive around 3 kHz range. For the model scale and related data shown in the diagrams, we will be looking at acoustic analyses in the range of 1 to 40 kHz which translates to 0.1 to 4 kHz in the full scale frequency range.

[1]The output from the FWH solver provided pressure perturbation data in the time and frequency domains, which were transformed to a dB scale for the band SPL. This is not a true conversion to 1/12th octave scale, but it provides a reasonable approximation nonetheless.

4.3.2 Acoustic Observations Based on POD Reconstructions

We provide the same reconstructed data sets to the acoustic solver that was calculated in the previous section for the snapshot reconstructions. Pressure and velocity information is extracted along the source lines at the benchmarks of 70%, 90%, 99%, and 99.9% reconstructed energy. Since the acoustic calculations will be based on the percent reconstructed energy, the number of modes taken from each of the pressure and velocity studies will differ. This is preferred since this enables us to capture the information in the most efficient manner possible. For instance, we are able to retain 99% of the pressure energy with a fewer number modes than required in the recovering 99% of the kinetic energy.

Figure 4-11(a) presents the acoustic signature generated using the 70% and 90% reconstructions along with the baseline acoustic spectrum. In the frequency range below 4 kHz, the acoustic information matches fairly well between the estimated and actual output. Toward the middle of the spectrum, it can be seen that the two reconstruction sets tend to over-predict the 4-degree baseline signature by 10-20 dB in the frequency range of 8-11 kHz. At approximately 35 kHz, the tonal peak of the original acoustic spectrum is located well by both reconstructions.

Figure 4-11(b) shows the acoustic output for the baseline data, as well as for reconstructions using 99% and 99.9% of the pressure and velocity energies. The acoustic results from these reconstructions show a general agreement with the baseline acoustic data. The trends of the baseline signal are followed closely in all frequency ranges. In the 10-20 kHz range, the 99% reconstructions tend to over-predict the acoustic noise by approximately 5 dB, but return to a better fit as the high-frequency peak is reached between 30-40 kHz. The peak dB level is resolved exactly by both 99% and 99.9% energy reconstructions.

The 6-degree slat aeroacoustic analysis was performed using reconstructions at the 70% and 90% energy benchmarks, and is shown in Figure 4-12(a). While the 70% spectrum did not accurately model the noise signature, it still was able to provide a signature in the appropriate dB range as the original data. The high frequency peak was also resolved to within 5 dB, although the reduced amplitude region leading up to that peak was not. In the 70% energy reconstruction as well as the 90% energy reconstruction, the acoustic signal over-predicts the original signal by 10-20 dB between octave bands in the 5-30 kHz range. The 90% reconstruction is only slightly more accurate in representing the baseline data,

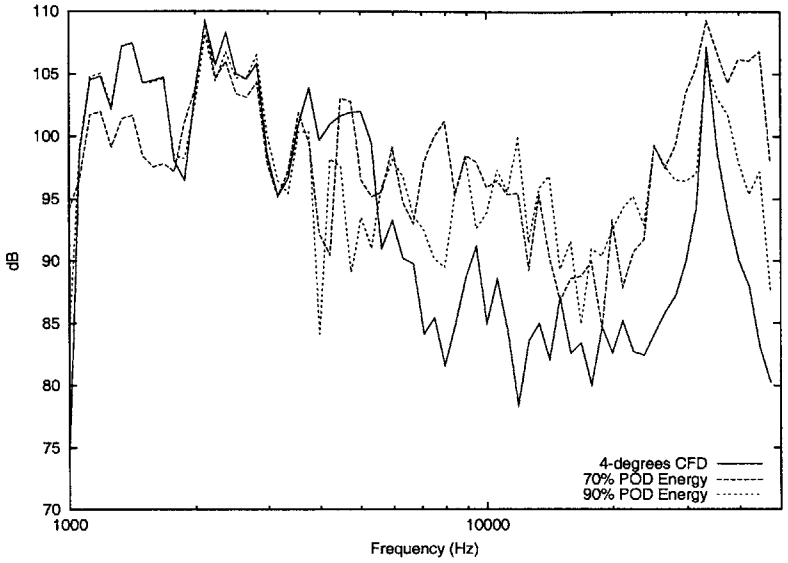

(a) Acoustic Signature – CFD vs. 70%, 90% energy reconstructions

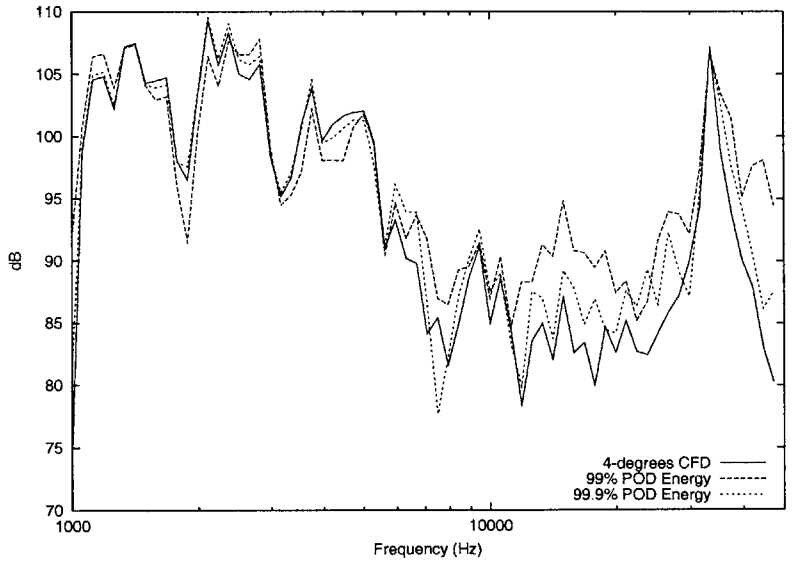

(b) Acoustic Signature – CFD vs. 99%, 99.9% energy reconstructions

Figure 4-11: Acoustic signatures at 4-degrees angle of attack.

providing amplitude variations that are roughly half as large as in the 70% case.

The 99% and 99.9% reconstructions at 6 degrees, shown in Figure 4-12(b), demonstrate a very good approximation to the baseline acoustic data for the lower frequencies below 10 kHz frequency. Acoustic levels based on the reconstructed data came within 3 dB of the baseline signature. Between 10 and 30 kHz, however, increased volatility in the signal of the reconstructed data sets appear. Oscillations of close to ± 10 dB are found in the 99.9% reconstruction near 20 kHz. In contrast, at 99% the volatility is lower, though this acoustic signature tends to over-predict the original data by 5-7 dB. The approximation of both systems improves leading into the high-frequency peak at 35 kHz.

Results from the third study are given in Figure 4-13(a) for the low-energy 8-degree approximations to the baseline acoustic spectrum. At 70% energy (Figure 4-13(a)), the acoustic signal is grossly underpredicted in the frequecies below 6 kHz. Beyond 8 kHz, both the 70% and 90% acoustic signals show an over-prediction of between 10-25 dB. This lack of accuracy is not unexpected, since the number of POD modes required to create the 70% reconstruction amounted to the first 2 pressure modes and the first 4 velocity modes. With so little information provided by the snapshot reconstruction, it would be difficult for the acoustic solver to generate a consistent acoustic spectrum.

Figure 4-13(b) plots the acoustic signatures for the reconstructions performed using 99% and 99.9% pressure and velocity energies. For these two studies, a favorable approximation is provided for frequencies below 10 kHz. Beyond 10 kHz and leading up to the high-frequency peak, the 99% reconstruction over-predicts the dB levels by 5-15 dB. The 99.9% reconstruction also over-predicts the original signature in this range, but does provide a slightly better approximation by approximately half of the dB magnitude compared to the spectrum at 99% energy. The tonal peak at 35 kHz is located and predicted well by all data sets.

We conclude this section with a look at the trends found in the acoustic analyses using the reconstructed snapshot ensembles. While the 70% reconstructions did not provide accurate representations of the acoustic signal, they still served to indicate the correct range of dB amplitude across the frequency spectrum. A noticeable trend in the majority of the reconstructions is that the acoustic signals based on those snapshots tended to over-predict the baseline signal in the important mid-frequency range. This can be used as an important characteristic of the acoustics based on snapshot reconstructions, as the associated acoustic

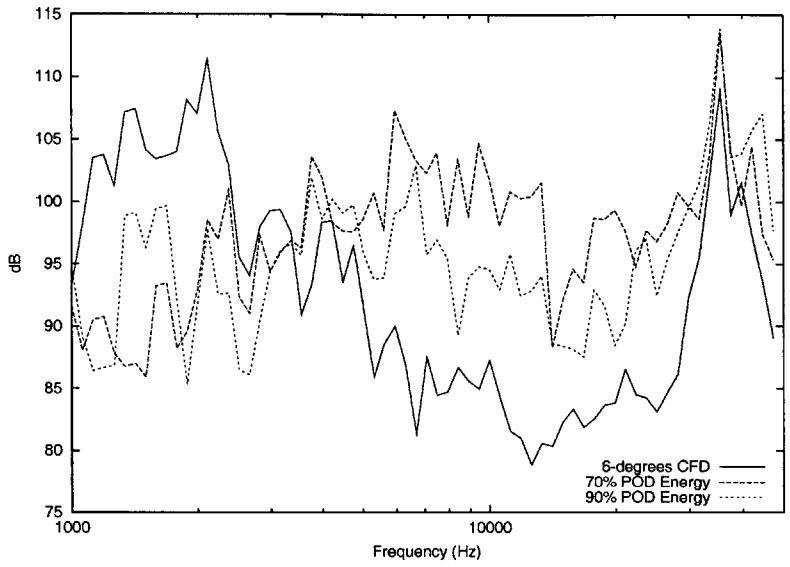

(a) Acoustic Signature – CFD vs. 70%, 90% energy reconstructions

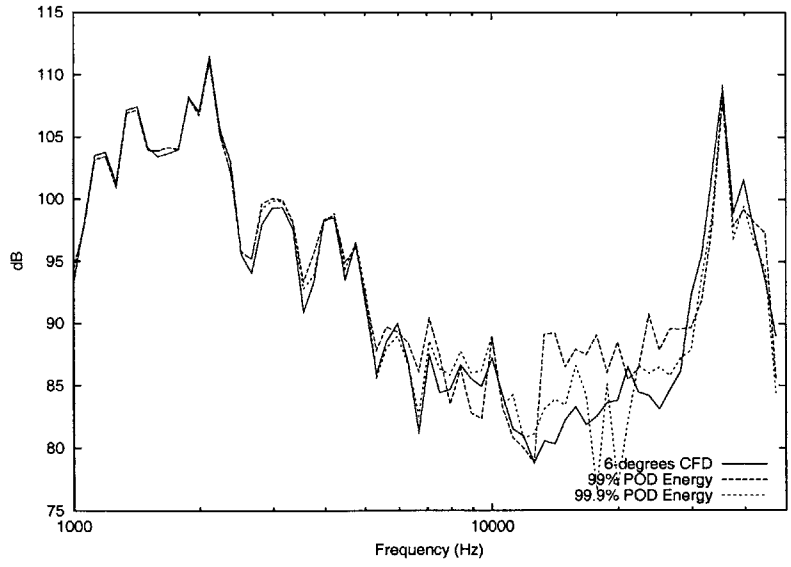

(b) Acoustic Signature – CFD vs. 99%, 99.9% energy reconstructions

Figure 4-12: Acoustic signatures at 6-degrees angle of attack.

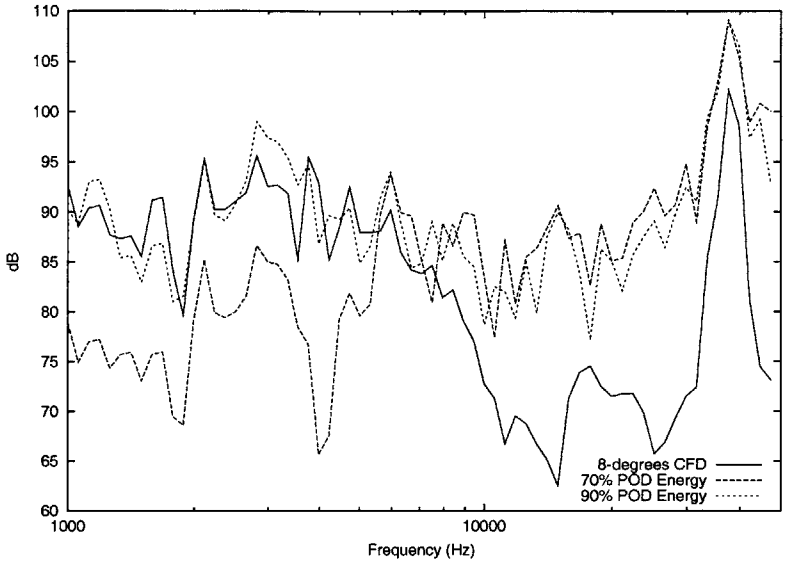

(a) Acoustic Signature – CFD vs. 70%, 90% energy reconstructions

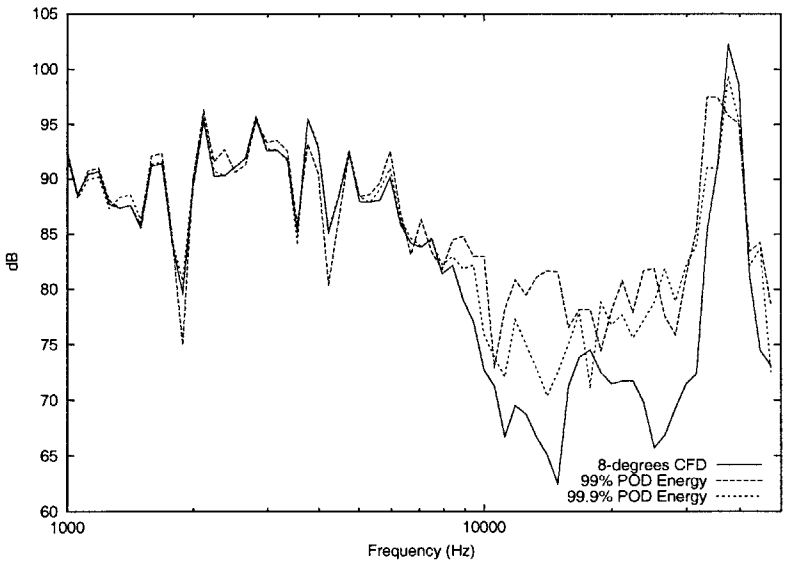

(b) Acoustic Signature – CFD vs. 99%, 99.9% energy reconstructions

Figure 4-13: Acoustic signatures at 8-degrees angle of attack.

signals may serve as upper bounds for the actual acoustic signature. This also suggests the percentage energy of the pressure and velocity fields are not the only defining parameters for resolving an acoustic signal.

It was discussed earlier that the high-frequency tonal peak was a result of the dynamics located at the slat trailing edge. The vortices shedding off this surface were in general highly organized in a vortex street pattern. Because of this, the POD was able to efficiently decompose the flow in this area into coherent structures. Therefore, when later reconstructed using the optimal POD basis, the slat flow dynamics at this trailing edge were finely recreated. This explains the ability of the acoustic solver to resolve the high-frequency peak even at the lower reconstruction states.

Convergence of POD vs. CFD Acoustics

The rate of convergence of the reconstructed data to the original baseline data is shown in Figure 4-14. This illustrates the L_2 norm of the difference between the acoustic pressure perturbation data of the original data and reconstructed snapshot data. The percentage error is calculated by

$$\%\text{Error} = \sum \frac{\|p^{(i)} - p_o\|}{\|p_o\|} \times 100,$$

where the $p^{(i)}$ represents the perturbation pressure results from the acoustic solver given at i = 70%, 90%, 99%, and 99% energy, prior to their conversion to 1/12 octave band SPL. The reference pressures p_o refer to the perturbation pressure output from the **fwh2d** solver when providing the original CFD data as inputs. The abcissa in the plot represents the number of POD modes used in the analysis, taken as an average between the number of pressure and velocity modes used per reconstruction set. It is seen that the acoustic results provided by the 70% and 90% reconstruction data do not predict the data well. This is not unexpected, considering the extremely low number of POD modes used in those experiments. The trend increases favorably, however, as more modes are included in the snapshot reconstructions. At 6-degrees, the 99% reconstruction provides pressure results that are within 25% of the expected value. At 99.9% reconstruction, the error drops below 20% for all three angles of attack. The 8-degree reconstructions provide the best approximation to the baseline acoustic signature, requiring the fewest POD modes to reconcile the acoustic spectrum to within 20% error.

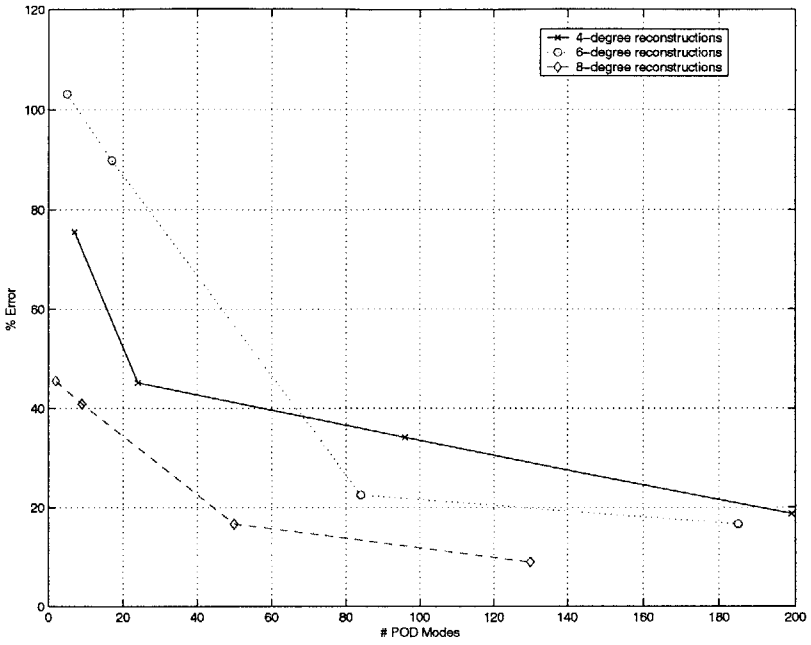

Figure 4-14: Rate of convergence of acoustic signals using reconstructed snapshot ensembles.

Even with 99.9% of the pressure and velocity energy recovered in the snapshot ensembles, there still appear errors in the range of 10%-20%. The lines for each angle of attack in the convergence plot appear to take on an asymptotic behavior, and thus it is unclear whether providing more modes to the reconstruction will provide a better acoustic analysis. It should be noted that the acoustic solver itself is very sensitive to the pressure and velocity data inputs, due to the fact that it processes perturbation quantities. Due to the numerical precision of the solver, which accepts single precision quantities, slight variations in the pressure and velocity inputs can induce variations in the SPL output of about 5-15 dB or greater. While the POD reconstructions provided decent pressure and velocity data, the lack of precision likely contributed to the large variances in the acoustic output.

Chapter 5

Parameterization of Slat Data

The previous two chapters presented a Proper Orthogonal Decomposition analysis of the slat cove simulations with respect to each angle of attack scenario. We would like to characterize the slat flow dynamics with regards to angle of attack, in an effort to identify a criterion to identify the change in behavior between the three states. We will look at the relationship between the POD modes at different angles of attack. We will also use this relationship to present a unified reconstruction to further reduce the amount of data necessary to represent the entire ensemble set used in this investigation.

5.1 Motivation

As a precursor to building a dynamic reduced-order model of the system, we must look for ways to characterize the important features of the flow. In this context, we would like to be able to encompass the three separate angle-of-attack scenarios with a set of POD modes from a single study. It was shown in the previous chapters that there are similarities between the POD mode shapes, especially in the dominant leading mode numbers. The analysis performed in this chapter intends to seek out a relationship between the three separate angle-of-attack studies. We will also look to linearize the mean flow in such a way that low order approximations of any realization from the original data set may be achieved using this reduced POD ensemble.

5.2 POD Modes Across Angles Of Attack

The previous POD studies decomposed the perturbation snapshots into POD bases that were specific to the angle of attack in question by extracting the mean flow pertaining to that particular ensemble set. This led to three separate sets of POD modes that were optimal for each of the three studies. We now return to those results to identify commonalities between them.

5.2.1 Cross-Projections

In a visual comparison of the first six POD modes in the separate POD systems of Figures 3-7, 3-12, and 3-16, there appear similarities in between a number of the modes across angles of attack. To identify similarities between modes, a cross-projection may be calculated across all the POD modes. This is done by taking the inner product of the set of POD modes from one angle-of-attack study (α_1) with those POD modes at a different angle of attack (α_2), written as $(\Psi^{(\alpha_1)}, \Psi^{(\alpha_2)})$, where the Ψ have been previously normalized to magnitude 1. The magnitudes of the projections of the first five POD modes at each angle of attack are shown in Figures 5-1 through 5-6. These plots depict the cross-projection of the initial five POD modes at a given angle of attack onto the first 40 POD modes from the other angles of attack.

The cross-projection magnitudes clearly show a relation between POD modes at the different angles of attack. The leading two 4-degree modes are correlated very well with the initial two 6-degree modes (Figure 5-1). Mode 3 exhibits an extremely strong correlation between 4- and 6-degrees, as does mode 4. In the projection onto the 8-degree modes (Figure 5-2), the third and fourth modes of the 4-degree system appear to correspond to the first and second modes of the 8-degree system. The fifth mode, on the other hand, appears to have projections made up of a number of 8-degree modes.

Projecting the 6-degree modes onto the 4-degree modes as seen in Figure 5-3, we expect to see the same behavior as before. It is interesting to note that the projections of the leading modes are strongest when projected onto the leading modes of the other systems, and that the correlation drops off as the projections are performed over higher mode numbers. The projection of 6-degree modes onto the 8-degree modes (Figure 5-4) shows an almost exact correlation of the 6-degree third and fourth modes with the first and second 8-degree modes.

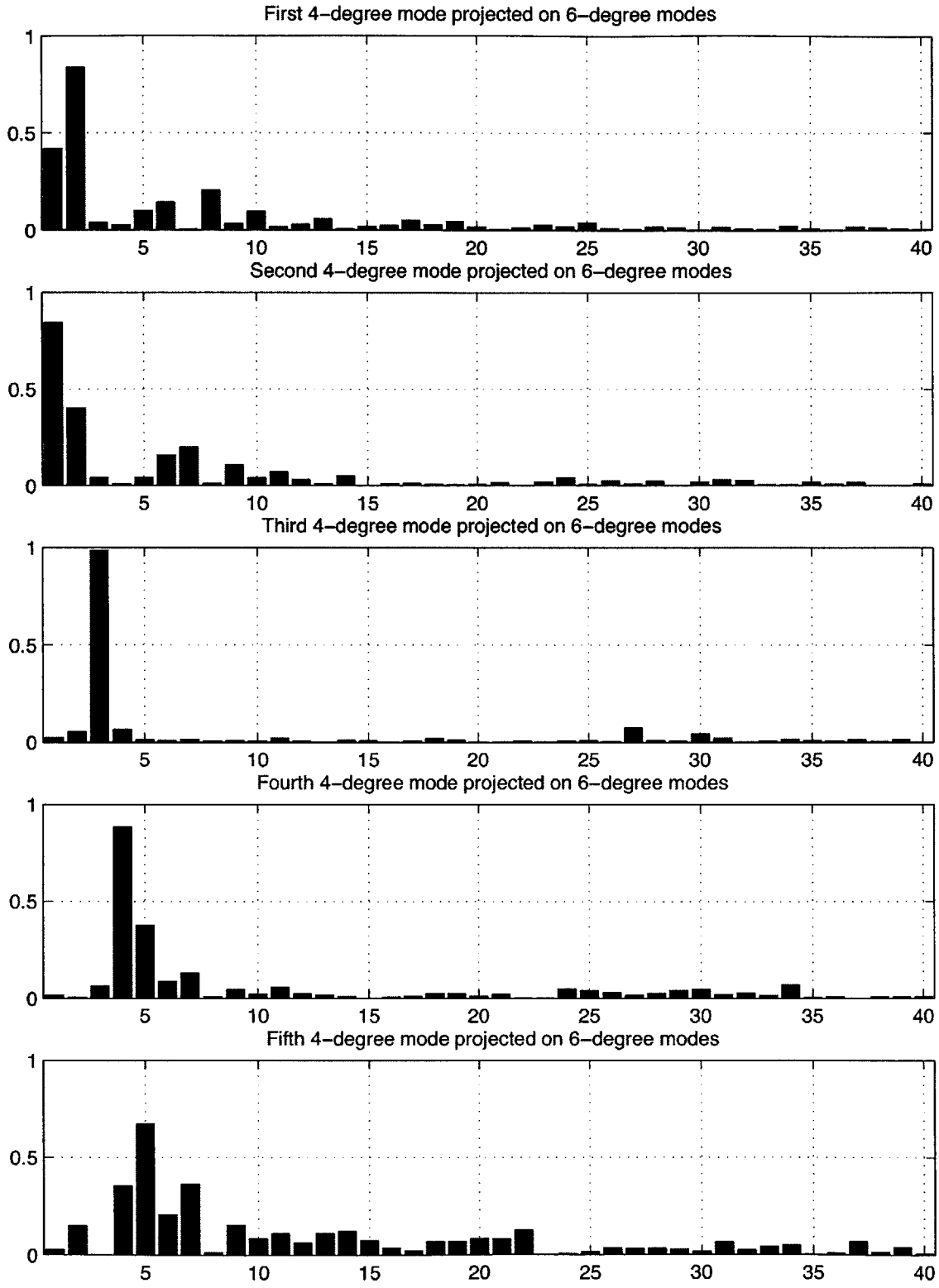

Figure 5-1: 4-degree pressure modes cross-projected onto 6-degree pressure modes.

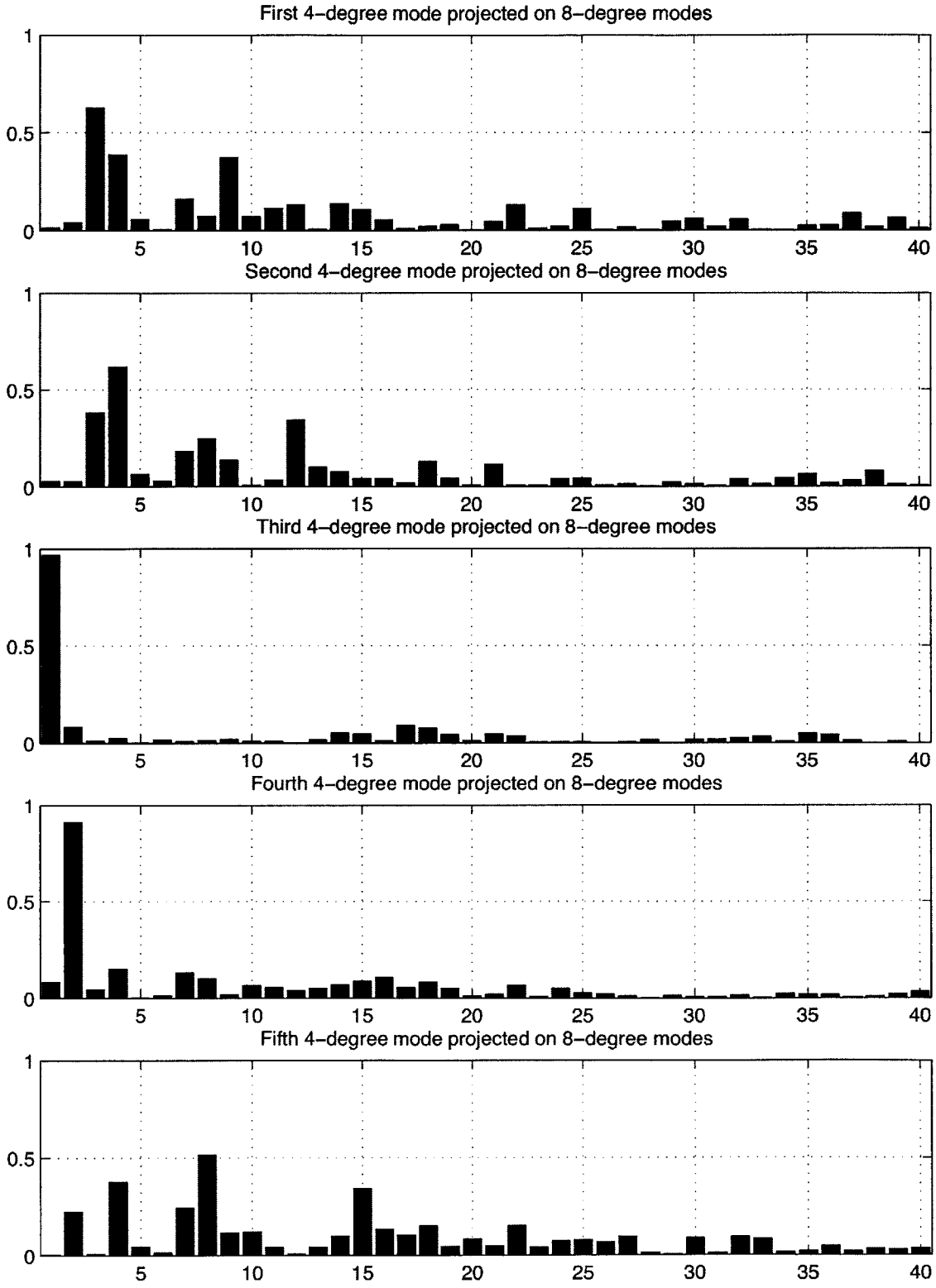

Figure 5-2: 4-degree pressure modes cross-projected onto 8-degree pressure modes.

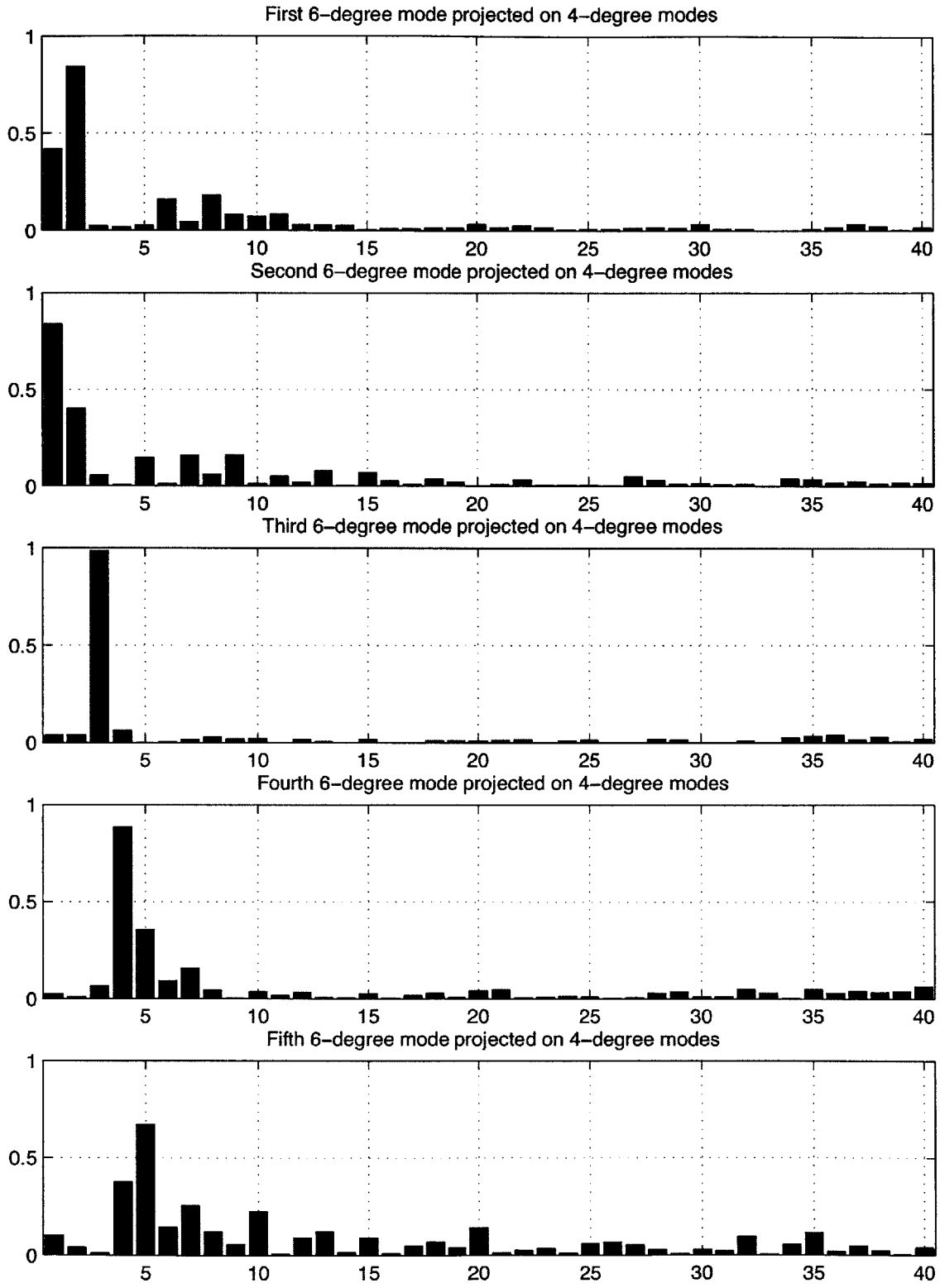

Figure 5-3: 6-degree pressure modes cross-projected onto 4-degree pressure modes.

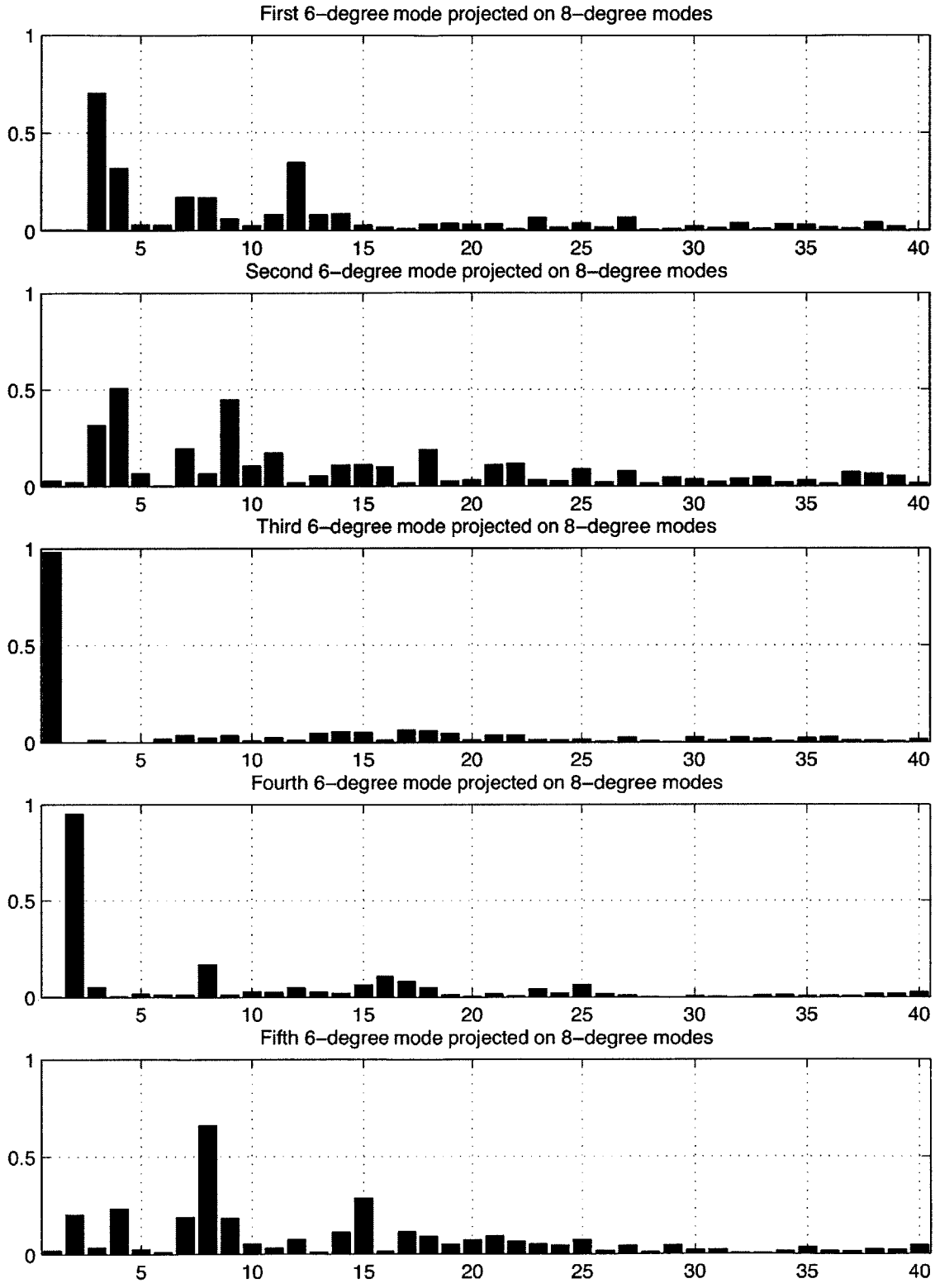

Figure 5-4: 6-degree pressure modes cross-projected onto 8-degree pressure modes.

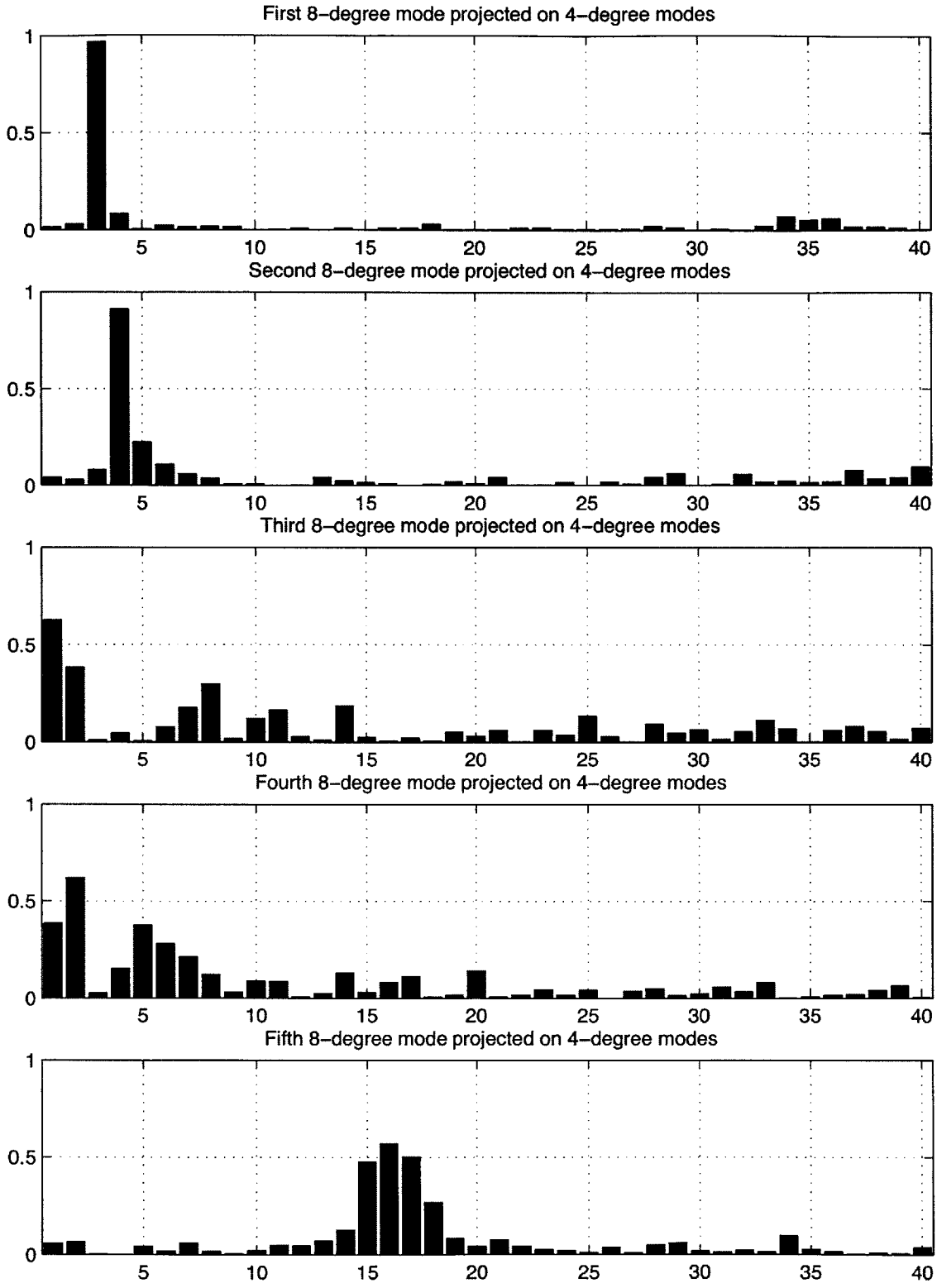

Figure 5-5: 8-degree pressure modes cross-projected onto 4-degree pressure modes.

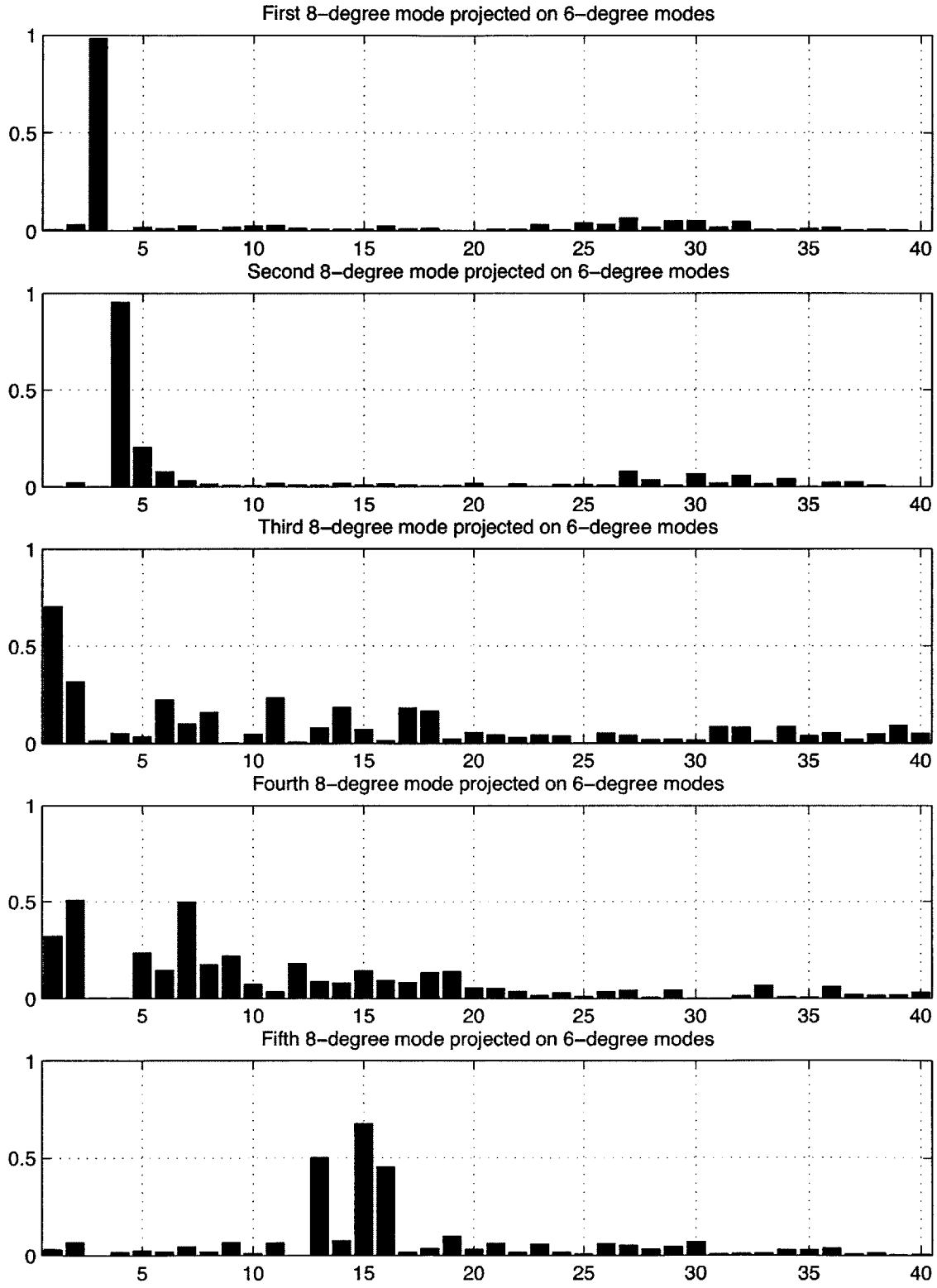

Figure 5-6: 8-degree pressure modes cross-projected onto 6-degree pressure modes.

Overall, it can be seen that there is a strong correspondence between the first 5 modes of each case with the first 10–15 modes of the other cases.

One notable difference in the 8-degree projections shown in Figures 5-5 and 5-6 is the fact that the first two 8-degree modes do not correlate with the two dominant modes of the other systems at 4- and 6-degrees angle of attack. While the initial two 4- and 6-degree modal projections showed that these dominant pieces of the system had some commonality between them, they do not correlate at all with the two initial 8-degree modes. A look at the two leading POD modes of the 4- and 6-degree systems in Figures 3-7(a) and 3-7(b), and 3-12(a) and 3-12(b) show that they contain structures leading to activity in the cove center region. Due to the constantly changing nature of the central core region in the 4- and 6-degree studies, this activity could not be extracted out to the mean flow. It was seen in the original CFD solutions, however, that the 8-degree system does not exhibit the same cove region dynamics. The fact that these two dominating modes are missing in the 8-degree system suggests that they can be used to characterize the shift from an active central core to one that exhibits a relatively stable flow field. Thus, it is suggested that the leading dominant POD modes be used to identify the strong dynamics of the central core.

5.2.2 Reconstructions Utilizing Cross-Projections

An interesting consequence of the cross-projection study is that it may be possible for any snapshot in the entire ensemble to be reconstructed using a single set of POD modes, say the 6-degree POD modes. We first start with a linearization of the mean flow.

Figure 5-7 displays the original mean states at the three angles of attack as extracted from their own ensembles. It can be seen that these are very similar in structure, and suggests that a linearization may be taken about the center system. We thus linearize about the 6-degree mean flow with respect to angle of attack, using

$$\Delta \mathbf{u}_{84} = \frac{\overline{\mathbf{u}^{(8)}} - \overline{\mathbf{u}^{(4)}}}{4^\circ} \tag{5.1}$$

where $\mathbf{u}^{(8)}$ and $\mathbf{u}^{(4)}$ represent the mean flow state at 8- and 4-degrees angle of attack, respectively. This was done for the pressure mean and is shown in Figure 5-7(d). We can

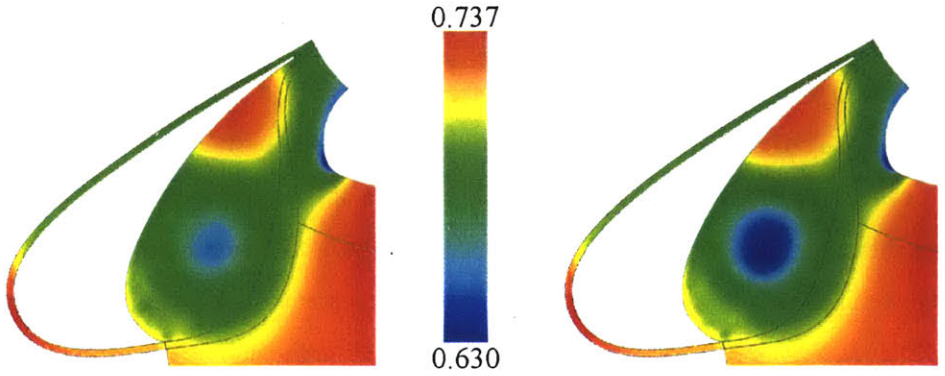

(a) 4° pressure mean flow

(b) Linearized 4° pressure mean flow

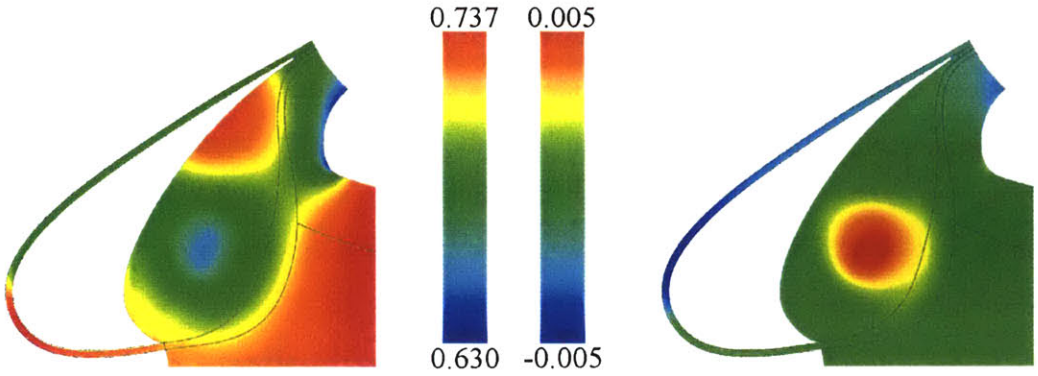

(c) 6° pressure mean flow

(d) Linearization factor $\Delta \mathbf{u}_{84}$

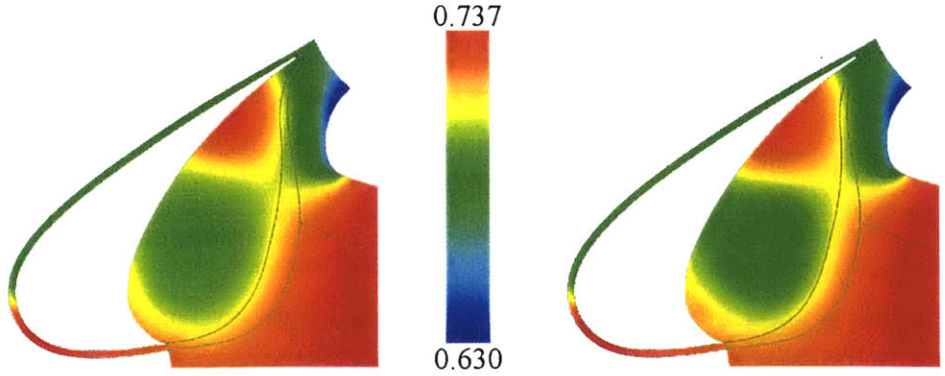

(e) 8° pressure mean flow

(f) Linearized 8° pressure mean flow

Figure 5-7: Extracted mean flows and linearization results.

then construct an approximate mean flow state at any angle of attack by

$$\overline{\mathbf{u}^{(\alpha)}} = \overline{\mathbf{u}^{(6)}} + \Delta\mathbf{u}_{84}(\alpha - 6^\circ). \tag{5.2}$$

We now return to the reconstruction utilizing cross-projections. We wish to reconstruct snapshots from any angle-of-attack ensemble using

$$\mathbf{u}^{(\alpha)}(\mathbf{x}) = \overline{\mathbf{u}^{(\alpha)}} + \sum_{n=1}^{M} A_n(t)\Psi_n^{(6)}(x) \tag{5.3}$$

where $\mathbf{u}^{(\alpha)}$ represents the snapshot at a given angle of attack α and $\Psi_n^{(6)}(x)$ represents the n-th basis vector from the collection of POD modes of the 6-degree analysis. The $A_n(t)$ are calculated by projecting the 6-degree POD basis vectors onto the snapshot ensemble at α-degrees. Substituting Equation 5.2 into Equation 5.3,

$$\mathbf{u}^{(\alpha)}(\mathbf{x},t) = \overline{\mathbf{u}^{(6)}} + \Delta\mathbf{u}_{84}(\alpha - 6^\circ) + \sum_{n=1}^{M} A_n(t)\Psi_n^{(6)}(\mathbf{x}) \tag{5.4}$$

The linearized mean pressure states for the 4- and 8-degree systems can be seen in Figures 5-7(b) and 5-7(f), respectively.

Reconstructions

Two snapshots were selected to be reconstructed using cross-projected modes from the 6-degree system. A snapshot selected in the 4-degree system is shown in Figure 5-8, and for the 8-degree system in Figure 5-9. These snapshot reconstructions illustrate the capability of representing any snapshot of the entire ensemble of solutions by using only the optimal POD modes of the 6-degree system. The energy benchmarks on which the snaphots were reconstructed belong to the 6-degree decomposition as seen in Table 4.1. For example, the 70% energy reconstruction was performed using cross-projections from the leading 5 POD modes from the 6-degree basis set.

The basic structures in the snapshots are represented well by the cross-projection. In the 4-degree snapshot, the larger pieces of the flow field were resolved using 90% and 99% of the 6-degree POD modes. The 99.9% reconstruction introduced increased volatility in the snapshot, especially along the inner surface where the small vortices begin to roll off

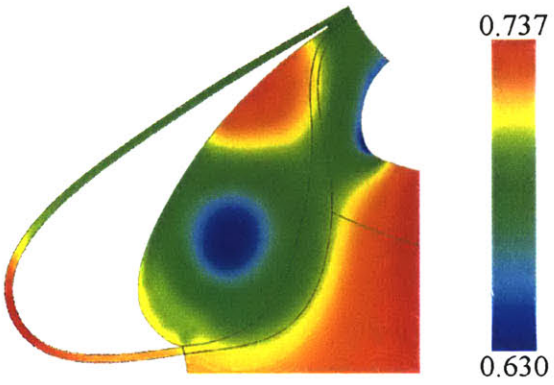

(a) Linearized 4° pressure mean flow

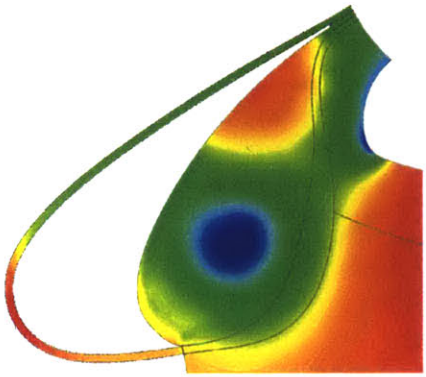

(b) Cross-projection with 70% pressure energy

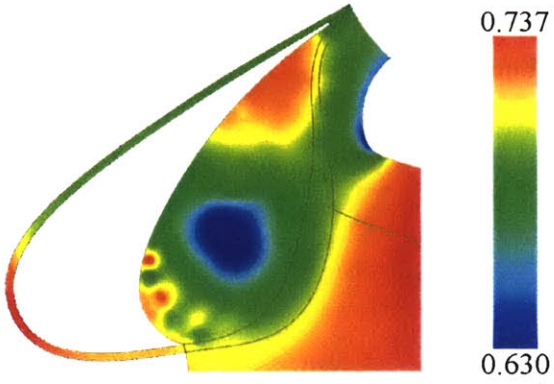

(c) Cross-projection with 90% pressure energy

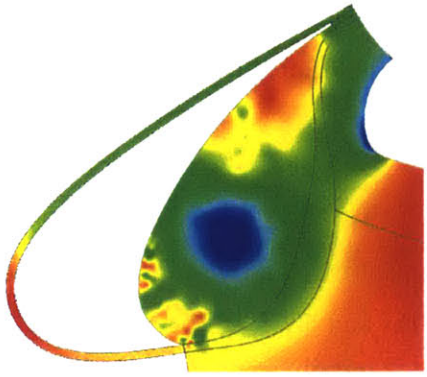

(d) Cross-projection with 99% pressure energy

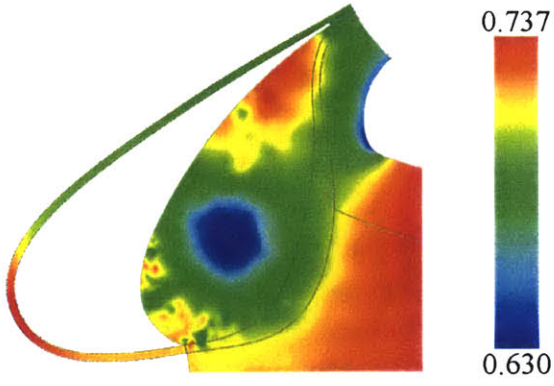

(e) Cross-projection with 99.9% pressure energy

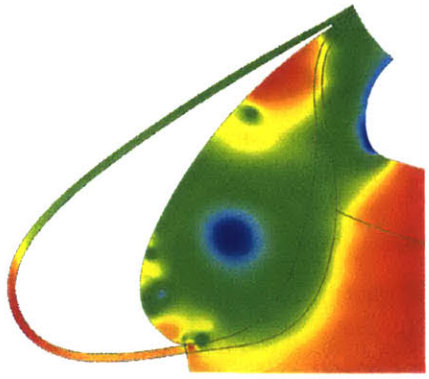

(f) 4° original pressure snapshot

Figure 5-8: 4-degree pressure reconstruction snapshots using 6-degree modes.

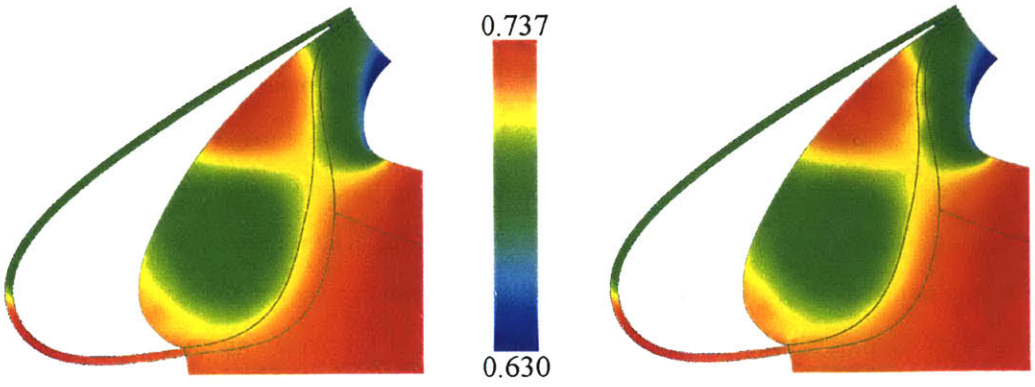

(a) Linearized 8° pressure mean flow

(b) Cross-projection Cross-projection with 70% pressure energy70%

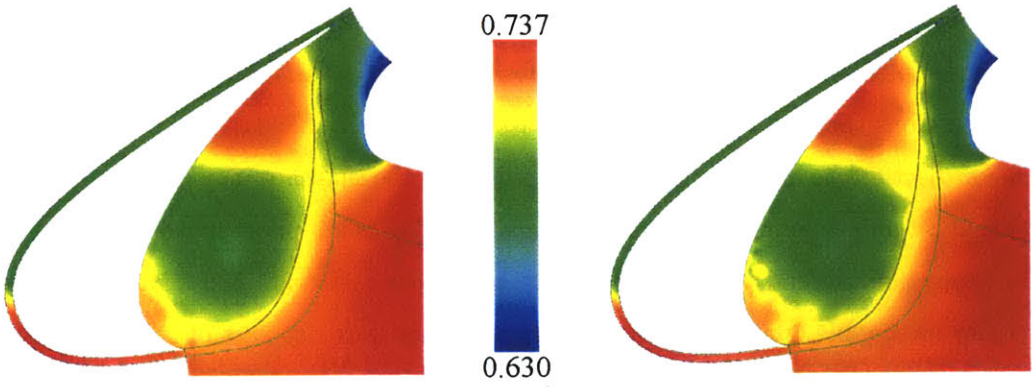

(c) Cross-projection with 90% pressure energy

(d) Cross-projection with 99% pressure energy

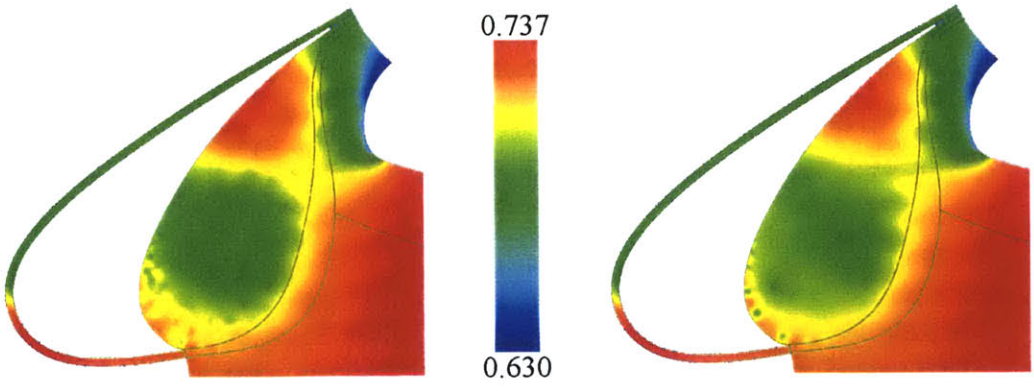

(e) Cross-projection with 99.9% pressure energy

(f) 8° Original pressure snapshot

Figure 5-9: 8-degree pressure reconstruction snapshots using 6-degree modes.

the boundary layer. This is due to the fact that the 6-degree POD basis vectors could not clearly define these structures at their individual locations.

The 8-degree snapshot reconstructions show that the larger features of the flow are well represented by the 6-degree POD modes. The pressure bands outside of the cove region appear well resolved following the 99% reconstruction. Difficulties arose once again along the inner surface where vortex cores can be seen in the original snapshot. As was seen in the 4-degree cross-projection reconstruction, in the effort to reproduce the vortex cores the 6-degree POD modes introduced unnecessary artifacts that have an undesirable effect on the rest of the slat cove region. However, the 99.9% reconstruction shows that the locations of these pressure cores could still be reasonably identified.

As higher modes are added from the 6-degree system, more unwanted artifacts begin to appear in the reconstruction. Because the 6-degree basis is not the optimal basis outside of its ensemble set, some coherent structures in the POD basis modes will appear in the reconstructions that are not physically apparent in the original snapshots. The addition of modal projections to resolve one important feature of the snapshot may bring an unwelcome modification in a different region of the snapshot. This is an unfortunate side effect of the cross-projection method. However, the 6-degree modes still contained enough information to create reasonable approximations to snapshots that were not part of its ensemble.

Chapter 6

Conclusion

6.1 Summary

The Proper Orthogonal Decomposition was applied to the computational fluid dynamics solutions modeling the flow in the slat region of an Energy Efficient Transport airfoil. This *a posteriori* analysis has shown that coherent structures may be educed from a highly unstructured flow. Eigenmode analysis has also enabled us to characterize the energy of the system and to identify the dominant features of the flow.

Using the optimal POD basis, low-order approximations of the original data ensemble were created, providing reasonable representations of the data using a minimum number of basis vectors. These reconstructions provided snapshots that were virtually indistinguishable from the original data from a visualization standpoint, using less than 30 percent of the modes available.

Acoustic modeling was performed using the low-order approximations of the data under the acoustic analogy framework. Pressure and velocity data, extracted from the snapshot reconstructions, were used as inputs to the acoustic solver. While the results generally indicated the correct magnitude of noise when compared with the acoustic signal generated from the original CFD solutions, the approximations tended to over-predict the actual noise signature when using a low number of modes in the reconstructed data set. These errors were due in part to the slight variations in the POD data and the inherent sensitivity of the **fwh2d** solver to small perturbations in the input data. With a larger number of POD modes used in the reconstruction analysis, the acoustic signal was better represented, though small variances were still present.

Many similarities were found between the systems at different angles of attack. It was seen that the slat cove activity could be linked to the two initial POD mode shapes of the 4- and 6-degree angle-of-attack systems, which were absent from the 8-degree case. A further attempt to reduce the necessary amount of data to be kept for reconstructing the solutions was made by showing that the entire ensemble set at all three angles of attack could be represented using the POD basis from just one study, in addition to a linearized mean flow. This effectively reduced the order of this large problem to one-third its size, while providing fairly reasonable approximations to the data.

6.2 Future Work

The results of this research can be applied to the development of a reduced-order model representing the dynamics of the slat flow. The POD analysis provides the first step by creating an optimal linear representation of the original data in a least-squares sense. The POD basis vectors may be projected onto the flow equations of motion, e.g. a Galerkin projection onto the Navier Stokes equation, to produce a finite system of ordinary differential equations.

With this new low-order model it is possible to quickly analyze the aerodynamic effects of different input forcing functions. Examples of forcing functions may include varying the far-field pressure or a sinusoidal perturbation of the freestream flow velocity to induce a change in the airfoil angle of attack. We saw the potential for a reduction in the number of states by a large factor, and thus further studies of a particular flow solution may be done with greater efficiency. Because the reduced order model can be made nearly as accurate as the original flow solution, additional studies may be performed without having to employ the flow solver again.

The reduced order model may also be used as a tool to analyze larger physical systems more efficiently. It may be possible to evaluate entire airframe systems as a result of the increased computational speed of the model. A detailed analysis of the entire wing system should be investigated in order to execute a realistic study of airframe noise. Some coupling effects may appear in the analysis of the entire slat, main wing, and flap system that affect the flow dynamics and corresponding acoustic signal. Highly resolved multi-element studies are still computationally expensive, but a reduced order model based on the POD basis

may enhance these efforts.

Appendix A

Eigenvalue Data

The following pages contain eigenvalue information from the decomposition of the pressure and velocity fields for the 4-, 6-, and 8-degree POD analyses. The eigenvalue plots of Figures 3-3 through 3-6 were constructed from this data. Eigenvalue data is provided for the first 120 POD modes in each system.

Table A.1: 4° pressure eigenvalue data.

#	Eigenvalue	% Energy	Total Energy	#	Eigenvalue	% Energy	Total Energy
1	0.26488×10^3	23.09264	23.09264	31	0.34541×10^1	0.30114	92.61892
2	0.20105×10^3	17.52833	40.62098	32	0.31231×10^1	0.27227	92.89119
3	0.10663×10^3	9.29637	49.91735	33	0.30751×10^1	0.26809	93.15929
4	0.75736×10^2	6.60284	56.52019	34	0.29450×10^1	0.25675	93.41603
5	0.71929×10^2	6.27088	62.79107	35	0.28593×10^1	0.24928	93.66531
6	0.62013×10^2	5.40643	68.19750	36	0.27044×10^1	0.23577	93.90109
7	0.38248×10^2	3.33457	71.53206	37	0.26132×10^1	0.22782	94.12891
8	0.31112×10^2	2.71244	74.24450	38	0.25788×10^1	0.22482	94.35373
9	0.26822×10^2	2.33842	76.58292	39	0.24179×10^1	0.21080	94.56453
10	0.21773×10^2	1.89821	78.48113	40	0.22547×10^1	0.19657	94.76110
11	0.20837×10^2	1.81665	80.29778	41	0.21216×10^1	0.18496	94.94606
12	0.16772×10^2	1.46217	81.75995	42	0.20591×10^1	0.17952	95.12557
13	0.12088×10^2	1.05387	82.81382	43	0.19790×10^1	0.17254	95.29811
14	0.10610×10^2	0.92504	83.73886	44	0.19287×10^1	0.16814	95.46626
15	0.94375×10^1	0.82278	84.56164	45	0.18630×10^1	0.16242	95.62867
16	0.89135×10^1	0.77709	85.33874	46	0.17300×10^1	0.15083	95.77950
17	0.87997×10^1	0.76718	86.10591	47	0.16235×10^1	0.14154	95.92104
18	0.83441×10^1	0.72745	86.83336	48	0.15897×10^1	0.13859	96.05963
19	0.75582×10^1	0.65893	87.49230	49	0.15186×10^1	0.13239	96.19202
20	0.72392×10^1	0.63113	88.12343	50	0.14287×10^1	0.12456	96.31658
21	0.65477×10^1	0.57084	88.69427	51	0.13474×10^1	0.11747	96.43405
22	0.58577×10^1	0.51068	89.20496	52	0.13133×10^1	0.11450	96.54855
23	0.54335×10^1	0.47370	89.67866	53	0.12491×10^1	0.10890	96.65745
24	0.50828×10^1	0.44313	90.12179	54	0.12107×10^1	0.10555	96.76300
25	0.47686×10^1	0.41574	90.53753	55	0.11843×10^1	0.10325	96.86625
26	0.46248×10^1	0.40320	90.94073	56	0.11284×10^1	0.09838	96.96463
27	0.42087×10^1	0.36693	91.30765	57	0.11056×10^1	0.09639	97.06102
28	0.39509×10^1	0.34445	91.65210	58	0.10472×10^1	0.09130	97.15231
29	0.38439×10^1	0.33512	91.98723	59	0.99426×10^0	0.08668	97.23899
30	0.37916×10^1	0.33056	92.31778	60	0.95772×10^0	0.08350	97.32249

#	Eigenvalue	% Energy	Total Energy
61	0.93734×10^0	0.08172	97.40421
62	0.89825×10^0	0.07831	97.48252
63	0.89075×10^0	0.07766	97.56018
64	0.84976×10^0	0.07408	97.63426
65	0.77207×10^0	0.06731	97.70157
66	0.73472×10^0	0.06405	97.76562
67	0.71458×10^0	0.06230	97.82792
68	0.69236×10^0	0.06036	97.88828
69	0.67763×10^0	0.05908	97.94736
70	0.67012×10^0	0.05842	98.00578
71	0.64773×10^0	0.05647	98.06225
72	0.61797×10^0	0.05388	98.11613
73	0.60013×10^0	0.05232	98.16845
74	0.59010×10^0	0.05145	98.21989
75	0.57751×10^0	0.05035	98.27024
76	0.53969×10^0	0.04705	98.31729
77	0.52266×10^0	0.04557	98.36286
78	0.50036×10^0	0.04362	98.40648
79	0.48981×10^0	0.04270	98.44919
80	0.47020×10^0	0.04099	98.49018
81	0.46272×10^0	0.04034	98.53052
82	0.43747×10^0	0.03814	98.56866
83	0.43286×10^0	0.03774	98.60640
84	0.42311×10^0	0.03689	98.64328
85	0.41206×10^0	0.03592	98.67921
86	0.40055×10^0	0.03492	98.71413
87	0.39177×10^0	0.03416	98.74829
88	0.38523×10^0	0.03359	98.78187
89	0.35481×10^0	0.03093	98.81280
90	0.35154×10^0	0.03065	98.84345

#	Eigenvalue	% Energy	Total Energy
91	0.34716×10^0	0.03027	98.87372
92	0.33113×10^0	0.02887	98.90259
93	0.31507×10^0	0.02747	98.93005
94	0.31433×10^0	0.02740	98.95746
95	0.30677×10^0	0.02674	98.98420
96	0.30149×10^0	0.02628	99.01049
97	0.29372×10^0	0.02561	99.03609
98	0.29278×10^0	0.02553	99.06162
99	0.27198×10^0	0.02371	99.08533
100	0.26682×10^0	0.02326	99.10859
101	0.25927×10^0	0.02260	99.13120
102	0.24985×10^0	0.02178	99.15298
103	0.24700×10^0	0.02153	99.17451
104	0.23611×10^0	0.02058	99.19510
105	0.22615×10^0	0.01972	99.21481
106	0.22408×10^0	0.01954	99.23435
107	0.21583×10^0	0.01882	99.25316
108	0.21258×10^0	0.01853	99.27170
109	0.21138×10^0	0.01843	99.29013
110	0.20212×10^0	0.01762	99.30775
111	0.19572×10^0	0.01706	99.32481
112	0.18955×10^0	0.01653	99.34134
113	0.18434×10^0	0.01607	99.35741
114	0.17732×10^0	0.01546	99.37287
115	0.17093×10^0	0.01490	99.38777
116	0.16840×10^0	0.01468	99.40245
117	0.15851×10^0	0.01382	99.41627
118	0.15490×10^0	0.01350	99.42977
119	0.15298×10^0	0.01334	99.44311
120	0.15070×10^0	0.01314	99.45625

Table A.2: 6° pressure eigenvalue data.

#	Eigenvalue	% Energy	Total Energy	#	Eigenvalue	% Energy	Total Energy
1	0.43437×10^{3}	31.73299	31.73299	31	0.29981×10^{1}	0.21903	94.89938
2	0.18694×10^{3}	13.65689	45.38989	32	0.27938×10^{1}	0.20410	95.10348
3	0.13158×10^{3}	9.61239	55.00228	33	0.26652×10^{1}	0.19471	95.29818
4	0.99384×10^{2}	7.26053	62.26281	34	0.25682×10^{1}	0.18762	95.48581
5	0.97979×10^{2}	7.15790	69.42071	35	0.24383×10^{1}	0.17813	95.66393
6	0.72097×10^{2}	5.26707	74.68778	36	0.23168×10^{1}	0.16926	95.83319
7	0.50312×10^{2}	3.67553	78.36331	37	0.22642×10^{1}	0.16541	95.99860
8	0.36575×10^{2}	2.67200	81.03531	38	0.20961×10^{1}	0.15313	96.15174
9	0.25321×10^{2}	1.84985	82.88516	39	0.19898×10^{1}	0.14536	96.29710
10	0.21941×10^{2}	1.60288	84.48804	40	0.18547×10^{1}	0.13549	96.43259
11	0.18006×10^{2}	1.31544	85.80348	41	0.17916×10^{1}	0.13088	96.56348
12	0.12841×10^{2}	0.93810	86.74158	42	0.16567×10^{1}	0.12103	96.68451
13	0.10545×10^{2}	0.77035	87.51193	43	0.15259×10^{1}	0.11147	96.79598
14	0.10037×10^{2}	0.73328	88.24521	44	0.14254×10^{1}	0.10413	96.90011
15	0.98133×10^{1}	0.71691	88.96212	45	0.13967×10^{1}	0.10204	97.00215
16	0.92016×10^{1}	0.67222	89.63434	46	0.13095×10^{1}	0.09567	97.09781
17	0.83315×10^{1}	0.60866	90.24300	47	0.12207×10^{1}	0.08918	97.18699
18	0.69885×10^{1}	0.51055	90.75355	48	0.12018×10^{1}	0.08780	97.27479
19	0.65359×10^{1}	0.47748	91.23103	49	0.11490×10^{1}	0.08394	97.35873
20	0.60552×10^{1}	0.44236	91.67339	50	0.11133×10^{1}	0.08133	97.44006
21	0.54660×10^{1}	0.39932	92.07271	51	0.11008×10^{1}	0.08042	97.52048
22	0.53685×10^{1}	0.39220	92.46491	52	0.10699×10^{1}	0.07816	97.59864
23	0.48641×10^{1}	0.35535	92.82026	53	0.97775×10^{0}	0.07143	97.67007
24	0.46275×10^{1}	0.33807	93.15833	54	0.94761×10^{0}	0.06923	97.73930
25	0.39177×10^{1}	0.28621	93.44454	55	0.94409×10^{0}	0.06897	97.80827
26	0.36900×10^{1}	0.26958	93.71411	56	0.88909×10^{0}	0.06495	97.87323
27	0.34865×10^{1}	0.25471	93.96882	57	0.85034×10^{0}	0.06212	97.93535
28	0.34062×10^{1}	0.24884	94.21766	58	0.81747×10^{0}	0.05972	97.99507
29	0.32577×10^{1}	0.23799	94.45566	59	0.79833×10^{0}	0.05832	98.05339
30	0.30757×10^{1}	0.22469	94.68035	60	0.75482×10^{0}	0.05514	98.10853

#	Eigenvalue	% Energy	Total Energy
61	0.74087×10^0	0.05412	98.16266
62	0.72362×10^0	0.05286	98.21552
63	0.67762×10^0	0.04950	98.26503
64	0.66246×10^0	0.04840	98.31342
65	0.63748×10^0	0.04657	98.35999
66	0.61439×10^0	0.04488	98.40488
67	0.59241×10^0	0.04328	98.44816
68	0.58735×10^0	0.04291	98.49107
69	0.55522×10^0	0.04056	98.53163
70	0.55184×10^0	0.04031	98.57194
71	0.54021×10^0	0.03947	98.61141
72	0.52373×10^0	0.03826	98.64967
73	0.51541×10^0	0.03765	98.68732
74	0.49009×10^0	0.03580	98.72313
75	0.48378×10^0	0.03534	98.75847
76	0.46405×10^0	0.03390	98.79237
77	0.44947×10^0	0.03284	98.82521
78	0.41629×10^0	0.03041	98.85562
79	0.40753×10^0	0.02977	98.88539
80	0.40051×10^0	0.02926	98.91465
81	0.38585×10^0	0.02819	98.94284
82	0.36439×10^0	0.02662	98.96946
83	0.35780×10^0	0.02614	98.99560
84	0.35449×10^0	0.02590	99.02149
85	0.33691×10^0	0.02461	99.04611
86	0.33187×10^0	0.02425	99.07035
87	0.32786×10^0	0.02395	99.09430
88	0.31750×10^0	0.02320	99.11750
89	0.31149×10^0	0.02276	99.14026
90	0.30089×10^0	0.02198	99.16224

#	Eigenvalue	% Energy	Total Energy
91	0.29056×10^0	0.02123	99.18346
92	0.28689×10^0	0.02096	99.20442
93	0.28014×10^0	0.02047	99.22489
94	0.27268×10^0	0.01992	99.24481
95	0.26449×10^0	0.01932	99.26413
96	0.25553×10^0	0.01867	99.28280
97	0.25101×10^0	0.01834	99.30114
98	0.24528×10^0	0.01792	99.31906
99	0.23929×10^0	0.01748	99.33654
100	0.23489×10^0	0.01716	99.35370
101	0.22916×10^0	0.01674	99.37044
102	0.21962×10^0	0.01604	99.38648
103	0.21579×10^0	0.01576	99.40225
104	0.20927×10^0	0.01529	99.41754
105	0.19788×10^0	0.01446	99.43199
106	0.19720×10^0	0.01441	99.44640
107	0.18753×10^0	0.01370	99.46010
108	0.18453×10^0	0.01348	99.47358
109	0.18440×10^0	0.01347	99.48705
110	0.17676×10^0	0.01291	99.49996
111	0.16539×10^0	0.01208	99.51205
112	0.15987×10^0	0.01168	99.52373
113	0.15514×10^0	0.01133	99.53506
114	0.15087×10^0	0.01102	99.54608
115	0.14824×10^0	0.01083	99.55691
116	0.14515×10^0	0.01060	99.56752
117	0.14335×10^0	0.01047	99.57799
118	0.13729×10^0	0.01003	99.58802
119	0.13287×10^0	0.00971	99.59772
120	0.12573×10^0	0.00919	99.60691

Table A.3: 8° pressure eigenvalue data.

#	Eigenvalue	% Energy	Total Energy	#	Eigenvalue	% Energy	Total Energy
1	0.16814E + 03	41.22177	41.22177	31	0.45604E + 00	0.11180	97.67052
2	0.12795E + 03	31.36708	72.58885	32	0.44304E + 00	0.10861	97.77914
3	0.17666E + 02	4.33093	76.91978	33	0.43044E + 00	0.10552	97.88466
4	0.12358E + 02	3.02964	79.94942	34	0.40893E + 00	0.10025	97.98491
5	0.11548E + 02	2.83105	82.78047	35	0.40042E + 00	0.09817	98.08308
6	0.10776E + 02	2.64175	85.42222	36	0.35491E + 00	0.08701	98.17009
7	0.87064E + 01	2.13442	87.55664	37	0.35018E + 00	0.08585	98.25594
8	0.66390E + 01	1.62759	89.18424	38	0.33116E + 00	0.08119	98.33712
9	0.46276E + 01	1.13449	90.31873	39	0.32346E + 00	0.07930	98.41642
10	0.33190E + 01	0.81367	91.13239	40	0.29338E + 00	0.07192	98.48835
11	0.29690E + 01	0.72787	91.86026	41	0.27351E + 00	0.06705	98.55540
12	0.26646E + 01	0.65324	92.51350	42	0.25084E + 00	0.06149	98.61689
13	0.26061E + 01	0.63891	93.15241	43	0.23669E + 00	0.05803	98.67492
14	0.21208E + 01	0.51992	93.67234	44	0.22373E + 00	0.05485	98.72977
15	0.16957E + 01	0.41572	94.08806	45	0.20173E + 00	0.04946	98.77923
16	0.15451E + 01	0.37880	94.46686	46	0.19876E + 00	0.04873	98.82795
17	0.15047E + 01	0.36888	94.83574	47	0.19115E + 00	0.04686	98.87481
18	0.13627E + 01	0.33406	95.16980	48	0.17977E + 00	0.04407	98.91889
19	0.12544E + 01	0.30753	95.47733	49	0.17427E + 00	0.04272	98.96161
20	0.11437E + 01	0.28039	95.75772	50	0.17011E + 00	0.04170	99.00331
21	0.11347E + 01	0.27818	96.03590	51	0.15149E + 00	0.03714	99.04045
22	0.87630E + 00	0.21483	96.25073	52	0.14386E + 00	0.03527	99.07572
23	0.83292E + 00	0.20420	96.45493	53	0.13884E + 00	0.03404	99.10976
24	0.75984E + 00	0.18628	96.64121	54	0.12863E + 00	0.03154	99.14129
25	0.74455E + 00	0.18253	96.82374	55	0.12656E + 00	0.03103	99.17232
26	0.67247E + 00	0.16486	96.98860	56	0.11666E + 00	0.02860	99.20092
27	0.62459E + 00	0.15312	97.14172	57	0.11278E + 00	0.02765	99.22857
28	0.58036E + 00	0.14228	97.28400	58	0.10887E + 00	0.02669	99.25526
29	0.57231E + 00	0.14031	97.42430	59	0.10493E + 00	0.02572	99.28099
30	0.54829E + 00	0.13442	97.55872	60	0.97672E − 01	0.02394	99.30493

#	Eigenvalue	% Energy	Total Energy
61	0.93871E − 01	0.02301	99.32794
62	0.88927E − 01	0.02180	99.34975
63	0.88159E − 01	0.02161	99.37136
64	0.87140E − 01	0.02136	99.39272
65	0.84847E − 01	0.02080	99.41352
66	0.76897E − 01	0.01885	99.43237
67	0.76403E − 01	0.01873	99.45110
68	0.71156E − 01	0.01744	99.46855
69	0.68108E − 01	0.01670	99.48525
70	0.66569E − 01	0.01632	99.50157
71	0.64759E − 01	0.01588	99.51744
72	0.63385E − 01	0.01554	99.53298
73	0.61627E − 01	0.01511	99.54809
74	0.58876E − 01	0.01443	99.56252
75	0.55543E − 01	0.01362	99.57614
76	0.54281E − 01	0.01331	99.58945
77	0.51207E − 01	0.01255	99.60200
78	0.49192E − 01	0.01206	99.61406
79	0.46957E − 01	0.01151	99.62557
80	0.45271E − 01	0.01110	99.63667
81	0.44109E − 01	0.01081	99.64748
82	0.42224E − 01	0.01035	99.65784
83	0.41486E − 01	0.01017	99.66801
84	0.39805E − 01	0.00976	99.67777
85	0.37372E − 01	0.00916	99.68693
86	0.37027E − 01	0.00908	99.69600
87	0.35123E − 01	0.00861	99.70462
88	0.34106E − 01	0.00836	99.71298
89	0.33820E − 01	0.00829	99.72127
90	0.33507E − 01	0.00821	99.72948

#	Eigenvalue	% Energy	Total Energy
91	0.31539E − 01	0.00773	99.73721
92	0.29815E − 01	0.00731	99.74452
93	0.29272E − 01	0.00718	99.75170
94	0.28257E − 01	0.00693	99.75863
95	0.26081E − 01	0.00639	99.76502
96	0.25279E − 01	0.00620	99.77122
97	0.25250E − 01	0.00619	99.77741
98	0.23696E − 01	0.00581	99.78322
99	0.23542E − 01	0.00577	99.78899
100	0.22918E − 01	0.00562	99.79461
101	0.21593E − 01	0.00529	99.79990
102	0.20876E − 01	0.00512	99.80502
103	0.20567E − 01	0.00504	99.81006
104	0.19953E − 01	0.00489	99.81495
105	0.19335E − 01	0.00474	99.81969
106	0.18746E − 01	0.00460	99.82429
107	0.18206E − 01	0.00446	99.82875
108	0.17766E − 01	0.00436	99.83311
109	0.17455E − 01	0.00428	99.83739
110	0.16569E − 01	0.00406	99.84145
111	0.15640E − 01	0.00383	99.84528
112	0.15241E − 01	0.00374	99.84902
113	0.15102E − 01	0.00370	99.85272
114	0.14438E − 01	0.00354	99.85626
115	0.13952E − 01	0.00342	99.85968
116	0.13375E − 01	0.00328	99.86296
117	0.13272E − 01	0.00325	99.86621
118	0.12822E − 01	0.00314	99.86936
119	0.12238E − 01	0.00300	99.87236
120	0.12191E − 01	0.00299	99.87535

Table A.4: 4° velocity eigenvalue data.

#	Eigenvalue	% Energy	Total Energy
1	0.11186E + 05	13.62264	13.62264
2	0.10524E + 05	12.81711	26.43975
3	0.94836E + 04	11.54950	37.98925
4	0.64912E + 04	7.90525	45.89450
5	0.50114E + 04	6.10307	51.99757
6	0.39125E + 04	4.76486	56.76243
7	0.32471E + 04	3.95449	60.71692
8	0.27481E + 04	3.34678	64.06370
9	0.21904E + 04	2.66755	66.73125
10	0.18194E + 04	2.21569	68.94694
11	0.15536E + 04	1.89208	70.83902
12	0.14532E + 04	1.76972	72.60874
13	0.11477E + 04	1.39767	74.00641
14	0.10513E + 04	1.28031	75.28672
15	0.10048E + 04	1.22366	76.51038
16	0.90316×10^3	1.09991	77.61029
17	0.87999×10^3	1.07169	78.68198
18	0.80987×10^3	0.98629	79.66827
19	0.79253×10^3	0.96518	80.63345
20	0.69936×10^3	0.85171	81.48515
21	0.67623×10^3	0.82354	82.30869
22	0.59805×10^3	0.72833	83.03702
23	0.58975×10^3	0.71823	83.75524
24	0.57015×10^3	0.69435	84.44960
25	0.56455×10^3	0.68754	85.13713
26	0.52195×10^3	0.63565	85.77278
27	0.50784×10^3	0.61847	86.39126
28	0.45973×10^3	0.55988	86.95113
29	0.44170×10^3	0.53792	87.48905
30	0.41801×10^3	0.50907	87.99812
31	0.37539×10^3	0.45716	88.45529
32	0.35677×10^3	0.43449	88.88978
33	0.33066×10^3	0.40269	89.29247
34	0.32144×10^3	0.39146	89.68393
35	0.29244×10^3	0.35615	90.04008
36	0.28010×10^3	0.34112	90.38120
37	0.25782×10^3	0.31399	90.69518
38	0.25372×10^3	0.30899	91.00418
39	0.23679×10^3	0.28837	91.29255
40	0.22388×10^3	0.27265	91.56520
41	0.21959×10^3	0.26743	91.83263
42	0.20896×10^3	0.25448	92.08711
43	0.20159×10^3	0.24551	92.33261
44	0.18892×10^3	0.23007	92.56269
45	0.18677×10^3	0.22746	92.79015
46	0.17956×10^3	0.21867	93.00882
47	0.17226×10^3	0.20979	93.21861
48	0.16496×10^3	0.20090	93.41951
49	0.16253×10^3	0.19793	93.61744
50	0.15815×10^3	0.19261	93.81004
51	0.14903×10^3	0.18150	93.99154
52	0.14385×10^3	0.17518	94.16672
53	0.13593×10^3	0.16554	94.33226
54	0.13053×10^3	0.15896	94.49122
55	0.12797×10^3	0.15585	94.64708
56	0.12027×10^3	0.14647	94.79355
57	0.11933×10^3	0.14532	94.93887
58	0.11428×10^3	0.13917	95.07804
59	0.11180×10^3	0.13615	95.21419
60	0.10941×10^3	0.13324	95.34743

#	Eigenvalue	% Energy	Total Energy
61	0.10424×10^3	0.12695	95.47438
62	0.10221×10^3	0.12448	95.59886
63	0.96912E + 02	0.11802	95.71689
64	0.94554E + 02	0.11515	95.83204
65	0.89728E + 02	0.10927	95.94131
66	0.88748E + 02	0.10808	96.04939
67	0.85931E + 02	0.10465	96.15404
68	0.82723E + 02	0.10074	96.25479
69	0.79191E + 02	0.09644	96.35123
70	0.78057E + 02	0.09506	96.44629
71	0.75911E + 02	0.09245	96.53874
72	0.73732E + 02	0.08979	96.62853
73	0.72462E + 02	0.08825	96.71678
74	0.70149E + 02	0.08543	96.80221
75	0.65585E + 02	0.07987	96.88208
76	0.65175E + 02	0.07937	96.96145
77	0.62720E + 02	0.07638	97.03784
78	0.60882E + 02	0.07414	97.11198
79	0.60574E + 02	0.07377	97.18575
80	0.59350E + 02	0.07228	97.25803
81	0.56537E + 02	0.06885	97.32688
82	0.54061E + 02	0.06584	97.39272
83	0.52239E + 02	0.06362	97.45634
84	0.51425E + 02	0.06263	97.51897
85	0.49468E + 02	0.06024	97.57921
86	0.47978E + 02	0.05843	97.63764
87	0.47175E + 02	0.05745	97.69509
88	0.45761E + 02	0.05573	97.75082
89	0.43783E + 02	0.05332	97.80414
90	0.42865E + 02	0.05220	97.85634

#	Eigenvalue	% Energy	Total Energy
91	0.42197E + 02	0.05139	97.90773
92	0.41126E + 02	0.05008	97.95782
93	0.39820E + 02	0.04849	98.00631
94	0.38902E + 02	0.04738	98.05369
95	0.36610E + 02	0.04459	98.09828
96	0.34528E + 02	0.04205	98.14033
97	0.34241E + 02	0.04170	98.18203
98	0.33913E + 02	0.04130	98.22333
99	0.33582E + 02	0.04090	98.26422
100	0.32636E + 02	0.03975	98.30397
101	0.31388E + 02	0.03823	98.34219
102	0.30881E + 02	0.03761	98.37980
103	0.29807E + 02	0.03630	98.41610
104	0.28869E + 02	0.03516	98.45126
105	0.27872E + 02	0.03394	98.48520
106	0.26992E + 02	0.03287	98.51808
107	0.26239E + 02	0.03195	98.55003
108	0.26201E + 02	0.03191	98.58194
109	0.25256E + 02	0.03076	98.61270
110	0.24892E + 02	0.03031	98.64301
111	0.24537E + 02	0.02988	98.67289
112	0.24203E + 02	0.02948	98.70237
113	0.23739E + 02	0.02891	98.73128
114	0.22808E + 02	0.02778	98.75906
115	0.22295E + 02	0.02715	98.78621
116	0.21674E + 02	0.02640	98.81260
117	0.21369E + 02	0.02602	98.83863
118	0.20560E + 02	0.02504	98.86367
119	0.20131E + 02	0.02452	98.88818
120	0.19474E + 02	0.02372	98.91190

Table A.5: 6° velocity eigenvalue data.

#	Eigenvalue	% Energy	Total Energy	#	Eigenvalue	% Energy	Total Energy
1	0.12208E + 05	14.81105	14.81105	31	0.29566E + 03	0.35870	90.80617
2	0.11056E + 05	13.41330	28.22435	32	0.28354E + 03	0.34399	91.15016
3	0.97911E + 04	11.87865	40.10300	33	0.25168E + 03	0.30534	91.45550
4	0.81536E + 04	9.89202	49.99502	34	0.23831E + 03	0.28911	91.74462
5	0.48120E + 04	5.83801	55.83303	35	0.23425E + 03	0.28420	92.02882
6	0.41654E + 04	5.05351	60.88654	36	0.22238E + 03	0.26979	92.29861
7	0.33421E + 04	4.05461	64.94114	37	0.21167E + 03	0.25680	92.55541
8	0.25272E + 04	3.06596	68.00710	38	0.19516E + 03	0.23677	92.79219
9	0.22468E + 04	2.72586	70.73296	39	0.18964E + 03	0.23008	93.02226
10	0.17523E + 04	2.12585	72.85882	40	0.18234E + 03	0.22121	93.24348
11	0.15453E + 04	1.87479	74.73361	41	0.17408E + 03	0.21120	93.45468
12	0.13531E + 04	1.64162	76.37523	42	0.17284E + 03	0.20969	93.66437
13	0.12410E + 04	1.50554	77.88076	43	0.16031E + 03	0.19449	93.85886
14	0.10399E + 04	1.26161	79.14238	44	0.15364E + 03	0.18640	94.04526
15	0.93251E + 03	1.13133	80.27370	45	0.14892E + 03	0.18067	94.22593
16	0.80603E + 03	0.97788	81.25158	46	0.14452E + 03	0.17534	94.40127
17	0.77429E + 03	0.93938	82.19096	47	0.13804E + 03	0.16747	94.56874
18	0.74178E + 03	0.89993	83.09089	48	0.12782E + 03	0.15507	94.72381
19	0.72052E + 03	0.87414	83.96504	49	0.12139E + 03	0.14728	94.87108
20	0.68559E + 03	0.83176	84.79679	50	0.11958E + 03	0.14507	95.01615
21	0.65060E + 03	0.78931	85.58611	51	0.11740E + 03	0.14243	95.15858
22	0.62909E + 03	0.76322	86.34933	52	0.10827E + 03	0.13135	95.28993
23	0.57782E + 03	0.70101	87.05034	53	0.10575E + 03	0.12830	95.41823
24	0.47577E + 03	0.57721	87.62755	54	0.10294E + 03	0.12489	95.54312
25	0.44543E + 03	0.54039	88.16794	55	0.99371E + 02	0.12056	95.66368
26	0.42468E + 03	0.51522	88.68316	56	0.94972E + 02	0.11522	95.77890
27	0.39846E + 03	0.48341	89.16657	57	0.94324E + 02	0.11444	95.89333
28	0.39754E + 03	0.48230	89.64888	58	0.89626E + 02	0.10874	96.00207
29	0.34887E + 03	0.42325	90.07212	59	0.87558E + 02	0.10623	96.10829
30	0.30938E + 03	0.37534	90.44747	60	0.84347E + 02	0.10233	96.21062

#	Eigenvalue	% Energy	Total Energy
61	0.82962E + 02	0.10065	96.31127
62	0.78408E + 02	0.09513	96.40640
63	0.76458E + 02	0.09276	96.49916
64	0.76353E + 02	0.09263	96.59179
65	0.72677E + 02	0.08817	96.67996
66	0.71967E + 02	0.08731	96.76727
67	0.70518E + 02	0.08555	96.85283
68	0.66826E + 02	0.08107	96.93390
69	0.65113E + 02	0.07900	97.01290
70	0.63047E + 02	0.07649	97.08938
71	0.62573E + 02	0.07591	97.16530
72	0.62015E + 02	0.07524	97.24053
73	0.61575E + 02	0.07470	97.31524
74	0.58890E + 02	0.07145	97.38668
75	0.55110E + 02	0.06686	97.45354
76	0.54638E + 02	0.06629	97.51983
77	0.52840E + 02	0.06411	97.58394
78	0.50938E + 02	0.06180	97.64573
79	0.49334E + 02	0.05985	97.70559
80	0.46190E + 02	0.05604	97.76162
81	0.45267E + 02	0.05492	97.81654
82	0.43763E + 02	0.05309	97.86964
83	0.43255E + 02	0.05248	97.92211
84	0.42266E + 02	0.05128	97.97339
85	0.40617E + 02	0.04928	98.02267
86	0.39567E + 02	0.04800	98.07067
87	0.38425E + 02	0.04662	98.11729
88	0.37938E + 02	0.04603	98.16331
89	0.36118E + 02	0.04382	98.20713
90	0.35383E + 02	0.04293	98.25006

#	Eigenvalue	% Energy	Total Energy
91	0.34149E + 02	0.04143	98.29149
92	0.32961E + 02	0.03999	98.33148
93	0.32519E + 02	0.03945	98.37093
94	0.30825E + 02	0.03740	98.40833
95	0.29987E + 02	0.03638	98.44471
96	0.29529E + 02	0.03582	98.48053
97	0.28692E + 02	0.03481	98.51534
98	0.27281E + 02	0.03310	98.54844
99	0.27109E + 02	0.03289	98.58133
100	0.25911E + 02	0.03144	98.61277
101	0.25587E + 02	0.03104	98.64381
102	0.25182E + 02	0.03055	98.67436
103	0.24438E + 02	0.02965	98.70401
104	0.24286E + 02	0.02946	98.73347
105	0.23744E + 02	0.02881	98.76228
106	0.22513E + 02	0.02731	98.78959
107	0.22057E + 02	0.02676	98.81635
108	0.21338E + 02	0.02589	98.84224
109	0.21060E + 02	0.02555	98.86779
110	0.20667E + 02	0.02507	98.89286
111	0.20376E + 02	0.02472	98.91758
112	0.19776E + 02	0.02399	98.94157
113	0.19090E + 02	0.02316	98.96473
114	0.18836E + 02	0.02285	98.98758
115	0.18526E + 02	0.02248	99.01006
116	0.17776E + 02	0.02157	99.03163
117	0.17378E + 02	0.02108	99.05271
118	0.16954E + 02	0.02057	99.07328
119	0.16727E + 02	0.02029	99.09357
120	0.16316E + 02	0.01979	99.11337

Table A.6: 8° velocity eigenvalue data.

#	Eigenvalue	% Energy	Total Energy	#	Eigenvalue	% Energy	Total Energy
1	0.12998E + 05	32.57933	32.57933	31	0.84094E + 02	0.21078	94.70517
2	0.12034E + 05	30.16236	62.74168	32	0.82114E + 02	0.20582	94.91099
3	0.23062E + 04	5.78054	68.52222	33	0.81431E + 02	0.20411	95.11510
4	0.15054E + 04	3.77323	72.29546	34	0.75085E + 02	0.18820	95.30330
5	0.10479E + 04	2.62666	74.92211	35	0.66018E + 02	0.16548	95.46878
6	0.83666E + 03	2.09710	77.01922	36	0.63694E + 02	0.15965	95.62843
7	0.73678E + 03	1.84675	78.86597	37	0.63206E + 02	0.15843	95.78686
8	0.73596E + 03	1.84471	80.71067	38	0.60092E + 02	0.15062	95.93748
9	0.65834E + 03	1.65014	82.36081	39	0.59474E + 02	0.14907	96.08655
10	0.55601E + 03	1.39365	83.75445	40	0.56966E + 02	0.14279	96.22934
11	0.49897E + 03	1.25069	85.00514	41	0.53719E + 02	0.13465	96.36399
12	0.41564E + 03	1.04181	86.04695	42	0.51453E + 02	0.12897	96.49296
13	0.34873E + 03	0.87408	86.92103	43	0.50062E + 02	0.12548	96.61844
14	0.30964E + 03	0.77611	87.69714	44	0.48964E + 02	0.12273	96.74116
15	0.27889E + 03	0.69905	88.39620	45	0.47184E + 02	0.11827	96.85943
16	0.25994E + 03	0.65155	89.04775	46	0.43113E + 02	0.10806	96.96749
17	0.23978E + 03	0.60100	89.64875	47	0.42245E + 02	0.10589	97.07338
18	0.22226E + 03	0.55710	90.20585	48	0.40341E + 02	0.10111	97.17450
19	0.21695E + 03	0.54379	90.74964	49	0.37438E + 02	0.09384	97.26833
20	0.19430E + 03	0.48702	91.23666	50	0.34429E + 02	0.08630	97.35463
21	0.18168E + 03	0.45538	91.69203	51	0.33050E + 02	0.08284	97.43747
22	0.16651E + 03	0.41736	92.10939	52	0.31591E + 02	0.07918	97.51665
23	0.15619E + 03	0.39150	92.50089	53	0.31028E + 02	0.07777	97.59443
24	0.14027E + 03	0.35160	92.85249	54	0.29127E + 02	0.07301	97.66743
25	0.13592E + 03	0.34068	93.19317	55	0.28242E + 02	0.07079	97.73822
26	0.12499E + 03	0.31329	93.50645	56	0.27699E + 02	0.06943	97.80765
27	0.10602E + 03	0.26573	93.77219	57	0.27030E + 02	0.06775	97.87540
28	0.10003E + 03	0.25074	94.02292	58	0.25614E + 02	0.06420	97.93961
29	0.98531E + 02	0.24697	94.26989	59	0.24977E + 02	0.06261	98.00221
30	0.89566E + 02	0.22450	94.49439	60	0.23440E + 02	0.05875	98.06096

#	Eigenvalue	% Energy	Total Energy
61	0.22287E + 02	0.05586	98.11683
62	0.21221E + 02	0.05319	98.17002
63	0.21089E + 02	0.05286	98.22288
64	0.19846E + 02	0.04974	98.27262
65	0.18726E + 02	0.04694	98.31956
66	0.18505E + 02	0.04638	98.36594
67	0.17912E + 02	0.04490	98.41084
68	0.17124E + 02	0.04292	98.45376
69	0.17078E + 02	0.04281	98.49657
70	0.16214E + 02	0.04064	98.53721
71	0.15575E + 02	0.03904	98.57625
72	0.15294E + 02	0.03833	98.61458
73	0.14998E + 02	0.03759	98.65217
74	0.14786E + 02	0.03706	98.68924
75	0.14394E + 02	0.03608	98.72531
76	0.13629E + 02	0.03416	98.75947
77	0.13205E + 02	0.03310	98.79257
78	0.13094E + 02	0.03282	98.82539
79	0.12561E + 02	0.03148	98.85688
80	0.12176E + 02	0.03052	98.88740
81	0.11957E + 02	0.02997	98.91737
82	0.11715E + 02	0.02936	98.94673
83	0.11453E + 02	0.02871	98.97544
84	0.10959E + 02	0.02747	99.00291
85	0.10484E + 02	0.02628	99.02919
86	0.10157E + 02	0.02546	99.05465
87	0.97996E + 01	0.02456	99.07921
88	0.95690E + 01	0.02398	99.10319
89	0.93597E + 01	0.02346	99.12665
90	0.90852E + 01	0.02277	99.14943

#	Eigenvalue	% Energy	Total Energy
91	0.88473E + 01	0.02218	99.17160
92	0.84176E + 01	0.02110	99.19270
93	0.78952E + 01	0.01979	99.21249
94	0.78222E + 01	0.01961	99.23210
95	0.75054E + 01	0.01881	99.25091
96	0.73398E + 01	0.01840	99.26931
97	0.71829E + 01	0.01800	99.28731
98	0.70104E + 01	0.01757	99.30488
99	0.68861E + 01	0.01726	99.32214
100	0.66123E + 01	0.01657	99.33872
101	0.64236E + 01	0.01610	99.35482
102	0.61251E + 01	0.01535	99.37017
103	0.60370E + 01	0.01513	99.38530
104	0.57354E + 01	0.01438	99.39968
105	0.56430E + 01	0.01414	99.41382
106	0.54914E + 01	0.01376	99.42759
107	0.53733E + 01	0.01347	99.44105
108	0.52623E + 01	0.01319	99.45424
109	0.50287E + 01	0.01260	99.46685
110	0.49923E + 01	0.01251	99.47936
111	0.46741E + 01	0.01172	99.49108
112	0.45714E + 01	0.01146	99.50254
113	0.43513E + 01	0.01091	99.51344
114	0.42677E + 01	0.01070	99.52414
115	0.42131E + 01	0.01056	99.53470
116	0.40505E + 01	0.01015	99.54485
117	0.39035E + 01	0.00978	99.55464
118	0.38033E + 01	0.00953	99.56417
119	0.36993E + 01	0.00927	99.57344
120	0.36889E + 01	0.00925	99.58269

Appendix B

POD Modes

B.1 POD Pressure Modes 13-36

The following pages contain an expanded collection of the POD pressure modes at 4-, 6-, and 8-degrees angle of attack. Modes 1-12 may be found in Figures 3-7 and 3-8 for the 4-degree decomposition, Figures 3-12 and 3-13 for the 6-degree decomposition, and Figures 3-16 and 3-17 for the 8-degree decomposition. POD mode numbers 13-36 are provided in the following pages for the pressure field decompositions at the three angles of attack.

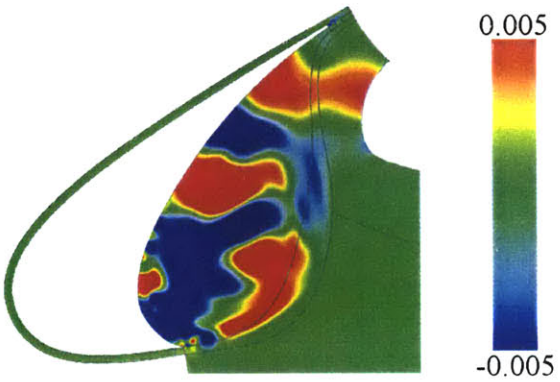

(a) 4° pressure mode 13

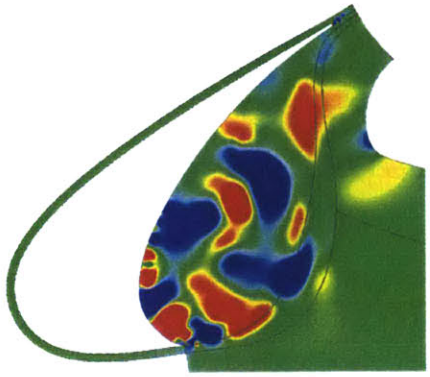

(b) 4° pressure mode 14

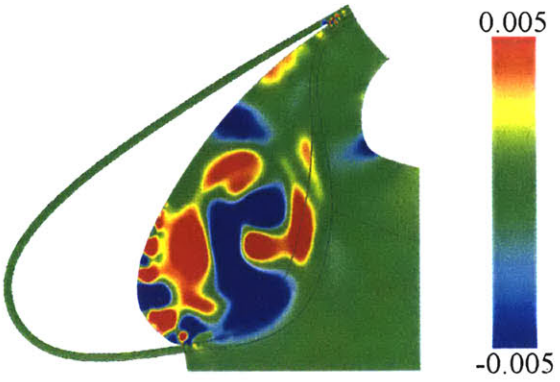

(c) 4° pressure mode 15

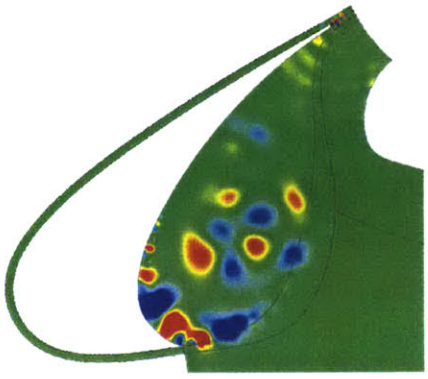

(d) 4° pressure mode 16

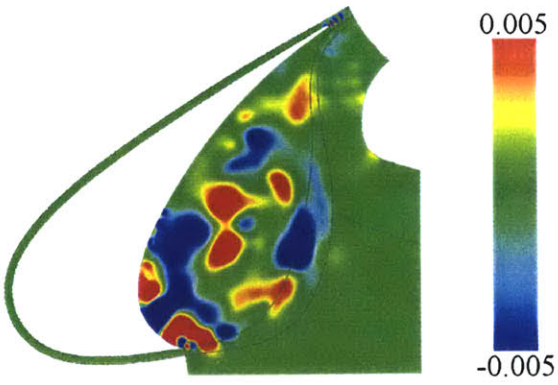

(e) 4° Pressure Mode 17

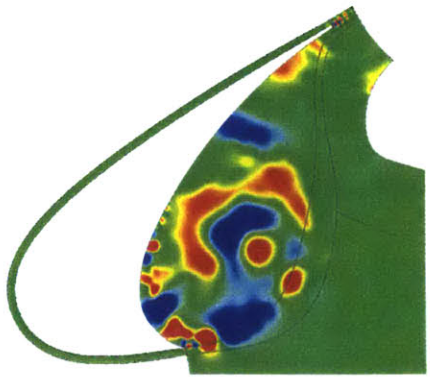

(f) 4° pressure mode 18

Figure B-1: 4-degree pressure modes 13–18.

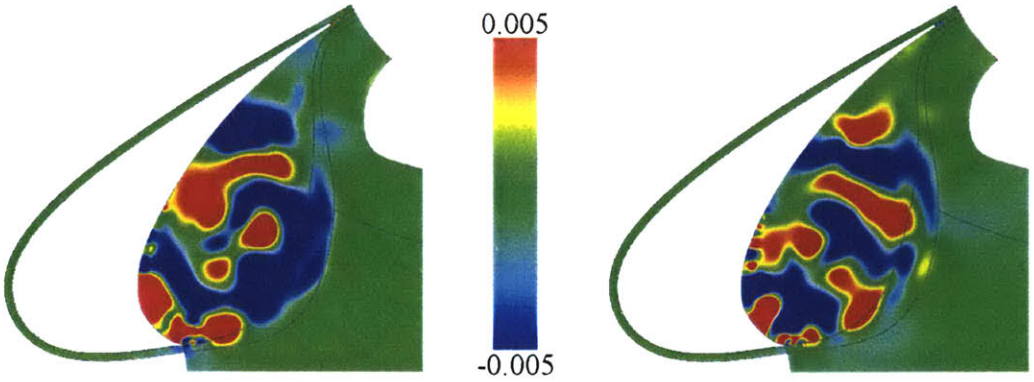

(a) 4° pressure mode 19

(b) 4° pressure mode 20

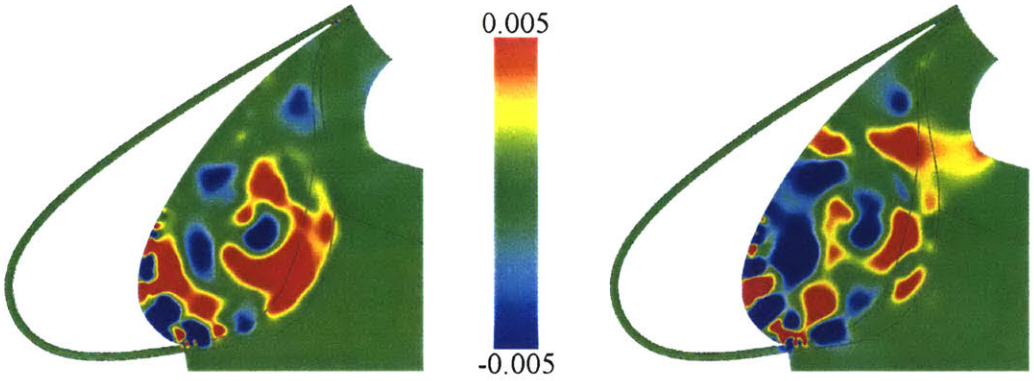

(c) 4° pressure mode 21

(d) 4° pressure mode 22

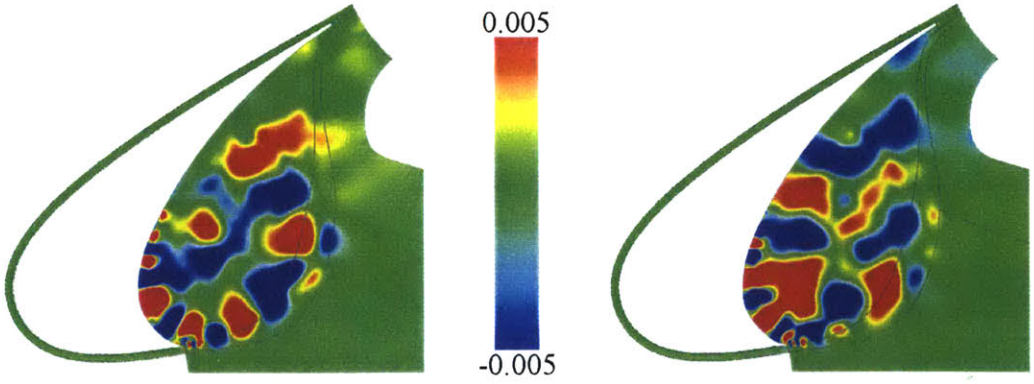

(e) 4° Pressure Mode 23

(f) 4° pressure mode 24

Figure B-2: 4-degree pressure modes 19–24.

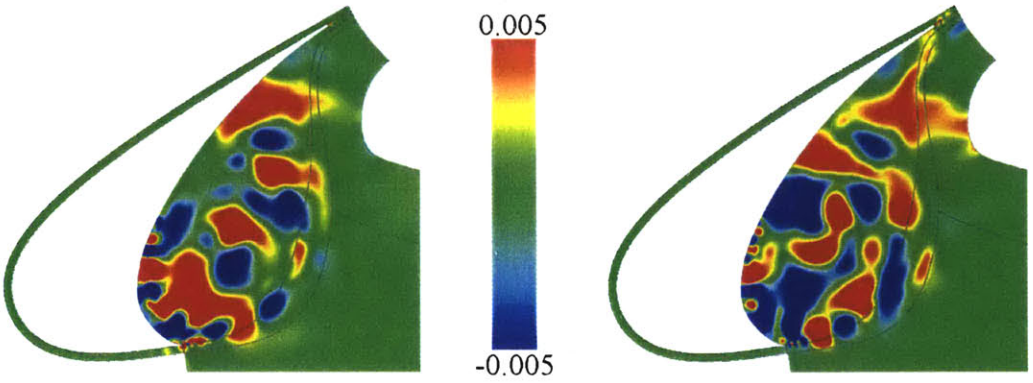

(a) 4° pressure mode 25

(b) 4° pressure mode 26

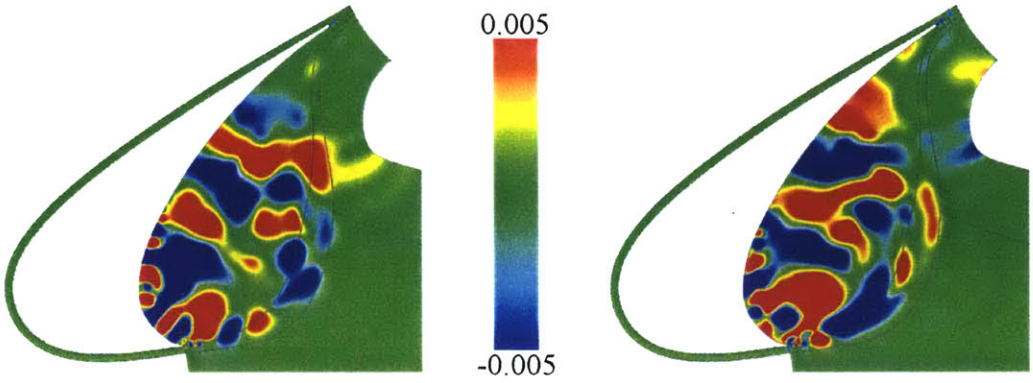

(c) 4° pressure mode 27

(d) 4° pressure mode 28

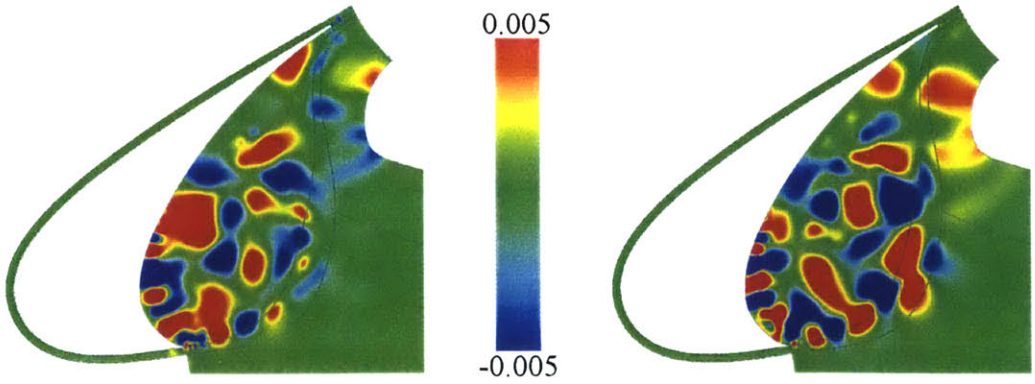

(e) 4° Pressure Mode 29

(f) 4° pressure mode 30

Figure B-3: 4-degree pressure modes 25–30.

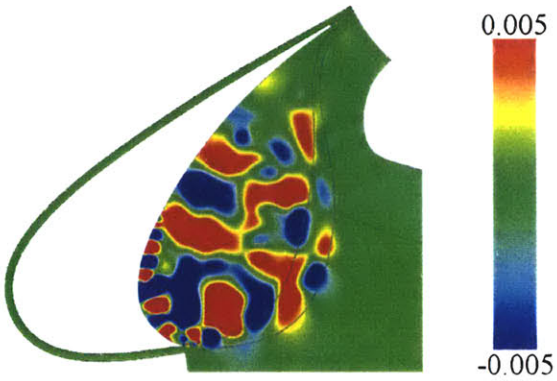

(a) 4° pressure mode 31

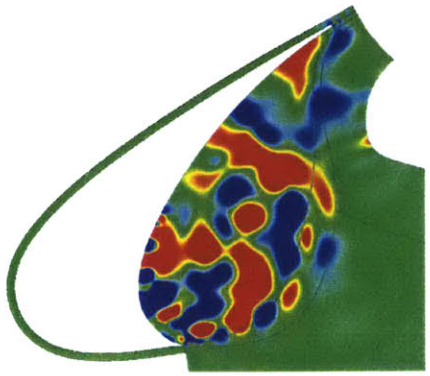

(b) 4° pressure mode 32

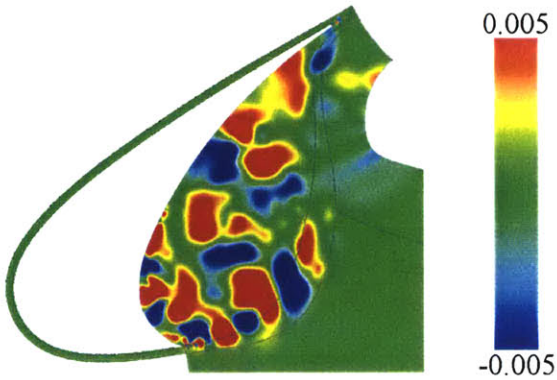

(c) 4° pressure mode 33

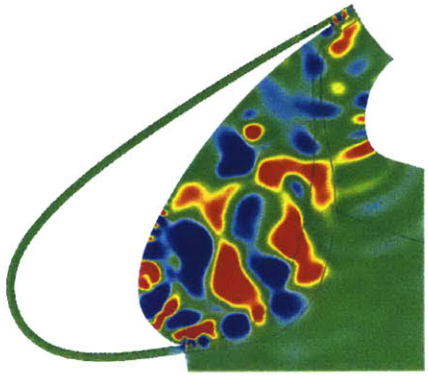

(d) 4° pressure mode 34

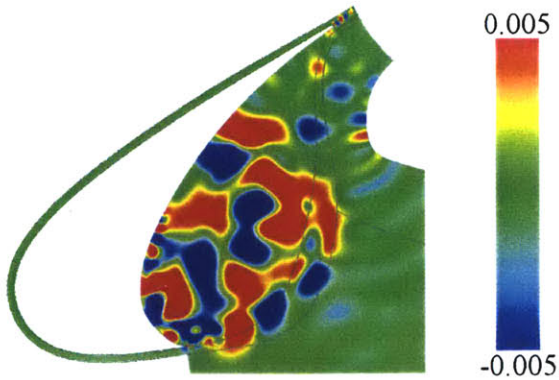

(e) 4° Pressure Mode 35

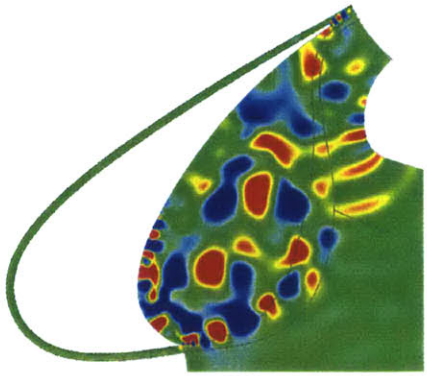

(f) 4° pressure mode 36

Figure B-4: 4-degree pressure modes 31–36.

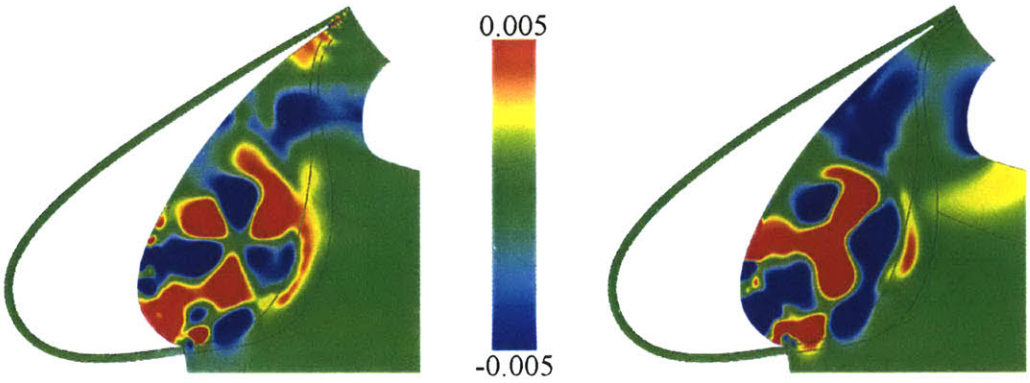

(a) 6° pressure mode 13

(b) 6° pressure mode 14

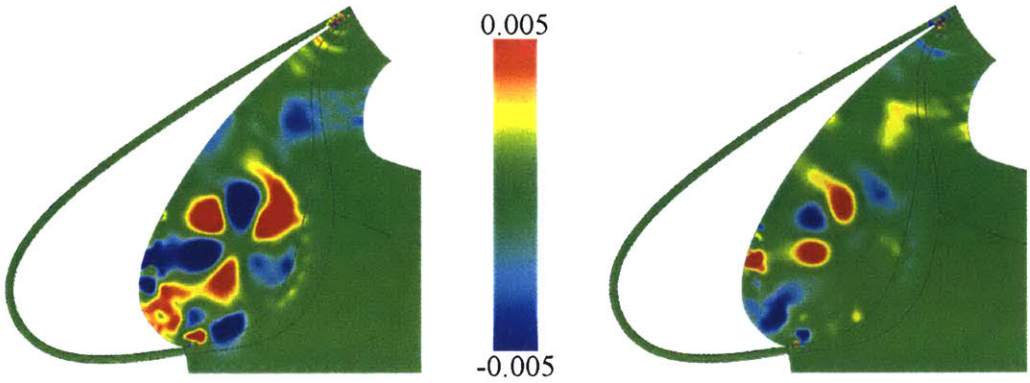

(c) 6° pressure mode 15

(d) 6° pressure mode 16

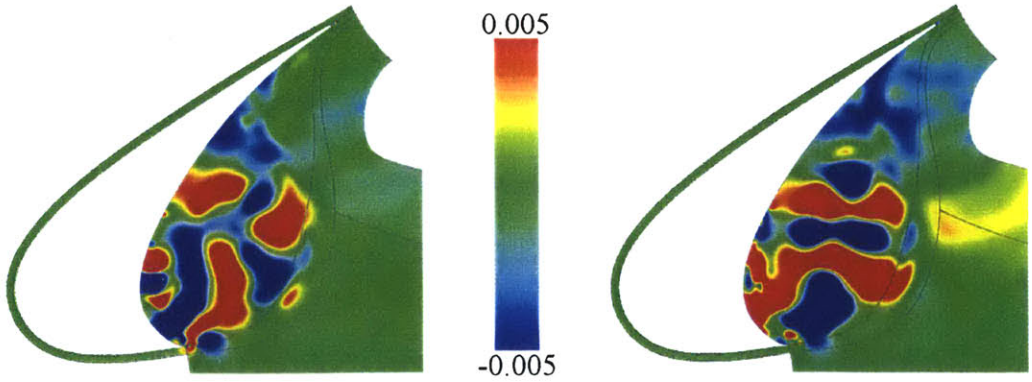

(e) 6° pressure Mode 17

(f) 6° pressure mode 18

Figure B-5: 6-degree pressure modes 13–18.

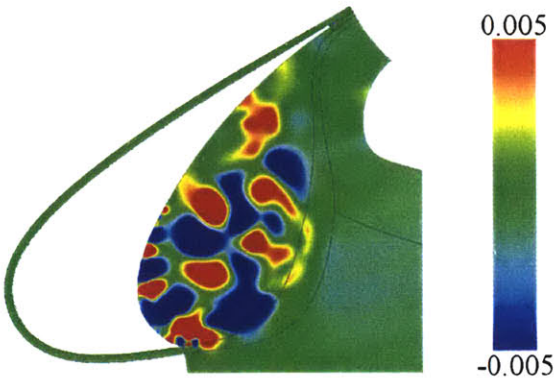

(a) 6° pressure mode 19

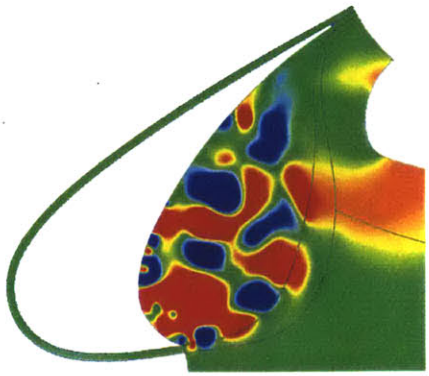

(b) 6° pressure mode 20

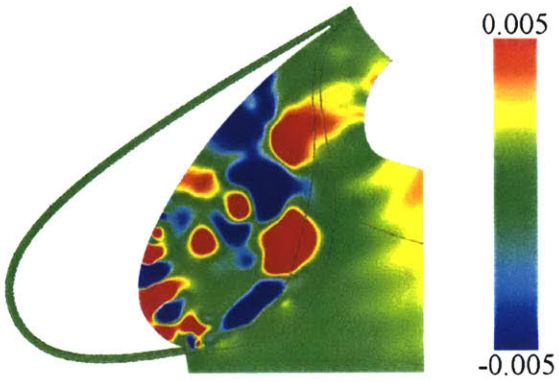

(c) 6° pressure mode 21

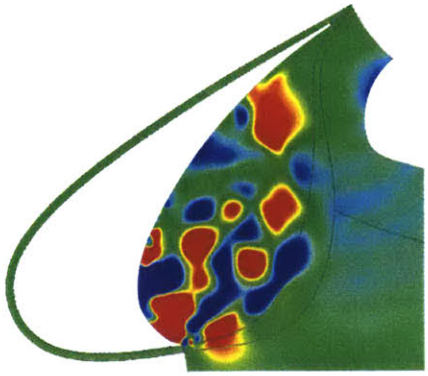

(d) 6° pressure mode 22

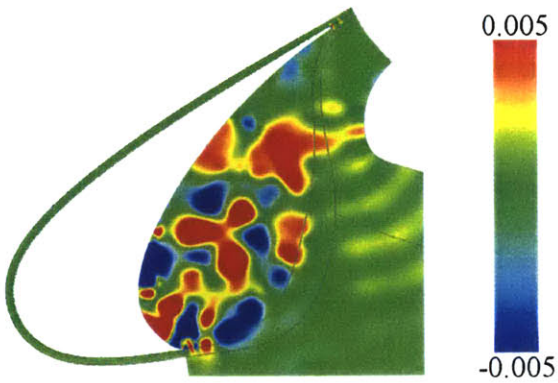

(e) 6° pressure Mode 23

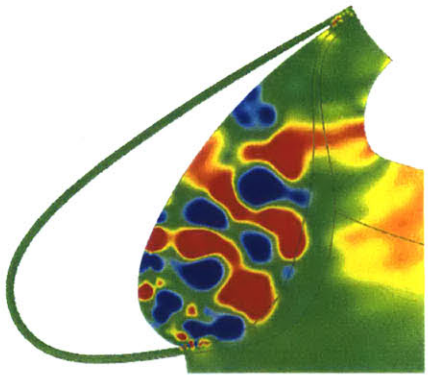

(f) 6° pressure mode 24

Figure B-6: 6-degree pressure modes 19–24.

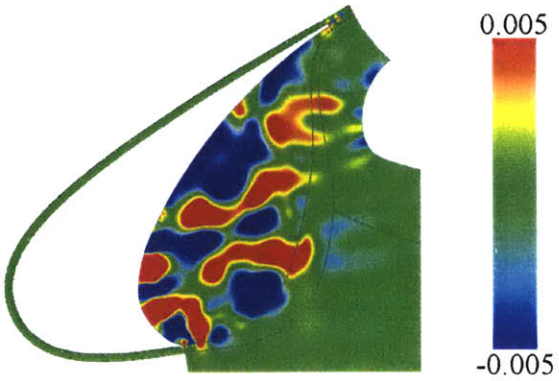

(a) 6° pressure mode 25

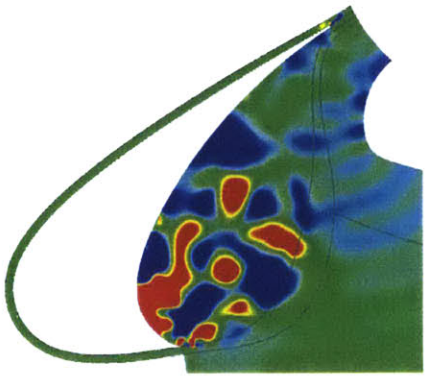

(b) 6° pressure mode 26

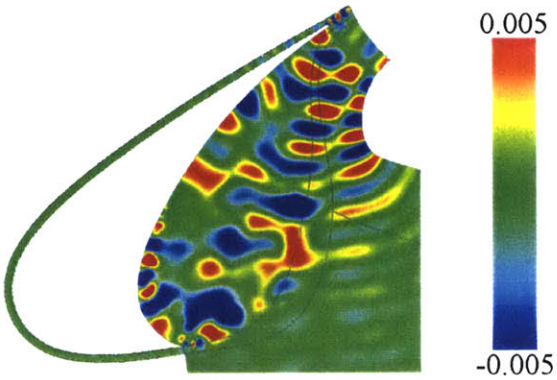

(c) 6° pressure mode 27

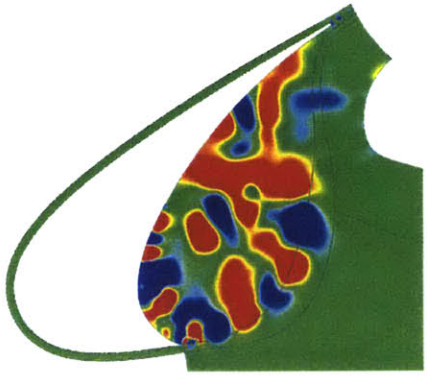

(d) 6° pressure mode 28

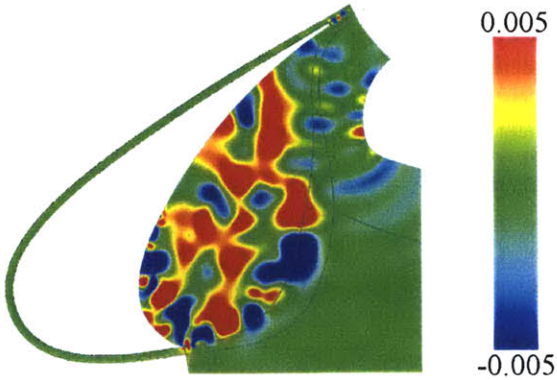

(e) 6° pressure Mode 29

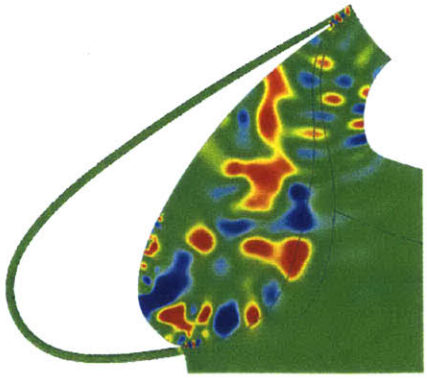

(f) 6° pressure mode 30

Figure B-7: 6-degree pressure modes 25–30.

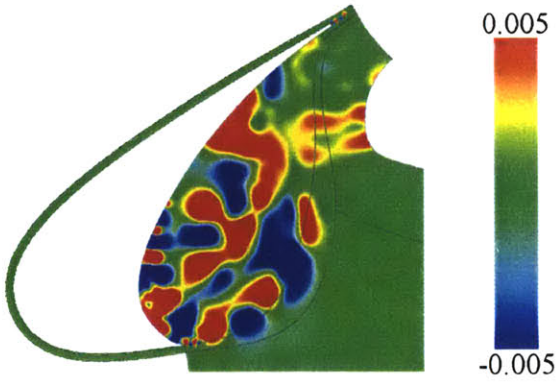

(a) 6° pressure mode 31

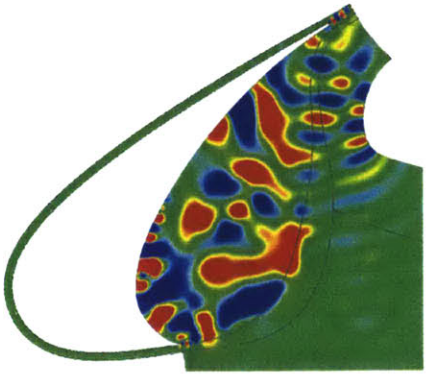

(b) 6° pressure mode 32

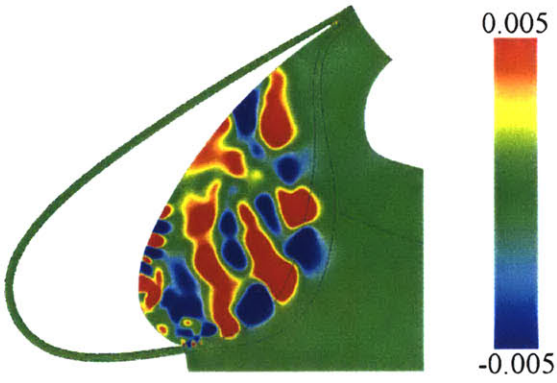

(c) 6° pressure mode 33

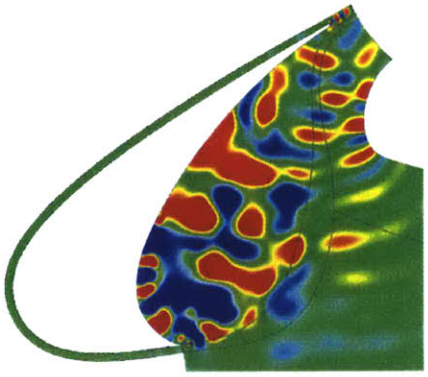

(d) 6° pressure mode 34

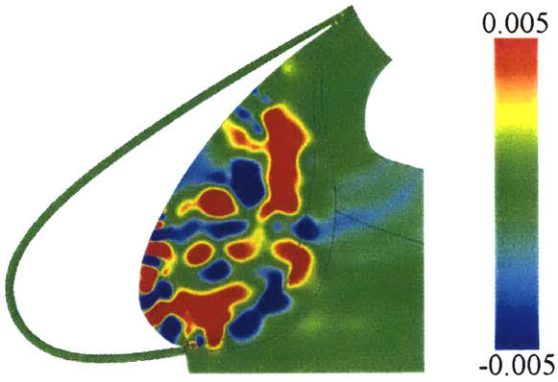

(e) 6° pressure Mode 35

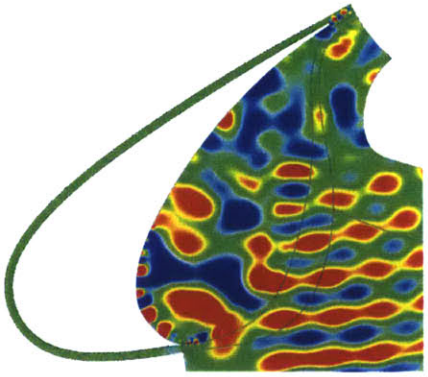

(f) 6° pressure mode 36

Figure B-8: 6-degree pressure modes 31–36.

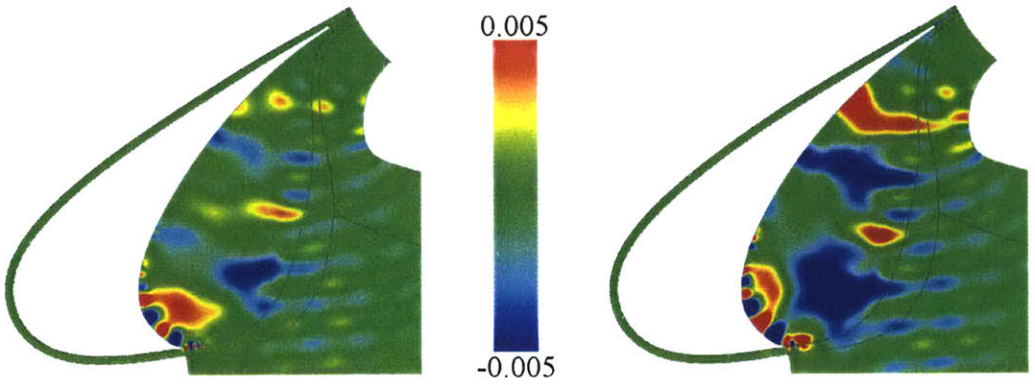

(a) 8° pressure mode 13

(b) 8° pressure mode 14

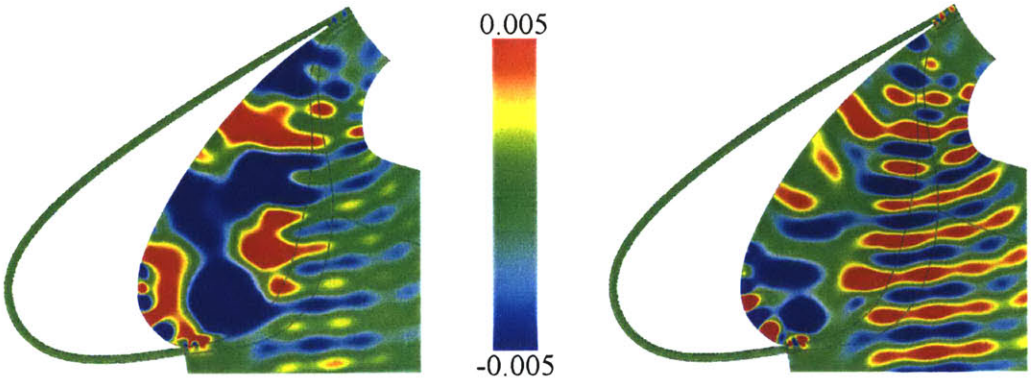

(c) 8° pressure mode 15

(d) 8° pressure mode 16

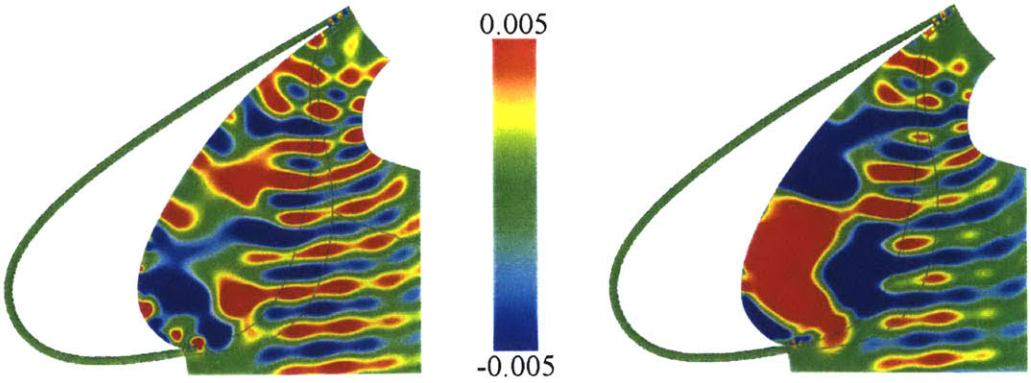

(e) 8° pressure Mode 17

(f) 8° pressure mode 18

Figure B-9: 8-degree pressure modes 13–18.

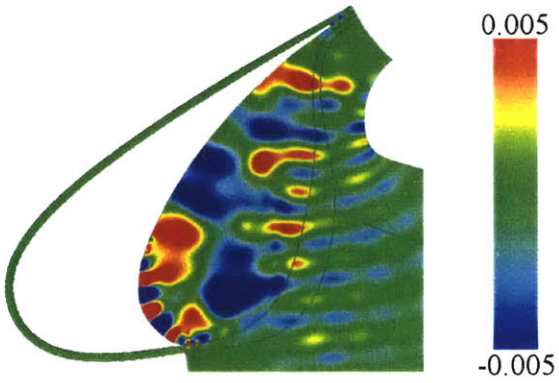

(a) 8° pressure mode 19

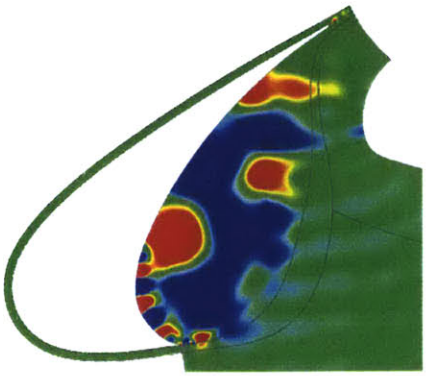

(b) 8° pressure mode 20

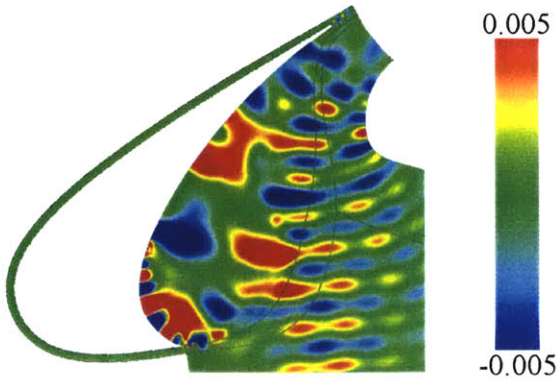

(c) 8° pressure mode 21

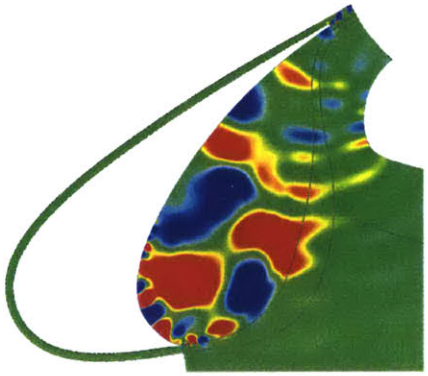

(d) 8° pressure mode 22

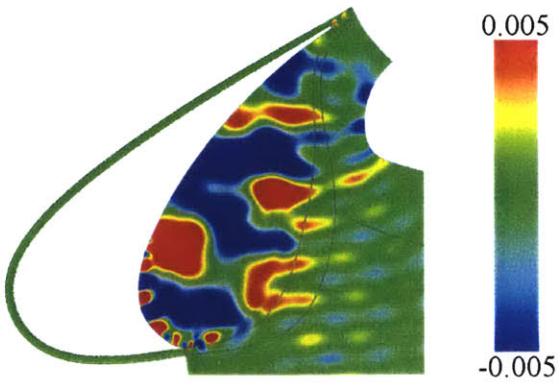

(e) 8° pressure Mode 23

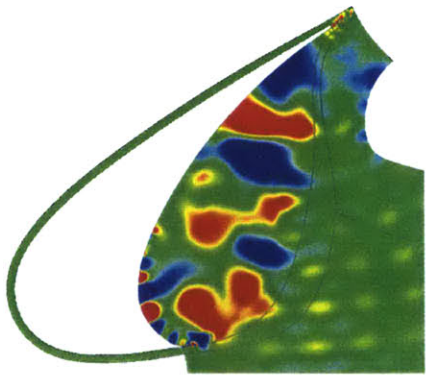

(f) 8° pressure mode 24

Figure B-10: 8-degree pressure modes 19–24.

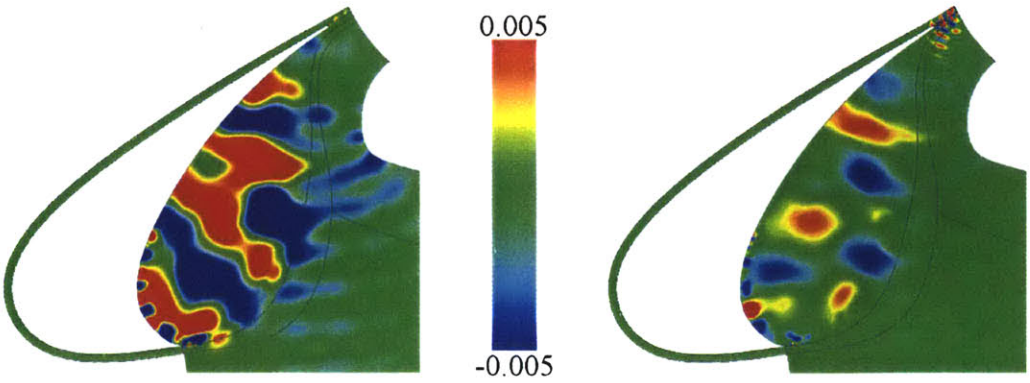

(a) 8° pressure mode 25

(b) 8° pressure mode 26

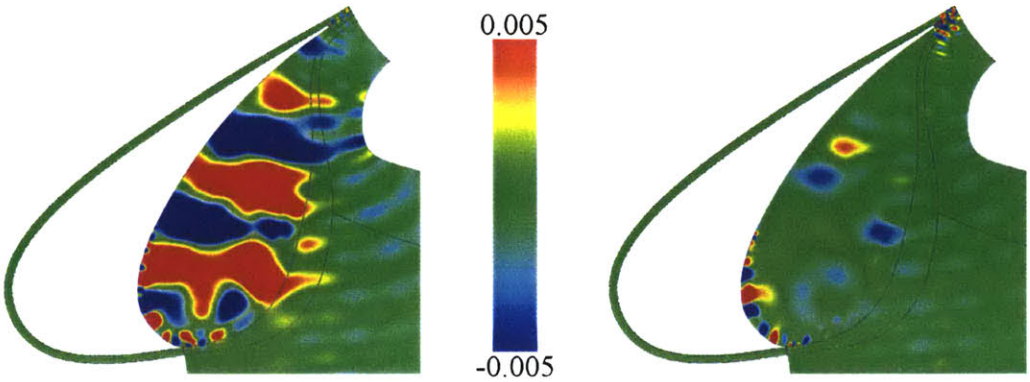

(c) 8° pressure mode 27

(d) 8° pressure mode 28

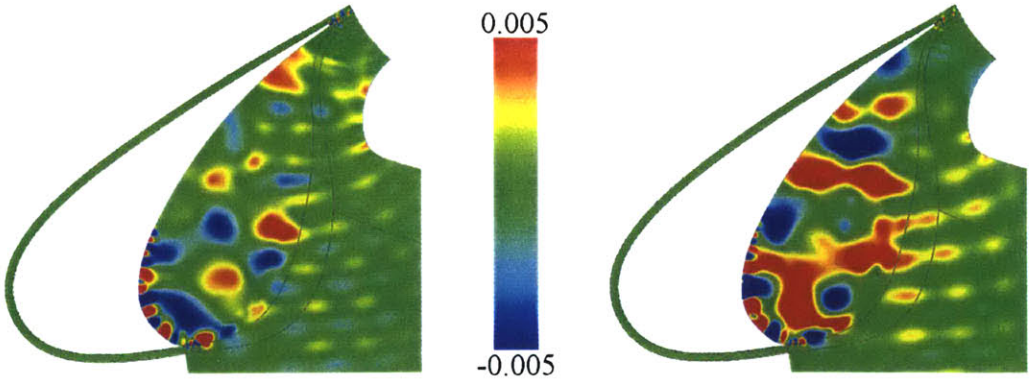

(e) 8° pressure Mode 29

(f) 8° pressure mode 30

Figure B-11: 8-degree pressure modes 25–30.

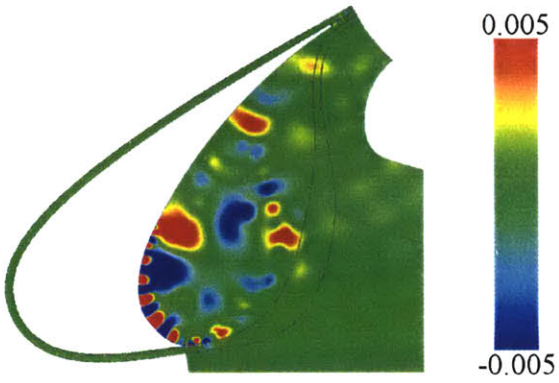

(a) 8° pressure mode 31

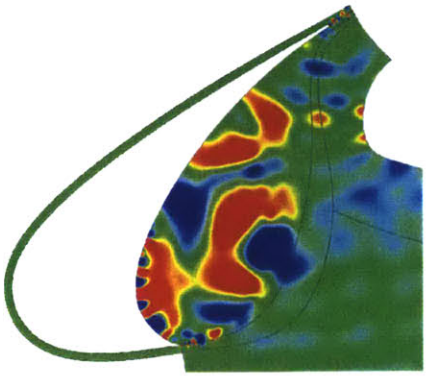

(b) 8° pressure mode 32

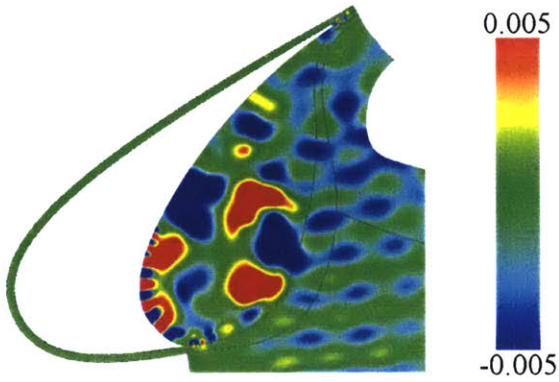

(c) 8° pressure mode 33

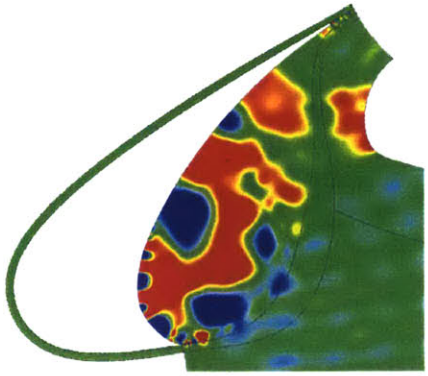

(d) 8° pressure mode 34

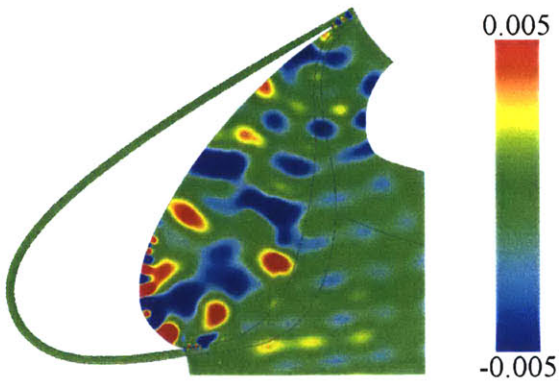

(e) 8° pressure Mode 35

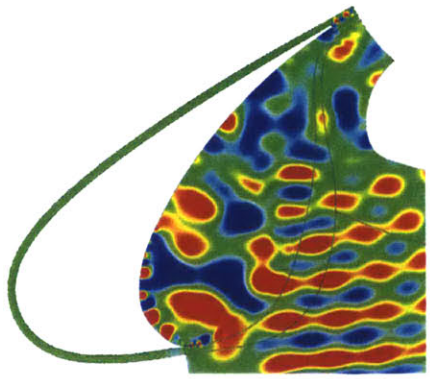

(f) 8° pressure mode 36

Figure B-12: 8-degree pressure modes 31–36.

B.2 POD Velocity Modes 13-36

The following pages contain an expanded collection of the POD pressure modes at 4-, 6-, and 8-degrees angle of attack. Modes 1-12 may be found in Figures 3-20 and 3-21 for the 4-degree decomposition, Figures 3-24 and 3-25 for the 6-degree decomposition, and Figures 3-29 and 3-30 for the 8-degree decomposition. POD mode numbers 13-36 are provided in the following pages for the velocity field decompositions at the three angles of attack.

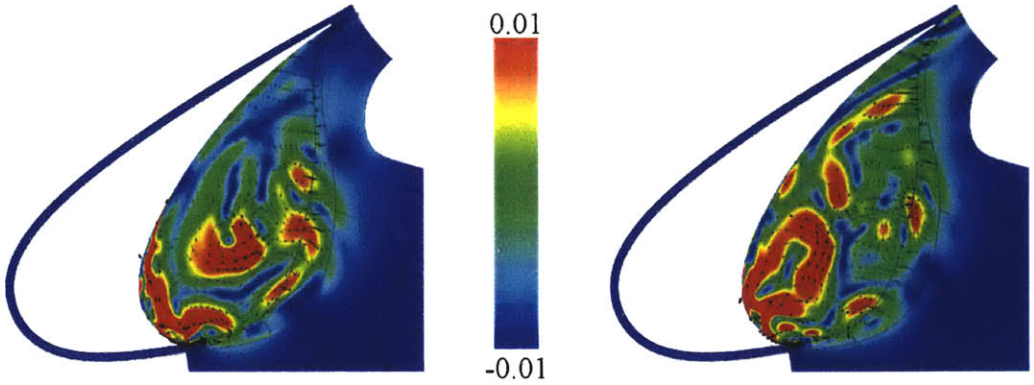

(a) 4° velocity mode 13

(b) 4° velocity mode 14

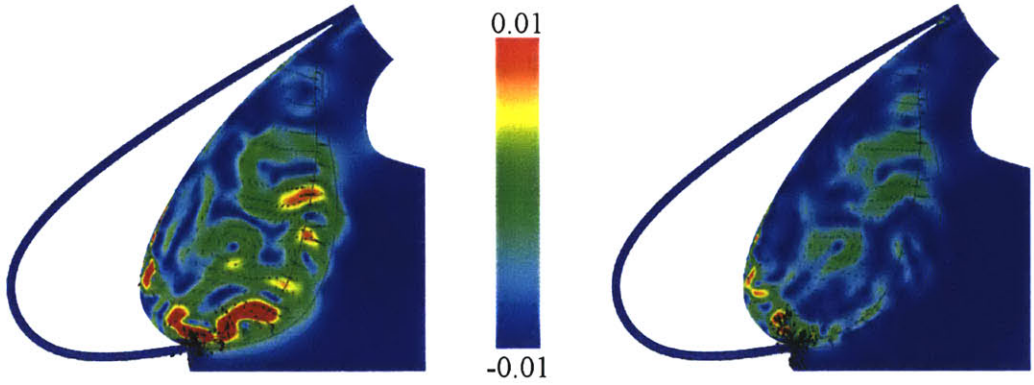

(c) 4° velocity mode 15

(d) 4° velocity mode 16

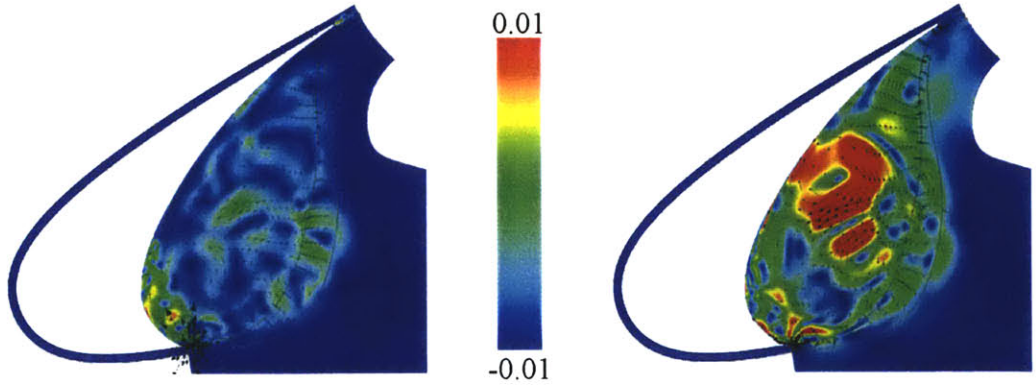

(e) 4° velocity Mode 17

(f) 4° velocity mode 18

Figure B-13: 4-degree velocity modes 13–18.

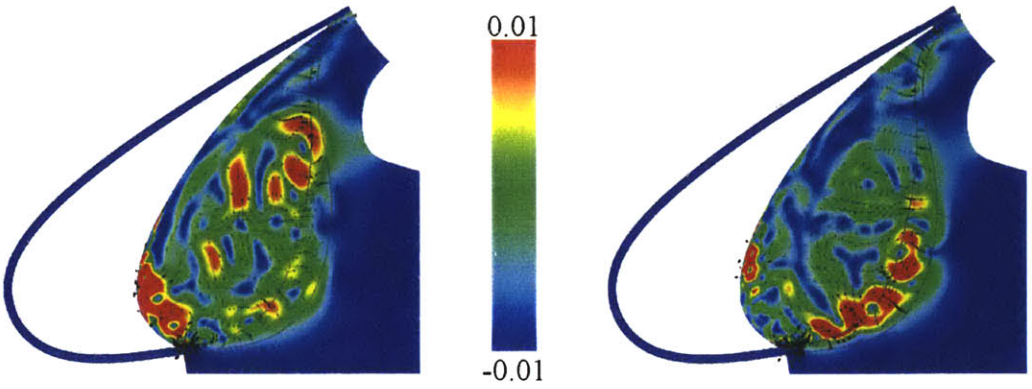

(a) 4° velocity mode 19

(b) 4° velocity mode 20

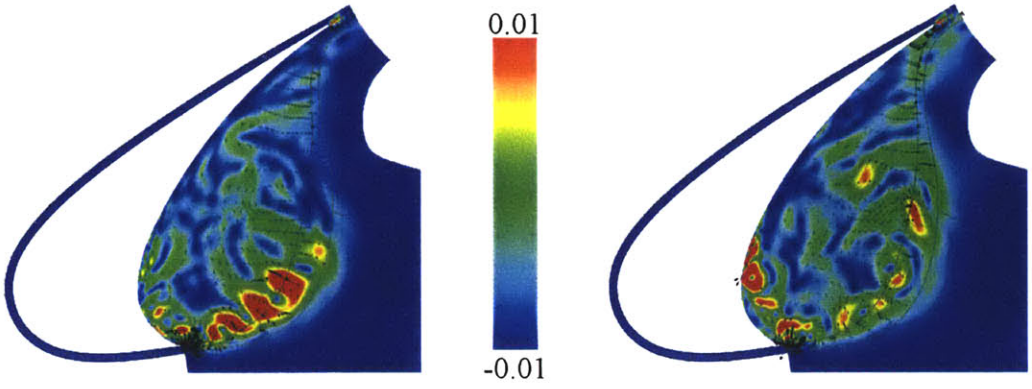

(c) 4° velocity mode 21

(d) 4° velocity mode 22

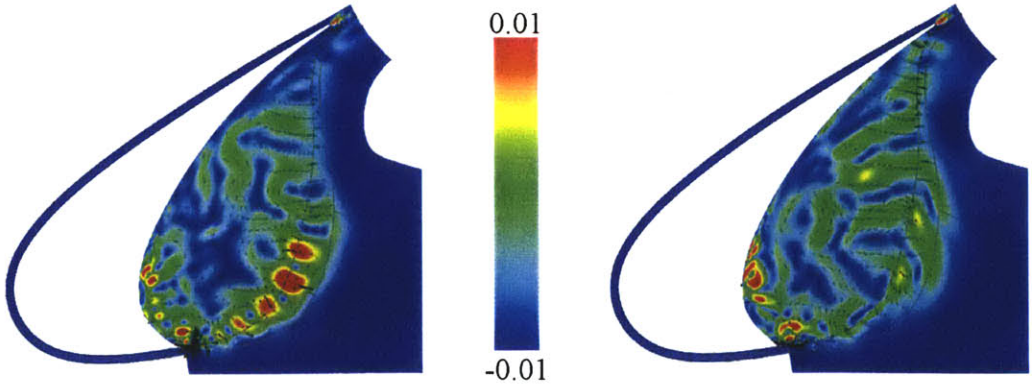

(e) 4° velocity Mode 23

(f) 4° velocity mode 24

Figure B-14: 4-degree velocity modes 19–24.

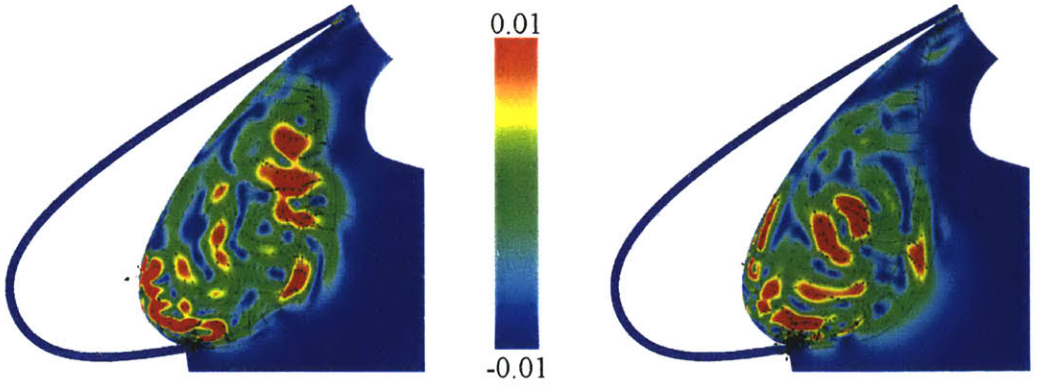

(a) 4° velocity mode 25

(b) 4° velocity mode 26

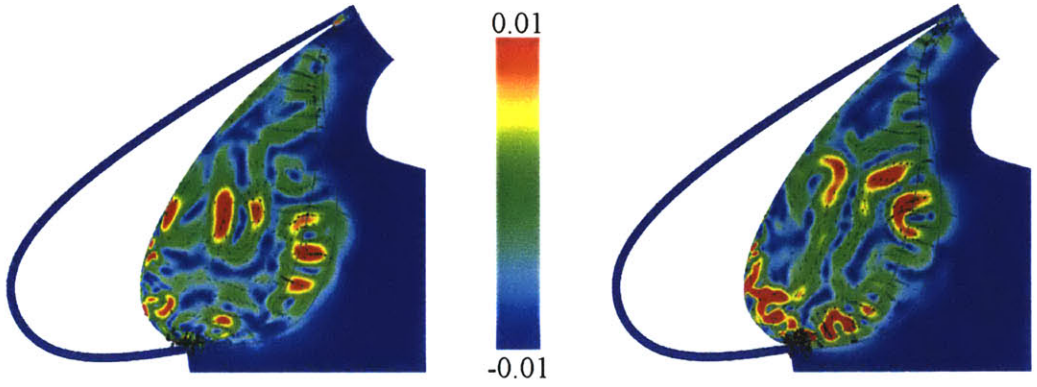

(c) 4° velocity mode 27

(d) 4° velocity mode 28

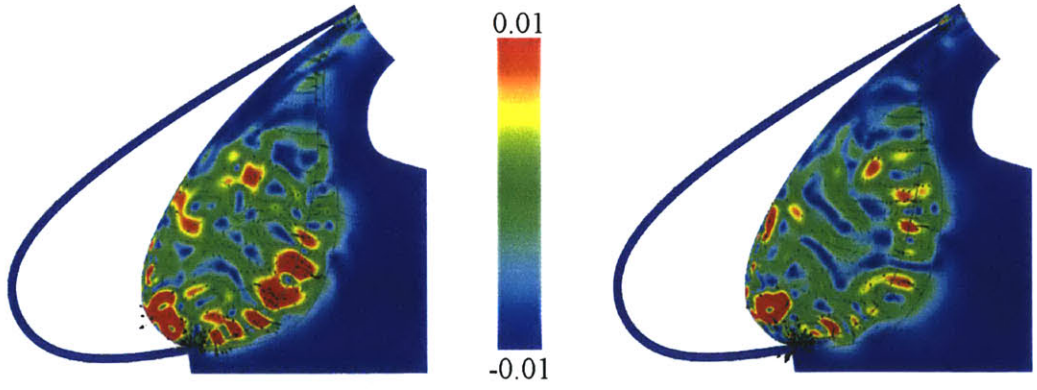

(e) 4° velocity Mode 29

(f) 4° velocity mode 30

Figure B-15: 4-degree velocity modes 25–30.

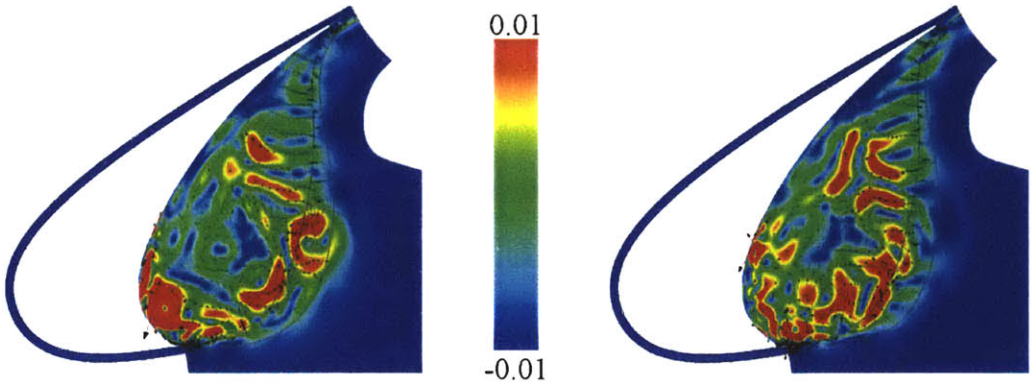

(a) 4° velocity mode 31

(b) 4° velocity mode 32

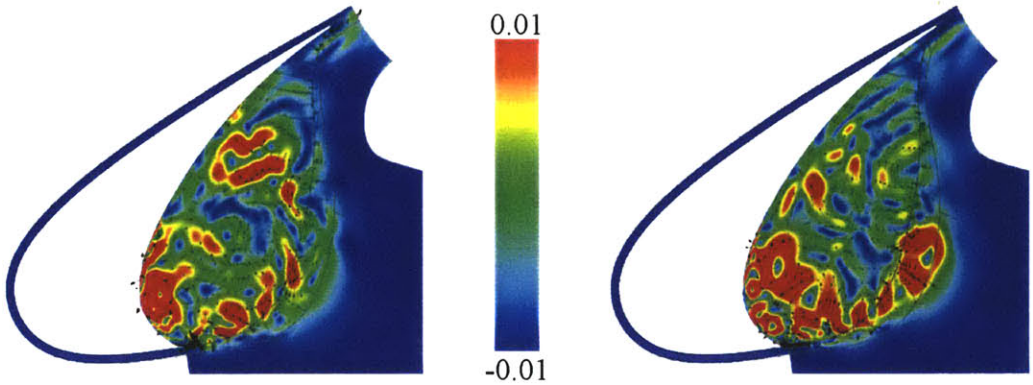

(c) 4° velocity mode 33

(d) 4° velocity mode 34

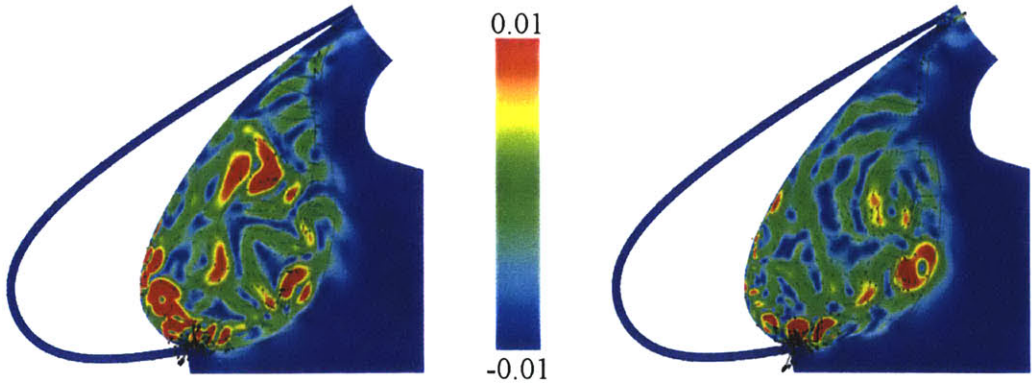

(e) 4° velocity Mode 35

(f) 4° velocity mode 36

Figure B-16: 4-degree velocity modes 31–36.

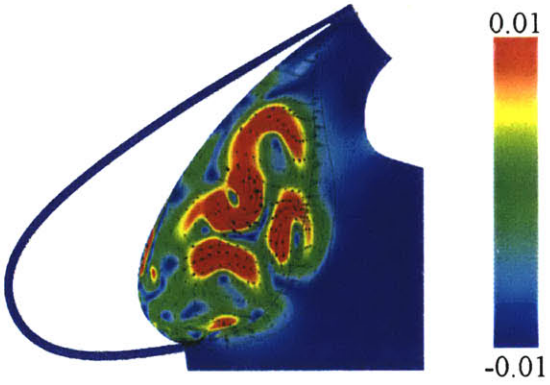

(a) 6° velocity mode 13

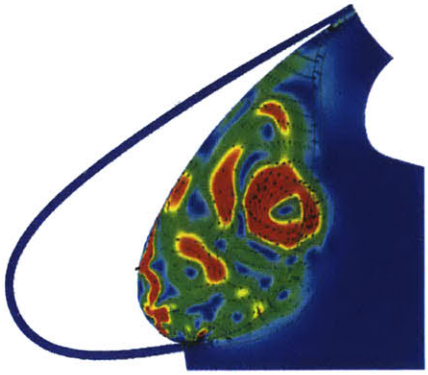

(b) 6° velocity mode 14

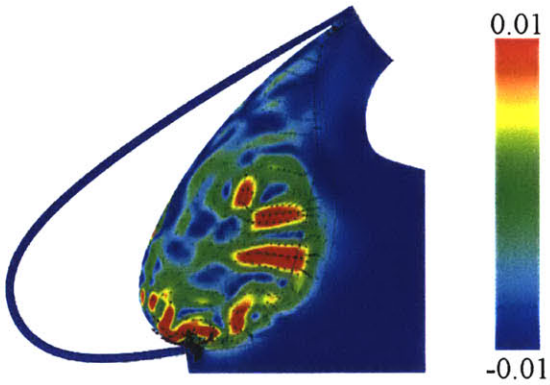

(c) 6° velocity mode 15

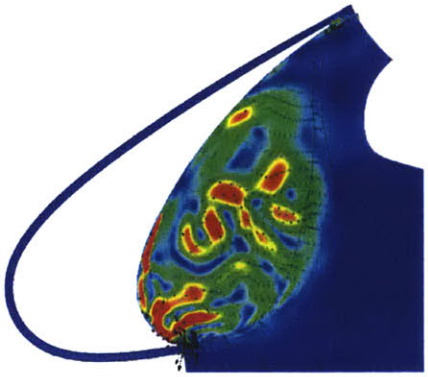

(d) 6° velocity mode 16

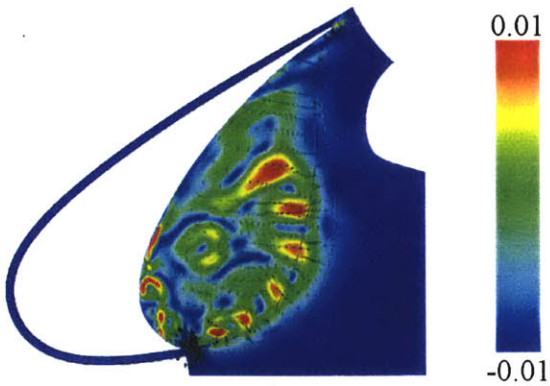

(e) 6° velocity Mode 17

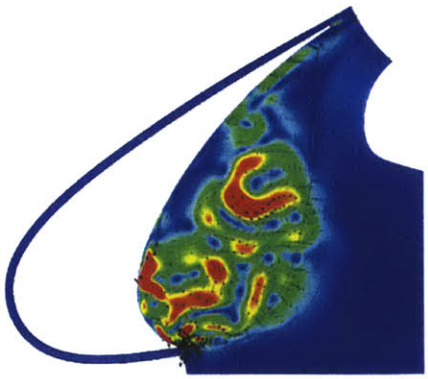

(f) 6° velocity mode 18

Figure B-17: 6-degree velocity modes 13–18.

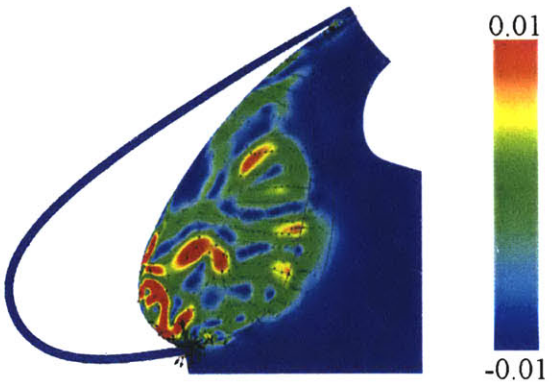

(a) 6° velocity mode 19

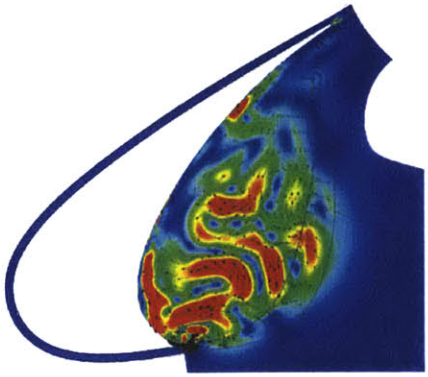

(b) 6° velocity mode 20

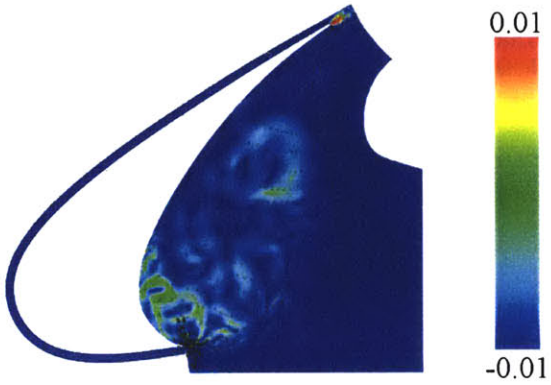

(c) 6° velocity mode 21

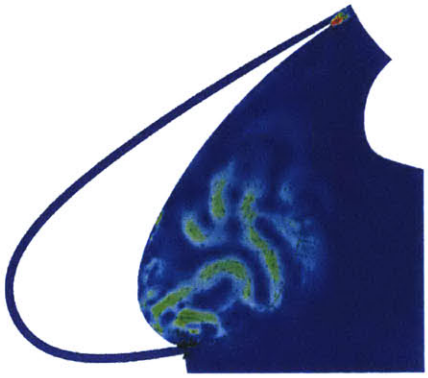

(d) 6° velocity mode 22

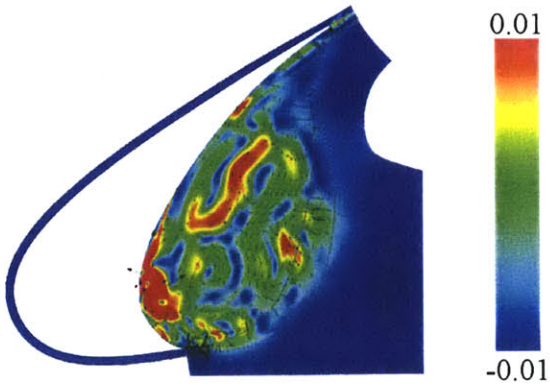

(e) 6° velocity Mode 23

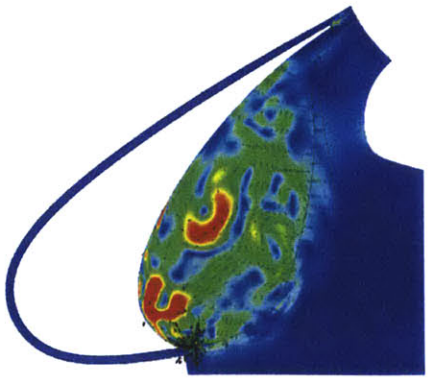

(f) 6° velocity mode 24

Figure B-18: 6-degree velocity modes 19–24.

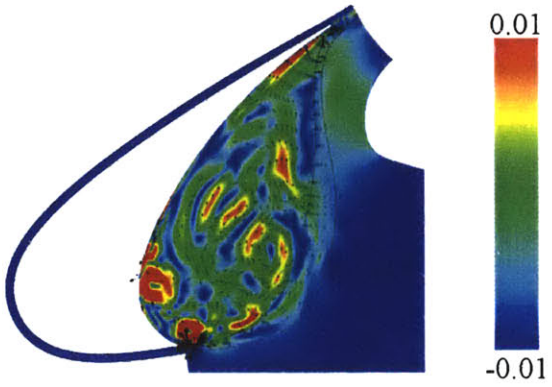

(a) 6° velocity mode 25

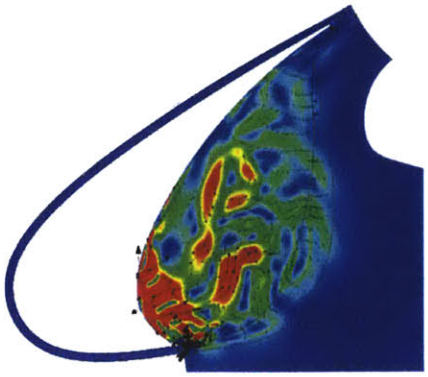

(b) 6° velocity mode 26

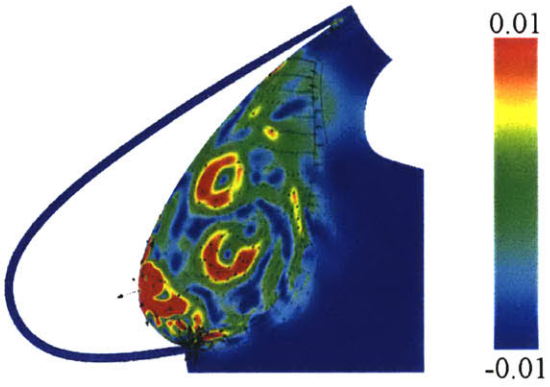

(c) 6° velocity mode 27

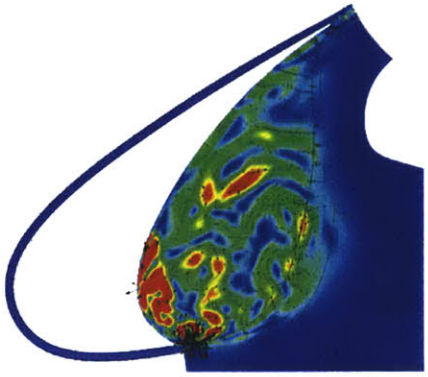

(d) 6° velocity mode 28

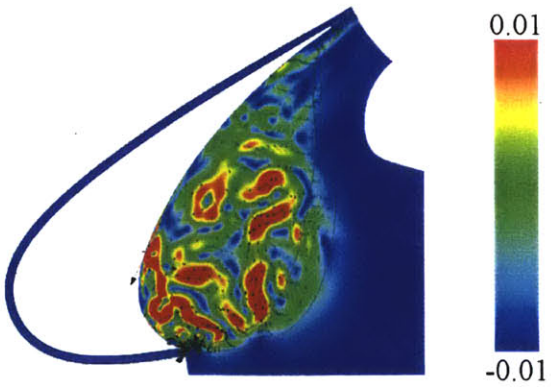

(e) 6° velocity Mode 29

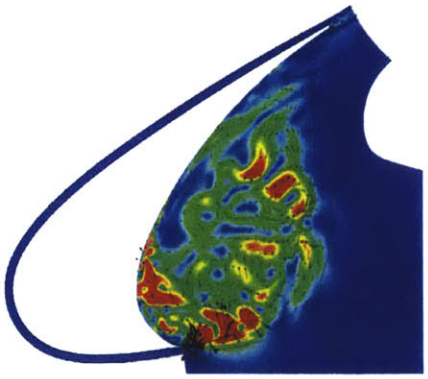

(f) 6° velocity mode 30

Figure B-19: 6-degree velocity modes 25–30.

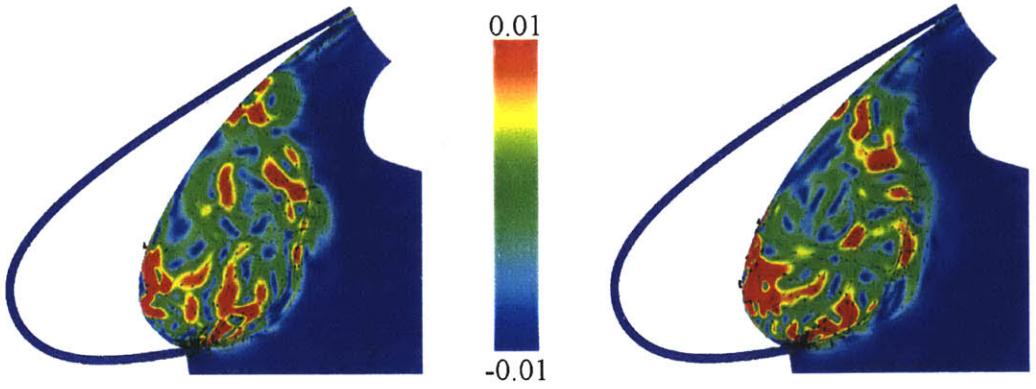

(a) 6° velocity mode 31

(b) 6° velocity mode 32

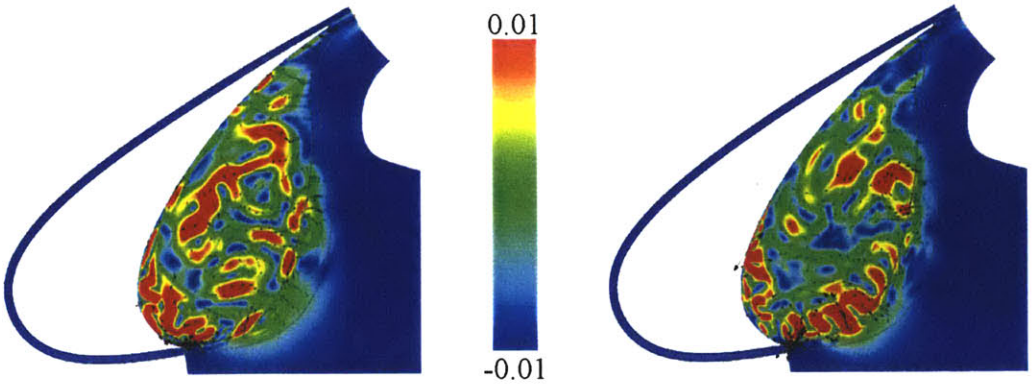

(c) 6° velocity mode 33

(d) 6° velocity mode 34

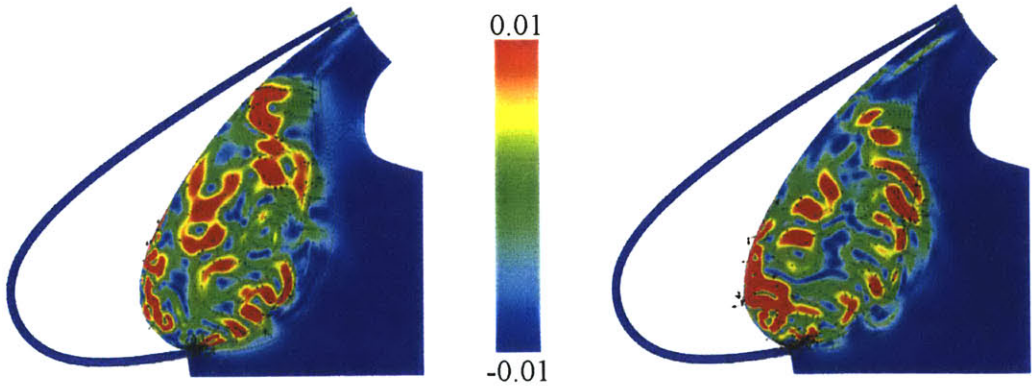

(e) 6° velocity Mode 35

(f) 6° velocity mode 36

Figure B-20: 6-degree velocity modes 31–36.

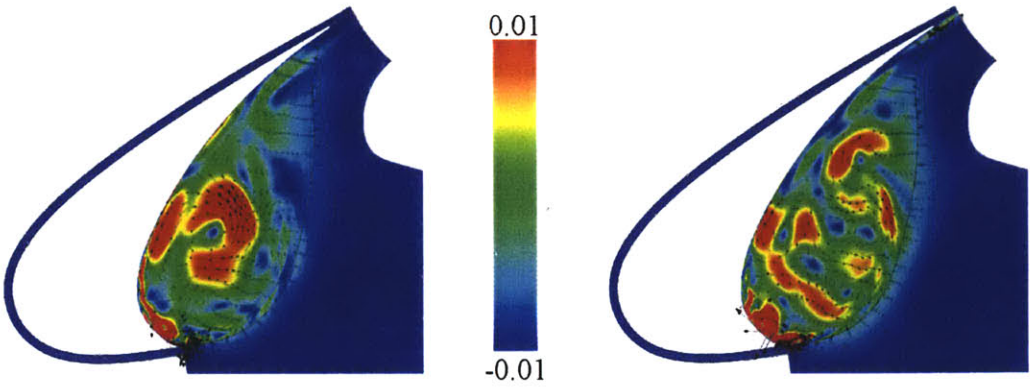

(a) 8° velocity mode 13

(b) 8° velocity mode 14

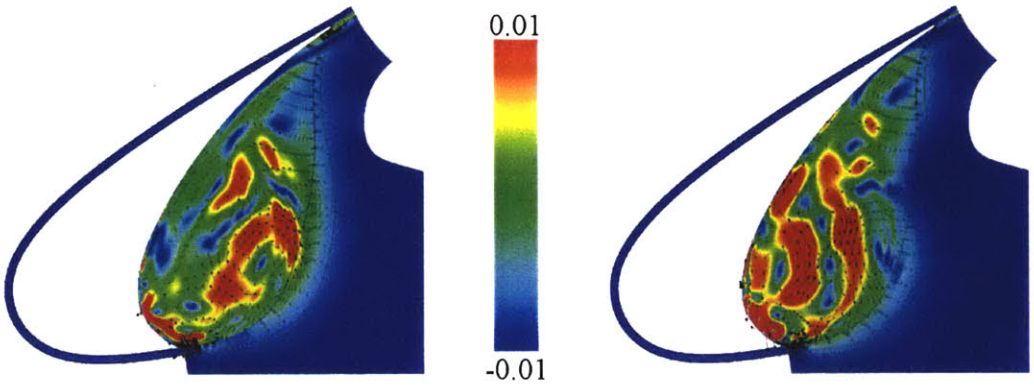

(c) 8° velocity mode 15

(d) 8° velocity mode 16

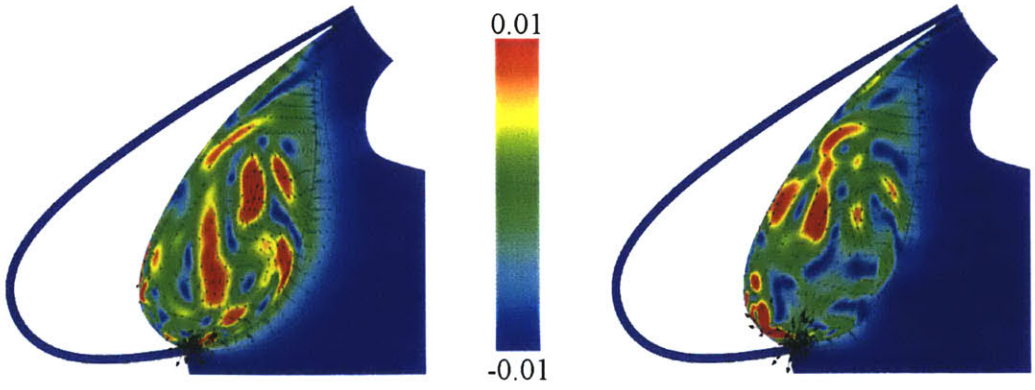

(e) 8° velocity Mode 17

(f) 8° velocity mode 18

Figure B-21: 8-degree velocity modes 13–18.

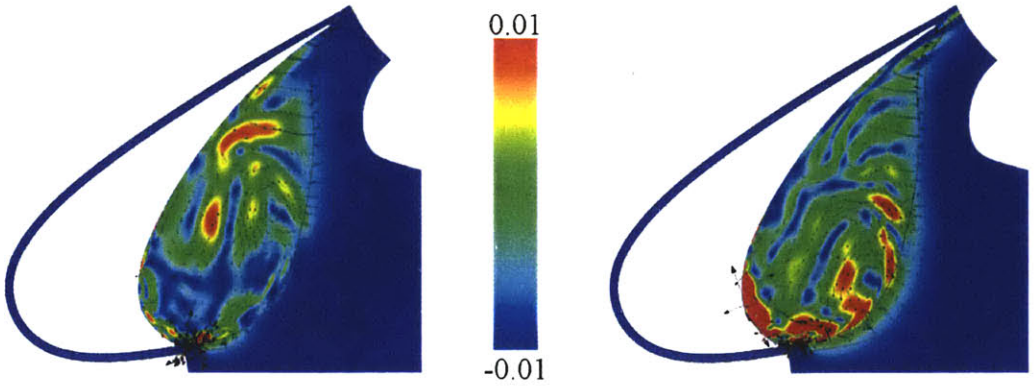

(a) 8° velocity mode 19

(b) 8° velocity mode 20

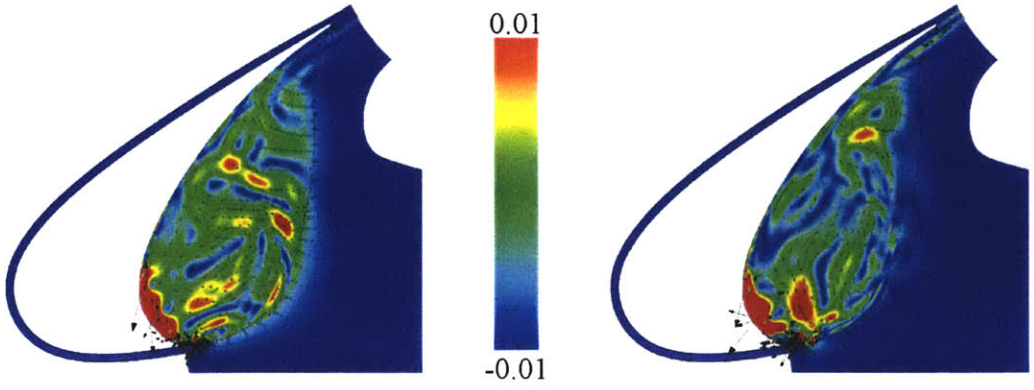

(c) 8° velocity mode 21

(d) 8° velocity mode 22

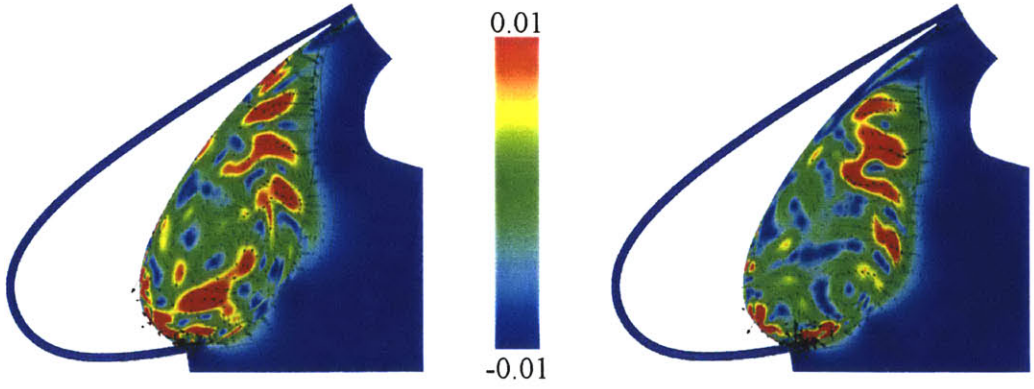

(e) 8° velocity Mode 23

(f) 8° velocity mode 24

Figure B-22: 8-degree velocity modes 19–24.

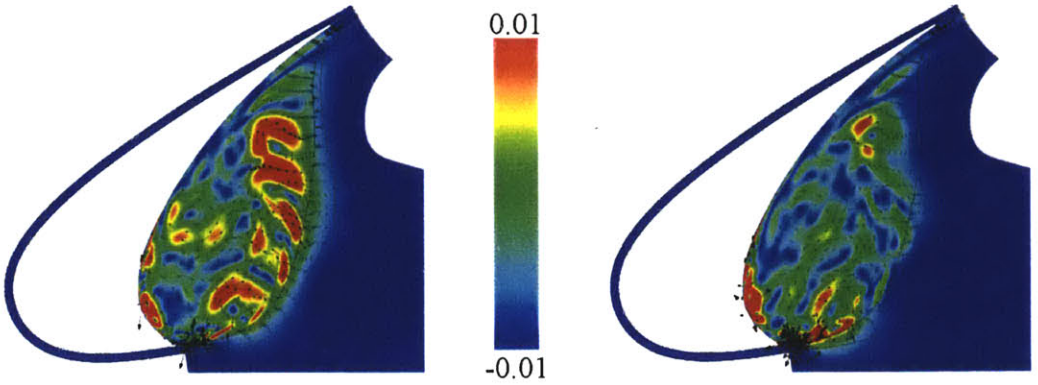

(a) 8° velocity mode 25

(b) 8° velocity mode 26

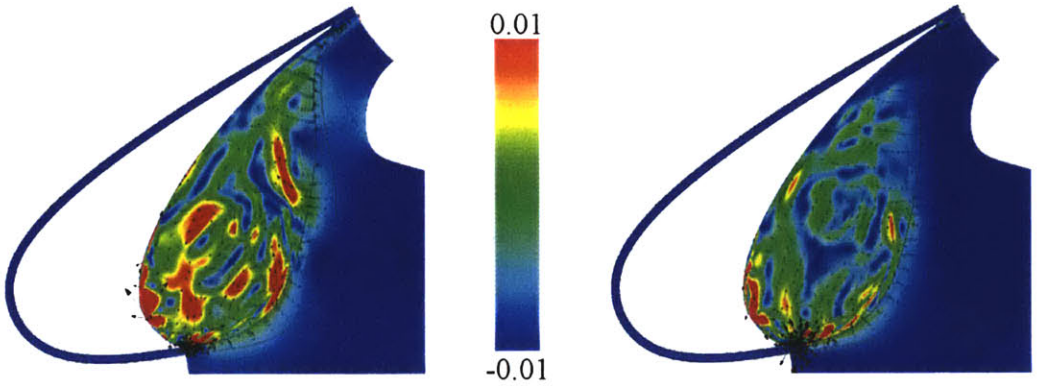

(c) 8° velocity mode 27

(d) 8° velocity mode 28

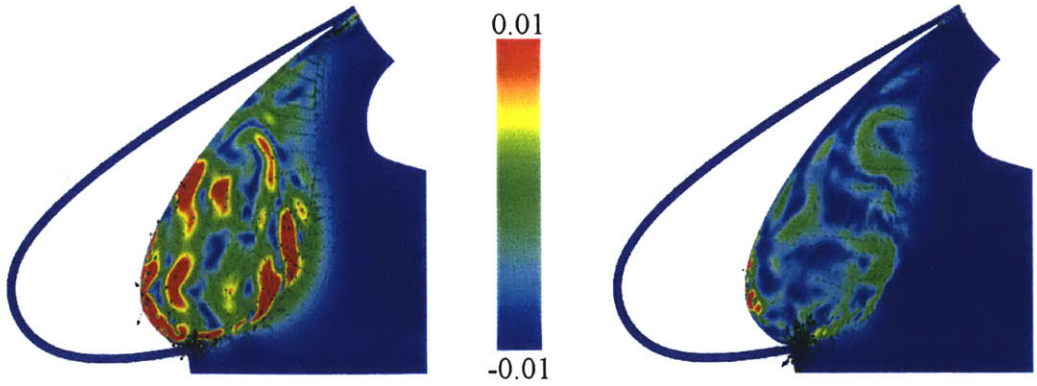

(e) 8° velocity Mode 29

(f) 8° velocity mode 30

Figure B-23: 8-degree velocity modes 25–30.

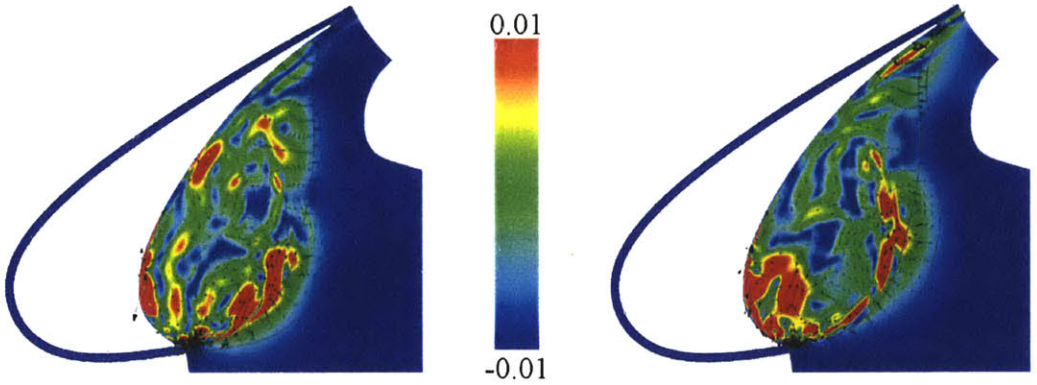

(a) 8° velocity mode 31

(b) 8° velocity mode 32

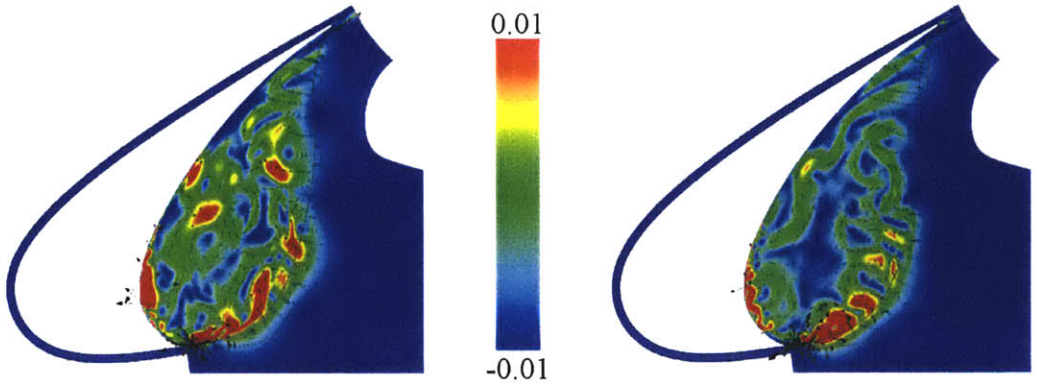

(c) 8° velocity mode 33

(d) 8° velocity mode 34

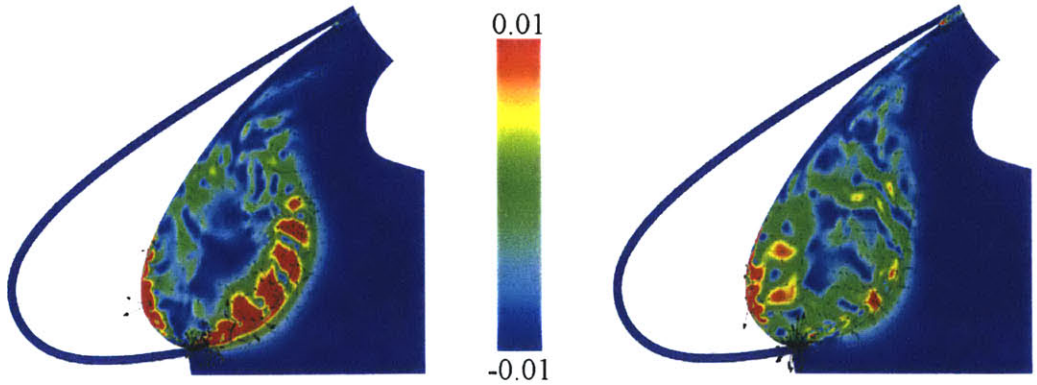

(e) 8° velocity Mode 35

(f) 8° velocity mode 36

Figure B-24: 8-degree velocity modes 31–36.

Bibliography

[1] National Aeronautics and Space Administration, *Roadmaps to the future: Strategic roadmaps in support of the Three Pillars and Ten Goals*, NASA (1986).

[2] ———, *NASA Strategic Plan 1998*, NASA Policy Directive (NPD) - 1000.1 (1998).

[3] V.R. Algazi and D.J. Sakrison, *On the optimality of the Karhunen-Loève expansion*, IEEE Transactions on Information Theory **15** (1969), 319–321.

[4] C.A. Andrews, J.M. Davies, and G.R. Schwartz, *Adaptive data compression*, Proc. IEEE **55** (1967), 267–277.

[5] H. Aubrey and S. Lumley, *The dynamics of coherent structures in the wall region of turbulent shear layer*, Journal of Fluid Mechanics **192** (1988), 115–175.

[6] K. Ball, K. Sirovich, and L. Keefe, *Dynamical eigenfunction decomposition of turbulent channel flow*, Int. Journal for Numerical Methods in Fluids **12** (1991), 585–604.

[7] M.E. Berkman, M.R. Khorrami, M. Choudhari, and S.S. Sadowski, *Investigation of high-lift flow field of an Energy Efficient Transport wing*, AIAA 2002-2604 (2002).

[8] G. Berkooz, *Turbulence, coherent structures, and low dimensional models*, Ph.D. thesis, Cornell University, 1991.

[9] G. Berkooz, P. Holmes, and J.L. Lumley, *The proper orthogonal decomposition in the analysis of turbulent flows*, Annual Review of Fluid Mechanics **25** (1993), 539–75.

[10] K.S. Brentner and F. Farassat, *An analytical comparison of the acoustic analogy and Kirchhoff formulation for moving surfaces*, AIAA Journal **36** (1998), no. 8, 1379–1386.

[11] T.F. Brooks and W.M. Humphreys, *Flap edge aeroacoustic measurements and predictions*, AIAA 2000-1975 (2000).

[12] A. Chatterjee, *An introduction to the proper orthogonal decomposition*, Current Science **78** (2000), no. 7, 808–817.

[13] M. Choudhari, M.R. Khorrami, H. Atkins, and G. Lilley, *Slat cove noise modeling: A posteriori analysis of unsteady rans simulations*, AIAA 2002-2468 (2002).

[14] L. Cordier and M. Bergmann, *Proper orthogonal decomposition: An overview*, Lecture Series 2000-04 on Post-Processing of Experimental and Numerical Data, Von Karman Institute for Fluid Dynamics (2002).

[15] ———, *Two typical applications of pod: Coherent structures eduction and reduced order modelling*, Lecture Series 2000-04 on Post-Processing of Experimental and Numerical Data, Von Karman Institute for Fluid Dynamics (2002).

[16] R. Courant and D. Hilbert, *Methods of mathematical physics Vol. 1*, John-Wiley and Sons, New York, 1953.

[17] J.P. Cusumano, M.T. Sharkady, and B.W. Kimble, *Experimental measurements of dimensionality and spatial coherence in the dynamics of a flexible-beam impact oscillator*, Philosophical Transactions of the Royal Society of London **A: 347** (1994), 421–438.

[18] H. Davy and R. Remy, *Airframe noise characteristics on a 1/11 scale Airbus model*, AIAA 98-2335 (1998).

[19] A.E. Deane, I.G. Kevrekidis, G.E. Karniadakis, and S.A. Orszag, *Low-dimensional models for complex geometry flows: Application to grooved channels and circular cylinders*, Phys. Fluids **7** (1991), no. 10.

[20] J. Delville, *Characterization of the organization in shear layers via the proper orthogonal decomposition*, Applied Scientific Research **53** (1994), 263–281.

[21] B.F. Feeny and R. Kappagantu, *On the physical interpretation of proper orthogonal modes in vibrations*, Journal of Sound and Vibration **211** (1998), no. 4, 607–616.

[22] J.E. Ffowcs Williams and D.L. Hawkings, *Sound generated by turbulence and surfaces in arbirtrary motion*, Philosophical Transactions of the Royal Society **A264** (1969), no. 1151, 321–342.

[23] E. Gillies, *Low-dimensional control of the circular cylinder wake*, Journal of Fluid Mechanics **371** (1998), 157–178.

[24] G.H. Golub and C.F. Van Loan, *Matrix computations*, North Oxford Academic, Oxford, 1983.

[25] S. Gordeyev, *Pod, lse, and wavelet decomposition: Literature review*, (2000).

[26] Y.P. Guo, *A discrete vortex model for slat noise generation*, AIAA 2001-2157 (2001).

[27] P. Holmes, J.L. Lumley, and G. Berkooz, *Turbulence, coherent structures, dynamical systems and symmetry*, Cambridge University Press, Cambridge, 1996.

[28] H. Hotelling, *Analysis of a complex of statistical variables into principal components*, Journal of Educational Psychology **24** (1933), 417–441.

[29] I.T. Joliffe, *Principal components analysis*, Springer-Verlag, New York, 1986.

[30] K. Karhunen, *Zur spektraltheorie stochasticher*, Prozessa Ann. Acad. Sci. Fennicae **37** (1946).

[31] M.R. Khorrami, M.E. Berkman, M. Choudhari, B.A. Singer, D.P. Lockard, and K.S. Brentner, *Unsteady flow computations of a slat with a blunt trailing edge*, AIAA 99-1805 (1999).

[32] M.R. Khorrami, B.A. Singer, and M.E. Berkman, *Time-accurate simulations and acoustic analysis of slat free-shear-layer*, AIAA 2001-2155 (2001).

[33] M.R. Khorrami, B.A. Singer, and D.P. Lockard, *Time-accurate simulations and acoustic analysis of slat free-shear-layer—Part II*, AIAA 2002-2579 (2002).

[34] M.R. Khorrami, B.A. Singer, and R.H. Radeztsky, *Reynolds averaged navier-stokes computations of a flap side-edge flow field*, AIAA 98-0768 (1998).

[35] M. Kirby and L. Sirovich, *Application of the Karhunen-Loève procedure for the characterization of human faces*, IEEE Transactions on Pattern Analysis and Machine Intelligence **12** (1990), no. 1, 103–108.

[36] D. Koditschek, W. Schwind, M. Garcia, and R. Full, *Cockroach posture identification using principal component analysis*, In preparation (1999).

[37] S.L. Krist, C. Rumsey, R.T. Biedron, and C. Rumsey, *CFL3D User's Manual (Version 5)*, NASA Langley Research Center, Aerodynamic and Acoustic Methods Branch, Hampton, VA, 1997.

[38] D.P. Lockard, *An efficient, two-dimensional implementation of the Ffowcs Williams and Hawkings equation*, Journal of Sound and Vibration (1999).

[39] ———, *An overview of computational aeroacoustic modeling at NASA Langley*, NASA-99-10tfaw (1999).

[40] ———, *A comparison of Ffowcs Williams-Hawkings solvers for airframe noise applications*, AIAA 2002-2580 (2002).

[41] M.M. Loève, *Probability theory*, Van Nostrand, Princeton, New Jersey, 1955.

[42] E.N. Lorenz, *Empirical orthogonal functions and statistical weather prediction*, MIT Department of Meteorology, Statistical Forecasting Project (1956).

[43] J.L. Lumley, *The structure of inhomogeneous turbulent flows*, Atmospheric Turbulence and Wave Propagation (1967), 166–178.

[44] M.G. Macaraeg, *Fundamental investigations of airframe noise*, AIAA 98-2224 (1998).

[45] M.G. Macaraeg, D.P. Lockard, and C.L. Streett, *In search of the physics: NASA's approach to airframe noise*, NASA-99-swing-mgm (1999).

[46] K.R. Meadows, T.F. Brooks, W.M. Humphreys, W.W Hunter, and C.H. Gerhold, *Acoustic and unsteady surface pressure measurements of a main element-flap configuration*, AIAA 97-1595 (1997).

[47] J.F. Mendoza, T.F. Brooks, and W.M. Humphreys Jr., *Aeroacoustic measurements of a wing/slat model*, AIAA 2002-2604 (2002).

[48] H.L. Morgan, *Model geometry description and pressure distribution data from tests of EET high-lift research model equipped with full-span slat and part-span flaps*, NASA TM 80048 (1979).

[49] A. Papoulis, *Probability, random variables, and stochastic processes*, McGraw-Hill, New York, 1965.

[50] R.H. Radeztsky, B.A. Singer, and M.R. Khorrami, *Detailed measurements of a flap side-edge flow field*, AIAA 98-700 (1998).

[51] M. Rathinam and L.R. Petzold, *A new look at proper orthogonal decomposition*, submitted to SIAM Journal on Numerical Analysis (2000).

[52] S. Ravindran, *Proper orthogonal decomposition in optimal control of fluids*, Tech. Report NASA/TM-1999-209113, March 1999.

[53] F. Reisz and B.S. Nagy, *Functional analysis*, Ungar, New York, 1955.

[54] R. Ruotolo and C. Surace, *Using SVD to detect damage detection in structures with different operational conditions*, Journal of Sound and Vibration **226** (1999), no. 3, 425–439.

[55] B.A. Singer, K.S. Brentner, D.P. Lockard, and G.M. Lilley, *Simulation of acoustic scattering from a trailing edge*, Journal of Sound and Vibration **230** (2000), no. 3, 541–560.

[56] B.A. Singer, D.P. Lockard, K.S. Brentner, M.R. Khorrami, M.E. Berkman, and M. Choudhari, *Computational aeroacoustic analysis of slat trailing-edge flow*, AIAA 99-1802 (1999).

[57] L. Sirovich, *Turbulence and the dynamics of coherent structures. Part 1: Coherent structures; Part 2: Symmetries and transformations; Part 3: Dynamics and scaling*, Quarterly of Applied Mathematics **45** (1999), no. 3, 561–590.

[58] L. Ukeiley, *Dynamics of large scale structures in a plane turbulent mixing layer*, Ph.D. thesis, Clarkson University, 1995.

[59] J.R. Underbrink and R.P. Dougherty, *Array design for non-intrusive measurements of noise sources*, Noisecon 96 (1996).

[60] K. Willcox, *Reduced-order aerodynamic models for aeroelastic control of turbomachines*, PhD thesis, Massachusetts Institute of Technology, Department of Aeronautics and Astronautics, November 1999.